

University of Alberta

**Study on the Microstructure and Mechanical Properties of Submerged Arc
Welded X80 Steel**

by

Syed Md Zakaria

A thesis submitted to the Faculty of Graduate Studies and Research
in partial fulfillment of the requirements for the degree of

Master of Science
in
Materials Engineering

Chemical and Materials Engineering

©Syed Md Zakaria
Fall 2012
Edmonton, Alberta

Permission is hereby granted to the University of Alberta Libraries to reproduce single copies of this thesis and to lend or sell such copies for private, scholarly or scientific research purposes only. Where the thesis is converted to, or otherwise made available in digital form, the University of Alberta will advise potential users of the thesis of these terms.

The author reserves all other publication and other rights in association with the copyright in the thesis and, except as herein before provided, neither the thesis nor any substantial portion thereof may be printed or otherwise reproduced in any material form whatsoever without the author's prior written permission.

Abstract

It is difficult to join high strength alloy steel which are produced by thermo mechanical controlled processing and get overmatched properties on the welds and heat affected zone (HAZ) when submerged arc welding (SAW) is used as joining process. Circumferential welds made in the mill to join shorter pipes into longer lengths generally employ SAW as this process offers excellent production rate. In this study two types of X80 steel plates (both 10.22 mm thick) with different carbon contents (0.06 wt% C versus 0.03 wt% C) were used. SAW was used to join the steel plates using varying heat inputs (from 1.5 to 2.25 kJ/mm) by varying the current. Charpy V-notch (CVN) results indicate that the higher carbon steel welds have better HAZ toughness than those with the lower carbon steel at all test temperatures (from 22 to -60°C). At higher temperatures the mode of fracture was found to be ductile in nature, whereas at lower temperatures (close to -40°C) both ductile and brittle behaviour were observed. Hardness results indicate that there is initial softening in the fine grain heat affected zone (FGHAZ) regions and hardening occurs predominantly in the coarse grain heat affected zone (CGHAZ) regions. Also, both steels demonstrate comparable results in that hardness in the HAZ decreases as the heat input increases. The transverse weld tensile specimens gave a good indication of ultimate strength; however, the degree of overmatching could not be resolved using transverse weld tensile testing, because of the limitation in measuring tensile properties of smaller individual regions (weld metal, CGHAZ and FGHAZ).

Acknowledgements

I would like to acknowledge and thank my supervisors Dr. Hani Henein and Dr. Douglas Ivey for their invaluable guidance and support throughout the duration of this research project. I would like to express my appreciation to Dr. Adrian Gerlich for his useful feedback and suggestions. Many thanks also go to Dr. Doug Boyd of Queen's University and Dr. Barry Wiskel for their guidance.

The Natural Sciences and Engineering Research Council (NSERC) of Canada and EVRAZ Inc. NA are gratefully acknowledged for their financial support for this project. The major experimental portion of this research work was due in part to the assistance and support of EVRAZ Inc. NA Research Division. Special thanks go to Chris Penniston, Laurie Collins and Jon Jackson.

I would also like to thank my colleagues/group members for helping me out with various technical aspects of this project. Nasseh Khodaie, Joel Pepin, Xiujun Li and Pooya Delshad Khatibi thank you very much for all your help and support.

Lastly my deepest gratitude goes to my friends, whose support and encouragement helped me tremendously during this study. Particularly I would like to thank Junaid Bhai, Mita Apu, Jony Bhaiya, Mohua Apu, Asif Bhai, Dita Apu, Emu Apu, Nafis Razzak, Porag Bhaiya, Susanjib Bhaiya and Sharif Abu Hayat. I am forever indebted to them for everything they have done for me.

Table of Contents

Chapter 1: Introduction	1
1.1 Overview	1
1.2 Objectives	3
1.3 Thesis Outline	3
Chapter 2: Literature Review	5
2.1 Thermo-mechanical Controlled Processing (TMCP)	5
2.2 Arc Welding Process Overview	9
2.2.1 Gas Metal Arc Welding (GMAW)	10
2.2.2 Gas Tungsten Arc Welding (GTAW)	12
2.2.3 Shielded Metal Arc Welding (SMAW)	14
2.2.4 Submerged Arc Welding (SAW)	16
2.3 SAW Welding Conditions and Process Variables	19
2.3.1 Heat Input	19
2.3.2 Arc Voltage	21
2.3.3 Welding Current	22
2.3.4 Travel Speed	24
2.3.5 Wire Size	25
2.3.6 Fluxes used in SAW	26
2.4 Welding Metallurgy	27
2.5 Weldability of TMCP Steels	31
2.6 Welding of Microalloyed Steel Using SAW	33
2.6.1 Weld and HAZ Microstructure	34
2.6.1.1 Polygonal Ferrite	37
2.6.1.2 Acicular Ferrite	38
2.6.1.3 Bainitic Ferrite	40
2.6.1.4 Bainite	41
2.6.1.5 Martensite	44
2.6.1.6 Widmanstätten Ferrite	47
2.6.1.7 M-A Constituent	50

Chapter 3: Materials and Experimental Methods	51
3.1 Materials	51
3.2 Welding Procedure and Parameters	52
3.3 Weld Characterization	60
3.3.1 Weld Geometry Measurement	60
3.3.2 Microhardness Measurement	62
3.3.3 Tensile Testing	64
3.3.4 Charpy Impact Testing	66
3.3.5 Metallographic Sample Preparation for Optical Microscopy	68
3.3.6 Grain Size Measurements	69
3.3.7 Scanning Electron Microscopy	73
3.3.8 Transmission Electron Microscopy	74
4.0 Summary	75
Chapter 4: Welding Performance and Weld Melting Efficiency	76
4.1 Welding Performance in Terms of Weld Bead Shape Parameters	76
4.2 Effect of Heat Input on Weld Bead Geometry	77
4.3 Effect of Total Molten Area/ Heat Input on Single and Tandem Electrode Welds	85
4.4 Bead Shape	91
4.5 Weld Melting Efficiency	94
4.6 Summary	100
Chapter 5: Mechanical Properties	101
5.1 Hardness Testing	101
5.2 Tensile Testing	108
5.3 Charpy Impact Testing	116
5.3.1 Fractographs	126
5.3.1.1 Effect of Variables on the Fracture Mode	131
5.4 Summary	134
Chapter 6: Microstructural Analysis	135
6.1 As-Rolled Base Metal Microstructure	135
6.1.1 TEM Precipitate Analysis of Steel X and Steel Y	141

6.2 As-Welded Microstructures	152
6.2.1 CGHAZ Microstructure	152
6.2.2 FGHAZ Microstructure	163
6.3 Correlation of Mechanical Properties with Microstructure	167
6.3.1 Correlation between Hardness and Microstructure in HAZ	167
6.3.2 Correlation between Tensile Strength and Microstructure	170
6.3.3 Correlation between CGHAZ Toughness and CGHAZ Microstructure	171
6.4 Summary	172
Chapter 7: Concluding Remarks	174
7.1 Conclusions	174
7.2 Future Recommendations	176
References	178
Appendix A	191

List of Tables

Table 3-1	Chemical composition (wt%) of X80 steel plates	52
Table 3-2	Single electrode welding parameters (OD)	54
Table 3-3	Tandem electrode welding parameters (OD)	54
Table 3-4	ID welding parameters	54
Table 3-5	Weld samples, parameters and notation	58
Table 3-6	Chemical analysis of solid wire electrode	60
Table 3-7	Welding flux chemistry	60
Table 3-8	Tensile specimen dimensions	66
Table 3-9	Etchants used for optical microscopy	69
Table 5-1	Measured elongation (%) for Steel X weldments	111
Table 5-2	Measured elongation (%) for Steel Y weldments	111
Table 5-3	Measured % shear area with their respective impact energy for sample A (Steel X welded using a 1.5 kJ/mm heat input) tested at - 40°C	120
Table 6-1	Grain size of as-rolled base metals	138
Table 6-2	As-welded optical microstructures of CGHAZ region for both Steel X and Steel Y for various heat inputs - tandem electrode weld	153
Table 6-3	As welded optical microstructures of CGHAZ region for both Steel X and Steel Y for various heat inputs - single electrode welds	154
Table 6-4	CGHAZ grain size of Steel X for various heat inputs – tandem and single electrode welds	154
Table 6-5	CGHAZ grain size of steel Y for various heat inputs – tandem and single electrode welds	155
Table 6-6	As-welded optical microstructures of FGHAZ region for both Steel X and Steel Y for various heat inputs - tandem electrode welds	164
Table 6-7	As welded optical microstructures of FGHAZ region for both Steel X and Steel Y for various heat inputs - single electrode welds	165
Table 6-8	FGHAZ grain size of Steel X for various heat inputs – tandem and	165

single electrode welds

Table 6-9 FGHAZ grain size of steel Y for various heat inputs – tandem and 166
single electrode welds

List of Figures

Figure 2-1	TMCP process as defined by IACS [Imai, 2002] (Reprinted with permission).	6
Figure 2-2	Schematic illustration of thermo-mechanical rolling of microalloyed steels [Imai, 2002] (Reprinted with permission).	6
Figure 2-3	A) Relationship between tensile strength and carbon equivalent for TMCP processed steel; B) TMCP steel showing better toughness than normalized steel [Imai, 2002] (Reprinted with permission).	8
Figure 2-4	Comparison of arrestability between TMCP steel and normalized steel [Imai, 2002] (Reprinted with permission).	9
Figure 2-5	A typical semiautomatic gas metal arc welding setup [AWS, 2004] (Reprinted with permission).	10
Figure 2-6:	Schematic of the GMAW process [AWS, 2004] (Reprinted with permission).	11
Figure 2-7	Typical GTAW setup [AWS, 2004] (Reprinted with permission).	12
Figure 2-8	Schematic of GTAW equipment arrangement [AWS, 2004] (Reprinted with permission).	13
Figure 2-9	Schematic of a typical welding circuit for shielded metal arc welding [AWS, 2004] (Reprinted with permission).	14
Figure 2-10	Schematic of SMAW process [AWS, 2004] (Reprinted with permission).	15
Figure 2-11	A) Equipment set-up for single wire submerged arc welding [AWS, 2004] and B) the SAW process [Kou, 2002] (Reprinted with permission).	17
Figure 2-12	Tandem electrode SAW [The Fabricator, Online source accessed on August 2012].	18
Figure 2-13	Effect of voltage on stickout and arc length [Pepin, 2009] (Reprinted with permission).	21
Figure 2-14	“Hat- shaped” bead, that is subject to cracking, due to high arc	

	voltage [SAW guide, ---] (Reprinted with permission).	22
Figure 2-15	Effect of welding current on SAW bead-on-plate weld cross section [Weman, 2003] (Reprinted with permission).	22
Figure 2-16	Range of currents that can be used for a given voltage, flux and wire diameter [SAW guide, ---] (Reprinted with permission).	23
Figure 2-17	Effect of varying travel speed on SAW bead-on-plate weld cross section [Weman, 2003] (Reprinted with permission).	25
Figure 2-18	Weld structure and distribution of temperature [Gourd, 1980] (Reprinted with permission).	28
Figure 2-19	Structural changes in the HAZ during welding of steel (based upon original images by Easterling, pg. 126, and Patchett) [Easterling, 1992] [Patchett, 1998] (Reprinted with permission).	29
Figure 2-20	Relationship between Pcm and preheat temperature [Imai, 2002] (Reprinted with permission).	33
Figure 2-21	Iron carbon phase diagram [Calphad, 2006] (Reprinted with permission).	35
Figure 2-22	Schematic of CCT diagram for a microalloyed linepipe steel [Collins, 1983] (Reprinted with permission- www.ingentaconnect.com/content/maney/cmj).	36
Figure 2-23	Optical micrograph of equiaxed (polygonal) ferrite and pearlite (dark) [Voort, 2004] (Reprinted with permission of ASM International. All rights reserved. www.asminternational.org).	38
Figure 2-24	Replica transmission electron micrograph of acicular ferrite plates in a steel weld deposit [Bhadeshia, 1993] (Reprinted with permission).	39
Figure 2-25	Schematic illustration of the effect of prior austenite grain size on the formation of acicular ferrite [Bhadeshia, 1993] (Reprinted with permission).	40
Figure 2-26	Optical micrograph illustrating sheaves of bainitic ferrite in a partially transformed (395°C) Fe-0.3C-4Cr wt% alloy [Bhadeshia, 2001] (Reprinted with permission).	41
Figure 2-27	Granular bainite showing islands of martensite (dark) and retained	

	austenite in a matrix of ferrite [Voort, 2004] (Reprinted with permission of ASM International. All rights reserved. www.asminternational.org).	42
Figure 2-28	Optical micrograph of bainite found in heat treated low alloy steel. 4% picral + 2% nital etch [Voort, 2004] (Reprinted with permission of ASM International. All rights reserved. www.asminternational.org).	43
Figure 2-29	Variation of M_s with austenite grain size [Yang, 2009] (Reprinted with permission).	44
Figure 2-30	Effect of carbon on hardness of martensite [Avner, 1974] (Reprinted with permission).	45
Figure 2-31	Optical micrograph of lath martensite [Voort, 2004] (Reprinted with permission of ASM International. All rights reserved. www.asminternational.org).	46
Figure 2-32	A) Optical micrograph plate martensite; B) Microstructure of plate martensite showing its midrib [Voort, 2004] (Reprinted with permission of ASM International. All rights reserved. www.asminternational.org).	47
Figure 2-33	Optical micrographs showing etched (nital) wedge-shaped Widmanstätten ferrite plates (white) in a matrix quenched to martensite [Bhadeshia, ---] (Reprinted with permission).	49
Figure 2-34	Morphology of primary and secondary Widmanstätten ferrite [Bhadeshia, ---] (Reprinted with permission)	49
Figure 3-1	Bevel design (not to scale) (dimensions are in mm).	53
Figure 3-2	Schematic drawing showing the SAW weld joint geometry.	55
Figure 3-3	Schematic of lead and trail electrode setup (all dimensions are in mm and not to scale).	56
Figure 3-4	Weld joint preparation.	59
Figure 3-5	Typical weld metal area used for measurements in Image J software.	61
Figure 3-6	Region where hardness tests were done.	63
Figure 3-7	Schematic showing the region where hardness indentations were	63

made.

Figure 3-8	Optical image showing hardness indentations. The red line indicates the fusion line.	64
Figure 3-9	Tensile specimen extraction.	65
Figure 3-10	Tensile specimen dimensions.	65
Figure 3-11	Schematic Charpy specimen extraction and notch location (not to scale).	67
Figure 3-12	CVN notch orientation relative to the welding direction.	68
Figure 3-13	Average intercept counts on 500 mm test patterns.	71
Figure 3-14	Schematic of grain size number calculation using Heyn method.	71
Figure 3-15	Typical grain area measurement using Image J software.	72
Figure 3-16	Schematic of TEM replica extraction.	74
Figure 4-1	Schematic illustration of the measurements required for determining welding performance.	77
Figure 4-2	Effect of heat input on a) penetration depth, b) reinforcement height and c) bead width for Steel X - tandem electrodes.	78
Figure 4-3	Effect of heat input on a) penetration depth, b) reinforcement height and c) bead width for Steel Y - tandem electrodes.	78
Figure 4-4	Effect of heat input on HAZ size in tandem welds.	80
Figure 4-5	Effect of heat input on HAZ size – single electrode welds.	80
Figure 4-6	Schematic of HAZ width calculations for two different situations.	81
Figure 4-7	Relationship between heat input and reinforcement area for Steel X and Steel Y-tandem electrode welds. Calculated values from Equation 4.1 are also shown.	82
Figure 4-8	Relationship between heat input and reinforcement area for Steel X and Steel Y - single electrode welds. Calculated values from Equation 4.1 are also shown.	82
Figure 4-9	Effect of heat input on the contact angle – tandem electrode welds.	84
Figure 4-10	Effect of heat input on the contact angle – single electrode welds.	85
Figure 4-11	Heat input vs. total molten area for Steel X.	86
Figure 4-12	Heat input vs. total molten area for Steel Y.	87

Figure 4-13	The effects of lead and trail electrodes on bead shape in tandem electrode welding [Kubli, 1956].	87
Figure 4-14	Effect of voltage on arc length and electrode stick-out [Pepin, 2009].	89
Figure 4-15	Variation of reinforcement area for single and tandem electrode welds for Steel X.	89
Figure 4-16	Variation of reinforcement area for single and tandem electrode welds for Steel Y.	90
Figure 4-17	Effect of welding speed on SAW bead-on-plate cross section [Wemen, 2003].	91
Figure 4-18	Schematic of two types of weld beads [Pepin, 2009].	92
Figure 4-19	Heat input vs. SP ratio for tandem electrode welds.	93
Figure 4-20	Heat Input vs. SP ratio for single electrode welds.	93
Figure 4-21	Melting efficiency (%) vs. heat input for Steel X - tandem electrode welds.	96
Figure 4-22	Melting efficiency (%) vs. heat input for Steel X - single electrode welds.	97
Figure 4-23	Melting efficiency (%) vs. heat input for Steel Y - tandem electrode welds.	97
Figure 4-24	Melting efficiency (%) vs. heat input for Steel Y - single electrode welds.	98
Figure 5-1	Microhardness variation for Steel X welded using a 1.5 kJ/mm heat input. The number zero on the distance axis denotes the fusion line. The negative distance values denote the weld metal region.	102
Figure 5-2	Microhardness variation for Steel Y welded using a 1.5 kJ/mm heat input. The number zero on the distance axis denotes the fusion line. The negative distance values denote the weld metal region.	102
Figure 5-3	Schematic of hardness variation due to microstructural changes in the CGHAZ and FGHAZ regions.	103
Figure 5-4	Hardness variation in the CGHAZ and FGHAZ region for different heat inputs (Steel X - tandem electrode welds).	104
Figure 5-5	Hardness variation in the CGHAZ and FGHAZ region for different	

	heat inputs (Steel Y - tandem electrode welds).	105
Figure 5-6	Hardness variation in the CGHAZ and FGHAZ region for different heat inputs (Steel X - single electrode welds).	105
Figure 5-7	Hardness variation in the CGHAZ and FGHAZ region for different heat inputs (Steel Y - single electrode welds).	106
Figure 5-8	Fractured tensile specimen showing the fracture location and position of the welded joint.	108
Figure 5-9	Typical stress-strain curves for Steel X welded using single electrodes for two heat inputs.	109
Figure 5-10	Typical stress-strain curves for Steel X welded using tandem electrodes for four heat inputs.	109
Figure 5-11	Typical stress-strain curves for Steel Y welded using single electrodes for two heat inputs.	110
Figure 5-12	Typical stress-strain curves for Steel Y welded using tandem electrodes for four heat inputs.	110
Figure 5-13	3D view of total weld metal volume produced by OD and ID.	112
Figure 5-14	Effect of total weld metal volume on percent elongation – Steel X welded using single electrodes.	113
Figure 5-15	Effect of total weld metal volume on percent elongation – Steel X welded using tandem electrodes.	113
Figure 5-16	Effect of total weld metal volume on percent elongation – Steel Y welded using single electrodes.	114
Figure 5-17	Effect of total weld metal volume on percent elongation – Steel Y welded using tandem electrodes.	114
Figure 5-18	Full size and sub-size toughness values for the two steels (base metal) at different temperatures.	116
Figure 5-19	HAZ toughness (sub-size) values for different heat inputs - Steel X with tandem welds.	117
Figure 5-20	Sub-size toughness values for different heat inputs - Steel Y with tandem welds.	117
Figure 5-21	Sub-size toughness values for different heat inputs - Steel X with	

	single pass.	118
Figure 5-22	Sub-size toughness values for different heat inputs - Steel Y with single pass.	118
Figure 5-23	SEM SE image of the fracture surface for Sample K (steel Y welded using 2.00 kJ/mm heat input), showing both ductile and brittle regions. The sample was tested at -40°C. The image was taken from the end portion of crack growth.	121
Figure 5-24	SEM SE image of the fracture surface for sample C (steel X welded using 2.00 kJ/mm heat input) tested at -40°C – ductile fracture. The image was taken from the mid portion of crack growth.	122
Figure 5-25	SEM SE image of the fracture surface for sample C (steel X welded using 2.00 kJ/mm heat input) tested at -40°C –brittle fracture. The image was taken from the end portion of crack growth.	122
Figure 5-26	A) SEM fractograph showing localized ductile zones (red boxes) inside the primarily brittle region, found in sample C (Steel X welded using 2.00 kJ/mm heat input) and tested at -40°C. B) higher magnification fractograph of one such zone clearly showing ductile region.	123
Figure 5-27	Schematic showing crack propagating through the weld metal instead of the CGHAZ region.	124
Figure 5-28	Full size Charpy notch location showing a pre-existing crack (indicated by the red box). The specimen is Steel X. Steel Y also had these types of cracks.	125
Figure 5-29	SEM SE image of Sample C (Steel X welded using a 2.00 kJ/mm heat input) tested at 22°C showing ductile fracture.	126
Figure 5-30	Mechanism for ductile crack growth. Based upon original images from [Anderson, 1994].	127
Figure 5-31	SEM SE image of Ti- rich and Ca-rich particles trapped inside dimples. Corresponding EDX analysis is shown as well. The image is from sample G (Steel X - 1.75 kJ/mm) tested at -20°C.	128
Figure 5-32	SEM SE image showing large broken Ti-rich particles found in	

	sample K (steel Y - 2.00 kJ/mm heat input) – tested at -40°C. EDX spectra from the particles indicated are also shown.	129
Figure 5-33	SEM SE image of a fracture surface showing a broken Ti-rich particle indicated by the red arrow - sample C (Steel X welded using 2.00 kJ/mm heat input) tested at -40°C.	130
Figure 5-34	SEM SE image of Sample J (Steel Y welded using 1.75 kJ/mm heat input) tested at -60°C, showing brittle fracture.	131
Figure 5-35	Schematic diagram showing initiation of microcracks from broken second phase particles.	133
Figure 6-1	As rolled optical microstructure of Steel X.	136
Figure 6-2	As rolled optical microstructure of Steel X (higher magnification).	136
Figure 6-3	As rolled optical microstructure of Steel Y.	137
Figure 6-4	As rolled optical microstructure of Steel Y (higher magnification).	137
Figure 6-5	SEM secondary electron (SE) image of Steel X showing bainitic region.	139
Figure 6-6	SEM SE image of Steel Y showing bainitic region.	139
Figure 6-7	Optical micrograph of Steel X showing white M-A region; etched with Le Pera's solution.	140
Figure 6-8	Optical micrograph of Steel Y showing white M-A region; etched with Le Pera's solution.	140
Figure 6-9	A) Representative TEM bright field (BF) images showing intermediate size particles in Steel X and B) Steel Y.	142
Figure 6-10	TEM BF image of Steel Y showing a cuboidal shaped particle (a) and a round shaped particle (b).	143
Figure 6-11	EDX spectra from point "a" (A) and point "b" (B) from Figure 7-10.	143
Figure 6-12	A) SEM SE image of fracture surface of Steel X showing points 1 and 2 where EDX analysis was carried out. B) EDX spectrum from point 1 in (a) showing a Ti peak along with a Ca peak. This Ca peak is most likely coming from a CaS inclusion. It is believed that the Ti particle heterogeneously nucleated on this Ca-rich inclusion during solidification. C) EDX spectrum of point 2 showing a Ti peak along	

	with a S peak and Ca peak. The Fe peak is an artifact coming from the surrounding matrix.	145
Figure 6-13	Intermediate size Nb-rich precipitate attached to a Ti-rich precipitate.	146
Figure 6-14	A) TEM BF images for Steel X and B) Steel (Y) showing very fine precipitates.	147
Figure 6-15	A) TEM BF image of Steel X showing fine particles and B) corresponding ring pattern obtained from the clustered region.	148
Figure 6-16	A) Region in Steel Y showing fine particles and B) corresponding SAD ring pattern obtained from the clustered region.	149
Figure 6-17	Particle size distribution for Steel X and Steel Y.	152
Figure 6-18	Variation of average CGHAZ PAGS with heat input.	155
Figure 6-19	A) SEM SE image of CGHAZ region of specimen A (Steel X welded using a 1.5 kJ/mm heat input - tandem electrode) showing large prior austenite grains; B) magnified prior austenite grain from Figure 6-19 (A) and C) magnified image of a prior austenite grain from Figure 6-19 (B).	157
Figure 6-20	Average lath length for different heat inputs. Lath length increases as the heat input increases. Also, single electrode welds have higher lath lengths compared with the same heat input welded using tandem electrodes.	159
Figure 6-21	Average lath width for different heat inputs.	159
Figure 6-22	A) SEM SE image of CGHAZ region of specimen F (Steel X welded using a 1.5 kJ/mm heat input - single electrode); B) magnified prior austenite grain from Figure 6-22(A) and C) magnified image of a prior austenite grain from Figure 6-22 (B).	161
Figure 6-23	Schematic showing dependency of hardness values due to ferrite lath sizes.	168

List of Symbols

A_f	Total molten area (mm ²)
A_p	Penetration area (mm ²)
A_r	Reinforcement area (mm ²)
I	Current (ampere)
k_y	Strengthening coefficient
p	Penetration depth (mm)
r	Reinforcement height (mm)
S	Travel speed (mm/min)
v	Travel speed (m/s)
V	Voltage (volts, V)
w	Bead width (mm)
W_1	Full bead width (mm)
W_2	Bead width at half penetration depth (mm)
θ	Bead contact angle (degrees)
σ_y	Yield strength (MPa)
σ_o	Friction stress (MPa)

Acronyms

AC	Alternating current
AcC	Accelerated cooling
AF	Acicular ferrite
AWS	American Welding Society
<i>bct</i>	Body centered tetragonal
BM	Base metal
BOP	Bead-on-plate (refers to welding)
C.E.	Carbon equivalent
CGHAZ	Coarse grain heat affected zone
CVN	Charpy V-notch
DC	Direct current
DJ	Double jointer (refers to pipe joining welding process)
EME	Electrode Melting Efficiency
FGHAZ	Fine grain heat affected zone
GB	Granular bainite
GMAW	Gas metal arc welding
GTAW	Gas tungsten arc welding
HAZ	Heat affected zone
HSLA	High strength low alloy
IACS	International Association of Classification Societies Ltd
ICHAZ	Inter-critical heat affected zone
ID	Inner diameter (refers to pipe face)
IIW	International Institute of Welding
M-A phase	A microstructure consisting of martensite with retained austenite
MAC	Martensite/ austenite/ carbide
MF	Massive ferrite
NACE	National Association of Corrosion Engineers

OD	Outer diameter (refers to pipe face)
PAGS	Prior austenite grain size
PF	Polygonal ferrite
PM	Parent metal
PME	Plate melting efficiency
PWHT	Post weld heat treatment
SAW	Submerged arc welding
SMAW	Shielded metal arc welding
SMYS	Specified minimum yield strength
SP Ratio	Semi-penetration ratio (refers to a shape characterization technique)
SSC	Sulphide stress cracking
SSCC	Sulphide stress corrosion cracking
TMCP	Thermo-mechanical controlled process
WFS	Wire feed speed
WM	Weld metal
WPME	Welding process melting efficiency
X80	A grade of pipeline steel with a specified minimum yield strength of 551.5 MPa (80 ksi)

Introduction

1.1 Overview

Increasing demand for energy throughout the world requires exploration of new energy resources located in areas where difficult ground conditions exist [Liessem, 2007]. The complex ground conditions and, in some cases, ambient climate imposes very strict requirements on pipeline material and design considerations. There is a strong need for line pipe steel that can withstand severe conditions, such as cold weather (e.g., arctic regions), regions where there is differential ground movement due to soil subsidence, thaw movement, frost heave and landslides, corrosive environment and deep seabeds [Liessem, 2007]. Moreover, the transport efficiency also needs to be improved by allowing higher operating pressures and gas transmission rates [Bae, 2006]. [Hillenbrand, 2002]. Under these strict criteria, large diameter pipes which can be operated under high pressure should be more economical [Pepin, 2009]. The use of high strength pipe materials provides several advantages including lower weight and lower manufacturing costs. High strength pipe materials can allow for the reduction of the pipe wall thickness, which reduces both the required steel tonnage and welding cost, making them more economical [Barbaro, 2010].

API5L-X80 grade steel (having toughness requirement and a specified minimum yield strength of 552 MPa or 80 ksi) has been widely used during the last two decades and provides excellent toughness, strength and weldability [Hillenbrand, 2002]. These steels

are designed by considering the strain hardening behaviour of both the base metal and girth welds. In strain based pipeline design both primary and secondary loads are taken into account [Mackenzie, 2004]. Internal pressure acting circumferentially along the pipe wall is an example of primary load. This primary load is independent of structural deformation of the pipeline. However, in arctic regions due to differential ground movement; secondary geotechnical loads are also applied. An example of a secondary load is the bending caused by frost heave. A strain based limit state design approach has been established to accommodate both these loads.

These pipe materials are produced using thermo-mechanical controlled processing (TMCP) of steel with small additions of alloying elements such as niobium, aluminium, vanadium, titanium, molybdenum and zirconium [Gladman, 1997]. The high strength steel possesses very fine microstructures, which yield high toughness values, and have low carbon contents, which improves the weldability of the steel. The unique mechanical properties found in steels produced through TMCP are mainly the result of strengthening from grain refinement, precipitation hardening, solid solution strengthening and dislocation hardening [Gladman, 1997]. These mechanisms allow the strength of the steel to be increased without increasing its carbon content. However, during welding, due to rapid temperature changes, the material adjacent to the weld metal forms different microstructures based on the heating and cooling rates. The heat affected zone (HAZ) regions may have varying microstructures and mechanical properties compared with the base material, degrading the structure formed by TMCP processing, which cannot be restored by thermal heat treatment [De Meester, 1997].

During TMCP steel pipe manufacturing, there are many different welds involved, including longitudinal, spiral and circumferential welds. Circumferential joints are made in the mill to join short pipes into longer lengths using submerged arc welding (SAW). However, in the field, gas metal arc welding (GMAW) is used to join the pipes. In order to ensure pipeline integrity and safety, it is expected that the weld metal and the HAZ should have sufficient strength and toughness to withstand circumferential elongation as well as longitudinal straining due to geotechnical reasons. In strain based pipeline design

one of the goals is to achieve longitudinal strength overmatching for the base material and welded joints, as well as to maintain at least a minimum level of fracture toughness [Hamad, 2008]. For high strength materials like X80 steel, achieving overmatched strength across the weld and HAZ in the field is easy. For field girth welding, usually shielded metal arc welding (SMAW) is used for the root pass and then GMAW is used for the fill and cap passes [Hillenbrand, 2002]. Since manual GMAW uses low heat input, it also provides lower base metal dilution, which makes it easier to control the weld metal chemistry in the field and, hence, achieve overmatching properties. However, high strength, X80 steel girth welding in the mill using SAW is challenging. TMCP steels are so lean in chemistry that in order to achieve acceptable weld metal chemistry, at high base metal dilution (SAW is a high heat input process providing high base metal dilution from a production view point), highly alloyed filler metal is required [Widgery, 2006]. Although it is not impossible to achieve overmatching properties using a suitable SAW welding flux/welding wire combination and welding variables. The following study is aimed at examining how strength and toughness of X80 steels are affected by the SAW process variables.

1.2 Objectives

The main objectives of this study are therefore:

- a.) To improve the understanding of how SAW parameters affect the HAZ mechanical properties of X80 steel.
- b.) To study the relationship between SAW process parameters and welding performance.

1.3 Thesis Outline

This thesis is divided into 7 chapters. Chapter 2 presents a comprehensive literature review, pertinent to this project. Chapter 3 discusses the materials and experimental methods used in this work. Chapter 4 discusses weld performance based on different

SAW process parameters. Chapter 5 discusses the mechanical properties of the welded joints and base metals. Chapter 6 presents the microstructural analysis of the base metal and the weld HAZ. Finally, conclusions are made in Chapter 7, along with recommendations for future work.

Literature Review

In this chapter, steel processing and properties and the application of thermo-mechanical controlled processing (TMCP) to steels will be discussed. A brief overview of different arc welding processes will be explained, with emphasis on submerged arc welding (SAW). Since this study deals with SAW welding of X80 steel plates, fundamental information about the SAW process and the effect of different SAW parameters on the properties of TMCP steel will be introduced. Controlled rolling microstructures and different fundamental microstructures, as found in welded structures, and their formation will also be discussed.

2.1 Thermo-mechanical Controlled Processing (TMCP)

TMCP was developed in the early 1980's by Japanese plate mills [Imai, 2002]. The goal was to achieve superior mechanical properties by producing a fine and uniform acicular ferrite microstructure, rather than having a conventional ferrite/pearlite type microstructure. Steels after TMCP have the same weldability and formability as mild steel, but better toughness due to the fine grained microstructure produced [Imai, 2002] [Hoskins, 2002].

TMCP technology involves both controlled rolling and accelerated cooling during steelmaking. In this process, total control is important during heating of the slabs,

especially during rolling and accelerated cooling. According to the definition by IACS (International Association of Classification Societies Ltd), TMCP has two stages [Imai, 2002], TMR (thermo-mechanical rolling) and AcC (accelerated cooling) as shown in Figure 2-1.

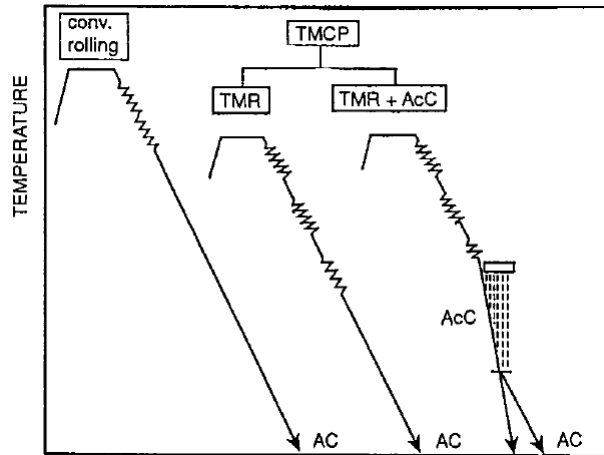


Figure 2-1: TMCP process as defined by IACS [Imai, 2002] (Reprinted with permission).

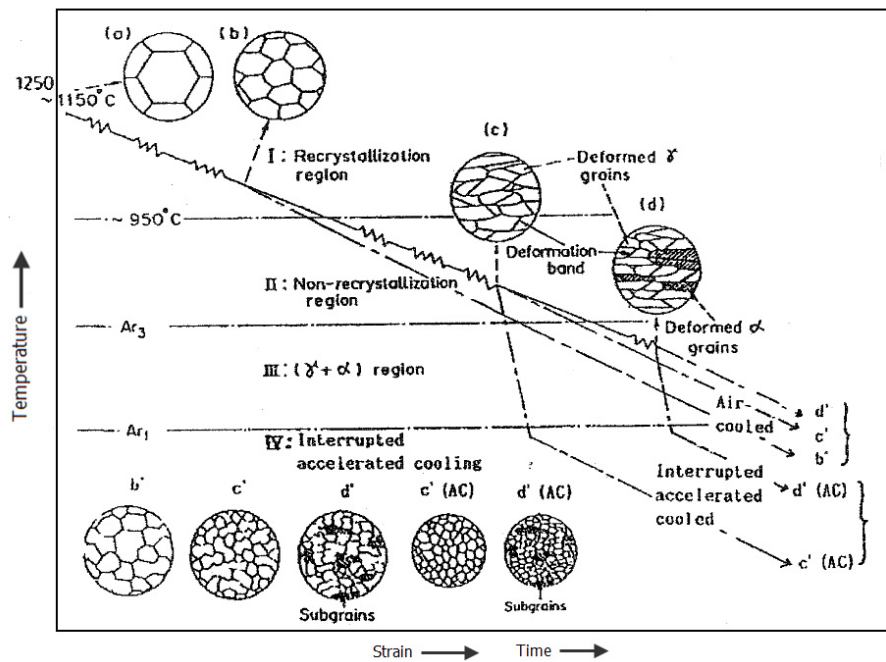


Figure 2-2: Schematic illustration of thermo-mechanical rolling of microalloyed steels [Imai, 2002] (Reprinted with permission).

A schematic of the overall TMCP cycle is shown in Figure 2-2. In TMCP, controlling the microstructure starts with reheating of the slab to a high enough temperature to dissolve the precipitates (Nb-carbonitrides and V-carbonitrides) [Pepin, 2009]. In this stage the microstructure is large austenite grains as can be seen in Figure 2-2-a. The next stage is rough rolling, where fine austenite grains are formed at temperatures above the recrystallization temperature (Figure 2-2-b) [Imai, 2002]. In the third finish rolling stage, the austenite grains are “pancaked”; where the rolling operation is done below recrystallization temperature (Figure 2-2-c). The deformed pancaked austenite increases the number of ferrite nucleation sites in the grain boundaries [Bai, 2002]. Austenite is transformed into fine acicular ferrite or upper bainite due to accelerated cooling, which is employed by spraying water from nozzles. Ferrite is nucleated on deformation bands as well (Figure 2-2-d) [Tanaka, 1995]. Thus, the microstructure is refined. In some mills, the steel may undergo a final deformation stage at temperatures between 350°C and 450°C [Bai, 2002]. This promotes the formation of dislocations, which assist with the formation of fine precipitates [Pepin, 2009] [Tanaka, 1995].

As stated earlier, TMCP steels have superior toughness and strength because of their fine and uniform acicular ferrite type microstructure (Figure 2-3). Figure 2-3-A shows higher strength for TMCP steels than as rolled steel with the same carbon equivalent. The toughness of TMCP steels is also superior to normalized steels as shown in Figure 2-3-B. The ductile to brittle transition temperature is lower in TMCP steels compared with normalized steels. The steels also have higher crack arrestability than normalized steels as shown in Figure 2-4. All these qualities make a TMCP steel suitable for arctic pipeline applications.

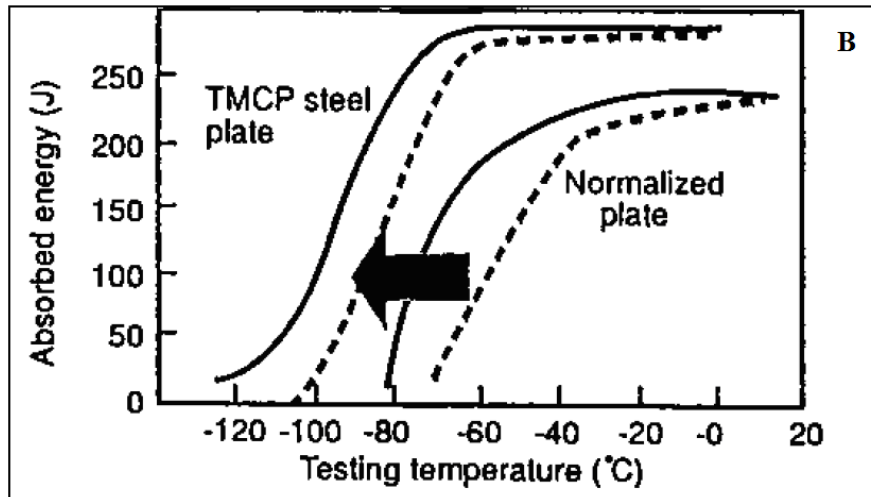
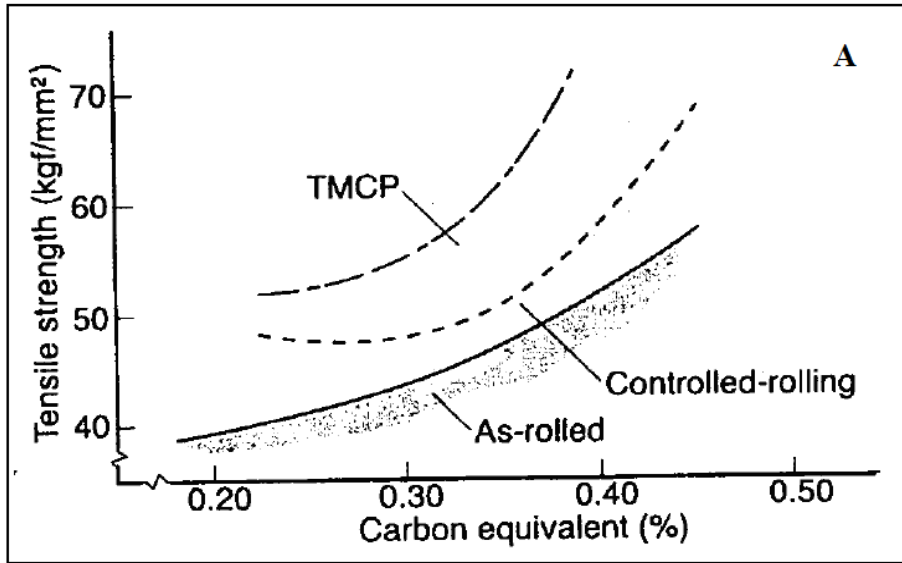


Figure 2-3: A) Relationship between tensile strength and carbon equivalent for TMCP processed steel; B) TMCP steel showing better toughness than normalized steel [Imai, 2002] (Reprinted with permission).

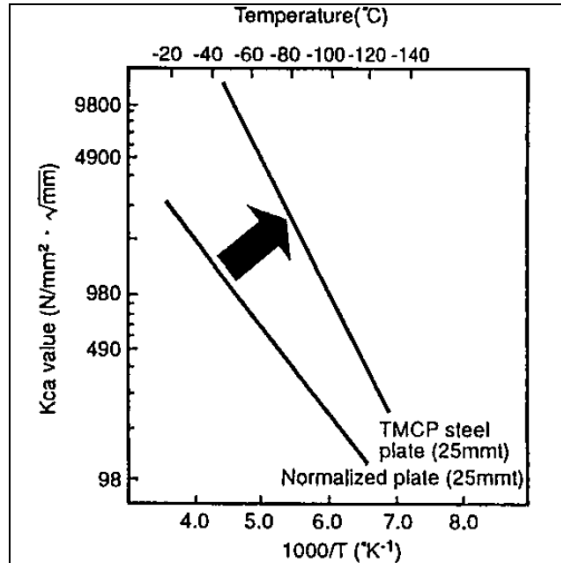


Figure 2-4: Comparison of arrestability between TMCP steel and normalized steel [Imai, 2002] (Reprinted with permission).

In the next section, a short overview of different arc welding processes will be discussed. Since this study deals with welding of TMCP microalloyed steels using submerged arc welding (SAW), this particular fusion welding process and its different parameters will be reviewed in detail.

2.2 Arc Welding Process Overview

Different arc welding processes will be described in this section. Most metals can be joined using different arc welding processes, the most common ones being gas metal arc welding, gas tungsten arc welding, shielded metal arc welding and submerged arc welding. Microalloyed steels can be joined using any of these welding processes [Gladman, 1997]. For joining pipelines in the field, a low heat input gas metal arc welding process is used [Koo, 2004]. For joining shorter pipes and making them longer, SAW is used. These types of joints are known as “Double Jointer” or DJ welds. DJ welds are produced by either using multiple

passes around the outer diameter (OD) or one pass around the inner diameter (ID) and another one from the OD [Pepin, 2009].

2.2.1 Gas Metal Arc Welding (GMAW)

This process is also known as metal inert gas welding (MIG). The process utilizes the heat of an arc between a continuously fed consumable electrode and the material to be welded. The heat of the arc melts the surface of the base metal and the end of the electrode [Kurny, 2002] [AWS, 2004]. A typical GMAW setup is shown in Figure 2-5.

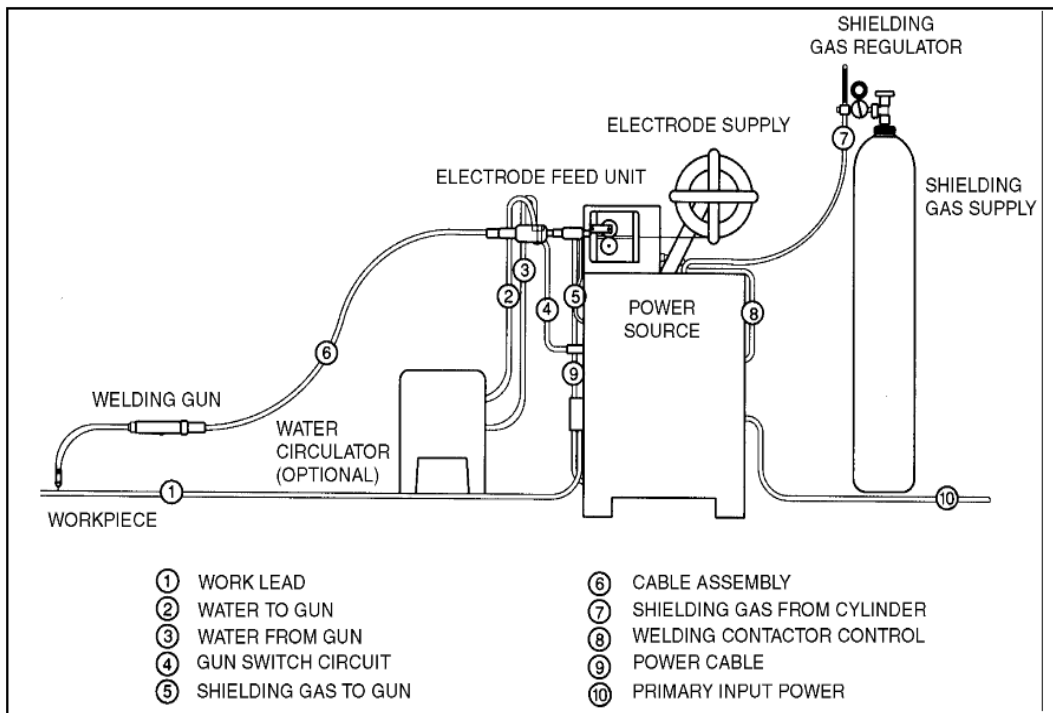


Figure 2-5: A typical semiautomatic gas metal arc welding setup [AWS, 2004]

(Reprinted with permission).

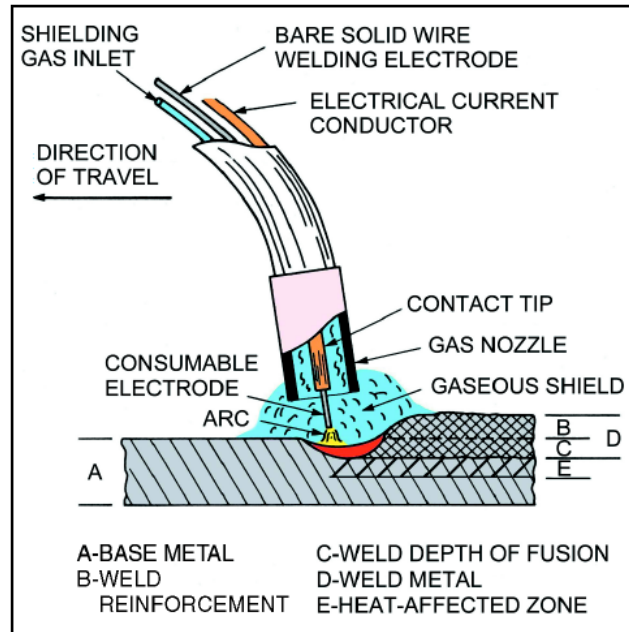


Figure 2-6: Schematic of the GMAW process [AWS, 2004] (Reprinted with permission).

The basic components of the GMAW process include a welding gun, electrode feeder, power source and shielding gas. In Figure 2-6 an enlarged view of the welding gun is shown. The GMAW process is used in the fields of industrial manufacturing, agriculture, ship building, mining and also for producing girth welds during pipeline assembly [AWS, 2004].

There are a number of advantages of using GMAW over other welding processes. GMAW offers a higher production rate compared to SMAW due to the increased deposition rate. There is no flux, slag or spatter to remove, which allows a considerable saving in welding cost. There is a continuous feed of electrode wire, which makes it free from defects that generally occur during start/stop points. This process can be implemented in semiautomatic and automated operations. However, there are certain limitations, which restrict the use of GMAW in some operations. The equipment is complex, costly and less portable compared to shielded metal arc welding. It is sometimes difficult to weld hard-to-reach places because of the welding gun assembly, which is large compared with shielded

metal arc welding. Another limitation is that high levels of radiated heat and arc intensities are produced [AWS, 2004].

2.2.2 Gas Tungsten Arc Welding (GTAW)

Gas tungsten arc welding (GTAW) is also known as *non-consumable electrode* welding and sometimes referred to as tungsten inert gas (TIG) welding. In this process the source of heat is an arc formed between a non-consumable tungsten electrode and the work piece. A typical GTAW operation is shown in Figure 2-7 and a schematic of the GTAW equipment arrangement is shown in Figure 2-8.

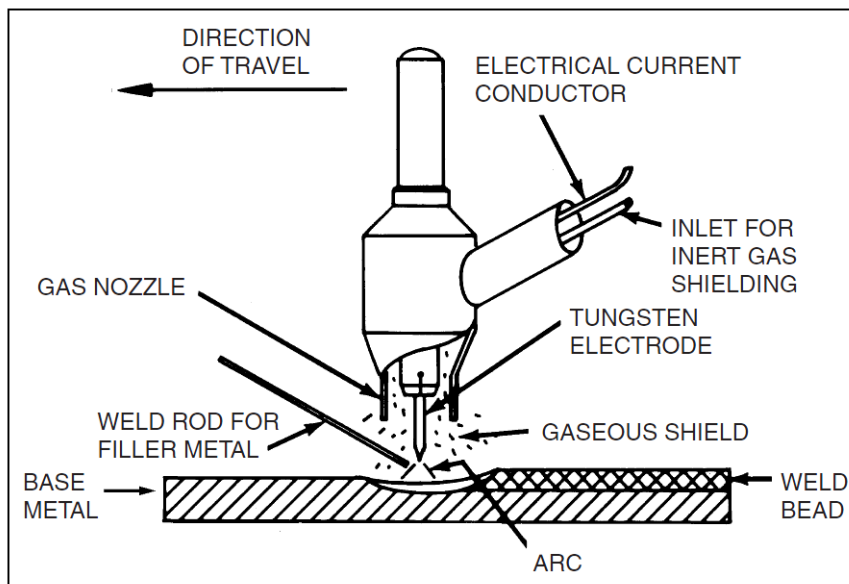


Figure 2-7: Typical GTAW setup [AWS, 2004] (Reprinted with permission).

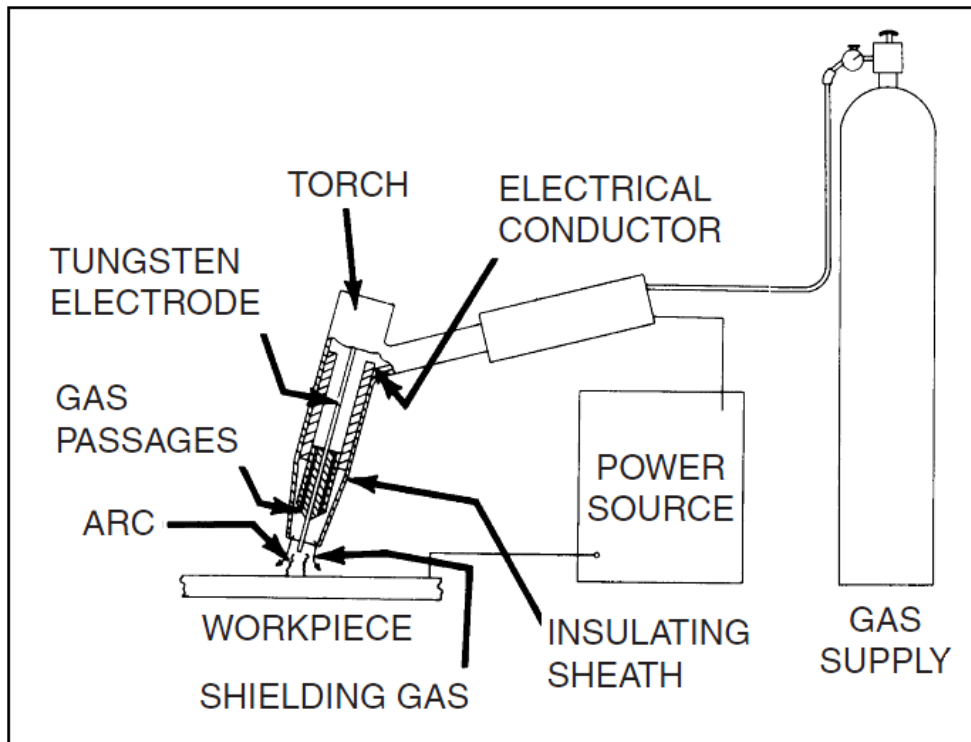


Figure 2-8: Schematic of GTAW equipment arrangement [AWS, 2004]
 (Reprinted with permission).

Unlike GMAW, the electrode is not consumed in this process. For joints where additional weld metal is needed, a filler rod is fed into the puddle as can be seen in Figure 2-7. The arc and the molten puddle are protected from atmospheric contamination with a gaseous shield of inert gas. An arc is produced by passing of current through a conductive ionized shielding gas and is established between the tip of the electrode and the work piece [AWS, 2004]. When the arc melts the surface of the work piece, a weld pool is produced and the arc is moved along the joint.

GTAW has many advantages over other arc welding processes. It can be used for producing welds at almost any position and can join all metals including dissimilar metals [AWS, 2004]. This process makes very high quality welds, with no slag produced, and since no flux is used in this process very little post weld

cleaning is required. The arc and weld pool is clearly visible and so the operator can observe the weld as it is being made.

GTAW has a wide range of applications. This process is used in the aerospace and nuclear industries. It is also used in some critical situations for the root pass where critical control of the HAZ properties and penetration are essential. The ease of operation makes it a choice for typical welding fabrication and repair jobs.

2.2.3 Shielded Metal Arc Welding (SMAW)

SMAW is one of the most commonly used arc welding processes. It is also known as manual metal arc welding (MMAW). In this process the arc is produced between a coated consumable electrode and the work piece.

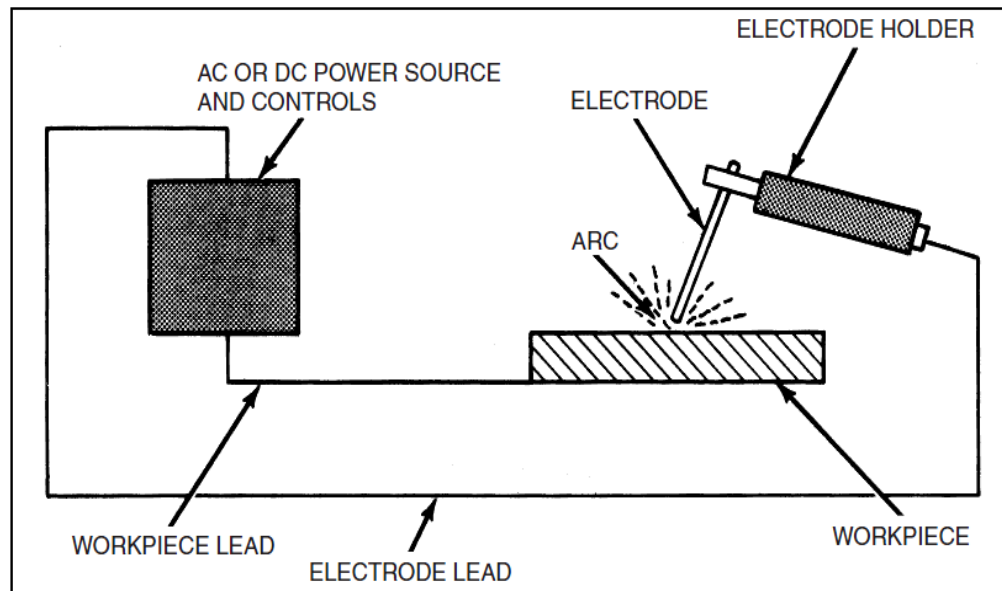


Figure 2-9: Schematic of a typical welding circuit for shielded metal arc welding [AWS, 2004] (Reprinted with permission).

As shown in the schematic of a typical circuit for SMAW in Figure 2-9, the power source is connected to a circuit with the electrode and the work piece. Since the

work piece is a part of the electrical circuit, it needs to be grounded depending on the application.

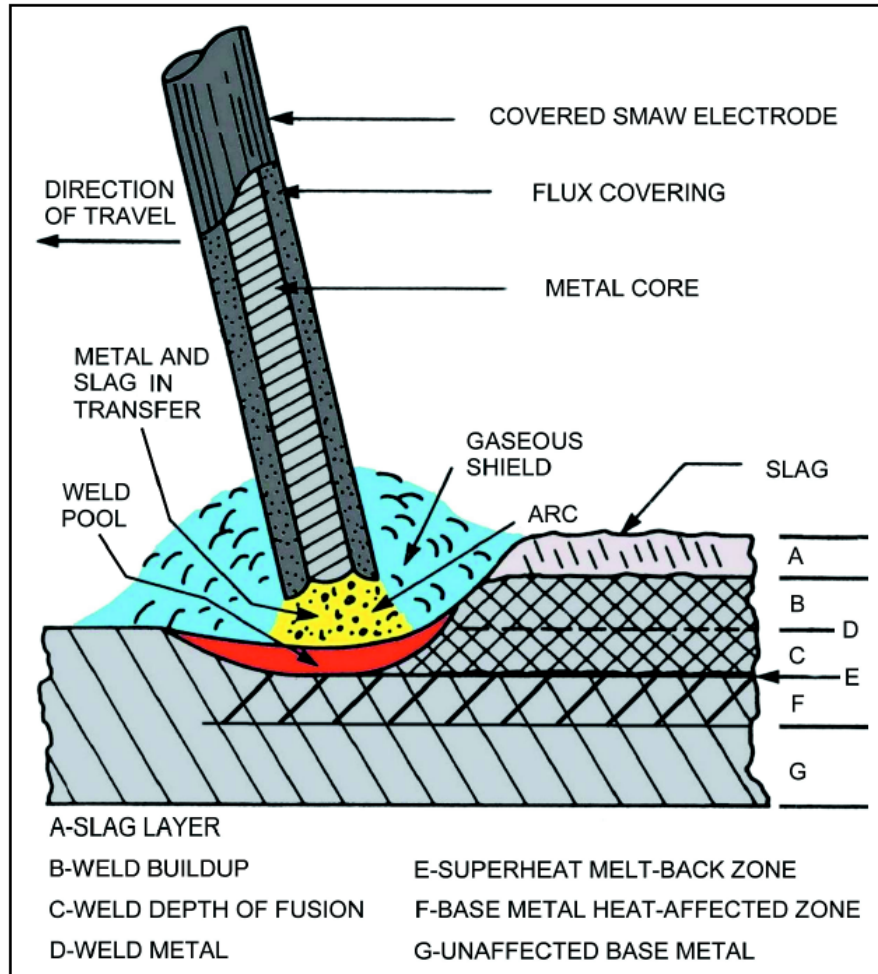


Figure 2-10: Schematic of SMAW process [AWS, 2004] (Reprinted with permission).

In Figure 2-10, a schematic of the SMAW process is shown. The intense heat from the welding arc, which melts the surface of the material being welded and the tip of the electrode, produces a weld pool. The metallic core wire is melted by the arc and transferred to the weld pool by molten droplets. Once the arc is established and the weld pool is defined, the welder continues to feed the

electrode into the arc and manipulates it within the weld joint. The welder has to maintain a constant arc length between the electrode tip and the weld pool. The mechanical properties and weld metal soundness depend on the arc length. Shorter arc lengths produce a weld, which is usually free from defects and has fewer spatters. The electrode coating also melts to form a gas shield around the arc and the weld pool as well as slag on the surface of the weld pool, thus protecting the cooling weld pool from the atmosphere. The slag must be removed after each layer.

SMAW has several advantages over other arc welding processes. It is very simple, inexpensive and portable. The electrode provides both the filler material and the required shielding gas. The dimensions of the electrode wire are suitable for reaching areas with limited access. The electrodes can be bent in order to weld hard-to-reach areas.

Among the limitations of SMAW, the most common limitation is operator variability. SMAW requires very skilled operators to produce sound welds, and this also has a dramatic influence on the reducing the deposition rates compared to GMAW. So when large weldments are needed, this process requires a significant amount of time. Metals with low melting points such as zinc, lead and their alloys cannot be welded using the SMAW process. Also, this process cannot be used for reactive metals such as niobium, titanium, etc. Another drawback of the SMAW process is stub loss. A stub is the grip end of the SMAW electrode, which is discarded. Stub loss affects the deposition efficiency.

2.2.4 Submerged Arc Welding (SAW)

The submerged arc process is essentially an automatic form of the metallic arc welding process in which the joining of metals is produced by heating with an arc or arcs between a bare metal electrode or electrodes and the work. In Figure 2-11, a schematic of SAW equipment layout and process is shown.

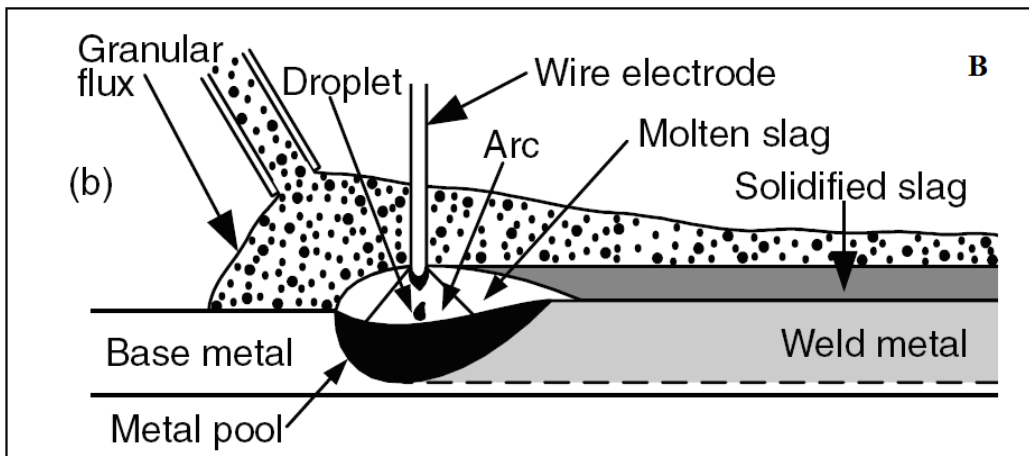
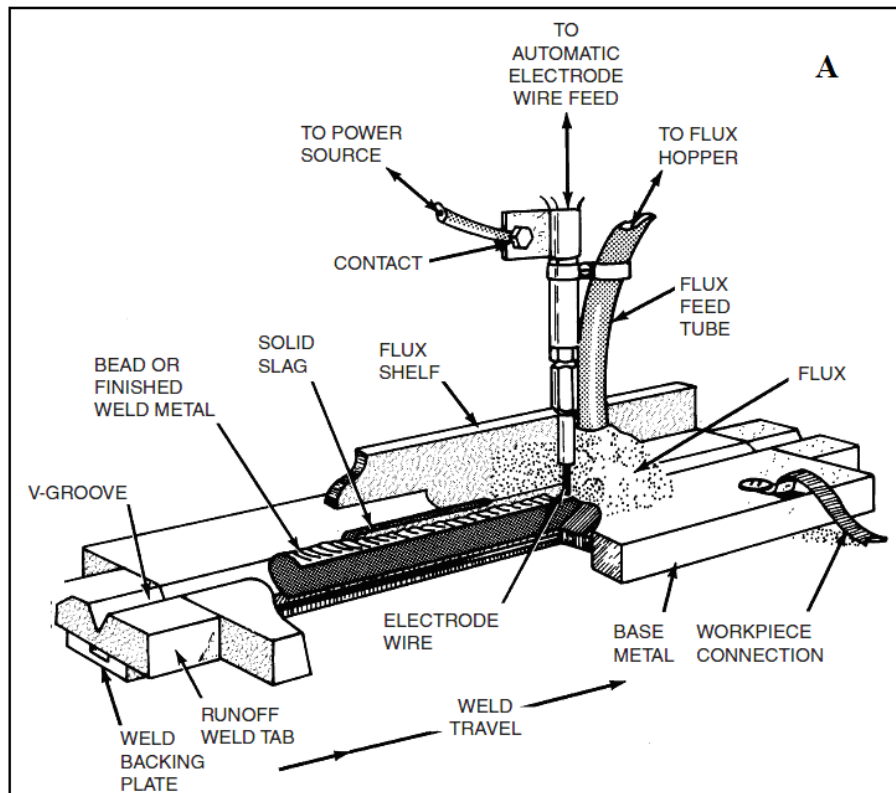


Figure 2-11: A) Equipment set-up for single wire submerged arc welding [AWS, 2004] and B) the SAW process [Kou, 2002] (Reprinted with permission).

There is a tube (flux feed tube in Figure 2-11-A) attached to the electrode holder, which delivers powdered flux to the prepared joint in advance of the electrode. The electrode is a coiled wire and is fed continuously by a feed unit of motor driven rollers. When the welding gun is switched on to start the arc, the tube starts

to flow powdered flux and covers the melting end and the arc. Much of the flux melts and rises to the top of the molten metal and forms a protective slag. The arc is not visible since it is always submerged with the weld metal under a layer of flux and slag; hence, the name submerged arc welding. The unused flux is collected using a vacuum system and can be reused. Apart from this simple process layout, there are a large number of process variations involving multi-wire systems (e.g., tandem electrode system – using two electrodes), which make SAW suitable over other welding processes. In Figure 2-12, an example of tandem electrodes is shown.

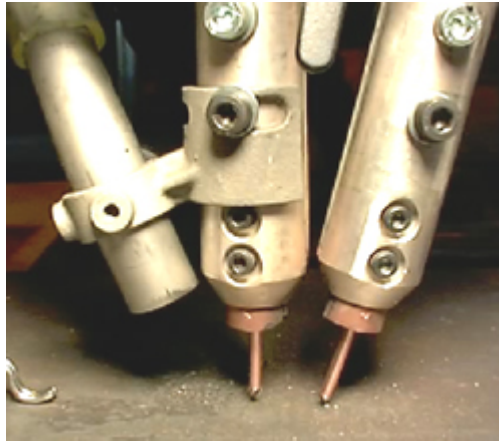


Figure 2-12: Tandem electrode SAW [The Fabricator, Online source accessed on August 2012].

SAW produces high quality welds, which are smooth and uniform with no or very little spatter. Since the arc is covered under the molten slag and flux, there is no discomfort from glare or fumes, which makes it attractive in terms of environmental and safety perspectives [Houldcroft, 1989] [Kielhorn, 2001]. The SAW process can be fully automated or semi-automated [Houldcroft, 1989]. In a fully automated process, little manual intervention is required; hence, skilled operators are not needed. SAW has a high deposition rate, which makes it suitable for welding larger sections more economically. Due to its advantages, it is a popular choice for welding structural shapes, large diameter pipes, vessels and tanks and also in the ship building industry for fabricating subassemblies [Kurny,

2002] [Houldcroft, 1989]. In pipe mills, SAW is used to join shorter pipes into longer lengths. SAW has some limitations in that it produces a large molten weld pool and the slag is very fluid, so it is not suitable for vertical and overhead positions. In addition, since the arc is covered with flux, it is impossible to see the root of the groove, so that proper filling and maintaining the desired weld line may be difficult.

Overall SAW is a welding process with high efficiency, high deposition rates and easy automation, which makes it a popular choice for welding pipes in the mill. It offers low rates of lack of fusion defects in the weld compared with other operator controlled arc welding processes. One of the disadvantages of SAW is that it produces very high heat input, which can degrade the HAZ microstructure of TMCP steels. In the next section different SAW welding conditions and process variables will be discussed.

2.3 SAW Welding Conditions and Process Variables

In order to get a welded joint free from any defects, careful selection of correct welding conditions, process variables and joint preparation is necessary [Houldcroft, 1989]. Welding conditions also affect the bead size, bead shape and depth of penetration, which in turn actually determine the quality of the weld and its performance in service. In this section different SAW process variables and their effects on welded joints will be discussed.

2.3.1 Heat Input

Three variables govern the total energy input to the work piece. These are a) heat input, b) heat distribution and c) welding travel speed [Gourd, 1980]. Among them, the heat input per unit length is calculated using the following equation [Antaki, 2003]:

$$HeatInput = \frac{V \times I}{v} \dots\dots\dots 2.1$$

Here, V = Voltage, I = Current and v = travel speed.

When there are two electrodes used during welding, the heat input can be calculated by adding the product of voltage and current of the individual electrodes divided by the travel speed [Pepin, 2009]. Equation 2.2 shows the heat input calculation for tandem electrodes.

$$Heat\ Input = [(V \times I)_{LEAD} + (V \times I)_{TRAIL}] / v \dots\dots\dots 2.2$$

Here, the voltage and current products for the lead electrode and trail electrode are added together, and then divided by the travel speed. Heat input is generally expressed in units of kJ/mm. In the automated SAW process, the voltage is generally kept constant [Gourd, 1980], so that the current and travel speed can be changed to change the heat input [Croft, 1984].

Increasing heat input increases the productivity of the welds produced. A higher heat input also generates higher heat, which affects the HAZ and thus contributes to HAZ coarsening. The increased productivity due to increasing heat input may come at the cost of inferior mechanical properties, as the HAZ toughness decreases due to grain coarsening. However, too low a heat input is also not desirable. Lower heat input decreases the productivity and affects the weld quality. Chandel and Bala [Chandel, 1986] reported that when the travel speed is high (low heat input), undercuts and lack of penetration occur in the weld. Generally, when heat input is increased, bead width, reinforcement area and depth of penetration are also increased [Pepin, 2009] [Gourd, 1980]. All these factors have an overall affect on the weld joint produced.

2.3.2 Arc Voltage

Arc voltage has no effect on HAZ dimensions; however, voltage is used to control bead shape [SAW guide, ---] [SAW, 1982]. The arc length increases as the arc voltage increases and vice versa. As can be seen in Figure 2-13, increasing the arc voltage increases the arc length and, hence, decreases the electrode stickout (approximately the length of electrode between the arc and the contact tip). Thus, increasing arc length produces a flatter and wider bead [SAW guide, ---].

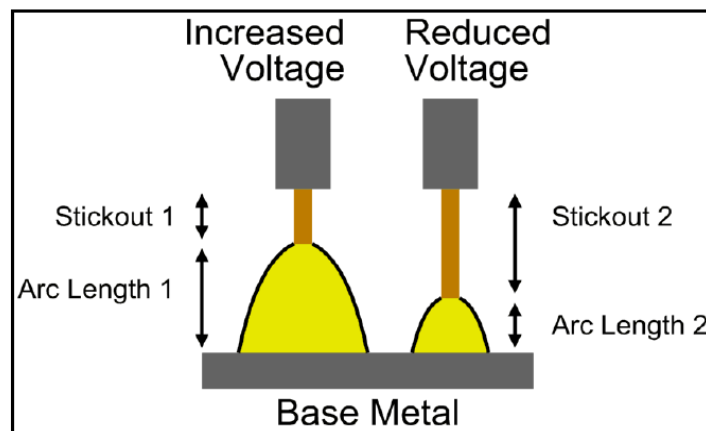


Figure 2-13: Effect of voltage on stickout and arc length [Pepin, 2009] (Reprinted with permission).

When the other variables are kept constant (i.e., current and travel speed), increasing arc voltage improves slag removal, increases flux consumption and reduces porosity caused by rust and mill scale [SAW guide, ---] [Arc Welding, 2000]. However, excessively high voltages produce a “hat-shaped” bead which is more prone to cracking in single pass welding (Figure 2-14) [SAW guide, ---]. A lower arc voltage produces higher reinforcement height and a narrow bead [SAW guide, ---], although slag removal in deep groove welds is improved. Arc voltages that are too low result in poor slag removal [SAW guide, ---].

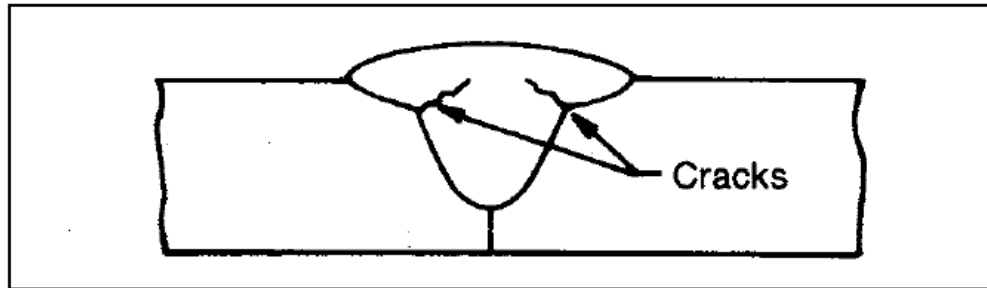


Figure 2-14: “Hat- shaped” bead, that is subject to cracking, due to high arc voltage [SAW guide, ---] (Reprinted with permission).

2.3.3 Welding Current

Welding current and wire feed speed (WFS) are directly related to each other because welding current increases with increasing WFS and vice versa [SAW, 1982]. This assumes that all other variables are constant and that a constant potential power source with a constant speed feeder is being used. Generally, welding current controls the wire melt-off rate, depth of penetration and base metal dilution [SAW, 1982]. As the welding current/WFS increases, penetration and wire melt-off rate increase (Figure 2-15).

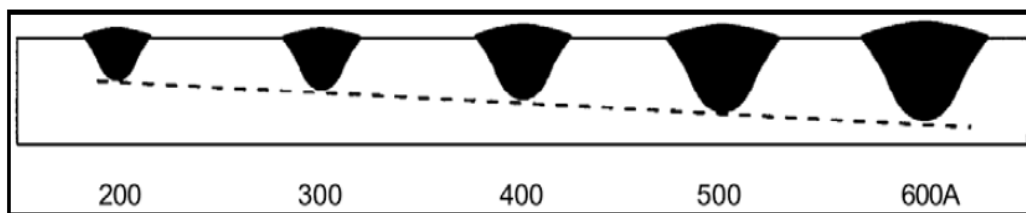


Figure 2-15: Effect of welding current on SAW bead-on-plate weld cross section [Weman, 2003] (Reprinted with permission).

Weld bead width increases with increasing welding current because of increasing deposition rate [Pepin, 2009]. At higher current values, penetration increases more

than the bead width [Gupta, 1987]. There is a critical current level above which increasing the welding current will actually decrease the bead width [Gupta, 1987]. Yang *et al.* [Yang, 1992] reported that for a particular electrode diameter and extension, the bead width increases initially as the current is increased, up to a maximum; after which bead width decreases as the welding current is increased further. Other literature work [Weman, 2003] opposes this idea; however, stating that higher current results in higher and narrower beads, with no critical current value. Gunaraj and Murugan [Gunuraj, 1999] also reported that depth of penetration, reinforcement size and dilution increase with increasing welding current/WFS, while weld bead width is unaffected. Too high a welding current for any given condition can lead to weld shrinkage, added stress and a chance of weld distortion [SAW, 1982]. Excessively low welding current/WFS produces an unstable arc. There is a range of welding currents that can be used for any given combination of wire diameter and flux (Figure 2-16).

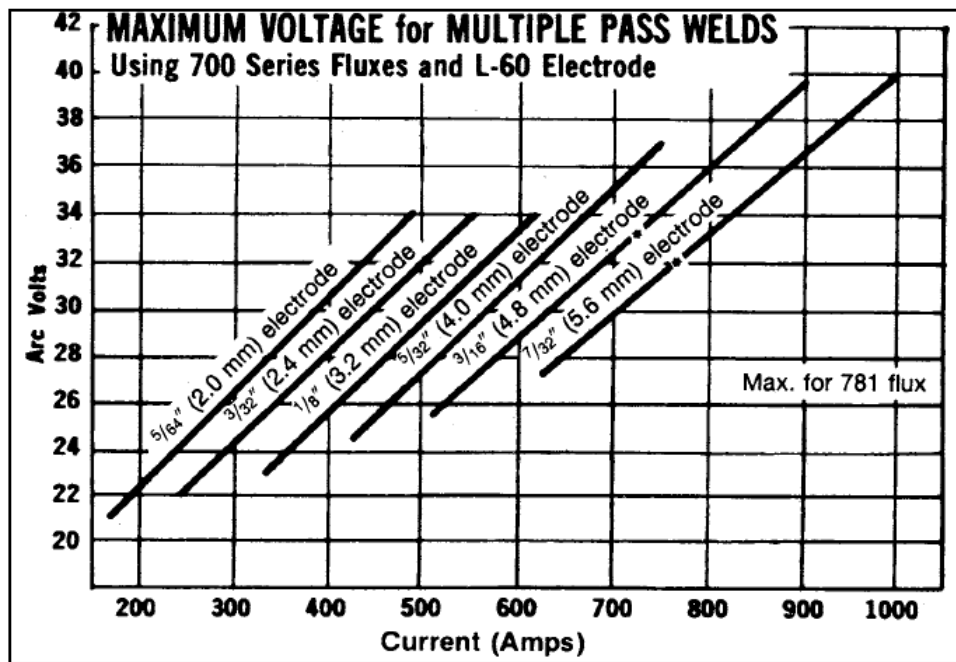


Figure 2-16: Range of currents that can be used for a given voltage, flux and wire diameter [SAW guide, ---] (Reprinted with permission).

2.3.4 Travel Speed

Changing the travel speed will change the weld size and penetration. Heat input can be increased or decreased by changing the travel speed (Equation 2-3). An increase in travel speed will decrease the heat input and will decrease the penetration depth, weld bead width and reinforcement height. Travel speed is one of the most important variables affecting the penetration depth and bead size.

Gunaraj and Murugan [Gunuraj, 1999] reported that the weld bead width and depth of penetration decrease with increasing welding speed (lower heat input). Other literature [Yang, 1992], however, reported that bead width increases initially as the welding speed is increased up to a maximum size, after which bead width decreases as the speed is increased. High welding speed produces porosity and non-uniform bead shapes [SAW, 1982]. Very low travel speeds produce bead shapes that are subject to cracking. When travel speed is very low, the deposited metal will pool on the parent metal's surface and will spread out, thus increasing the bead width. However, the penetration will be higher in the centerline of the weld bead, producing a "T-shaped" penetration profile (Figure 2-17), which is very susceptible to hot and cold cracking [Weman, 2003] [Lincoln, 1994]. Too low a travel speed produces an uncontrollable molten pool, which results in a rough bead and possible slag inclusions [SAW, 1982].

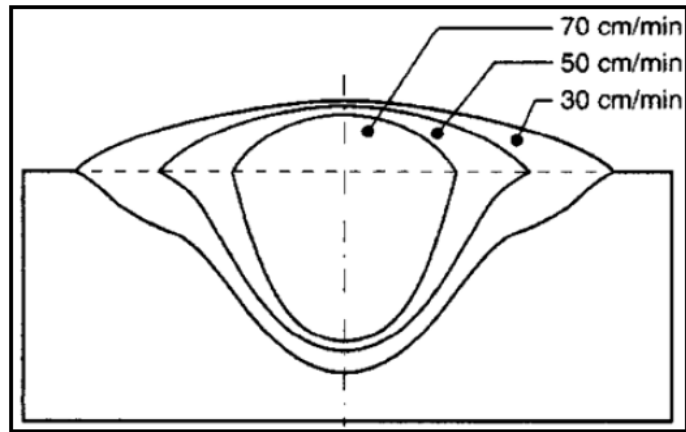


Figure 2-17: Effect of varying travel speed on SAW bead-on-plate weld cross section [Weman, 2003] (Reprinted with permission).

2.3.5 Wire Size

For a constant current setting, the electrode diameter affects the weld bead shape and penetration depth [Houldcroft, 1989]. Electrode diameter also affects the deposition rate. For a given current setting, a small diameter electrode will have a higher current density, producing a higher deposition rate than a larger diameter wire. However, a larger wire can carry more current, so deposition rate increases as the current increases. For a given diameter, if the current increases the current density also increases; this in turn will increase the penetration depth of the base metal. A lower current for the same diameter wire will produce a lower current density; the result is a lower penetration depth. There is a range of currents that can be used for a given wire diameter and arc voltage (Figure 2-16). Large diameter wire is generally used to weld large root openings. On the other hand, small diameter wires are used mostly for tandem wire systems and in semi-automated applications [Houldcroft, 1989].

2.3.6 Fluxes used in SAW

The granular material that covers the welding area during welding with SAW is referred to as “flux”. This material performs other functions in addition to those associated with a fluxing agent. The flux used in SAW protects the melting metal from oxidation and adds small amounts of elements into the metal to get desired quality welds. Fluxes can be divided by the various methods used to manufacture them. According to this classification, fluxes are of four types:

- a.) Fused Fluxes
- b.) Bonded Fluxes
- c.) Agglomerated Fluxes and
- d.) Mechanically Mixed Fluxes

The basicity index is calculated using Tuliani’s formula [Tuliani, 1969]:

$$B = \frac{\%CaO + \%MgO + \%BaO + \%SrO + \%Na_2O + \%K_2O + \%Li_2O + 1/2(\%MnO + \%FeO)}{\%SiO_2 + 1/2(\%Al_2O_3 + \%TiO_2 + \%ZrO_2)}$$

.....2.3

Here B is the basicity index and % refers to weight percentage of the components.

The classification based on the basicity index has the following ranges:

Acidic < 1

Neutral = 1-1.5

Semi-basic = 1.5-2.5

Basic > 2.5

According to Thomas [Thomas, 1977], semi-basic fluxes have more advantages than others. They offer excellent toughness and good operating characteristics. Since the semi-basic fluxes have very low oxygen content, they produce high quality welds. The toughness of the weld metal is reduced by oxygen

contamination, which usually comes from acid fluxes. The composition of the flux is an important factor since the weld metal chemistry is affected by the electrochemical reactions at the weld pool-flux interface. In addition, flux particle size is important because the size influences weld bead shape, appearance and weld current levels [Houldcroft, 1989]. Usually when the welding current is increased, the average flux particle size should decrease. Too high a current for a given particle size will produce an unstable arc with uneven bead edges. This is why flux manufacturers provide literature reporting allowable currents that can be used for a specific mesh size flux. However, coarser particles are used for rusty plates to ensure easy removal of fumes during welding. Only properly dried fluxes should be used during welding. Moist fluxes cause unstable arcs resulting in poor bead shape. Also, recovered flux is mixed with new flux before it is reused.

2.4 Welding Metallurgy

In fusion welding, the metallurgical processes occurring in the weld when the weld metal is in the molten state or begins to solidify are very important. The melting and cooling conditions of the weld itself, and the associated structural changes that occur in the adjacent zone, determine the properties of the welded joint as a whole [Kurny, 2002]. A welded joint can be divided into four different microstructural regions [Gourd, 1980]. They are the weld metal (WM), the fusion line, the heat affected zone (HAZ) and the unaffected parent metal (PM) zone. In Figure 2-18 a typical structure of a single V-weld is shown along with the distribution of temperature.

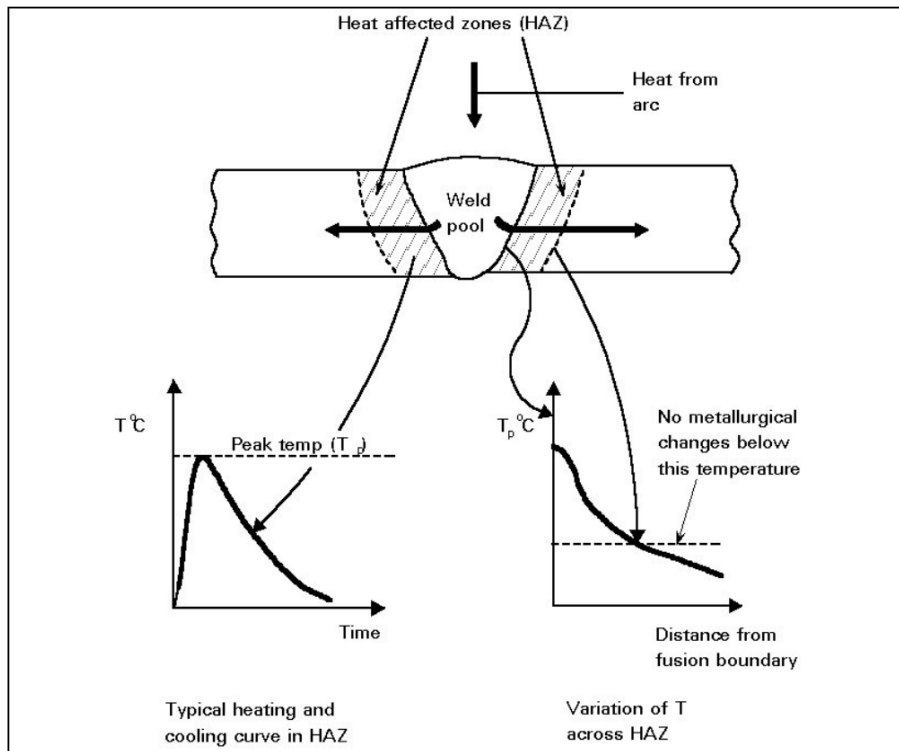


Figure 2-18: Weld structure and distribution of temperature [Gourd, 1980]
(Reprinted with permission).

The weld metal, also known as the fusion zone, is obtained by melting the base metal along with the filler metal and flux [Gourd, 1980]. The temperature in this region exceeds the melting temperature [AWS, 2004]. The weld interface, also known as the fusion line, is a narrow line which separates the weld metal from the HAZ. It is a thin band of the parent metal which has undergone melting during welding or partially melted, but before any mixing takes place it solidifies [Gourd, 1980]. This zone is very narrow, but is crucial in regard to the performance of the weld joint [Kurny, 2002]. The HAZ is adjacent to the weld metal and is formed in the parent metal of all welds. In this zone the structure of the parent metal is changed due to rapid heating and cooling during the welding process; however, the chemical composition remains unchanged. Figure 2-19 shows a schematic of a welded steel plate. An iron-iron carbide phase diagram is included in the

schematic to illustrate the microstructural changes that occur at various temperatures.

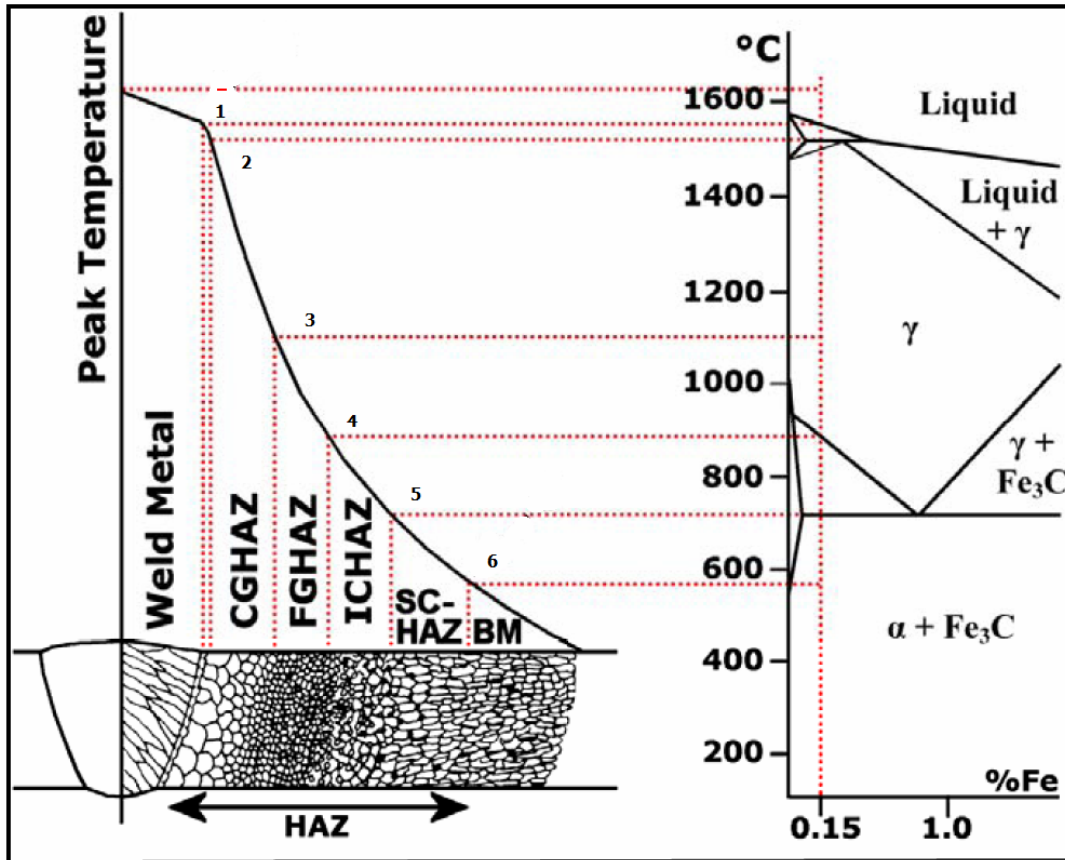


Figure 2-19: Structural changes in the HAZ during welding of steel (based upon original images by Easterling, pg. 126, and Patchett) [Easterling, 1992] [Patchett, 1998] (Adapted with permission).

Section 1-2 in Figure 2-19 is the fusion zone. Next to the fusion zone four distinct HAZ regions are formed (Section 2-6). The HAZ regions are designated as coarse grain HAZ, fine grain HAZ, intercritical HAZ and subcritical HAZ (CGHAZ, FGHAZ, ICHAZ and SCHAZ, respectively).

In Section 2-3 (Figure 2-19), the metal is overheated leading to grain coarsening and the formation of an acicular (Widmanstätten) structure [Kurny, 2002]. The temperature of the metal in Section 3-4 does not exceed 1100°C. In this section,

grains are transformed into austenite, but they do not coarsen, due to the lower peak temperature and grain boundary pinning by precipitates. Rapid recrystallization and nucleation dominates over grain growth. This is why the FGHAZ has improved toughness relative to the CGHAZ [Aran, 1984] [Liessem, 2004]. Section 4-5 is heated to a temperature between the upper and lower critical temperatures. (The upper critical temperature is the temperature below which ferrite starts to form as a result of ejection from austenite and the lower critical temperature is the temperature of the austenite to pearlite transformation. Below this temperature austenite does not exist.). In this section, the metal is partially austenized during welding. The strength of the metal of this zone is between that of completely recrystallized materials and the base metal [Kurny, 2002]. No microstructural changes normally occur in the steel in Section 5-6. However, if the metal is subjected to plastic deformation before welding, then recovery occurs in this region [Kurny, 2002]. The parent metal exhibits no metallurgical changes since the temperature is not high enough. However, the parent metal near the HAZ is likely to have high residual stresses, as the weld metal shrinks during cooling [Gourd, 1980].

As was described earlier, the properties and microstructures cannot be restored to a TMCP microalloyed steel after welding. Therefore, it is necessary to determine how to minimize the detrimental effects of the inhomogeneous HAZ on the overall properties of the steel and the welded joint. By optimizing different welding conditions and variables, it is possible to lower the detrimental effects of the HAZ region.

2.5 Weldability of TMCP Steels

The term “weldability” literally means ability to weld. However, this definition is no longer applicable, because most industrial materials are now somewhat “weldable” [Poorhaydari, 2005]. Rather, the term “weldability” is now used, particularly for steel, as a criterion to define the quality of the weld and the in-service behavior of the weldments [Gourd, 1995]. Some researchers have related weldability to how susceptible a weld is to cracking during or after welding [Dolby, 1983]. However, anything that makes the final joint unsuitable for service can be related by the term weldability. This can be solidification cracking in the weld metal, unacceptable oxidation on the surface of the HAZ (titanium alloys), liquidation cracking in the HAZ, hydrogen cracking or other factors. Easterling expressed the weldability of steels in terms of the Carbon Equivalent (C.E.) limit, which is generally considered as 0.4 [Easterling, 1992]. The formula for calculating C.E. according to the International Institute of Welding (IIW) is given in Equation 2.4. This equation is only valid for carbon levels >0.15 wt % [Patchett, 1998]. For very low carbon (<0.15 wt%) microalloyed steel the Ito-Besseyo formula is used (Equation 2.5); this is known as P_{cm} . Here the values for different elements are in wt%.

$$C.E. = \%C + \frac{\%Mn + \%Si}{6} + \frac{\%Cr + \%Mo + \%V}{5} + \frac{\%Cu + \%Ni}{15} \dots\dots\dots 2.4$$

$$P_{cm} = \%C + \frac{\%Mn + \%Cr + \%Cu}{20} + \frac{\%Si}{30} + \frac{\%Mo}{15} + \frac{\%V}{10} + \frac{\%Ni}{60} + 5\%B \dots\dots\dots 2.5$$

In TMCP microalloyed steel, the carbon level is much lower, making it more “weldable”. This allows TMCP microalloyed steel to be welded, with very little or no preheat, which in turn is more cost effective [Imai, 2002] [Spanos, 1995].

Figure 2-20 shows the relationship between P_{cm} and preheat temperature. On the right side of the plot, the level of preheat (temperature) is shown with respect to the P_{cm} values to avoid cracking. On the left side, P_{cm} values are plotted against plate thickness of different steels (normalized steel plate and TMCP steel plate). It was shown that for normalized steel plate with a thickness of 50 mm in order to avoid cracking a preheat temperature of around 120°C should be used. TMCP steel plates of similar thickness require no preheat at all. Note that the P_{cm} values for TMCP steel plate are quite low compared with normalized steel plates with similar thickness.

The high strength of TMCP steel is the result of several strengthening mechanisms. The main ones are grain refinement, precipitation hardening, solid solution strengthening and dislocation hardening [Gladman, 1997]. Lu found that for an X80 steel, grain refinement provides approximately 50% of the strengthening component; precipitation hardening provides around 10% of the strengthening. The remaining 40% is provided by solid solution and dislocation strengthening components [Lu, 2005]. These mechanisms allow the strength of the steel to be increased without increasing the carbon content of the steel, or drastically reducing the toughness of the steel. Low carbon steel (with low P_{cm} values) is much less likely to form martensite in the HAZ, which increases the weldability of the weld joint. Thus, these strengthening mechanisms act individually without decreasing the weldability of the steel. However, during welding, due to the rapid temperature change, the material adjacent to the weld metal forms different microstructures based on the cooling rate. These HAZ regions may have widely varying microstructures and mechanical properties compared with the base material. In other words, the structure formed by TMCP processing is destroyed in the HAZ regions. One important aspect of welding TMCP steel is that the structure produced is impossible to duplicate by any other thermal heat treatment [De Meester, 1997]. So, once the structure of the base material adjacent to the weld metal is destroyed, it cannot be restored.

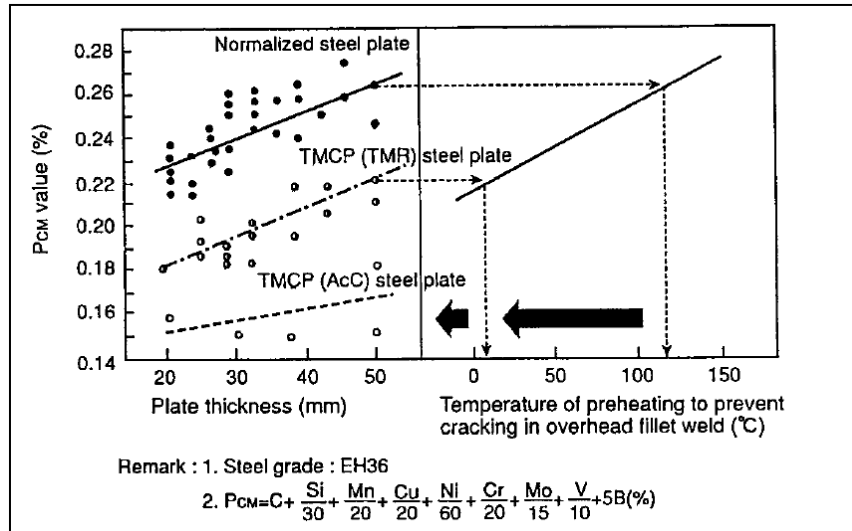


Figure 2-20: Relationship between Pcm and preheat temperature [Imai, 2002]
 (Reprinted with permission).

2.6 Welding of Microalloyed Steel Using SAW

There is a large number of SAW welding variables that can be controlled and manipulated when welding microalloyed steels. Many of these variables affect the bead shape and size and, hence, affect the mechanical properties of the welded joints [Pepin, 2009]. Previous work done in this regard mostly emphasized BOP welds of X70 steels using SAW [Pepin, 2009]. A detail weld bead shape variation based on different waveform manipulation was performed for various heat inputs. It was found that the mechanical properties, i.e., CVN values, are influenced by these bead shape geometrical changes. A shape parameter, i.e., SP ratio, was developed to better explain the change of bead shapes and this parameter was further used to establish relationships with CVN values. Strong relationships between Charpy V-notch values and bead shape parameters were found. It was found in the study by Pepin that increasing SP ratio increases the CVN values. Other bead shape parameters (penetration depth, reinforcement height and bead width) were also affected by the heat input values. Increasing heat input increases

the penetration depth, reinforcement height and bead width. The ultimate affect of these changes on the mechanical properties of the welded joints can be understood by means of microstructural changes. No such correlation between mechanical properties and microstructure was made in the previous study. In this study, modified bevel joints are used to join X80 steel plates using SAW, which closely simulates the actual production weld during in-house pipeline welding. The aim of the study is to see whether different SAW welding parameters affect the bead shape of the bevel welded joint in a manner similar to BOP weld joints. Furthermore, different microstructural characterization techniques are used to explain the mechanical properties of the welded joints.

Joining of X80 steels using SAW, with desired overmatched properties, is quite difficult but not impossible. By using proper electrodes, heat input, flux system and other SAW parameters effectively, it is possible to get overmatched welded joints. This study aims to get valuable information linking SAW parameters with microstructural characterization and their affect on overall mechanical properties on the welded joints of X80 steel plates. In the following section the weld and HAZ microstructure will be described, since the microstructures of welded joints are ultimately responsible for the overall mechanical properties and the service performance of pipeline steels.

2.6.1 Weld and HAZ Microstructure

To better understand the steel microstructure and different phases that are present in the steel, it is a good idea to start with the metastable iron carbon phase diagram shown in Figure 2-21. The diagram shows the different phase transformations that can occur in steel during heating and cooling under metastable equilibrium conditions. The steels used in this study have carbon contents of 0.03 wt% and 0.06 wt%. Therefore, the main regions of interest should be phase transformation from austenite to ferrite at those carbon percentages. Under equilibrium cooling conditions, steels containing such low

carbon percentages would transform to ferrite and a small amount of cementite; the amount will depend upon the carbon percentage and other alloying elements [Smith, 1993]. However, in steelmaking, equilibrium cooling conditions are not achieved. The final microstructure of steel is basically influenced by the kinetics of the transformation. The steel undergoing transformation will have a structure which depends both on time and temperature during processing. Hence, to understand the final transformation products, continuous cooling transformation (CCT) curves are used, which show the effect of both time and temperature during steel processing. In Figure 2-22, one such CCT diagram is shown for a typical microalloyed steel.

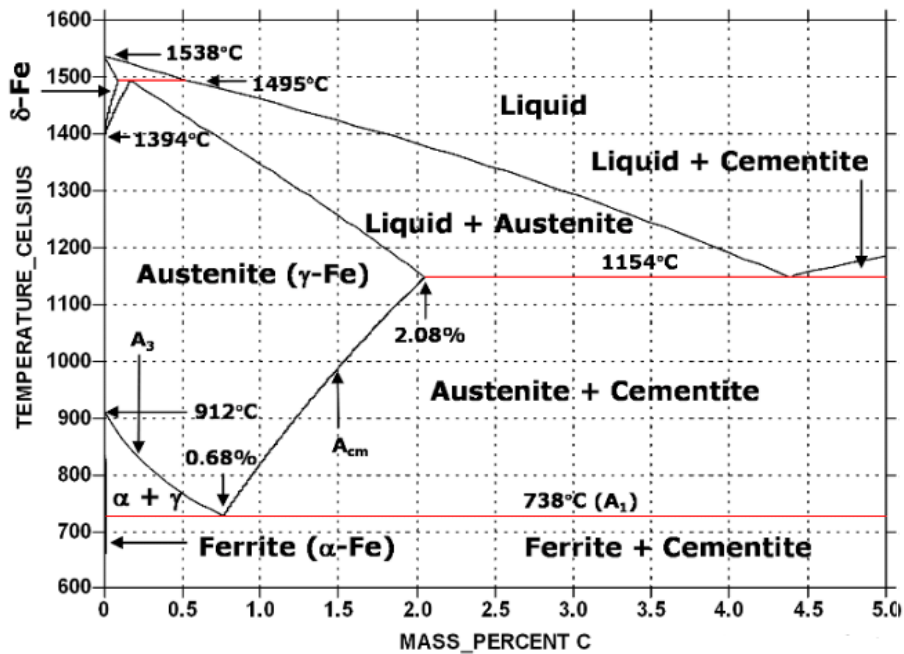


Figure 2-21: Iron carbon phase diagram [Calphad, 2006] (Reprinted with permission).

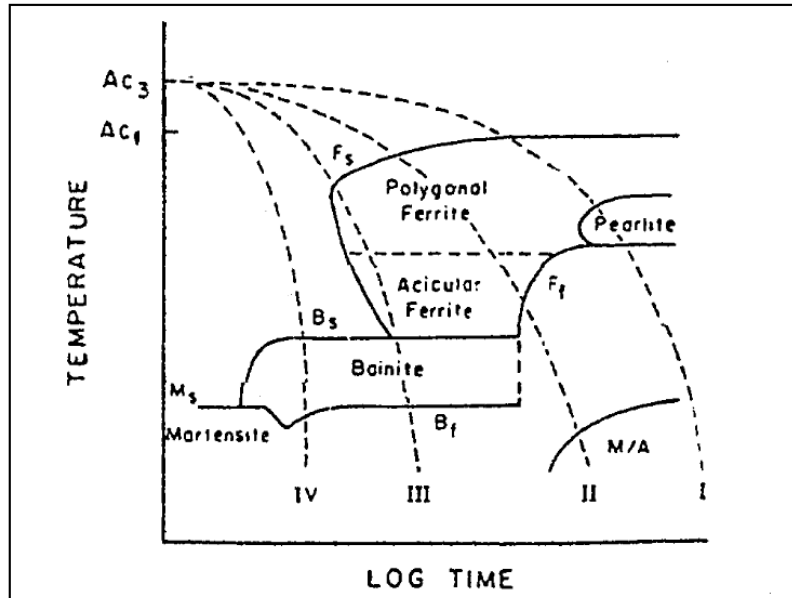


Figure 2-22: Schematic of CCT diagram for a microalloyed linepipe steel [Collins, 1983] (Reprinted with permission- www.ingentaconnect.com/content/maney/cmj).

In Figure 2-22, F_s and F_f refer to ferrite start and finish temperatures, respectively. B_s and B_f refer to bainite start and bainite finish temperatures, respectively. M_s refers to the martensite start temperature. M/A refers to a martensitic–austenitic region. Different cooling rates are shown as I, II, III and IV; I being the slowest cooling rate and IV the highest cooling rate. In TMCP processing, the final microstructure is governed by the exact chemistry and processing history [Hoskins, 2002]. The most common microstructures found in microalloyed steels are polygonal ferrite, acicular ferrite, bainite and martensite [Collins, 1983].

Although the final microstructure of microalloyed TMCP steel is fairly straightforward, the HAZ microstructural changes during welding are not that simple. There are differences relative to usual steel making processes, because of non-equilibrium conditions and steep temperature gradients induced by rapid heating during the welding thermal cycle [Losz, 1990]. During the weld heating cycle, due to rapid heating to a high temperature, large austenite grains develop in

the CGHAZ. This increases the hardenability of the steel, so much so that the usual CCT diagram developed in normal steel production for temperatures from 800°C to 900°C, is no longer applicable [Spanos, 1995]. Weld CCT diagrams are based on very high austenizing temperatures (1350-1400°C) [Easterling, 1992]. On the other hand, in the FGHAZ region the peak temperature is lower compared to the CGHAZ region, which upon cooling transforms to a different microstructure from the CGHAZ due to the slower cooling rate. For the reasons described above, the microstructure of the HAZ is very complex and heterogeneous in nature, varying from location to location. In the following section, different features of commonly found phases in microalloyed steel and in the weld metal and HAZ will be discussed.

2.6.1.1 Polygonal Ferrite

Polygonal ferrite (PF) has an equiaxed structure, which forms when cooling from the austenite region at a slow rate such that almost equilibrium cooling conditions prevail. Between the temperatures of 900°C and 700°C, ferrite starts to nucleate and grow on the grain boundaries of austenite. The solubility of carbon in ferrite is low, so the excess carbon diffuses to the untransformed austenite increasing its carbon content. As the temperature is slowly decreased, more and more ferrite is formed resulting in less untransformed austenite in the steel. When the temperature reaches the eutectoid temperature (~723°C) the remaining austenite with increased carbon content transforms to pearlite. However, TMCP steels have very low amounts of carbon and the addition of carbide forming elements, such as Nb, Ti and V, tends to decrease the possibility of pearlite formation [Hoskins, 2002]. Some researchers have observed pearlite in TMCP steels with carbon levels as low as 0.05 wt% and carbide forming elements Nb (0.09 wt%), Ti (0.014 wt%) and V (0.025 wt%) [Zhou, 2010].

The dislocation density in PF is very low [Collins, 1983]. PF has a distinct grain boundary, with no discernable prior austenite grains in the final microstructure. In

Figure 2-23, a typical microstructure of polygonal ferrite along with some pearlite is shown.

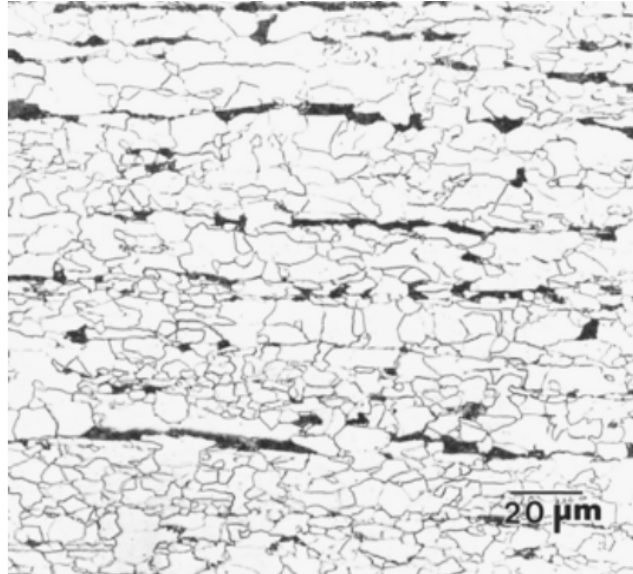


Figure 2-23: Optical micrograph of equiaxed (polygonal) ferrite and pearlite (dark) [Voort, 2004] (Reprinted with permission of ASM International. All rights reserved. www.asminternational.org).

2.6.1.2 Acicular Ferrite

Acicular ferrite (AF) is a very fine irregular and sub-structured ferrite, which is formed when the cooling rate from the austenite region is higher than that for polygonal ferrite [Losz, 1990] [Collins, 1983]. AF is formed by a combination of diffusion and shear modes. It is believed to be formed intragranularly, by a two stage process [Hoskins, 2002] [Poorhaydari, 2005] [Losz, 1990]. The grain boundaries are filled with proeutectoid ferrite. The primary ferrite plates nucleate within the grains at inclusions and then small side plates nucleate and grow from these primary ferrite plates [Losz, 1990]. The shape of AF in three dimensions is plate-like or needle/lath-like with typical dimensions of about 5 to 10 μm in length and around 1 μm in diameter [Bhadeshia, 1993] [Laitinen, 2006]. The term

acicular ferrite comes from the needle-like morphology in two dimensions (Figure 2-24). It is reported in the literature that both acicular ferrite and bainite have similar transformation mechanisms [Bhadeshia, 1993] [Laitinen, 2006] [Madariaga, 2001]. Figure 2-25 illustrates the effect of prior austenite grain size in determining whether the microstructure is predominantly acicular ferrite or bainite. A larger prior austenite grain size has a large number of inclusion sites, which favors the formation of acicular ferrite, whereas a small prior austenite grain size has a larger amount of grain boundary area for nucleation so bainite dominates [Bhadeshia, 1993]. Due to the interlocked nature of its ferrite laths, AF provides the best combination of strength and toughness compared with polygonal ferrite, bainite and martensite [Bhadeshia, 1993] [Kim, 2005].

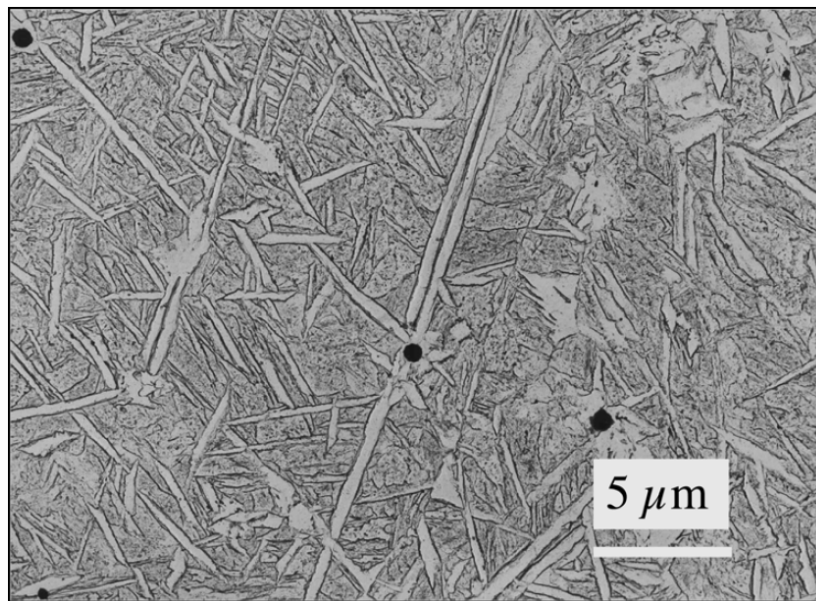


Figure 2-24: Replica transmission electron micrograph of acicular ferrite plates in a steel weld deposit [Bhadeshia, 1993] (Reprinted with permission).

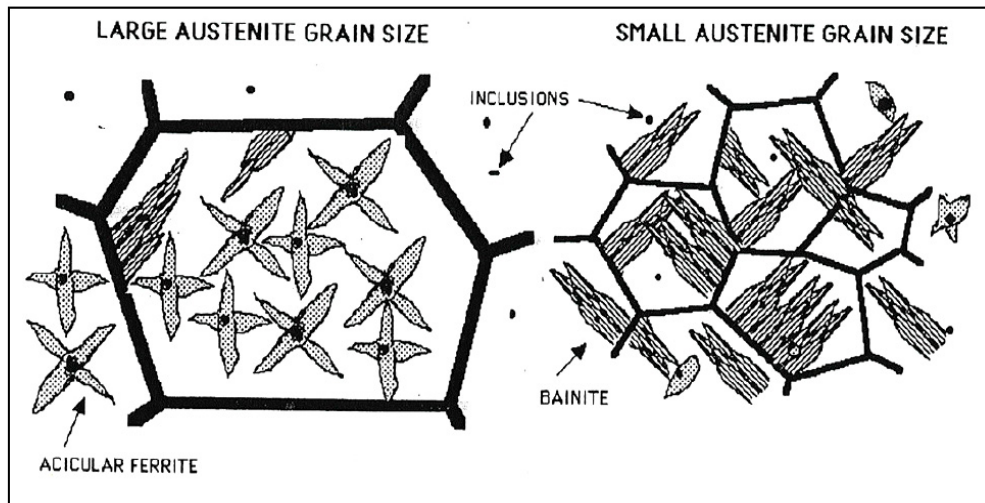


Figure 2-25: Schematic illustration of the effect of prior austenite grain size on the formation of acicular ferrite [Bhadeshia, 1993] (Reprinted with permission).

2.6.1.3 Bainitic Ferrite

Bainitic ferrite is formed at considerably higher cooling rates (between III and IV in Figure 2-21). It is hard to distinguish between acicular ferrite and bainitic ferrite and, hence, they are sometimes considered as one phase in the CCT diagram [Lu, 2009]. Bainitic ferrite grows in the form of “packets” of lath ferrite (Figure 2-26). It offers good strength and toughness similar to acicular ferrite. However, bainitic ferrite is different from acicular ferrite, because acicular ferrite nucleates intragranularly in steels containing a greater number density of inclusions than austenite grain surface nucleation sites [Yang, 1986]. This type of microalloyed steel produces a continuous stress-strain curve [Lu, 2009] [Bhadeshia, 2001].



Figure 2-26: Optical micrograph illustrating sheaves of bainitic ferrite in a partially transformed (395°C) Fe-0.3C-4Cr wt% alloy [Bhadeshia, 2001] (Reprinted with permission).

2.6.1.4 Bainite

Bainite can be defined as “a non-lamellar aggregate of ferrite and cementite”, which forms during austenite deformation [Joarder, 1991]. The transformation temperature of bainite is below that for acicular ferrite and above the martensite start temperature [Hoskins, 2002]. Its structure when observed optically is very similar to acicular ferrite. However it is evident from the literature that the prior austenite grain boundaries that are retained in bainite are not distinguishable in acicular ferrite [Collins, 1983]. This is why prior austenite grains have a profound effect on its properties [Poorhaydari, 2005]. Bainite has a small grain size (lath size is 0.5-2.0 μm in thickness) and relatively high dislocation density, carbon supersaturation and carbide distribution depending on its size and location [Poorhaydari, 2005]. All these factors contribute to the strength of bainite. When

present in line pipe steel, bainite is only found as a minor component [Collins, 1983]. According to some researchers, the decomposition of austenite in the bainitic temperature zone leads to the formation of three types of bainite [Samuel, 1984] [Hrivnak, 1995]. These are:

- a) Granular Bainite
- b) Upper Bainite
- c) Lower Bainite

Granular bainite is actually massive ferrite (MF) (massive ferrite is a high temperature transformation of austenite to ferrite without a compositional change, in very low carbon steels) with M-A islands (Figure 2-27) [Krauss, 2005] [Mangonon, 1976]. It is observed in HSLA (high strength low alloy) steel, especially in welded joints formed using high heat inputs and slow cooling rates [Poorhaydari, 2005] [Hrivnak, 1995]. GB is also found in continuously cooled steel microstructures [Poorhaydari, 2005]. GB lowers the toughness of the steel.

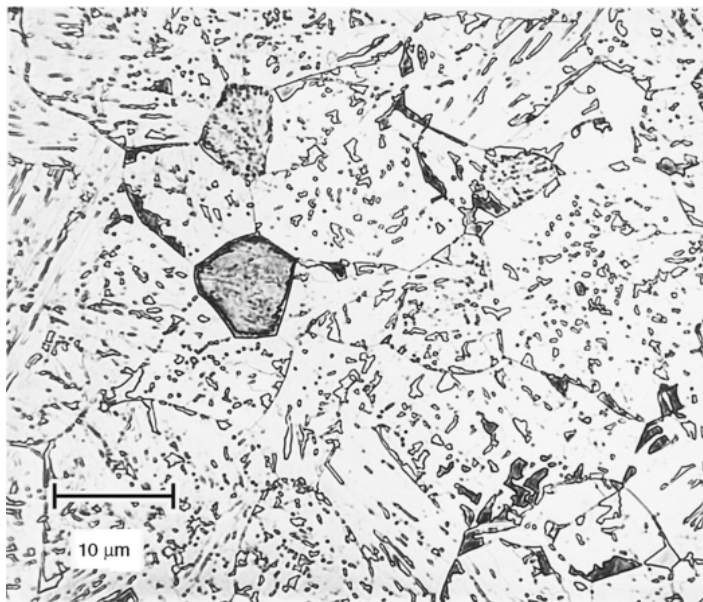


Figure 2-27: Granular bainite showing islands of martensite (dark) and retained austenite in a matrix of ferrite [Voort, 2004] (Reprinted with permission of ASM International. All rights reserved. www.asminternational.org)

When the transformation temperature is in the high end of the temperature zone (400°C to 550°C) required for bainite formation, upper bainite is formed [El-Khazen, 2009]. During the transformation, when the ferrite laths are growing, the excess carbon is rejected to the untransformed austenite. Upon further cooling, the carbon-rich austenite is transformed into cementite along the ferrite laths or even retained as austenite in the final microstructure [Losz, 1990]. Based on optical microstructural observation, these types of microstructures are quite similar to ferrite with an aligned second phase martensite/austenite/carbide (MAC), which has a lamellar microstructure [Ranasen, 1972] [Thaulow, 1985].

Lower bainite is formed when the transformation temperature is lower than that of formation of upper bainite (250°C to 400°C). In this type of bainite, the carbides are trapped in the ferrite laths [Losz, 1990]. Figure 2-28 shows a typical microstructure of bainite.

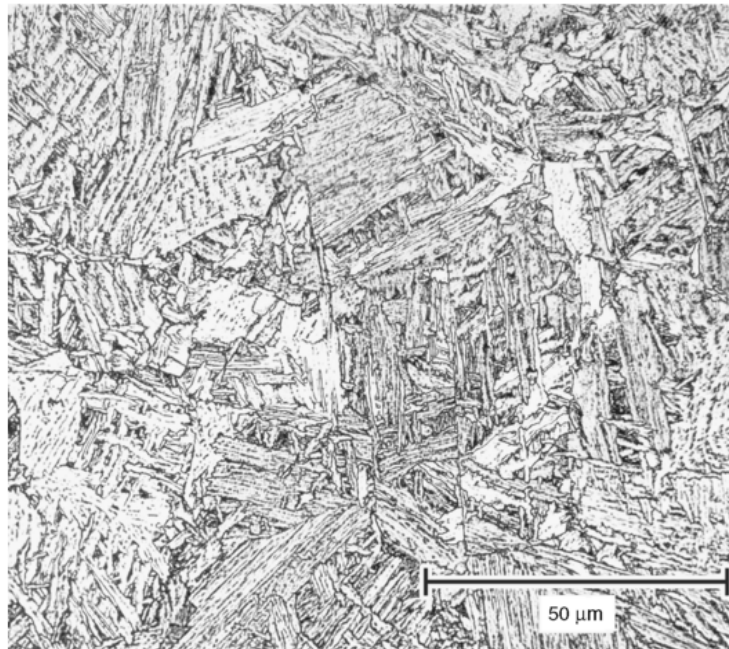


Figure 2-28: Optical micrograph of bainite found in heat treated low alloy steel. 4% picral + 2% nital etch [Voort, 2004] (Reprinted with permission of ASM International. All rights reserved. www.asminternational.org).

2.6.1.5 Martensite

Martensite is transformed from austenite in a diffusionless manner. It is a very hard structure, which forms by a sudden shear in the austenite lattice [Bhadeshia, --]. The martensitic transformation is highly crystallographic in nature, which leads to a characteristic lath microstructure. In low carbon martensite the shear mechanism for transformation can be divided into “primary shear and glide (slip)”, whereas in high carbon martensite the mechanism is “primary shear and twinning” [Ranasen, 1972]. The martensite transformation reaction in steels is athermal in nature. The martensitic reaction begins at the martensitic start temperature, M_s , which can vary over a wide temperature range from as high as 500°C to well below room temperature [Bhadeshia, ---]. The M_s temperature depends primarily on the concentration of different austenite-stabilizing alloying elements [Bhadeshia, ---]. It was recently found that M_s is dependent on austenite grain size, as shown in Figure 2-29.

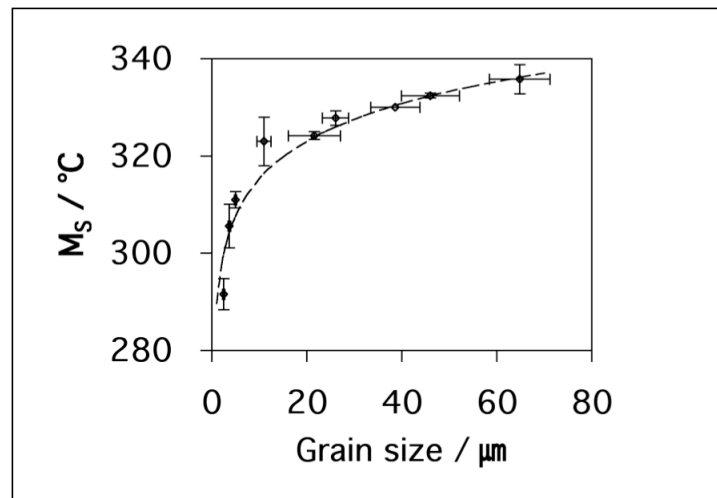


Figure 2-29: Variation of M_s with austenite grain size [Yang, 2009] (Reprinted with permission).

Once the M_s is reached, further transformation takes place during cooling until the reaction ceases at the martensite finish temperature, M_f . This is the temperature where all the austenite should have transformed to martensite. However, in practice a small proportion of the austenite does not transform. The amount of austenite retained in the final microstructure depends on the M_f temperature, which can be lower than room temperature in some highly alloyed steels.

Martensite has a *bct* (body centered tetragonal) crystal structure; however, in low carbon steels the structure is essentially *bcc* (body centered cubic) [Poorhaydari, 2005]. Carbon is trapped in *bcc* iron during the martensitic transformation producing a *bct* structure. Lower carbon levels mean less distortion, which produces a crystal structure closer to *bcc*. The hardness of martensite is solely a function of carbon percentage [Bhadeshia, ---]. Figure 2-30 shows the effect of carbon content on the hardness of martensite.

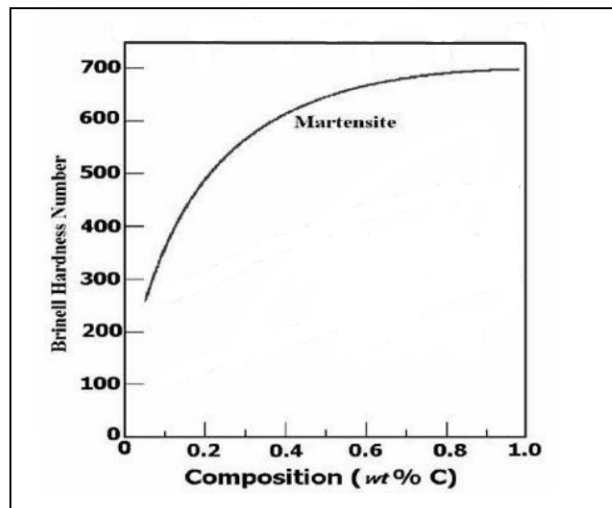


Figure 2-30: Effect of carbon on hardness of martensite [Avner, 1974]
(Reprinted with permission).

There are two main types of martensite that are found in ferrous materials. These are:

- a) Lath martensite and
- b) plate martensite

Lath martensite is found in plain carbon steels and low alloy steels with carbon amounts up to 0.5 wt%. It is also known as “massive martensite” or “packet martensite” [Poorhaydari, 2005]. Lath martensite has an acicular type or “needle like” morphology in 2D and a plate shape morphology in 3D [Voort, 2004] [55]. The microstructure is similar to upper bainite, so it is sometimes considered as upper bainite which has not fully transformed [Poorhaydari, 2005]. It has a lath width of 0.2-0.4 μm . Figure 2-31 shows an optical micrograph of lath martensite.

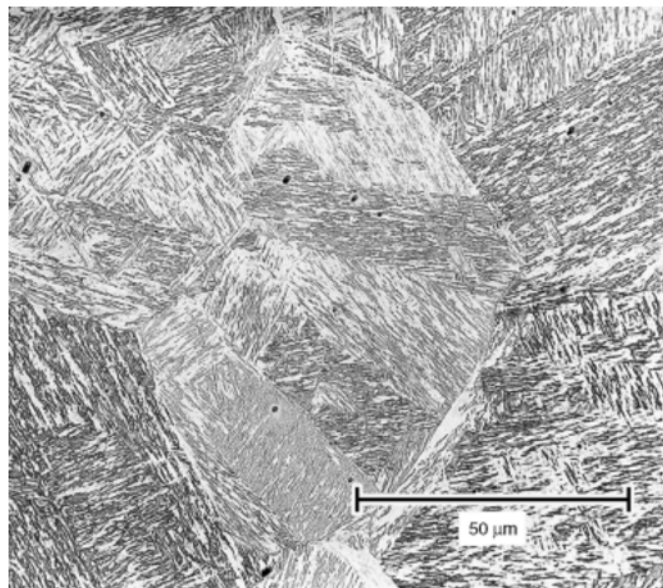


Figure 2-31: Optical micrograph of lath martensite [Voort, 2004] (Reprinted with permission of ASM International. All rights reserved. www.asminternational.org).

Plate martensite is formed mainly in medium and high carbon steels, Fe-Ni steels and Fe-Bi-C carbon steels [Poorhaydari, 2005]. It has a *bct* crystal structure. Plates first start to form in steels with about 0.5 wt% carbon, and can be concurrent with lath martensite in the range 0.5 wt%-1.0 wt% carbon [Bhadeshia, -

--]. Unlike lath martensite, the lenticular plates form in isolation rather than in packets, as shown in Figure 2-32.

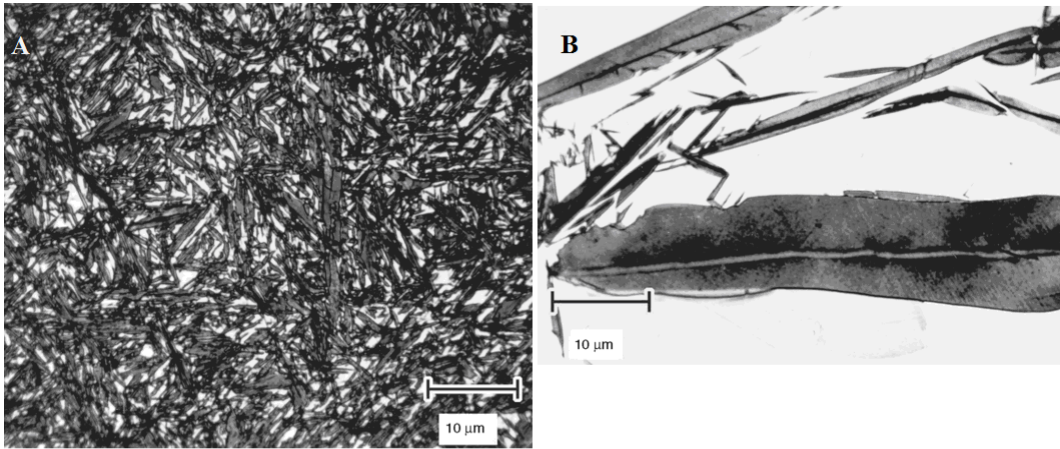


Figure 2-32: A) Optical micrograph plate martensite; B) Microstructure of plate martensite showing its midrib [Voort, 2004] (Reprinted with permission of ASM International. All rights reserved. www.asminternational.org)

2.6.1.6 Widmanstätten Ferrite

Widmanstätten ferrite forms by a mixed displacive and diffusional mechanism [Poorhaydari, 2005]. Although the growth of Widmanstätten ferrite is somewhat understood, the nucleation process is still debated [Bhadeshia, 1982] [Bhadeshia, July 1985] [Bhadeshia, 1985]. During undercooling or at intermediate cooling temperatures, ferrite grows bilaterally as plates or laths from the prior austenite grain boundary or within the austenite grains [Poorhaydari, 2005]. The lengthening rate of an individual plate/lath depends on alloy chemistry and transformation temperature [Ali, 1990]. The Widmanstätten start temperature (W_s) can be defined as the highest isothermal transformation temperature, at which Widmanstätten ferrite forms in detectable quantities [Ali, 1990]. The W_s temperature is more dependent on alloy chemistry than the A_{e3} temperature, which is the highest temperature where ferrite and austenite can coexist in equilibrium [Ali, 1990]. It should be noted that both Widmanstätten ferrite and

bainitic ferrite have similar formation mechanisms, morphology and crystallography; however, the transformation temperature for Widmanstatten ferrite is lower than that of bainite [Ohmori, 1992]. In general, the formation of Widmanstatten ferrite depends on three factors [Kurny, 2002]. These are:

- a) Chemical composition;
- b) The amount of austenite that will give rise to a secondary structure (i.e., the extent of overheating);
- c) The rate of cooling from the austenite state. The same cooling rate can produce a cellular structure if the austenite grain size is relatively small, or it can produce Widmanstatten structure if the austenite grain size is large.

Figure 2-33 shows a typical microstructure of Widmanstatten ferrite. Two types of morphology have been observed for Widmanstatten ferrite. These are primary Widmanstatten ferrite and secondary Widmanstatten ferrite [Bhadeshia, ---]. Primary Widmanstatten ferrite grows directly from the austenite grain surfaces, whereas secondary Widmanstatten ferrite forms from any allotriomorphic ferrite that is present in the austenite grains. Figure 2-34 shows a schematic of both morphologies.

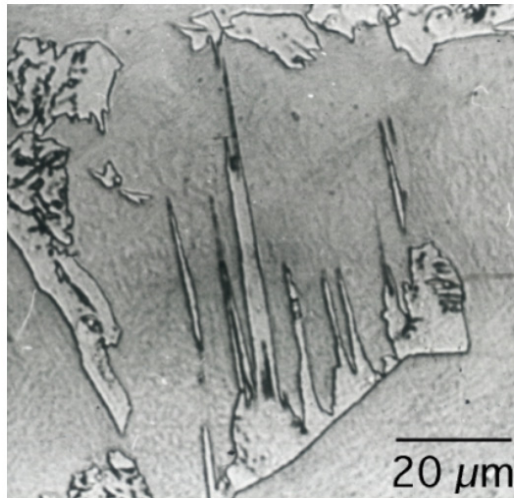


Figure 2-33: Optical micrographs showing etched (nital) wedge-shaped Widmanstätten ferrite plates (white) in a matrix quenched to martensite [Bhadeshia, ---].

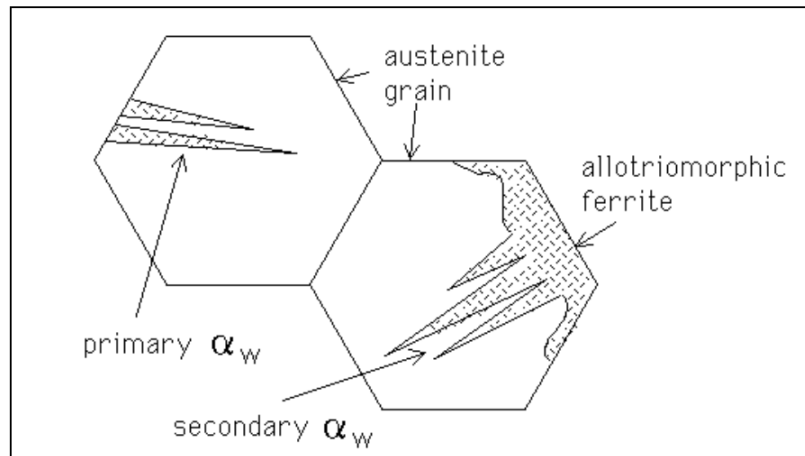


Figure 2-34: Morphology of primary and secondary Widmanstätten ferrite [Bhadeshia, ---] (Reprinted with permission)

2.6.1.7 M-A constituent

In pipeline steel, when cooling from the austenite state, austenite first transforms into polygonal ferrite during continuous cooling. Since the ferrite cannot have excess carbon, the carbon concentrates in the untransformed austenite. When this carbon-rich austenite is cooled below the martensite start temperature (M_s), it partially transforms to martensite in the austenite matrix and forms martensite-austenite (M-A) constituents. The amount of M-A is dependent on the critical carbon content of the residual austenite [Wang, 1992] [Shi, 2008]. The formation of M-A constituent depends on the composition and cooling rate [Godden, 1981]. M-A constituents have a detrimental effect on the toughness of the steel [Godden, 1981] [Matsuda, 1991].

So far in this chapter a general overview of processing of TMCP steels has been discussed. The weldability of TMCP steels in terms of composition has also been briefly explained. Since this study is aimed at the submerged arc welding of microalloyed steel, i.e., X80 steel, the overall SAW welding process has been discussed along with some other arc welding processes. Advantages and disadvantages of SAW welding over other arc welding processes have also been explained. SAW welding parameters (arc voltage, current, travel speed, flux system, number of electrodes, etc.) affect the weld and, hence, affect the overall mechanical properties of the welded joints. These parameters were briefly discussed. In the next chapter experimental design and different methodologies used in this study will be explained in detail.

Materials and Experimental Methods

In this chapter, the composition of the steels that are investigated is reported. This is followed by the different SAW welding parameters used in the study. Methodologies used to characterize the weld using geometric variables and for measuring thermal impact during welding are explained. Background information of different mechanical tests (hardness, tensile test and Charpy test) are provided, along with sample preparation techniques (scanning electron microscopy, optical microscopy and transmission electron microscopy), that are used for microstructure and precipitate analysis.

3.1 Materials

Two types of X80 steel plates were used in this study; both 10.22 mm thick. One of the steel plates was higher in carbon content (0.06 wt% carbon) and the other one was lower in carbon content (0.03 wt% carbon). All compositions, unless otherwise specified, are given in wt%. The X80 steel plates are named steel X (0.06 % carbon) and steel Y (0.03 % carbon), respectively, and this nomenclature will be used throughout the rest of the thesis. The steel plates were provided by EVRAZ Inc NA. The compositions of the steel plates are given in Table 3-1. Note that the main difference between the two steels is the carbon content.

Table 3-1: Chemical composition (wt%) of X80 steel plates

Identification	C	Mn	Mo	Nb	V	N	Ti	Pcm
Steel X	0.058	1.67	0.287	0.088	0.001	0.0075	0.015	0.190
Steel Y	0.028	1.71	0.293	0.089	0.001	0.0075	0.016	0.163

3.2 Welding Procedure and Parameters

Submerged arc welding was used to fabricate all the experimental weldments analyzed in this work. Welding was performed using two Lincoln Electric Power Wave® AC/DC 1000TM power sources. Two power sources were used for the two separate electrodes required for tandem welding. The weld joints were V-grooved bevel welds and the design is shown in Figure 3-1. The weld joint design was adapted from ASME B 31.3 code; Figure 328.4.2 (a) [ASME, 2008]. It is a common joint design generally used in Alberta for pipe material [Email communication with Iulian Radu, PhD, Welding Specialist, PCL Contractors Inc on August, 2009].

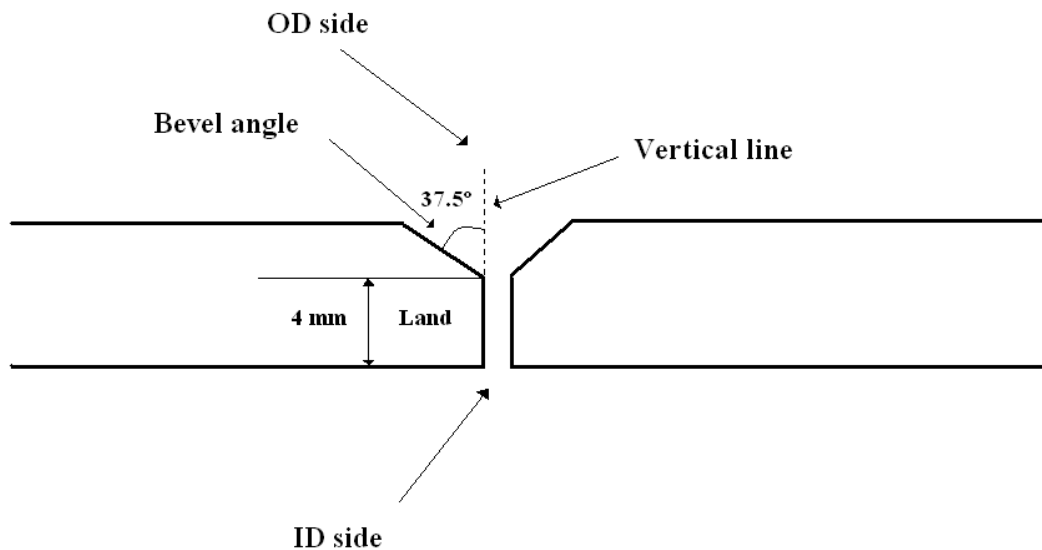


Figure 3-1: Bevel design (not to scale) (dimensions are in mm).

A two pass weld joint design was used during the study. The first pass, which is referred to as OD (outer diameter), was done on the groove side of the joint and the second pass, which is referred to as ID (inner diameter), was done on the opposite side of the V-groove. Four types of root face/land geometry (the perpendicular face of the weld joint as shown in Figure 3-1) were used, but the bevel angle was kept constant at 37.5° (Figure 3-1). The land was chosen to accommodate higher heat inputs, without “burn throughs”. It was seen during several test welds that if a lower land (e.g., 4 mm land) was used for a relatively high heat input (e.g., 2.0 kJ/mm) there was burn through ^[1]. To avoid burn-throughs and at the same time use higher heat inputs, different land geometries were used. For lower heat inputs (e.g., 1.5 kJ/mm) a lower land (4 mm land) was used. For higher heat input (e.g., 2.25 kJ/mm) the land was increased to 6.95 mm. Both tandem and single electrode wire welds were performed. For tandem electrode welding, the heat input was varied (from 1.5 kJ/mm to 2.25 kJ/mm) by varying the current; both the travel speed and the voltage were kept constant. Single electrode welding was done for only two sets of heat inputs (1.5

^[1]Burn through - the electrode melts through the steel plate creating a gap instead of welding.

kJ/mm and 1.75 kJ/mm). The experimental welding parameters are listed in Table 3-2 to Table 3-4.

Table 3-2: Single electrode welding parameters (OD)

Heat input (kJ/mm)	Current (A)	Voltage (V)	Travel speed (mm/s)
1.5	525	36	12.5
1.75	615	36	12.5

Table 3-3: Tandem electrode welding parameters (OD)

Heat input (kJ/mm)	Lead current (A)	Lead voltage (V)	Trail current (A)	Trail voltage (V)	Travel speed (mm/s)
1.5	525	28	420	34	19.35
1.75	615	28	492	34	19.35
2	700	28	560	34	19.35
2.25	790	28	632	34	19.35

Table 3-4: ID welding parameters

Heat input (kJ/mm)	Current (A)	Voltage (V)	Travel speed (mm/s)	Used for
1	400	34	12.62	Tandem
1.25	500	34	12.62	Single

It was found during the test welds that single electrode welds have greater penetration for a given heat input than tandem electrode welds. For example, when a heat input of 2.25 kJ/mm was used with a single electrode to produce a BOP weld on a 10.22 mm thick steel plate, burn through occurred. This was an indication that high heat inputs (higher than 2.00 kJ/mm) with single electrode welds could not be used for any land geometry combination for welding 10.22 mm thick steel plates. As such, only two experimental heat inputs were used for single electrode welds. Also, to ensure that there was no burn through with the two heat inputs (1.5 kJ/mm and 1.75 kJ/mm), the land dimension was increased accordingly. For the 1.5 kJ/mm heat input used for single electrode welding, a 6.2 mm land was used and for the 1.75 kJ/mm heat input used for single electrode welding a 6.95 mm land was used. Similar lands (6.2 mm and 6.95 mm) were used for 2.00 kJ/mm and 2.25 kJ/mm heat inputs, respectively, for tandem electrode welds. The combination of heat inputs and land dimensions was chosen in such a way that the penetration remained approximately $\frac{3}{4}$ of the total thickness of the steel plate. The OD pass was done first with this $\frac{3}{4}$ penetration. The ID pass was done on the opposite side, to replicate an actual production weld. The lower heat input values for ID passes were to ensure that the remaining $\frac{1}{4}$ of the total thickness of the steel plate was covered by this weld pass and also overlapped the OD pass within the thickness of the steel plate. Figure 3-2 shows a schematic diagram of a typical weld joint.

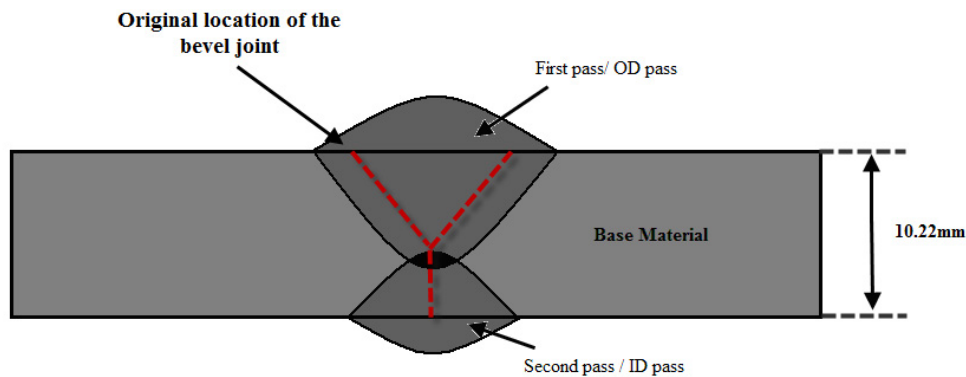


Figure 3-2: Schematic drawing showing the SAW weld joint geometry.

An AC/AC square wave with 90 Hz frequency was used in all cases examined in this thesis. Preliminary test welds were conducted using 60 Hz, however, it was found that if both the electrodes were using an AC/AC square wave and the frequency was low (e.g., 60 Hz), the bead shape and appearance were unacceptable. This was attributed to excessive attraction and repulsion between the two electrodes, affecting the bead appearance. Increasing the frequency to 90 Hz produced the desired bead appearance and this was chosen for all subsequent welds. The offset and the balance were kept at their default settings, that is 50% balance and 0% offset was used. For single electrode welds, the electrode was kept perpendicular relative to the base material. For tandem electrode welds, the lead electrode was kept perpendicular relative to the base material and the trail electrode was at an angle of 15° with the vertical (the angular dimensions could vary by $\pm 2^\circ$). Figure 3-3 shows a schematic of the lead and trail electrodes relative to the base material.

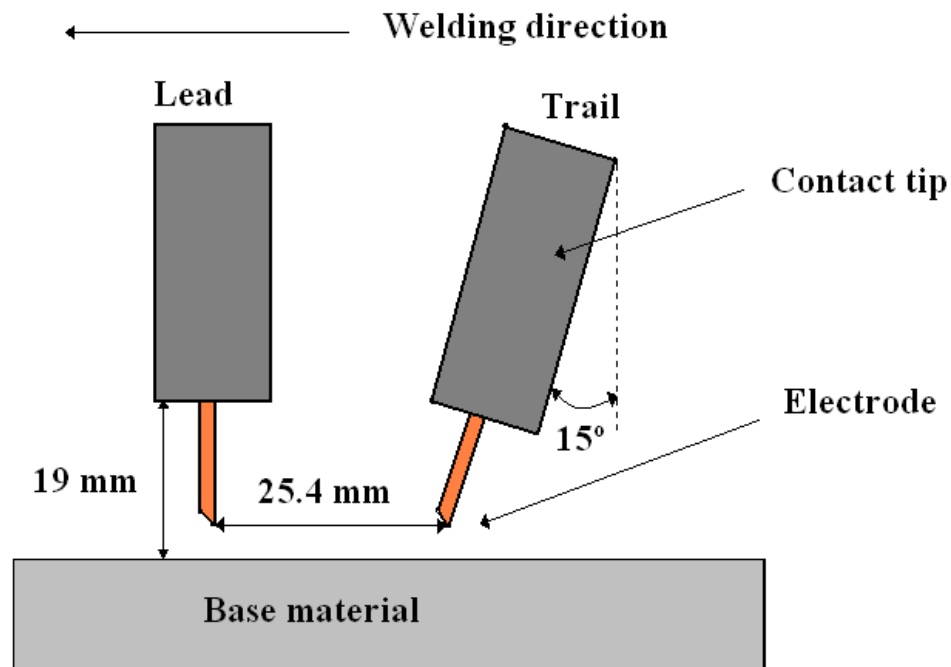


Figure 3-3: Schematic of lead and trail electrode setup (all dimensions are in mm and not to scale).

The distance between the lead and trail electrode was kept at approximately 25.4 mm (1 inch) for all cases. The contact tip was kept approximately 19 mm (3/4 inch) above the base material. The end of the electrode was clipped with a cutter to an angle of 45° angle to make arc initiation easier.

A Hypermax Corporation Powermax 1650 plasma cutter was used to cut weld coupons from the larger X80 steel plates. Approximately 432 mm × 280 mm weld coupons were cut and used for welding. The 280 mm side of the smaller weld coupons was kept parallel to the rolling direction of the plate. A total of 12 smaller weld coupons were cut from steel X plate to produce 6 welds (four welds for tandem electrode welding and two welds for single electrode welding). Similar numbers of smaller coupons were cut from steel Y as well. Table 3-5 shows the number of weld joints produced for this study along with their parameters and notation. This notation is used throughout the thesis.

The bevel geometry was machined on the 432 mm side of the weld coupons. Two coupons were then placed close together, so that there was no gap between them. If there is a gap, then there is a chance for molten metal to penetrate between the pieces causing a burn through. Figure 3-4 shows the joint preparation. The joint was then tack welded using a Powerwave 455 MIG welder. Run-off and run-on tabs of similar composition steel plates were also tack welded on both sides of the groove joint. These run-off and run-on tabs helped produce a clean weld on the test specimen by allowing the crater (that forms while the arc is extinguishing) to form on them rather than on the test specimen during the initial stages of arcing. These tabs were removed after welding. All welds were done on a flux-backed copper plate, to ensure that if there was any burn through then removal of the specimen from the copper plate was possible.

Table 3-5: Weld samples, parameters and notation

Heat input (kJ/mm)	Percent Carbon	Land (mm)	No. of electrodes	Notation
1.5	0.06	4	Tandem	A
1.75	0.06	5.3	Tandem	B
2	0.06	6.2	Tandem	C
2.25	0.06	6.95	Tandem	D
1.5	0.03	4	Tandem	I
1.75	0.03	5.3	Tandem	J
2	0.03	6.2	Tandem	K
2.25	0.03	6.95	Tandem	L
1.5	0.06	6.2	Single	F
1.75	0.06	6.95	Single	G
1.5	0.03	6.2	Single	N
1.75	0.03	6.95	Single	O

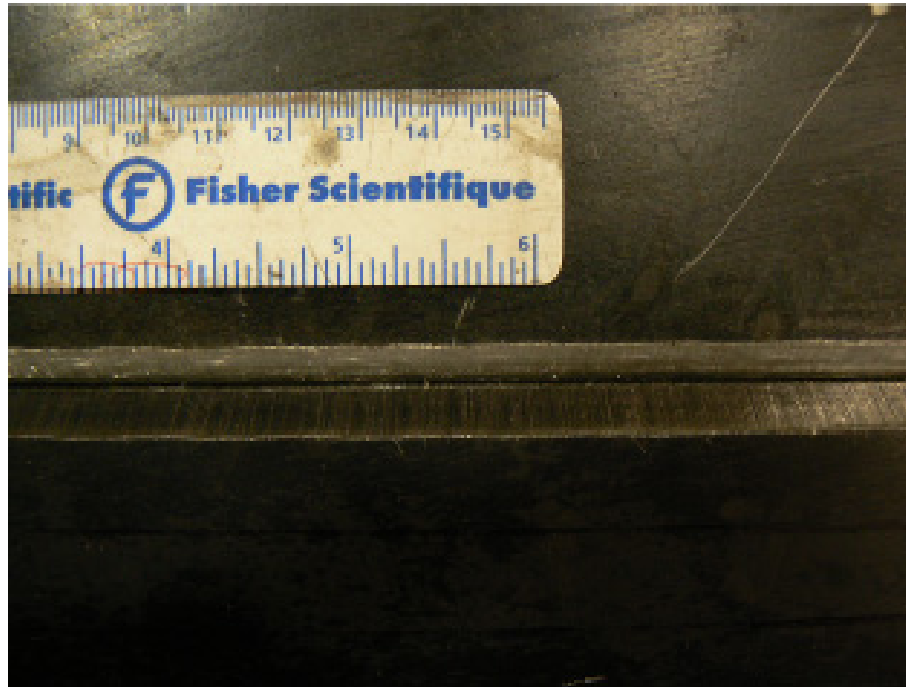


Figure 3-4: Weld joint preparation.

The OD pass was done first. The weld was then cooled to room temperature and the ID pass was done on the opposite side. Although it was expected that the ID pass would overlap the OD pass as shown in Figure 3-2, there was no way to ensure overlap during welding. Later it was found out that for two welds (specimen I and specimen K) the ID pass did not overlap the OD pass. It was decided that these ID passes and their subsequent weld metals and CGHAZ would not undergo any further analysis.

The wire used for this study was EN S3NiCrMo 2.5, with a wire diameter of 3.2 mm. The wire composition is given in Table 3-6 as reported by the manufacturer (Bavaria Schweisstechnik). An alumina basic flux system was used, which was dried at 150°C for two hours to reduce the amount of moisture. The flux

composition is given in Table 3-7 and the flux has a basicity index of 1.4 (neutral) as reported by the manufacturer (Bavaria Schweisstechnik).

Table 3-6: Chemical analysis of solid wire electrode

Identification	C	Si	Mn	P	S	Mo	Ni	Cr	Cu
EN S3NiCrMo	0.07-	0.10	1.20-	0.02	0.02	0.40	2.00	0.30	0.3
2.5	0.15	-	1.80			-	-	-	
		0.25				0.70	2.60	0.85	

Table 3-7: Welding flux chemistry

SiO₂ + TiO₂	Al₂O₃ + MnO	CaO + MgO	CaF₂
20%	35%	20%	20%

3.3 Weld Characterization

Six principle methods were used to evaluate the mechanical properties of the test materials in this study. These include: Weld geometry measurements, microhardness measurements, tensile testing, Charpy impact tests, optical microscopy, scanning electron microscopy (SEM) and transmission electron microscopy (TEM). These experimental methods are described in detail in the following sections.

3.3.1 Weld Geometry Measurement

Weld geometry measurements were performed from transverse cross sections that were polished and etched using 2% Nital before examination with an optical microscope. Figure 3-5 shows a typical picture used for geometry measurement (weld metal area) using Image J software (Version 1.43u). The bead width (W_1), bead width at half penetration depth (W_2), reinforcement height (r), penetration

depth (P), HAZ size, contact angle (Θ), reinforcement area (A_r) and penetration area (A_p) were measured. Details of these bead shape parameters are discussed in Section 4.1 in the next chapter. The boundaries of the geometries were first outlined with a pencil and then the image was scanned into the computer. For each weldment, two cross-section specimens were used for geometry measurements. Before each measurement, the software was calibrated using an image of known area. The software measures the number of pixels on a line or a given area and based on that calculation gives a number (area or length).

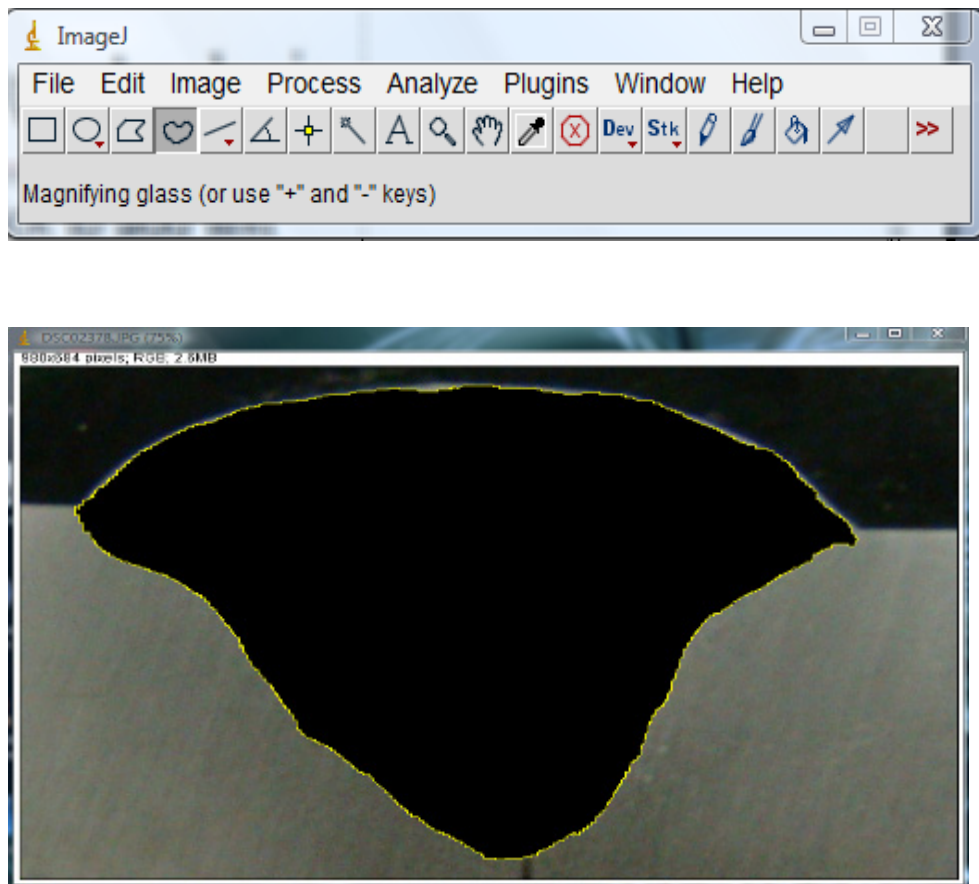


Figure 3-5: Typical weld metal area used for measurements in Image J software.

3.3.2 Microhardness Measurement

Microhardness testing was carried out from the weld metal through the HAZ and into the base metal. Testing was done parallel to the top surface of the base metal. A Mitutoyo microhardness tester was used for all hardness measurements. A region of approximately 10 mm² area was selected as shown in Figure 3-6. This region was selected because it was equivalent to the notch position of the CVN samples. The position of the CVN notch was next to the fusion line in the upper portion of the OD weld (CVN specimen notch position will be discussed in Section 3.3.4). A total of five lines of indentations, as shown in the schematic (Figure 3-7), were carried out. Each line was separated by 0.2 mm and the indentations were separated by 0.2 mm. A load of 500 g was used for 15 seconds for measuring hardness, according to ASTM Standard E92-82 (2003) [ASTM E92, 2003]. The load and loading time were selected so that large indentations would form, which would be easier to measure using the microscope. Figure 3-8 shows actual indentations that were made; the black dots are the hardness indentations. Figure 3-8 shows only a portion of the hardness measurements that were taken near the fusion boundary (outlined as a red line in the figure). The fusion boundary was identified by over etching the sample and was also correlated by observing the microstructure. Due to the limitations of the microscope magnification, entire indentations cannot be shown in a single image.

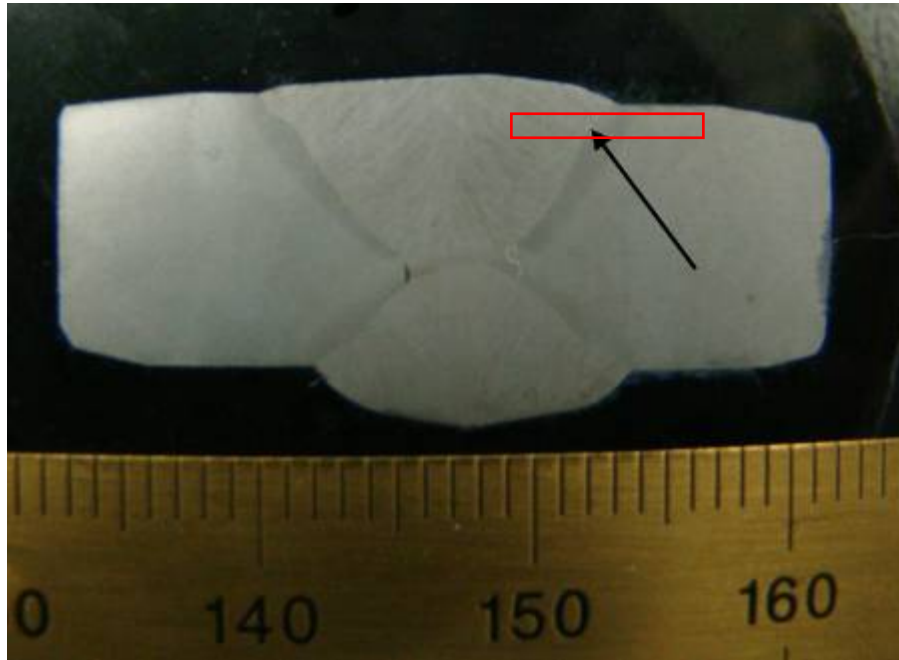


Figure 3-6: Region where hardness tests were done.

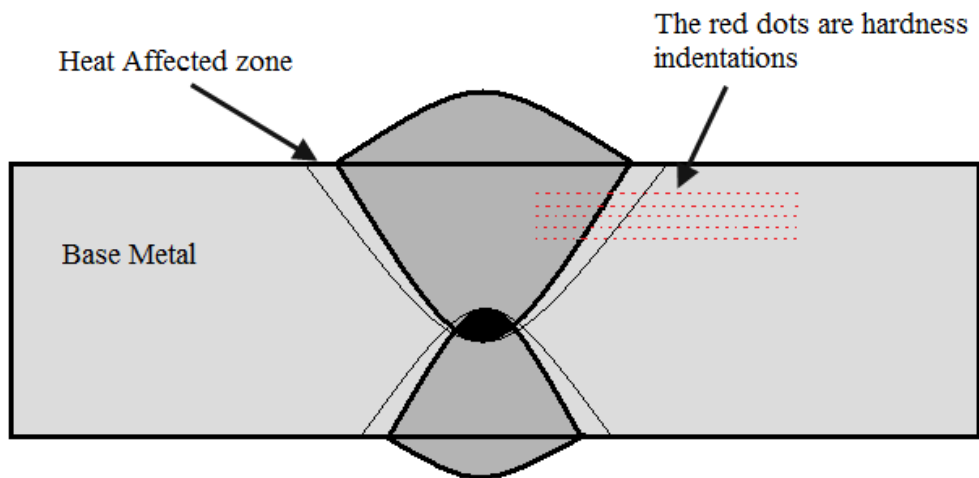


Figure 3-7: Schematic showing the region where hardness indentations were made.

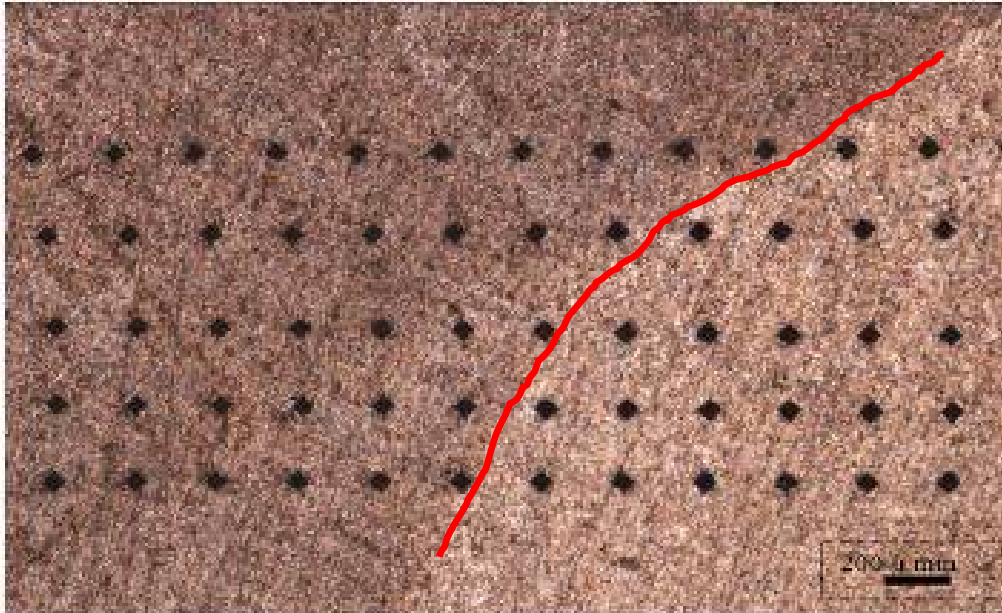


Figure 3-8: Optical image showing hardness indentations. The red line indicates the fusion line.

3.3.3 Tensile Testing

Tensile tests were done on sub-sized transverse weld tensile specimens. ASTM standards (ASTM A370-07b) were followed in choosing sub-sized tensile specimen dimensions [ASTM A370, 2003]. A schematic for tensile specimen extraction is shown in Figure 3-9. Approximately 500 mm × 50 mm blanks were cut from the welded steel plates. The specimens were extracted from these plates. One sample from each welding condition was used to determine the tensile strength. The welded joint was kept in the mid section of the tensile specimen. The weld reinforcement was not removed. The justification for not removing the weld reinforcement came from the idea that it closely resembles the actual situation. The reinforcement is not removed from the actual circumferential weld [Private communication with Chris Penniston, Evraz Inc. NA]. It is to be noted that in ASME Section IX, it is suggested that the weld reinforcement be removed

before doing any tensile testing [ASME, 2008]. However, in the AWS standard, it is mentioned that transverse tensile specimens can have weld reinforcement [AWS, 2004]. Specimens were tested using an Instron Universal Tensile testing machine interfaced with MTS software package - Model No. 5500. The crosshead speed used was 5mm/min and the strain rate was 0.1/min. Tensile specimen dimensions are given in Table 3-8 and in Figure 3-10.

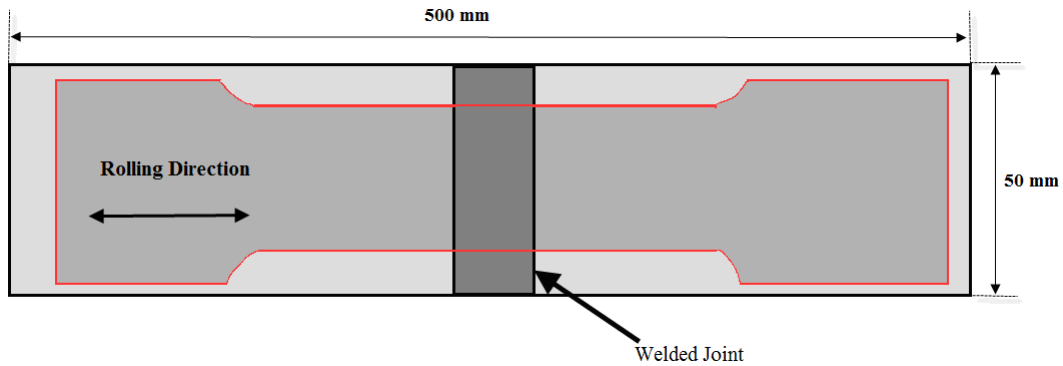


Figure 3-9: Tensile specimen extraction.

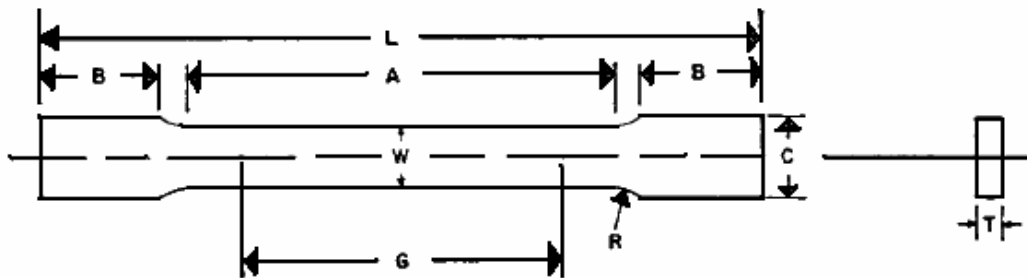


Figure 3-10: Tensile specimen dimensions.

Table 3-8: Tensile specimen dimensions

Notations in Figure 3-10	Subsize specimen dimensions, mm
G - Gauge length	50 +/- 0.010
W - Width	12.5 +/- 0.25
T - Thickness	10.22 (thickness of the plate, no machining required)
R - Radius of fillet	13 +/- 1.25
L - Overall length	334
A - Length of reduced section	60 +/- 1
B - Length of grip section	112 +/- 1
C - Width of grip section	40

3.3.4 Charpy Impact Testing

Sub-sized (55 mm × 10 mm × 5 mm) Charpy V-notch tests were performed at five different temperatures (22°C, 0°C, -20°C, -40°C and -60°C) in compliance with ASTM A370-03a and ASTM E23-02a [ASTM A370, 2003] [ASTM E23, 2003]. The lower temperatures were achieved by immersing the specimens in a bath containing ethanol and dry ice. The specimens were kept at the desired temperature for at least 10 minutes to ensure the specimens were at the desired temperature. CVN specimen location with respect to the welded joint is shown schematically in Figure 3-11.

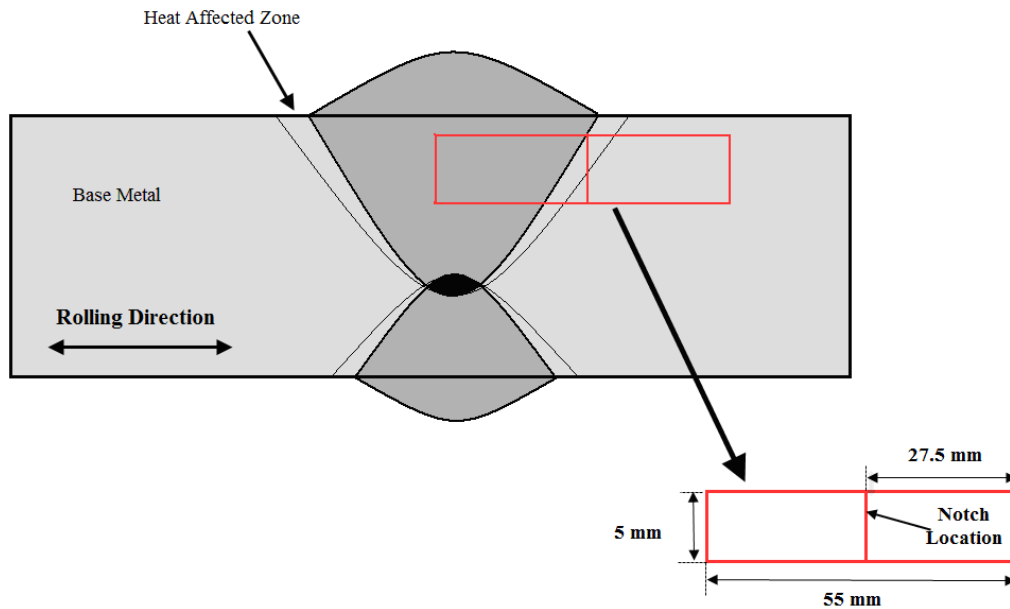


Figure 3-11: Schematic Charpy specimen extraction and notch location (not to scale).

Samples were extracted as close to the top surface as possible, only to evaluate the OD HAZ. This was done to avoid the ID weld metal and HAZ as well as the overlapping region of OD and ID weld metal and HAZ. As discussed earlier in Section 3.2, ID HAZ and weld metal were excluded from further evaluation.

For each temperature and welding parameter, a total of three specimens were extracted. The extracted specimen surfaces were ground to a 600 grit finish. They were etched with 6% Nital followed by immersion in acetone and then rinsed in running tap water to reveal the fusion line and the weld metal region, so that the notch placement was easier to locate. The notch was placed at the intersection of the fusion line and the upper surface of the sample as shown in Figure 3-11. This location was chosen so that the notch was placed preferentially in the weld HAZ to give toughness values only in that location. Before the notch was placed, the location was identified and outlined using a pencil. The notch was oriented in such a way that fracture propagation would be parallel to the weld direction as shown in Figure 3-12.

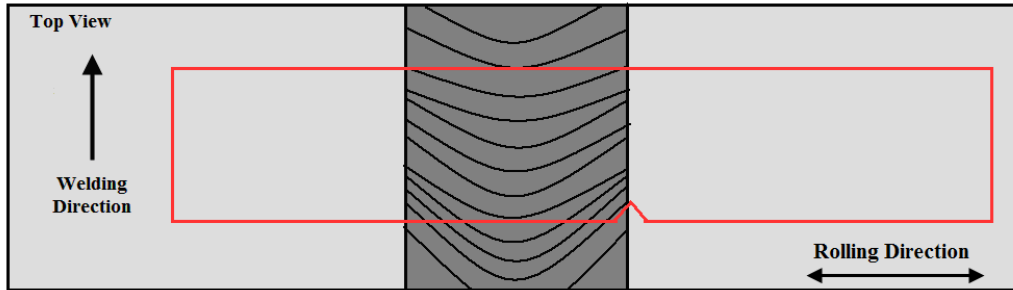


Figure 3-12: CVN notch orientation relative to the welding direction.

3.3.5 Metallographic Sample Preparation for Optical Microscopy

Small samples were cut from the welded coupons using a band saw. The samples were then mounted with conducting bakelite (Buehler -Konductomet, Product No. 20-3375-016), a mounting resin which can conduct electricity making it easier for SEM observation without coating. A hot press machine (Struers Prontopress-20) was used for mounting the small samples. The metallographic specimens were initially ground using a belt grinder, with 60 grit polishing paper. Later the surfaces were ground using wet and SiC embedded polishing wheels in the sequence of 240, 320, 400 and 600 grit sizes. After grinding, the samples were polished using 3 μm and 1 μm diamond paste. The final polishing was done using 0.05 μm alumina slurry.

When the surfaces were scratch free, they were etched with different etchants to reveal the microstructures of the weld CGHAZ and FGHAZ. The etchants are reported in Table 3-9 [Sharma, 2009]. 2% Nital was used to reveal the ferrite grain boundaries. It is also good for revealing martensite. 10% Nital was used to reveal the weld fusion line and different HAZ regions in the specimen. Modified Le Pera's etch was used to identify martensite-austenite regions in the steel. After etching, the specimens were rinsed with water and then with alcohol. The etched specimens were examined with an optical microscope.

Table 3-9: Etchants used for optical microscopy

Etchants	Composition	Etching Time
Nital	a) 2% Nital (2% nitric acid in ethanol) b) 10% Nital (10% nitric acid in ethanol)	a) 4-6 seconds b) 4-6 seconds
Modified Le Pera	a) 10% HCL in water b) Saturated solution of picric acid (4%) in 100ml ethanol c) 1g sodium metabisulphite and 1g EDTA in 100 ml water.	Sample was etched with a) for 15 seconds, repolished to a 0.05 μm alumina finish and then immersed in a mixture of b) and c) in equal parts for as long as necessary to produce black spots across the sample

3.3.6 Grain Size Measurements

The grain size of different samples was also measured using a linear intercept procedure, which is also known as the Heyn Method. This procedure is described in Section 13 of the ASTM E112-96 Standard [ASTM E112, 2006]. The basic steps according to this procedure are given below:

- a) On a single field of view, five random straight lines of known length were placed on the image. The combined length of the test line was L.

b) The total number of intercepts, which is denoted as P, between the test lines and the grain boundaries was counted. Triple junctions were counted as 1.5.

c) The total number of intercepts, P, was divided by the total length, L.

d) Steps a) - c) were repeated for an additional 2 to 4 fields of view.

e) The average of the results found in step c), P_L , was obtained for all fields of view.

f) The ASTM grain size number is given as:

$$n = -3.3 + 6.65 \log_{10} (P_L) \dots\dots\dots 3.1$$

Here P_L is given in mm^{-1} .

Apart from using Equation 3.1, Figure 3-13 was also used to determine the ASTM grain size number from the average intercept counts on a 500 mm test pattern. Figure 3-14 shows a schematic of the calculation of grain size numbers using this method.

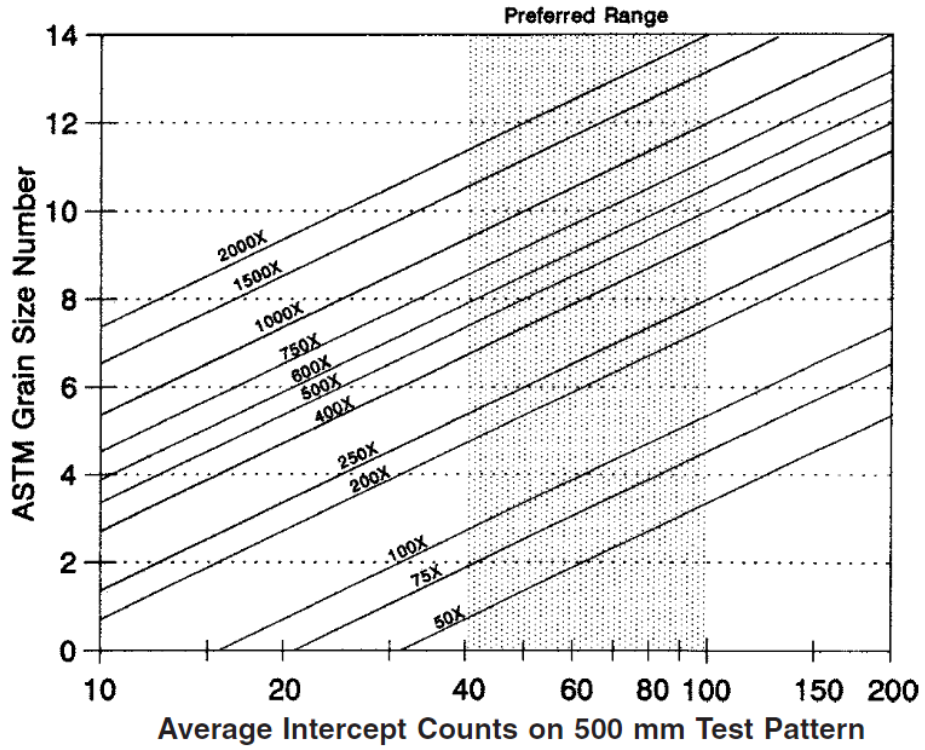


Figure 3-13: Average intercept counts on 500 mm test patterns.

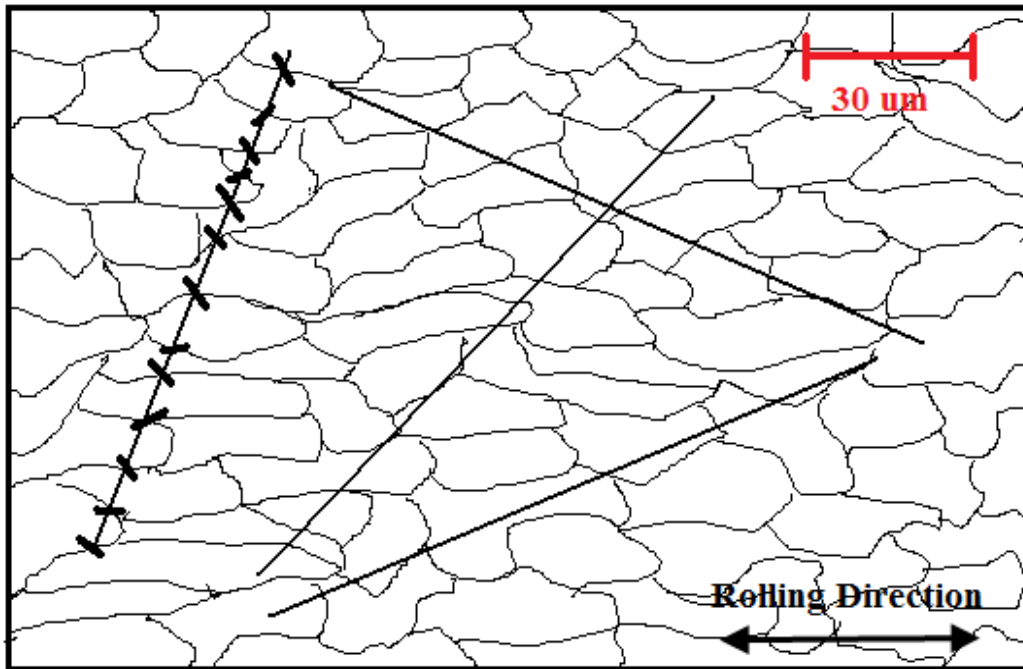


Figure 3-14: Schematic of grain size number calculation using Heyn method.

The method explained above involves human error, especially for HSLA steels, where the microstructure is heavily deformed and identifying a grain boundary intercept with the test line(s) can be subjective, which in turn affects reproducibility of the data. Another method was employed to determine the grain size and these values were compared with the Heyn method. In this method, a microstructure was printed out and individual grains were outlined using a pencil. The microstructure was scanned and the area of individual grains (outlined previously) was calculated using image analysis software such as Image J (details about Image J and measuring area/lengths are explained in Section 3.3.1). For FGHAZ grain size measurements approximately 70 grains were measured. For CGHAZ grain measurements around 15 grains were measured. Measuring the grains with this method directly provides an average area of the grains. Figure 3-15 shows a typical grain area measurement using Image J.

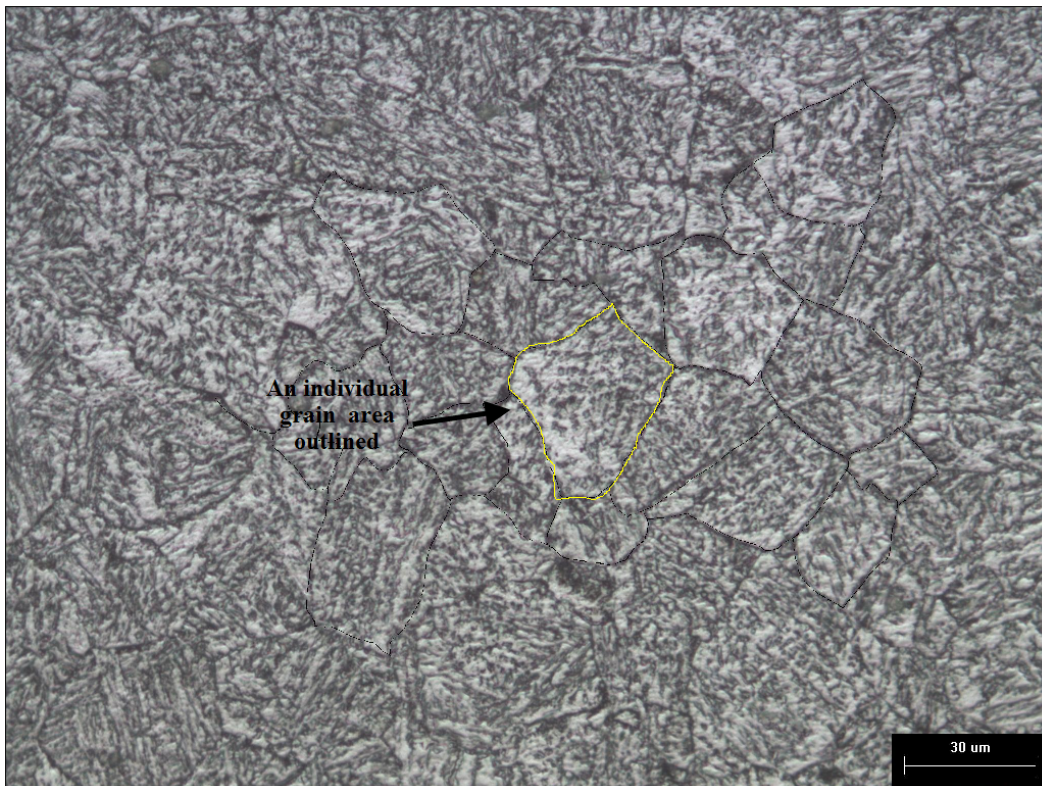


Figure 3-15: Typical grain area measurement using Image J software.

3.3.7 Scanning Electron Microscopy

Samples used for optical metallography (base metals and welded specimens) and fractured Charpy V-notch impact samples tested at various temperatures were examined in a scanning electron microscope (SEM). Two types of SEMs were used for imaging and fractography. One was a Hitachi S-2700 equipped with a secondary electron (SE) detector, a backscattered electron (BSE) detector and an energy dispersive x-ray (EDX) detector. The other SEM was manufactured by FEI (Model No. XL30) and was equipped with only SE and BSE detectors. Both SEMs were operated at 10-20 kV, depending on the image conditions. Valuable information regarding the mechanism and nature of the fracture, such as inclusions and brittle and ductile fracture features, were determined using SEM. Before SEM observation, fractured Charpy samples were immersed in acetone for at least 30 minutes followed by ultrasonic cleaning. Metallographic samples used for optical microscopy were also observed in an SEM. Sample preparation, similar to optical microscopy, was followed. Higher magnification imaging with the SEM allowed for the study of lath sizes in the CGHAZ region and revealed other information. Metallographic samples that were etched with 2% Nital were cleaned using acetone before SEM observation.

3.3.8 Transmission Electron Microscopy

Transmission electron microscopy (TEM) analysis was carried out for both steel X and steel Y using a JEOL 2010F TEM. Carbon replicas were extracted from the mid section of the plate (across the thickness) (Figure 3-16). The samples were initially polished and then etched with 5% Nital to remove some of the iron matrix, so that the precipitates could protrude from the surface. A thin carbon film (approximately 20 nm) was evaporated onto the etched specimen surface from a carbon rod using a vacuum evaporator. The replica was sectioned into small squares using a pen. Then the sample was immersed into a 10% Nital solution. The protruding precipitates were lifted off from the surface. The replicas were then transferred to a solution with 50% deionised water and 50% methanol to rinse off the Nital solution. The replicas were transferred to a beaker containing deionised water, where they floated to the surface and spread out due to the surface tension of the water. The replicas were then collected on a 300 mesh copper grid and were ready for TEM observation. In the TEM, the replicas were observed and bright field images were captured. Later these images were used for particle counting and size measurement using image analysis software (Image J).

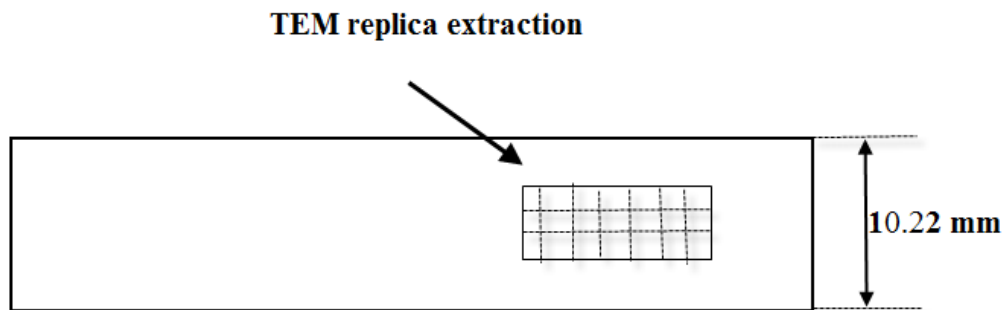


Figure 3-16: Schematic of TEM replica extraction.

4.0 Summary

In this chapter the various materials and experimental techniques used in this study were described. A detailed description of weld geometry measurements and grain size measurements using both ImageJ software and ASTM methods were presented. Details of mechanical testing, such as microhardness testing, tensile testing and Charpy impact testing, were also discussed. Optical microscopy, SEM and TEM imaging techniques, for further characterization of base metals and welded specimens, were also described. In the next chapter results obtained from weld geometry measurements and weld melting efficiency will be presented and discussed.

Welding Performance and Weld Melting Efficiency

A previously conducted study [Pepin, 2009] showed that heat input in SAW increases the weld dimensions such as penetration depth, reinforcement height and bead width during bead-on-plate (BOP) welding. In this chapter, the relationship between different welding variables and weld bead geometry was studied for bevel welds. It was expected that trends showed in the previous study done for BOP welds would also hold for bevel welds produced using SAW. Charpy V-notch results were also linked with weld geometrical values and different relationships were established. Weld melting efficiencies are discussed in Section 4.5 and the dependence on heat input is also explained. In the next section, definitions of different weld bead geometric values that were evaluated in this study are given.

4.1 Welding Performance in Terms of Weld Bead Shape Parameters

Three parameters are usually used to evaluate the welding performance of weldments. These are: deposition rate, hardness and dilution [Gunuraj, 1999]. The bead shape parameters, which are used to describe welding performance, are shown in Figure 4.1. Here r is the reinforcement height, p is the penetration depth and w is the bead width. The bead contact angle, θ is defined as $(\theta_1 + \theta_2)/2$.

It is also possible to measure reinforcement area, penetration area (which is the cross-sectional area of the weld deposit below the surface of the parent metal) and total molten area (which is the simple addition of reinforcement area and penetration area) - A_r , A_p and " A_r+A_p ", respectively, in Figure 4.1.

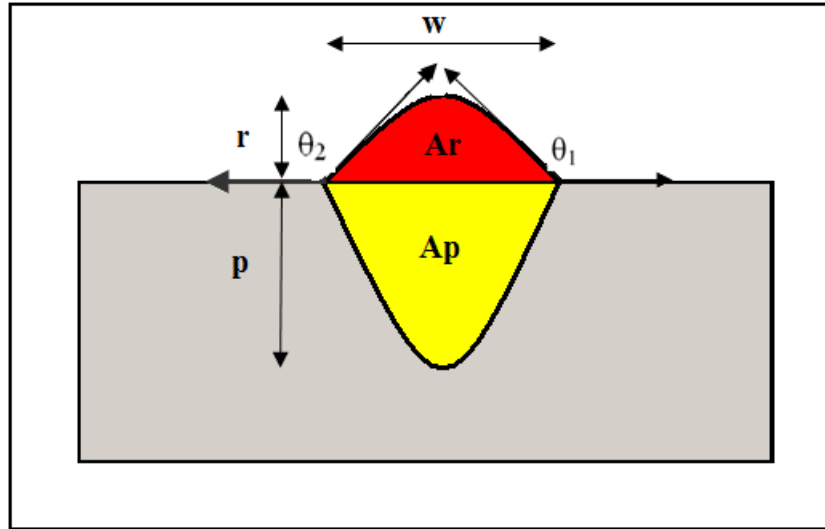


Figure 4-1: Schematic illustration of the measurements required for determining welding performance.

4.2 Effect of Heat Input on Weld Bead Geometry

In this study, current was varied in order to control the heat input, while travel speed and voltage were kept constant. In this way it is easier to find the effect of current (which directly affects heat input) for different weld bead geometries. The effects of heat input on weld beads produced using tandem electrode welds were plotted against penetration depth, bead width and reinforcement height (Figure 4-2 and Figure 4-3). It should be noted that only one sample for each different welding conditions was used to determine these values. The error bars are from repeat measurements.

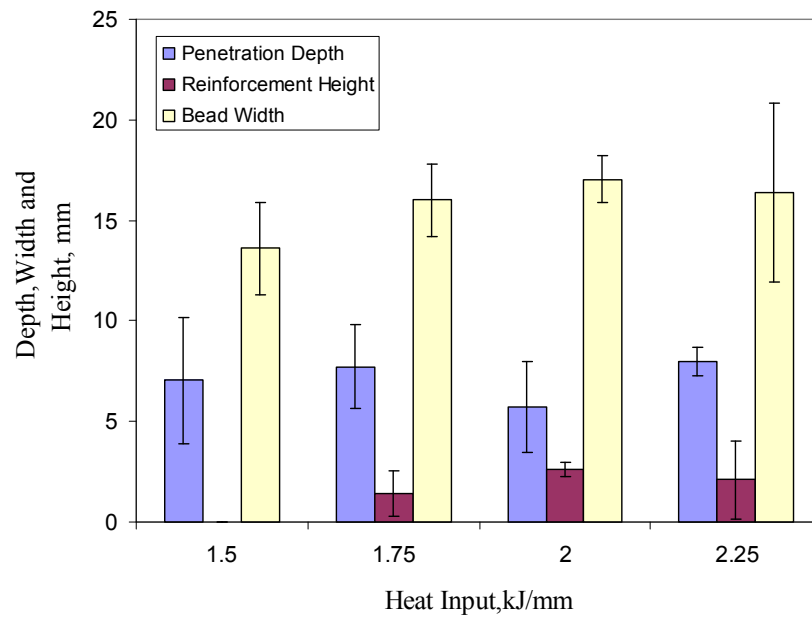


Figure 4-2: Effect of heat input on a) penetration depth, b) reinforcement height and c) bead width for Steel X - tandem electrodes.

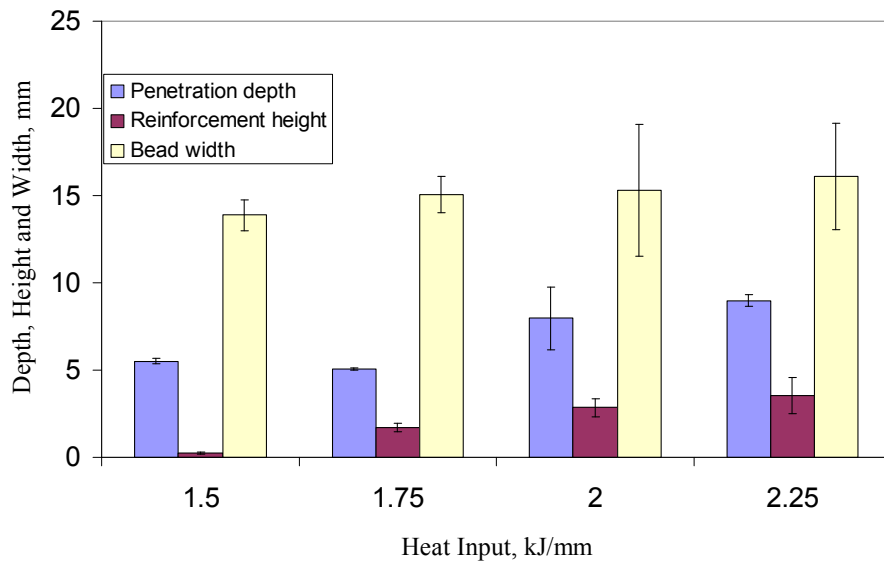


Figure 4-3: Effect of heat input on a) penetration depth, b) reinforcement height and c) bead width for Steel Y - tandem electrodes.

It can be seen from these plots that there is a general trend; as heat input increases the penetration depth, reinforcement height and bead width increase. There are some variations for penetration depth and bead width, i.e., increasing heat input initially decreases the penetration depth followed by an increase. A similar kind of variation for bead width is also observed. When heat input increases from 1.75 kJ/mm to 2.00 kJ/mm, there is a slight decrease in the bead width. It should be noted that the experimental results may vary based on the positions of the weld cross sections that were used to measure the penetration depth and bead width. For example, a section cut from the initial region of the weld may differ from a section which is cut from the mid section of the weld. Apart from these variations, the results are in agreement with the literature [Pepin, 2009] [Yang, 2008]. An increase in heat input occurs as a result of an increase in current (with travel speed and voltage constant), which increases both plate and electrode melting. It is worth mentioning that plate melting is associated with penetration depth and HAZ size, whereas electrode melting is related to weld bead shape [Gunuraj, 1999]. As the heat input increases, a large molten metal pool is created and it remains molten for a longer period of time during welding. This results in a larger penetration depth and HAZ size (Figure 4-4 and Figure 4-5). Close examination of Figure 4-4 reveals that the HAZ size for Steel Y initially decreases with increasing heat input (1.5 kJ/mm to 1.75 kJ/mm) and then again increases. A similar variation for Steel X is also found, i.e., a decrease in HAZ size when the heat input is increased from 1.75 kJ/mm to 2.00 kJ/mm. This decrease in the HAZ size is unexpected. The region used for the HAZ calculation should also be taken into account in this regard. The HAZ size was measured in the upper portion of the base metal, as shown in the Figure 4-6. In some cases (where there are variations in that region), three measurements were taken and the average was recorded. For most results only two measurements were recorded. It is possible that HAZ size may vary in some other regions along the weld fusion line, which is not taken into account when measuring the HAZ size in this study.

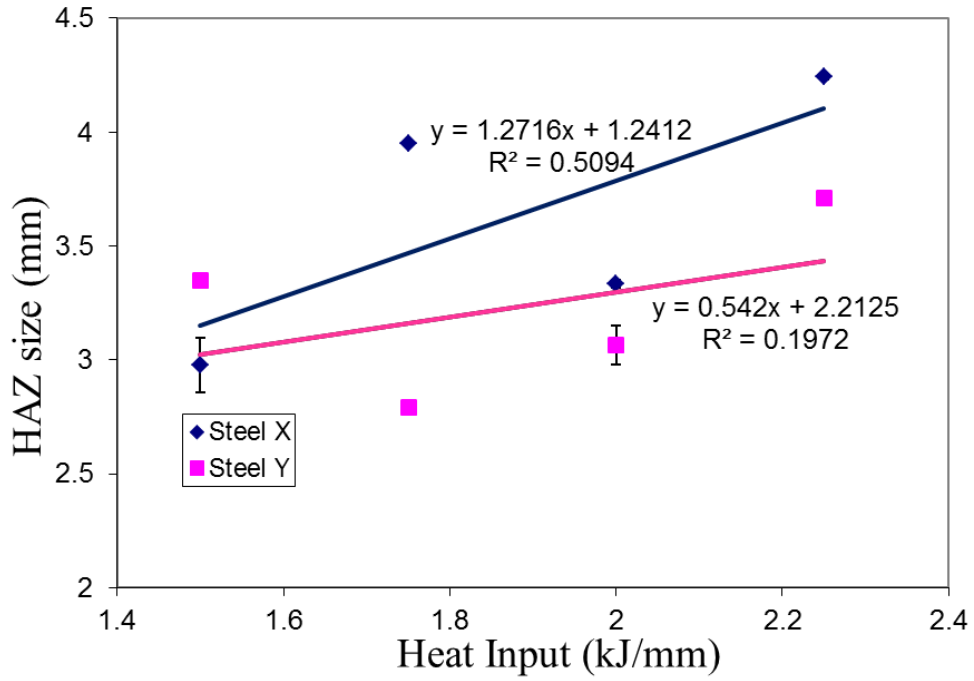


Figure 4-4: Effect of heat input on HAZ size in tandem welds.

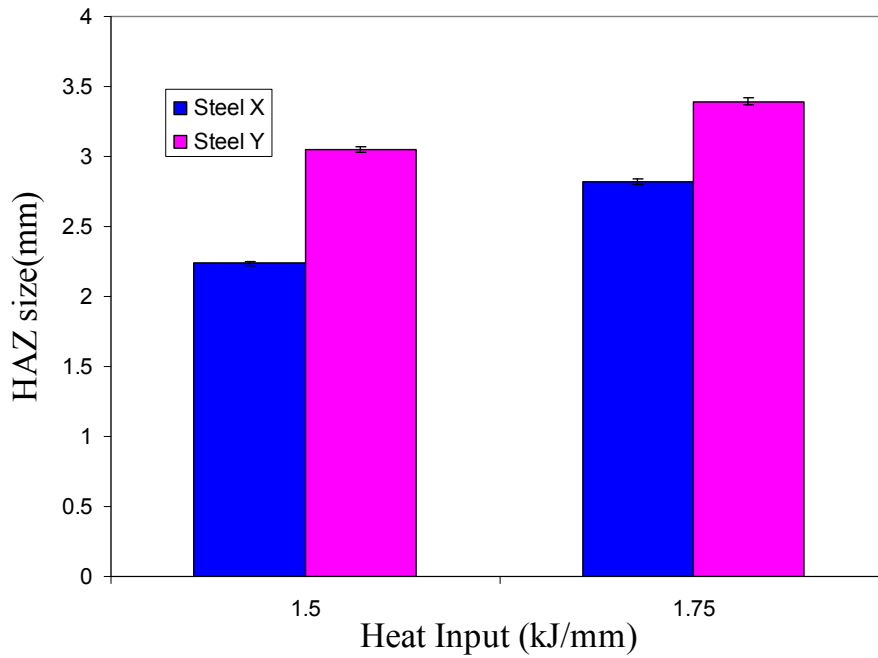


Figure 4-5: Effect of heat input on HAZ size – single electrode welds.

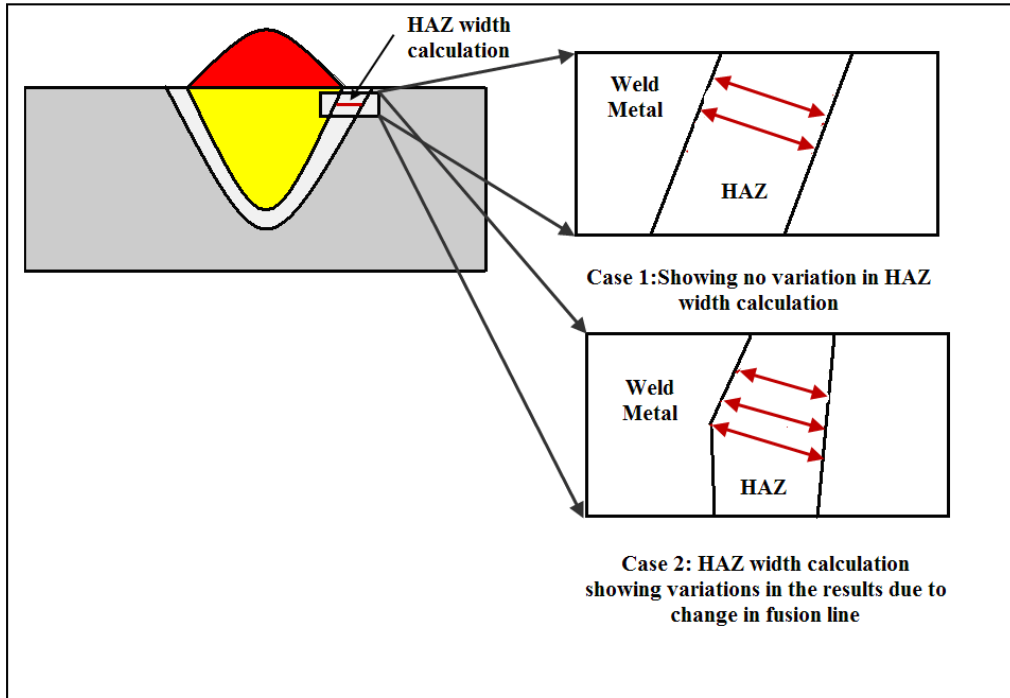


Figure 4-6: Schematic of HAZ width calculations for two different situations.

An increase in heat input is also related to electrode melting, which in turn controls the weld shape (bead width and reinforcement height). So, as the welding current (or heat input) is increased, reinforcement area is also increased because of increased electrode melting (Figure 4-7 and Figure 4-8).

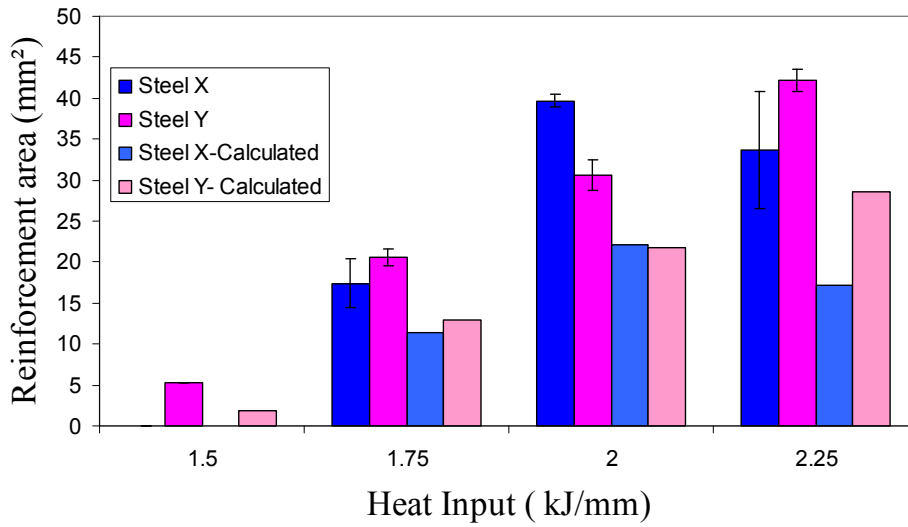


Figure 4-7: Relationship between heat input and reinforcement area for Steel X and Steel Y - tandem electrode welds. Calculated values from Equation 4.1 are also shown.

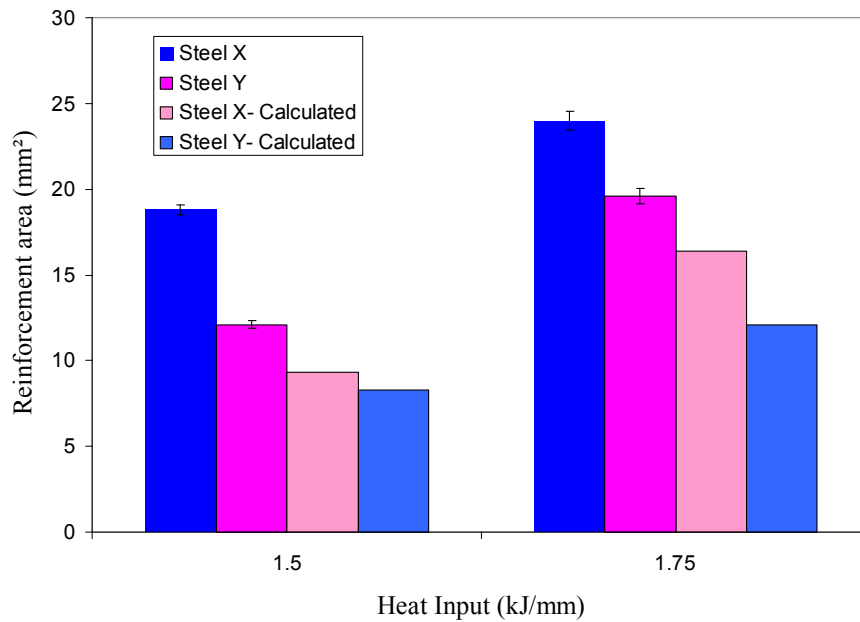


Figure 4-8: Relationship between heat input and reinforcement area for Steel X and Steel Y - single electrode welds. Calculated values from Equation 4.1 are also shown.

Reinforcement area is related to reinforcement height by the following equation [Yang, 2008]:

$$r = w \times [\tan (180-\theta)] / 2 = 2Ar/w \dots\dots\dots 4.1$$

Here, r is the reinforcement height, Ar is the reinforcement area, w is the bead width and θ is the contact angle.

Since reinforcement area is proportional to reinforcement height; an increase in reinforcement height is expected as the heat input increases because of increasing reinforcement area. This equation was not used to calculate reinforcement area from reinforcement height; rather Image J software was used to measure both the reinforcement height and area individually. This equation gives a good approximation of the reinforcement area and also explains the relationship in a simple manner.

So far the results shown in the above sections are in good agreement with the previous work done in this field [Yang, 2008]. Increasing heat input increases penetration depth, reinforcement height and bead width; however, it should be noted that when designing the experiments different land geometries were used for accommodating different heat inputs (Section 3.2). In other words, higher heat inputs were accommodated through higher land geometries to prevent burn through. As such, the relationships between heat input and bead shape for the bevel welds, which are produced using different land geometry, should be carefully interpreted. Penetration depth and bead width are likely to be affected by the land geometry. However, there are two variables which are less likely to be affected by the land geometry, i.e., contact angle and reinforcement height [Yang, 2008]. If both reinforcement height and contact angle have any relationship with SAW parameters for bevel welds then the bead shape factors should also have a relationship with SAW parameters for bevel welds.

The effect of contact angle was plotted against heat input and is shown in Figure 4-9 and Figure 4-10. It can be seen from these figures that as the heat input increases the contact angle decreases. This result agrees with the literature [Yang, 2008]. Equation (4.1) shows that reinforcement height is proportional to $\tan(180-\theta)$. As welding current increases, reinforcement height increases and, hence, $\tan(180-\theta)$ increases. Therefore the contact angle decreases.

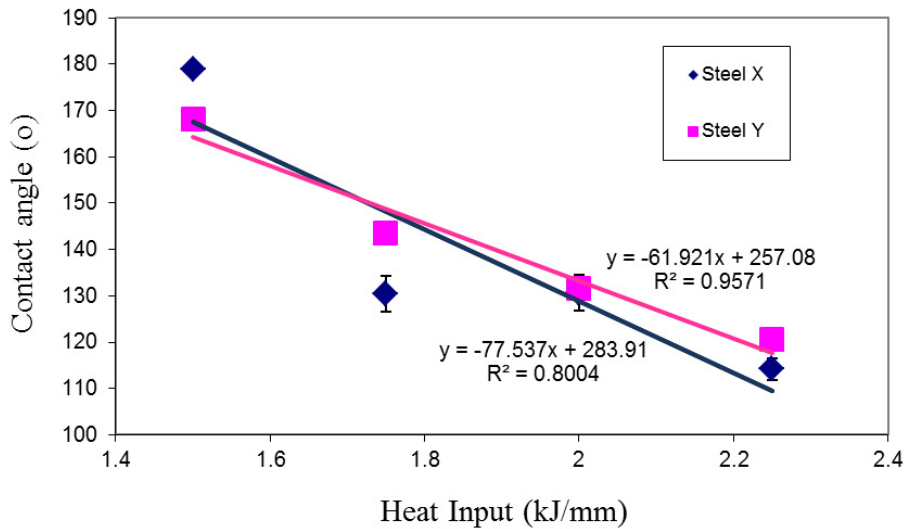


Figure 4-9: Effect of heat input on the contact angle – tandem electrode welds.

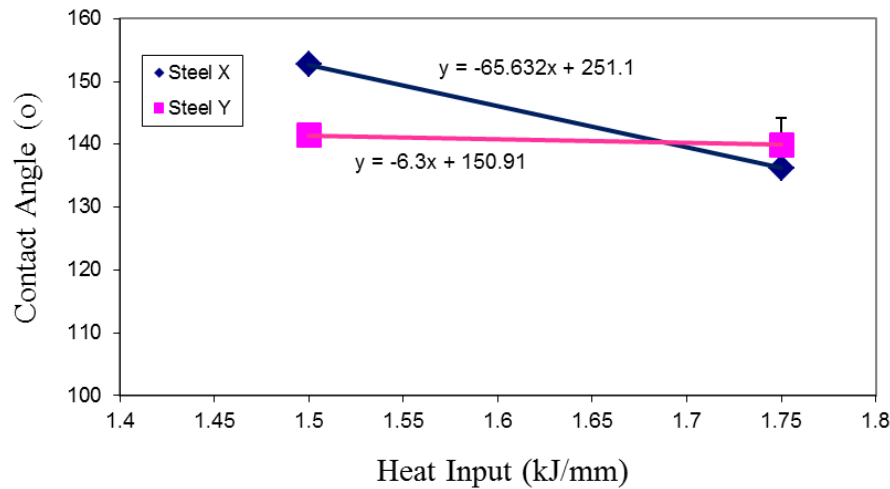


Figure 4-10: Effect of heat input on the contact angle – single electrode welds.

4.3 Effect of Total Molten Area/ Heat Input on Single and Tandem Electrode Welds

The total molten area is sometimes used as an alternative estimate of heat input where the heat input calculation is complex [ASME, 2007]. It is worth noting that although similar heat input values were used for both single and tandem electrode welds (1.5 kJ/mm and 1.75 kJ/mm), they produced different amounts of total molten area. This is an indication that the straightforward heat input equation is not adequate to explain the phenomena that are happening in single and tandem electrode welds. Single electrode welds produce more total molten metal than tandem electrode welds. Total molten area in the welds is plotted against different heat input in Figure 4-11 and Figure 4-12. In Figure 4-11, it can be seen that for Steel X welded using a 1.75 kJ/mm heat input, both single and tandem electrode welds have quite similar total molten area. This apparent variation could be taken as an outlier, as the location of the specimens (whether the weld cross sections were extracted from the initial region of the weld start line or from the middle)

used to measure the total molten area also plays a role. Apart from this outlier, for both steels, a similar trend was observed. To explain this phenomenon, some key points should be noted, which are the effect of lead and trail arc on bead shape, the effect of voltage and arc stick-out and the effect of travel speed on bead shape. It is well established that in tandem welds the lead arc actually dictates the penetration of the weld bead and the trail arc promotes high deposition [Kubli, 1956]. This can be seen in Figure 4-13.

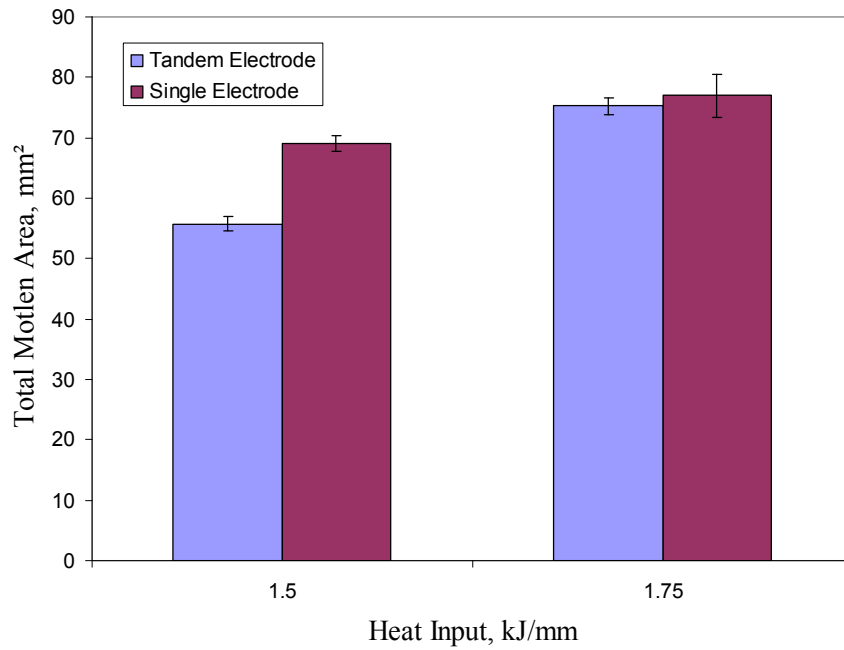


Figure 4-11: Heat input vs. total molten area for Steel X.

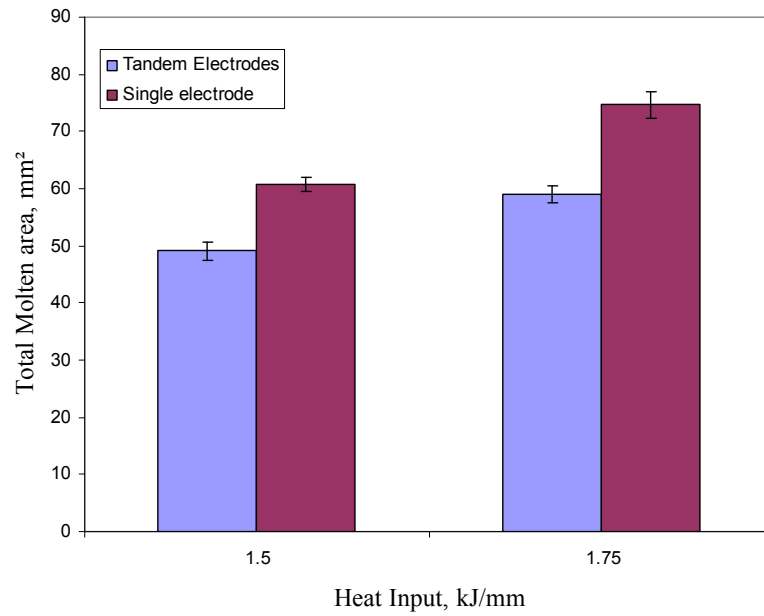


Figure 4-12: Heat input vs. total molten area for Steel Y.

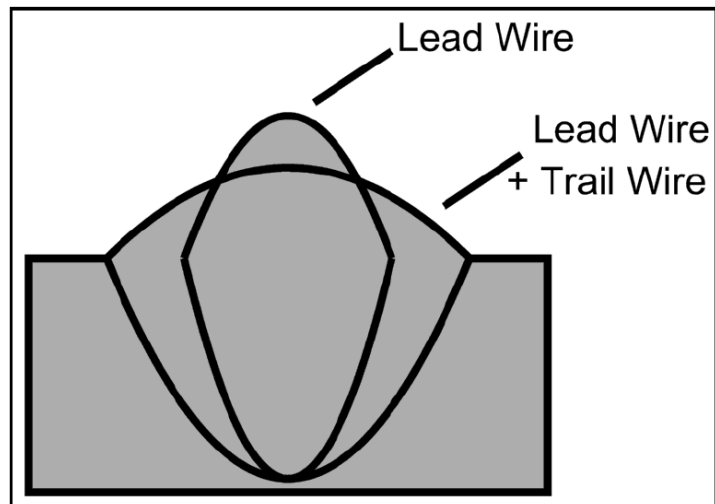


Figure 4-13: The effects of lead and trail electrodes on bead shape in tandem electrode welding [Kubli, 1956].

For the tandem welds that were produced, the heat input was calculated using the following equation.

$$\text{Heat Input} = [(V \times I)_{\text{LEAD}} + (V \times I)_{\text{TRAIL}}] / v \dots\dots\dots 4.2$$

Here V and I are voltage and amperage of the lead and trail arcs respectively and v is the travel speed. From Equation 4.2, it can be seen that for tandem electrode welds the heat input is actually calculated by simply adding the individual heat input from each electrode.

When a 1.5 kJ/mm heat input is used in tandem electrode welds, one can assume that 0.75 kJ/mm heat input is coming from the lead arc and the remaining 0.75 kJ/mm heat input is coming from the trail arc. It can also be assumed that the 0.75 kJ/mm heat input, which is provided by the lead arc, is used mostly for penetration. The other half of the heat input provided by the trail arc is used for deposition. For single electrode welds with the same heat input (e.g., 1.5 kJ/mm) this heat is used partly for penetration and partly for deposition. It can also be safely assumed that the portion of the heat input in a single electrode weld used for penetration is higher than 0.75 kJ/mm. Hence, the penetration area would be larger in single electrode welds than in tandem electrode welds. Also, single electrode welds use much higher voltages than tandem electrode welds (36 V for single electrode welds compared with 28 V for the lead arc and 34 V for the trail arc for tandem electrode welds). This has an effect on the deposition rate and affects reinforcement area too. When the arc voltage is increased, arc length is also increased [Wemen, 2003]. This in turn increases the bead width as can be seen in Figure 4-14. Since single electrode welds were produced using higher voltages, the bead width was also increased according to the discussion above. Hence, the overall reinforcement area will also increase. Figure 4-15 and Figure 4-16 show the variation in reinforcement area for single and tandem electrode welds for Steel X and Steel Y.

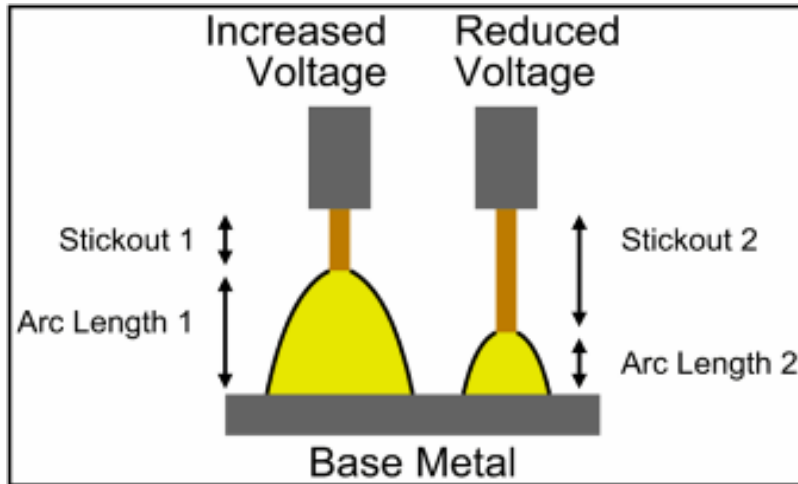


Figure 4-14: Effect of voltage on arc length and electrode stick-out [Pepin, 2009].

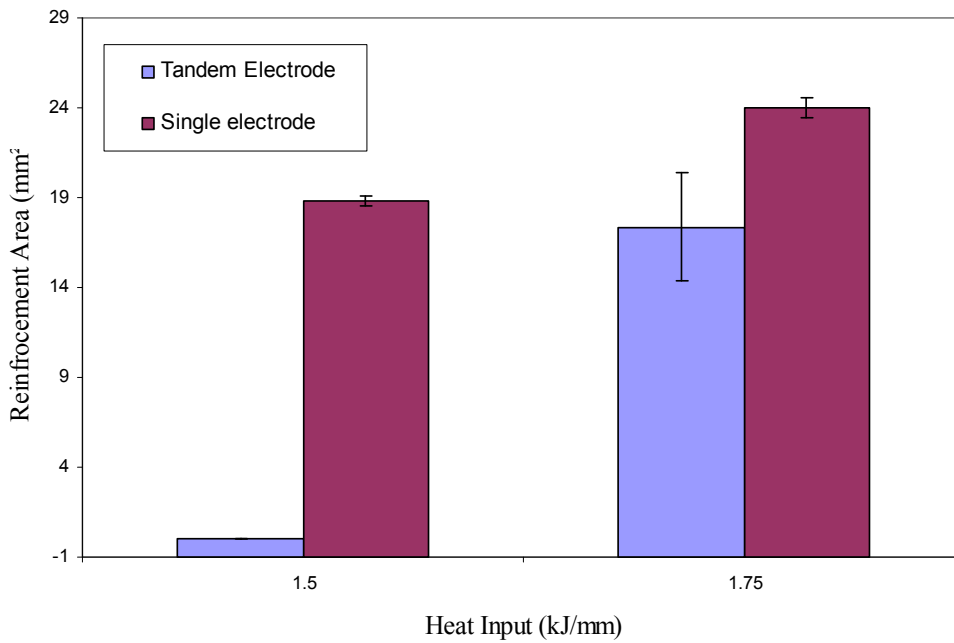


Figure 4-15: Variation of reinforcement area for single and tandem electrode welds for Steel X.

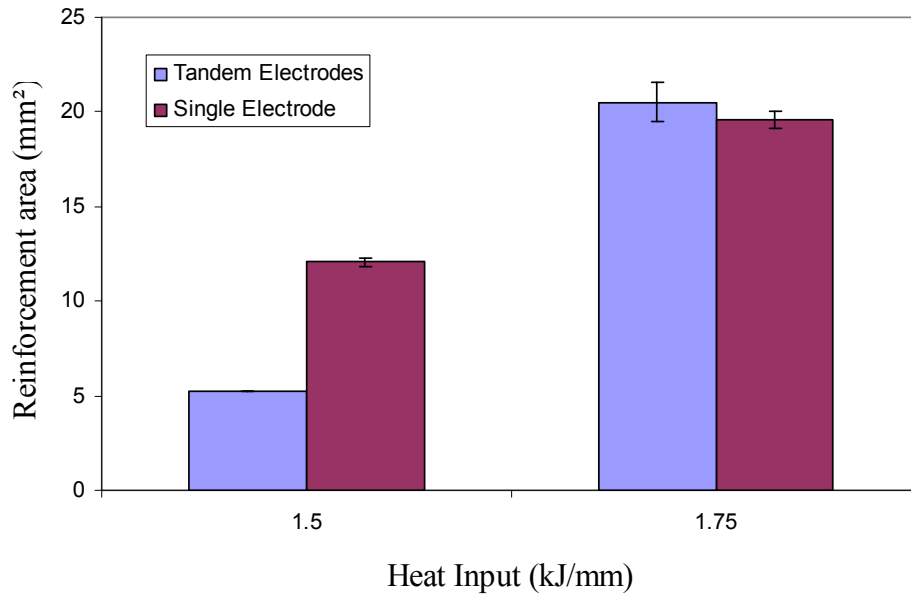


Figure 4-16: Variation of reinforcement area for single and tandem electrode welds for Steel Y.

Another factor that contributes to total molten metal area is travel speed. It can be seen from Table 3-2 and Table 3-3 that for tandem electrode welds a travel speed of 19.35 mm/s was used. For single electrode welds the travel speed was much lower, i.e., 12.5 mm/s. Lower travel speeds tend to spread out the deposited molten metal on the surface of the base metal [Wemen, 2003]. However, due to the higher welding current this bead penetration reduction is somewhat mitigated, because at higher currents the higher arc pressure will be able to displace molten metal from the arc pool [Gupta, 1987]. The penetration will be much higher in the weld centerline as shown in Figure 4-17, creating a T-shaped penetration. The overall effect is a higher total molten area.

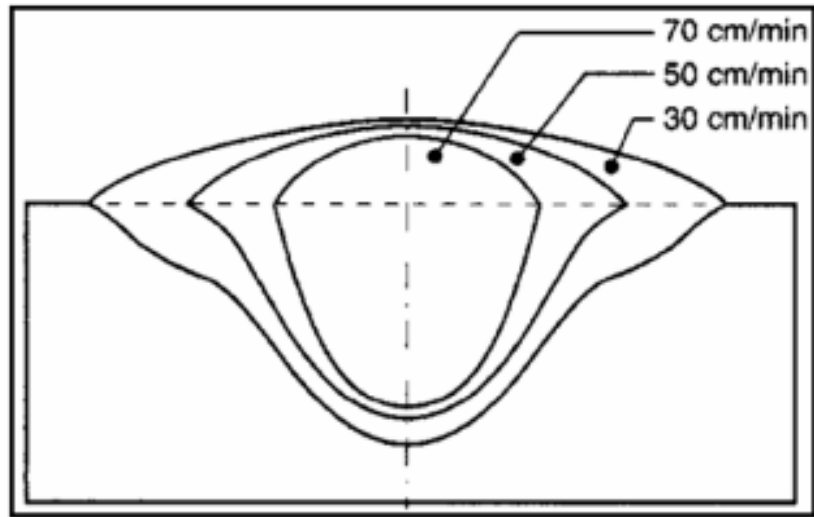


Figure 4-17: Effect of welding speed on SAW bead-on-plate cross section
[Wemen, 2003].

All the above factors contribute to the fact that single electrode welds have higher total molten areas than welds produced by tandem electrodes. In addition, due to these complexities, a simple equation for calculating heat inputs for single and tandem electrode welds is not feasible.

4.4 Bead Shape

It is clear from the above sections that measurable quantities such as bead width, penetration area and reinforcement area can be used to express the differences between different weld beads. These differences are more distinguishable when observed with the naked eye. However, when a large number of weld bead shapes need to be evaluated, a more effective approach would be to use a numerical shape factor [Pepin, 2009]. This method was developed to better understand the shape of a weld bead. It compares the full width to the width of half penetration of

a weld bead [Pepin, 2009]. The parameter was named “SP ratio” (semi penetration ratio) and can be calculated using the simple equation given below:

$$\text{SP Ratio} = W_2/W_1 \dots\dots\dots 4.3$$

Here W_1 is the full bead width and W_2 is bead width at half penetration depth. Penetration depth P is defined as $P = P_1 + P_2$, where it is assumed that P_1 and P_2 are equal (Figure 4-18). In Figure 4-18 two types of weld bead schematics are shown. The schematic on the right shows a T-shaped profile having a lower SP ratio value (i.e., W_2/W_1 is less because of the smaller W_2). The schematic on the left demonstrates a more bulbous shape with a higher SP ratio due to the high value of W_2 .

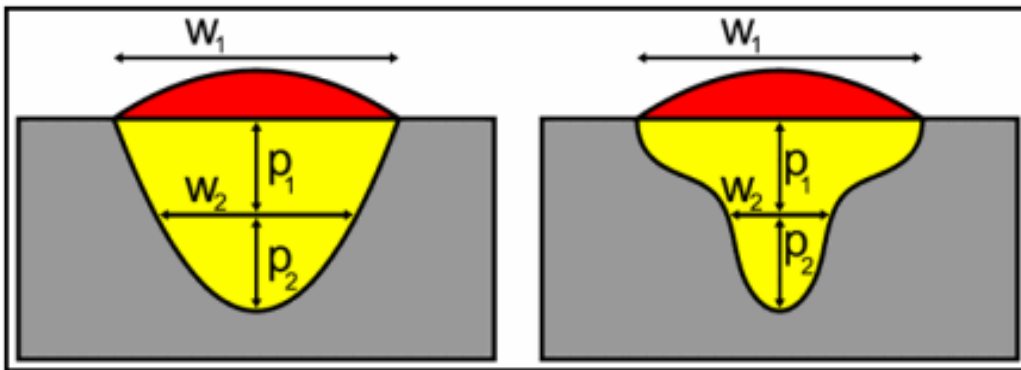


Figure 4-18: Schematic of two types of weld beads [Pepin, 2009].

When heat input is plotted against SP ratio a trend is observed. Figure 4-19 and Figure 4-20 show that there are some slight variations in the results plotted in the figures. For example, for Steel X there is a decrease in the SP ratio values followed by an increase. For Steel Y, there is an initial decrease and then the SP ratio increases for a heat input of 2.00 kJ/mm. For Steel Y welded using a single electrode, there was no such increase or decrease in SP ratio. These variations/ deviations from the expected trend can be regarded as outliers. It is noted that the

location of the specimens extracted for calculation of SP ratio values affects the calculated values. Nevertheless, there is a trend that can be observed in these figures, i.e., increasing heat input decreases the SP ratio values.

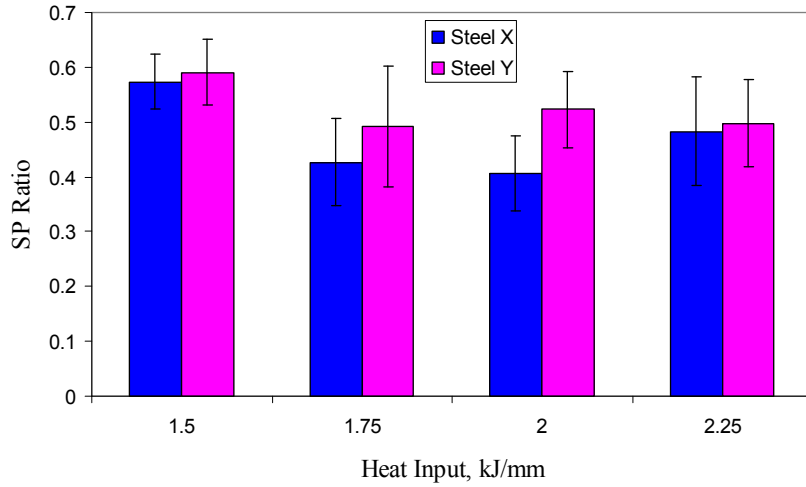


Figure 4-19: Heat input vs. SP ratio for tandem electrode welds.

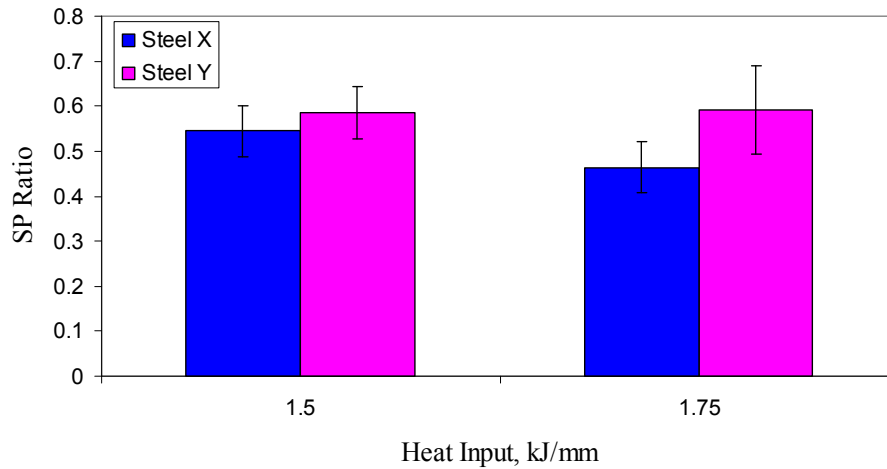


Figure 4-20: Heat Input vs. SP ratio for single electrode welds.

From these figures it is evident that as the heat input increases the bead shape tends to shift from “bulbous” to “T-shaped”. In other words there is a

relationship between these two variables. It should be mentioned that as the heat input increases - more specifically as the current increases - the penetration depth also increases, which leads to a subsequent decrease in the value of W_2 , reducing the SP ratio. Also, an increase in current increases the bead width (i.e., W_1), which will affect the SP ratio values by decreasing it. However, it should be noted that these heat input values are for tandem welds, which utilize two electrodes. As predicted in the literature [Pepin, 2009], an increase in voltage also decreases the SP ratio. The effect of voltage used in the two electrodes also played a role in this regard. In tandem welds, the combined effects of lead and trail current and voltage and how they control the bead shape are still uncertain. More work is required in this regard to better understand the effect. Another observation worth noting is that the SP ratio values for Steel X are always lower than those for Steel Y under similar welding conditions. It was found during the test welds that steel composition had little effect on the penetration depth and bead width and, therefore, little effect on SP ratio. However, this was not the case for the data in Figure 4-19 and Figure 4-20. These figures suggest that there is a relationship between steel composition and SP ratio values. An explanation of this phenomenon is not available at this time and requires further investigation.

4.5 Weld Melting Efficiency

As described in the previous sections, welding parameters affect the size of the weld bead and the HAZ differently and this is attributed to the way these parameters affect the various melting efficiencies.

In various studies regarding welding process variables, electrode melting and plate melting efficiencies, it was found that increasing welding current and voltage also increased plate melting efficiency [Niles, 1975] [Yang, 1992]. It was found through the work of Chandel [Yang, 1992] that, with a total energy input of 3 kJ/mm, the melting efficiency of SAW can vary between 30 and 75% depending on the combination of the process variables. Jackson and Shrubsall [Jackson,

1950] also reported that the plate melting efficiency varied between 5 to 35% depending on the welding process variables. However, they also reported that the electrode melting efficiency was independent of the process variables and was 15%.

It should be noted that not all the heat that is produced during welding is used for melting the electrode and plate. The proportion of the total energy (expressed in %) during welding that is used to create the total fusion zone is known as melting efficiency [Niles, 1975]. The proportion of heat input (expressed in %) that is used for plate melting is termed as “plate melting efficiency” [Wells, 1952]. The proportion of the total energy that is used for wire melting is termed “electrode melting efficiency” [Yang, 1992]. The melting efficiency is actually the sum of electrode and plate melting efficiencies. Based on Chandel’s work [Yang, 1992] the three melting efficiencies for submerged arc welding are given below:

$$\text{Electrode Melting Efficiency (EME) (\%)} = \frac{(100 \times S \times A_r)}{(0.0854 \times V \times I)} \dots\dots\dots 4.4$$

$$\text{Plate Melting Efficiency (PME) (\%)} = \frac{[100 \times S \times (A_f - A_r)]}{(0.0854 \times V \times I)} \dots\dots\dots 4.5$$

$$\text{Welding Process Melting Efficiency (WPME) (\%)} = \frac{(100 \times S \times A_f)}{(0.0854 \times V \times I)} \dots\dots\dots 4.6$$

Here V is the voltage, I is the current, S is travel speed (mm/min), A_r is reinforcement area (mm²) and A_f is the total molten area (mm²).

It was reported in a study [Lee, 2000] that HAZ size is related to plate melting efficiency. According to the researchers the welding process variables that

promote plate melting will increase the size of the HAZ. Also, they assumed that most of the heat used for plate melting is used for creating the HAZ, whereas the heat from the reinforcement area is used for melting the flux. In Figure 4-21 to Figure 4-24, melting efficiency is plotted against heat input (i.e., welding current) for steel X and Y. Both steels show the same trend.

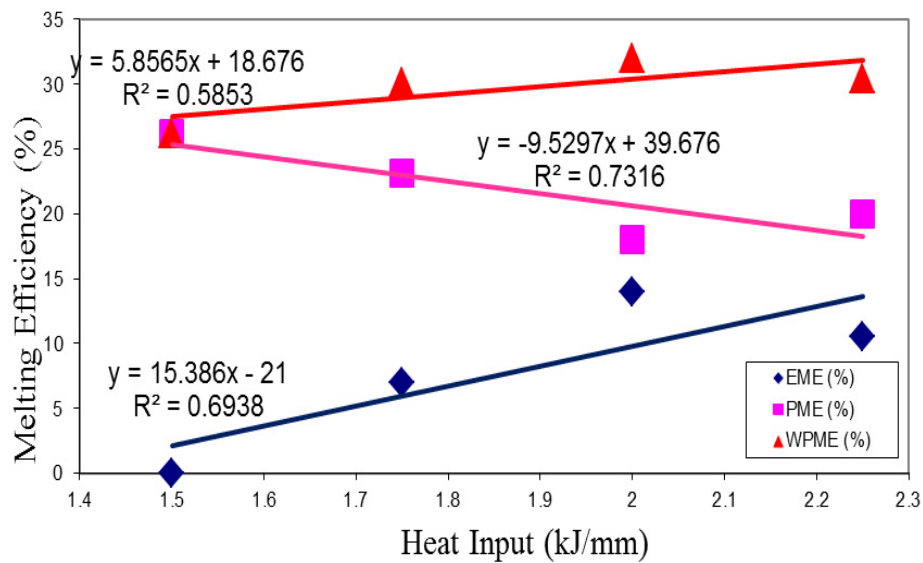


Figure 4-21: Melting efficiency (%) vs. heat input for Steel X - tandem electrode welds.

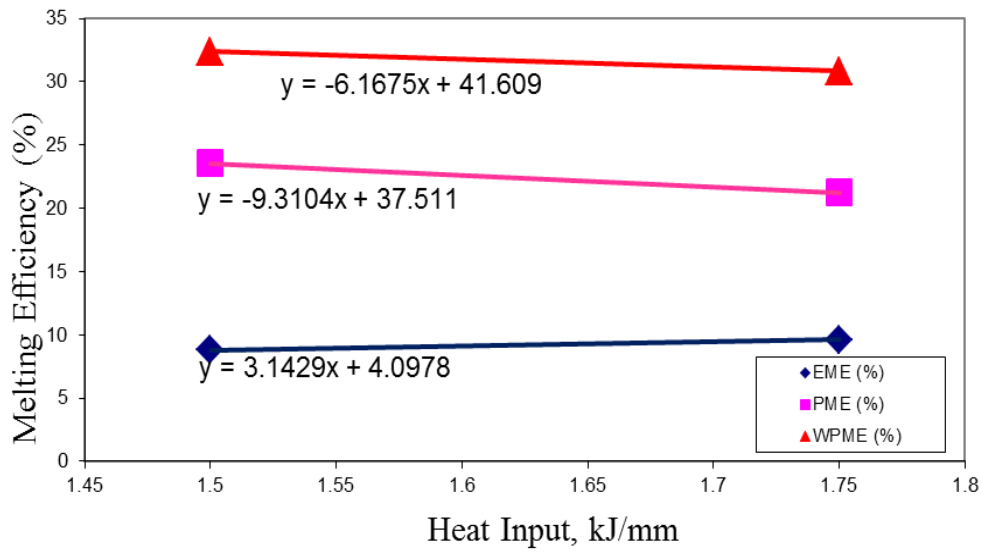


Figure 4-22: Melting efficiency (%) vs. heat input for Steel X - single electrode welds.

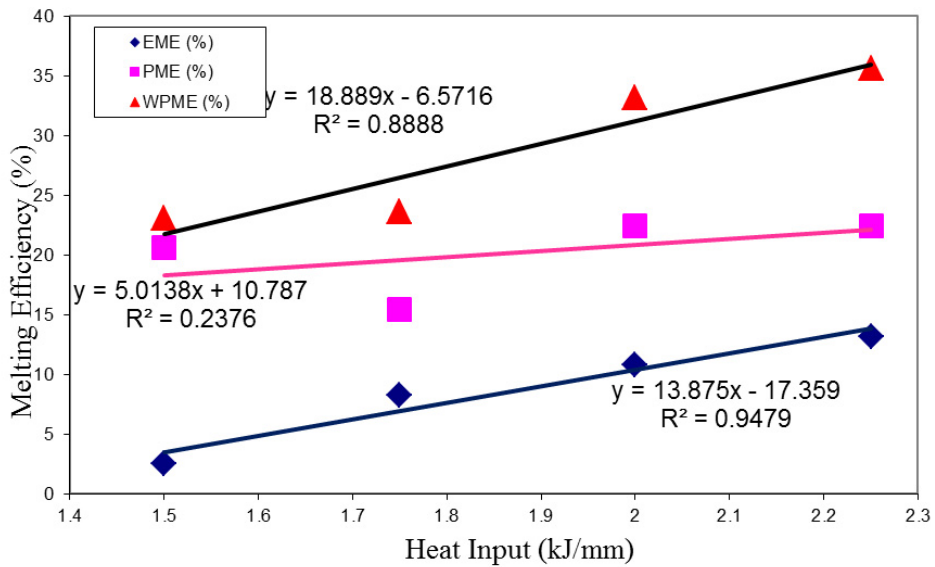


Figure 4-23: Melting efficiency (%) vs. heat input for Steel Y - tandem electrode welds.

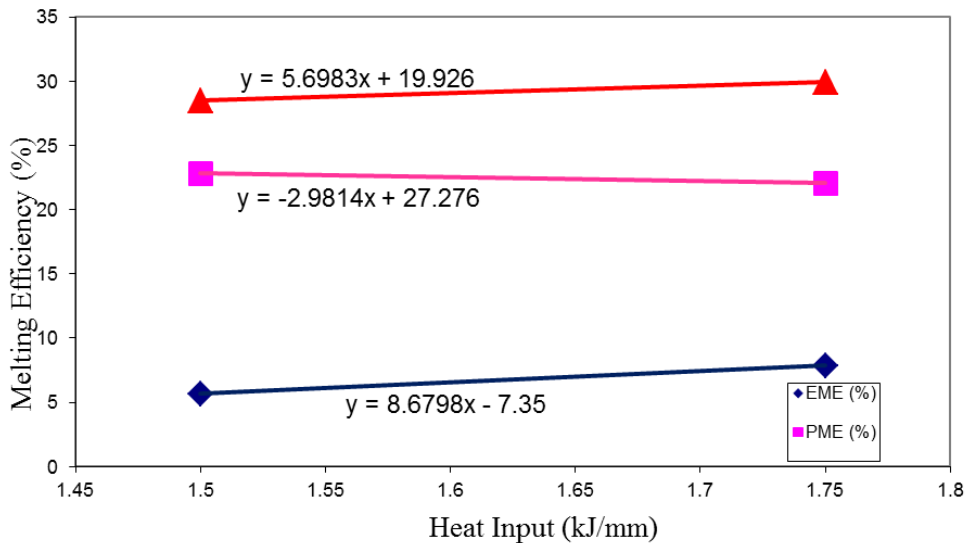


Figure 4-24: Melting efficiency (%) vs. heat input for Steel Y - single electrode welds.

For tandem electrode welds (Figure 4-21 and Figure 4-23), increasing heat input results in increased weld melting efficiency. It is also evident that EME is clearly related to heat input, when tandem electrode welds are taken into account. Reinforcement area of the weldment for a given electrode material, diameter and voltage will increase with increasing welding current. Hence, EME is also increased. It should be noted that only two heat inputs were used for single electrode welds, so it was not possible to come up with a trend, although similar behavior to tandem electrode welds is expected.

As described in the literature, electrode melting is associated with weld bead shape (reinforcement height and contact angle). If the electrode melting efficiency of tandem electrode welds is compared with that of single electrode welds, it can be seen that single electrode welds have higher electrode melting efficiencies than tandem electrode welds. This result is in agreement with the values found previously for contact angles for these two cases, i.e., single electrode welds have

lower contact angles than tandem electrode welds (higher heat input gives a lower contact angle).

Plate melting efficiency also is related to heat input. It is expected that increasing heat input will increase plate melting efficiency. High heat input will produce a high temperature columnar shaped welding plasma, which will transfer some of its heat to the parent metal. Higher heat generated in the arc column will increase plate melting. Also, molten metal droplets from the electrode are superheated as they pass through the arc column; when these droplets come in contact with the parent metal, plate temperature again increases. For Steel Y this trend is somewhat apparent in Figure 4-23. However, Steel X shows a complete opposite trend (Figure 4-21); increasing heat input actually decreases the plate melting efficiency. Further investigation showed that not only does Steel X show an opposite trend to Steel Y, but it is also has higher plate melting efficiency than Steel Y. As described earlier, HAZ size is related to plate melting, so a higher plate melting efficiency will result in a larger HAZ size. Since Steel X has a higher plate melting efficiency, it also has a larger HAZ size than Steel Y for similar heat inputs (Figure 4-4). It is then evident that the opposite trend found for Steel X is not an outlier, rather it has some significance. One possible explanation for this phenomenon could be related to the flux material. During welding, flux was applied to the joint surface. The amount of flux used to cover the joint was applied manually and no other measuring was done. It is possible that for Steel X a lower amount of flux was used, which resulted in heat loss during melting. This may be responsible for the observation that higher heat input yields lower plate melting efficiency. Apart from this discrepancy, the results obtained in this section are consistent with the work reported by Chandel [Yang, 1992].

4.6 Summary

In this study submerged arc welding was used to produce bevel joints using both tandem electrodes and single electrodes. A previous study done on bead-on-plate (BOP) welds showed that there was a relationship between weld bead geometry and SAW parameters [Pepin, 2009]. Increasing heat input in SAW increased weld dimensions, such as penetration depth, reinforcement height and bead width during BOP welding. A similar relationship was found for bevel welds. Increasing heat input (i.e., current) increased the penetration depth, bead width and reinforcement height. Since different land geometries were used, the trends found for penetration depth and bead width should be carefully interpreted. Expected trends were observed for contact angle and reinforcement height, which showed that increasing heat input decreased the contact angle and increased the reinforcement height which further confirmed the relationship found in the previous study.

Single electrode welds had higher total molten areas than tandem electrode welds, for similar heat inputs. This phenomenon shows that the heat input equation used for tandem electrode welds is not applicable and needs to be corrected by careful interpretation of the individual effects of lead and trail electrodes.

Weld melting efficiency was calculated and plotted against heat input. Increasing heat input also increased the weld melting efficiency for single and tandem electrode welds, which also supports previous work done in this regard.

Mechanical Properties

In this chapter, the results obtained from microhardness measurements, tensile testing and Charpy impact testing are presented for both steels. The correlations between Charpy impact toughness, strength and hardness of both materials are discussed with SAW process variables.

5.1 Hardness Testing

The variation in microhardness with distance from the fusion line, for a Steel X weldment (welded using a 1.5 kJ/mm heat input - tandem electrode) is shown in Figure 5-1. A similar variation for a Steel Y weldment (welded using a 1.5 kJ/mm heat input - tandem electrode) is shown in Figure 5-2. Since the hardness distributions are quite similar, microhardness distributions for the rest of the specimens are provided in Appendix A. A schematic of the hardness profile trend for all specimens is shown in Figure 5-3.

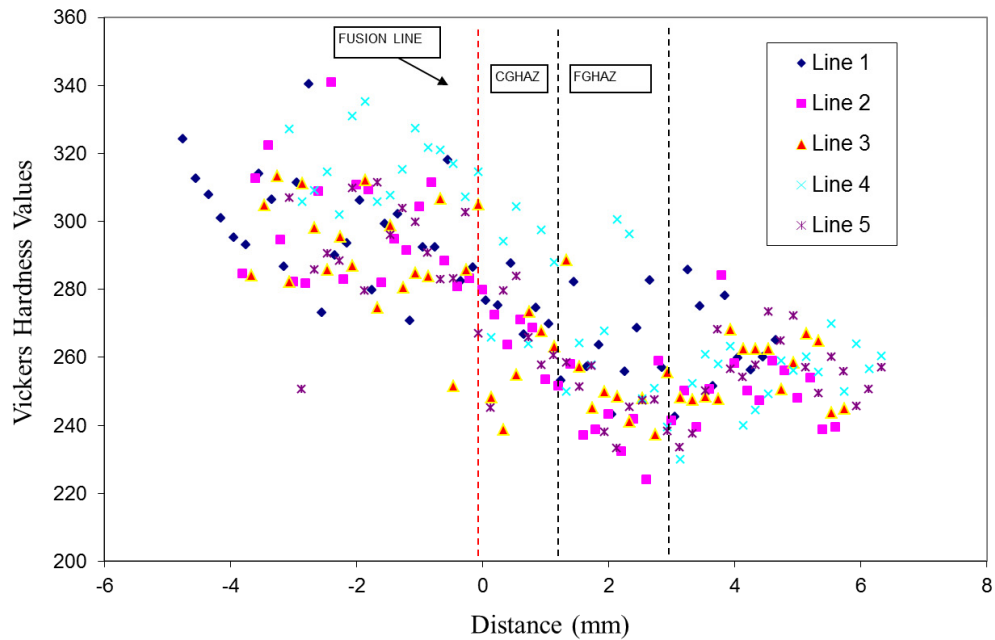


Figure 5-1: Microhardness variation for Steel X welded using a 1.5 kJ/mm heat input. The number zero on the distance axis denotes the fusion line. The negative distance values denote the weld metal region.

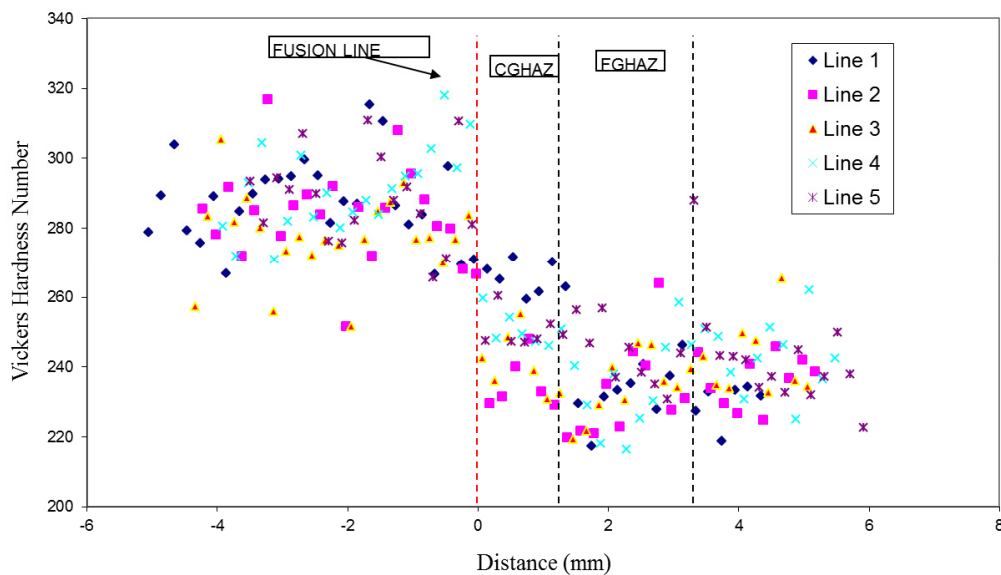


Figure 5-2: Microhardness variation for Steel Y welded using a 1.5 kJ/mm heat input. The number zero on the distance axis denotes the fusion line. The negative distance values denote the weld metal region.

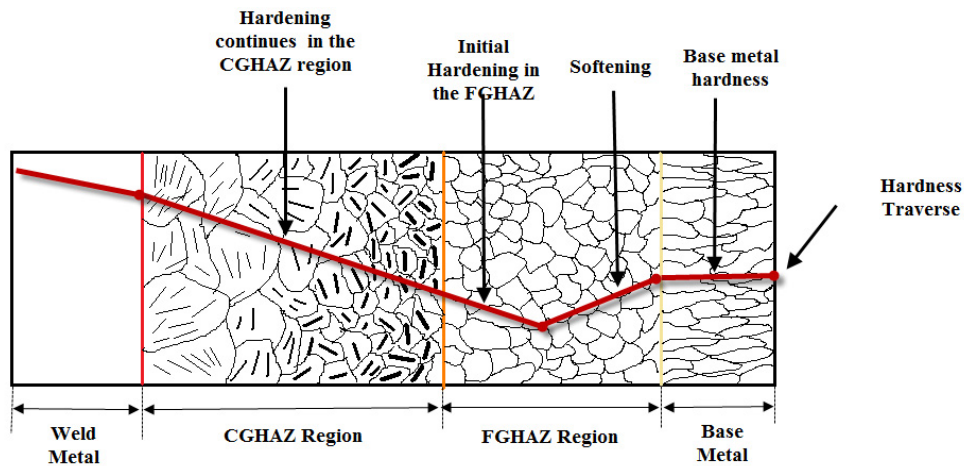


Figure 5-3: Schematic of hardness variation due to microstructural changes in the CGHAZ and FGHAZ regions.

The base metal hardnesses for Steel X and Steel Y were 256 ± 7 HV and 248 ± 7 HV. Steel X has a higher percentage carbon, which results in a higher hardness. Upon careful observation of Figure 5-1 and Figure 5-2, it is evident that for each individual region in the HAZ, the weld metal and in the base metal there is a range (e.g., a band) within which the hardness values fall. The hardness values for each individual region are scattered and clustered within this range. It is believed that the hardness values are representative of the individual regions and the scatter in the data is normal for these types of hardness measurements. In general, the hardness relationship for all the weldments produced using Steel X and Steel Y can be expressed as follows: $VHN_{WM} > VHN_{CGHAZ} > VHN_{BM} > VHN_{FGHAZ}$. The base metal hardness was found to be lower than the CGHAZ hardnesses and FGHAZ hardness was lower than the base metal hardness. There are isolated hardness values in the FGHAZ region, which are quite high (e.g., Figure 5-2; line 2 has a FGHAZ hardness value exceeding 263 HV. It is speculated that very high hardness values in the FGHAZ region are due to the indenter hitting a hard particle.

There was initial softening in the fine grain HAZ (FGHAZ) relative to the base metal, with hardening occurring predominantly in the CGHAZ. There was an increase in the

hardness level beyond the CGHAZ region and into the weld metal. Peak hardness was found in the weld metal region. The average weld metal hardness in Steel X was $\sim 293 \pm 9$ HV and in Steel Y it was $\sim 288 \pm 10$ HV, with no variation with the heat input. Hardness variation in the CGHAZ and FGHAZ region due to heat input differences, for Steel X and Steel Y welded using tandem and single electrode welds, are shown in Figure 5-4 to Figure 5-7. The point 0 on the X-axis denotes the fusion line and point 1 denotes the base metal region. The dashed line on the far right side denotes the boundary between FGHAZ and base metal and the dashed line in the middle denotes the boundary between FGHAZ and CGHAZ. It should be noted that although the ratio of CGHAZ width to FGHAZ width appears to be the same for different heat inputs, as shown in Figure 5-4 to Figure 5-7, in reality they are different for different heat inputs. The values here are normalized with respect to CGHAZ and FGHAZ widths.

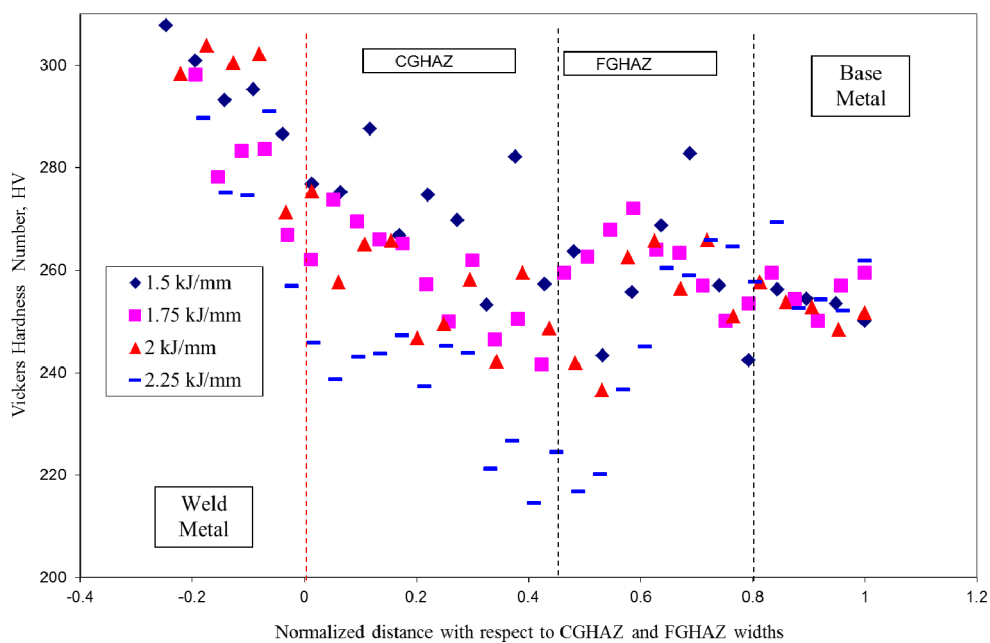


Figure 5-4: Hardness variation in the CGHAZ and FGHAZ region for different heat inputs (Steel X - tandem electrode welds).

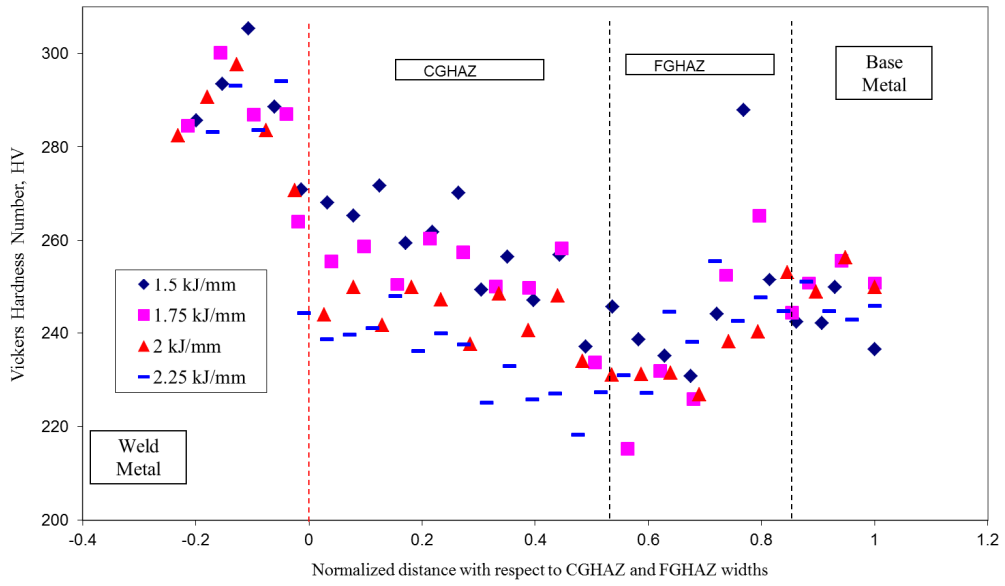


Figure 5-5: Hardness variation in the CGHAZ and FGHAZ region for different heat inputs (Steel Y - tandem electrode welds).

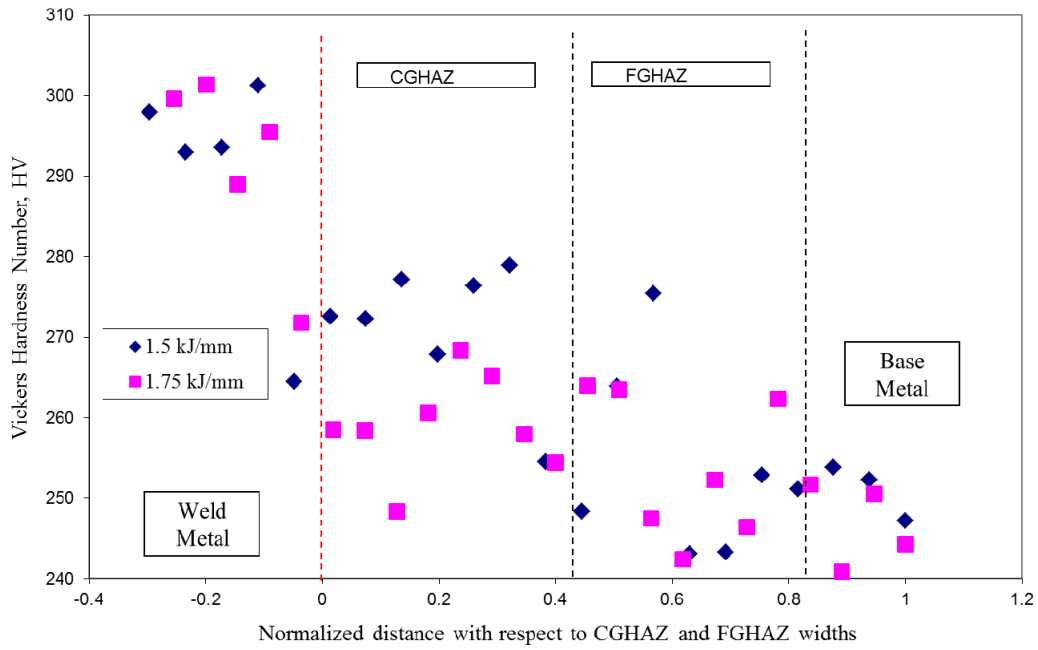


Figure 5-6: Hardness variation in the CGHAZ and FGHAZ region for different heat inputs (Steel X - single electrode welds).

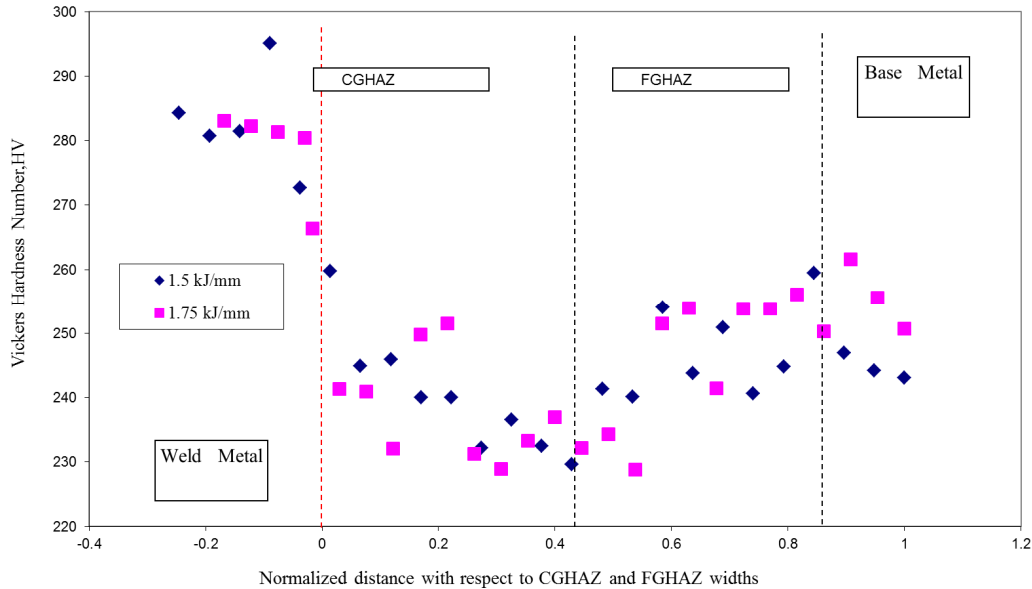


Figure 5-7: Hardness variation in the CGHAZ and FGHAZ region for different heat inputs (Steel Y - single electrode welds).

It is clear that lower heat inputs yield high hardness values in the CGHAZ region, irrespective of the number of electrodes used and the type of steel (Figure 5-4 - Figure 5-7). However, in Figure 5-7, two points (in the CGHAZ region) show an opposite trend (high heat input has high hardness), but these can be considered as outliers and may be due to the indenter hitting hard particles that are present in the steel.

It can be seen from the figures (compare FGHAZ region in Figure 5-4 - Figure 5-7) that the FGHAZ hardness variation depends little on the heat input values. Here, unlike the CGHAZ regions, hardness does not seem to vary a lot as heat input changes. The hardness values are clustered together in the FGHAZ region (Figure 5-3 and Figure 5-4). The explanation is related to the microstructure of the FGHAZ and will be discussed in the next chapter (Chapter 6).

The hardness values in the weld metal region and in the base metal region are also clustered together. These regions have only minor variations in their respective

microstructure with increasing heat inputs. This will be discussed in detail in the next chapter (Chapter 6).

The hardness values of the parent materials, the welds and their HAZs play important roles in determining the sulphide stress cracking (SSC) resistance of carbon and low alloy steels [NACE, 2009]. SSC can be controlled in an acceptable manner by controlling the hardness level of the steel and the welded region. Excessive hardening and softening is detrimental to steel. Excessive hardening in the welded region can lead to stress corrosion cracking and cold cracking [Poorhaydari, 2005]. On the other hand, softening makes the steel susceptible to sulphide stress corrosion cracking (SSCC) and ductile fracture [Poorhaydari, 2005] [NACE, 2009] [Shiga, 1990]. According to NACE MR0175 standard, the maximum allowable hardness values for low alloy steel welds should be 250 HV in the weld root, base metal and HAZ. For this work, although the base metal falls within this acceptable value, the hardening occurring in the CGHAZ and the high hardness values in the weld metal region make the steel unsuitable for application in sour environments as it will be susceptible to corrosion attack.

5.2 Tensile Testing

The purpose of this section is to examine the effect of SAW welding parameters on the tensile properties of both steels. The tensile properties were assessed using transverse tensile tests. Test parameters used for the testing were previously described in Section 3.3.3.

A typical fracture location on the tensile specimen is shown in Figure 5-8. Fracture occurred for both steels, welded using different heat inputs, in the base metal region.

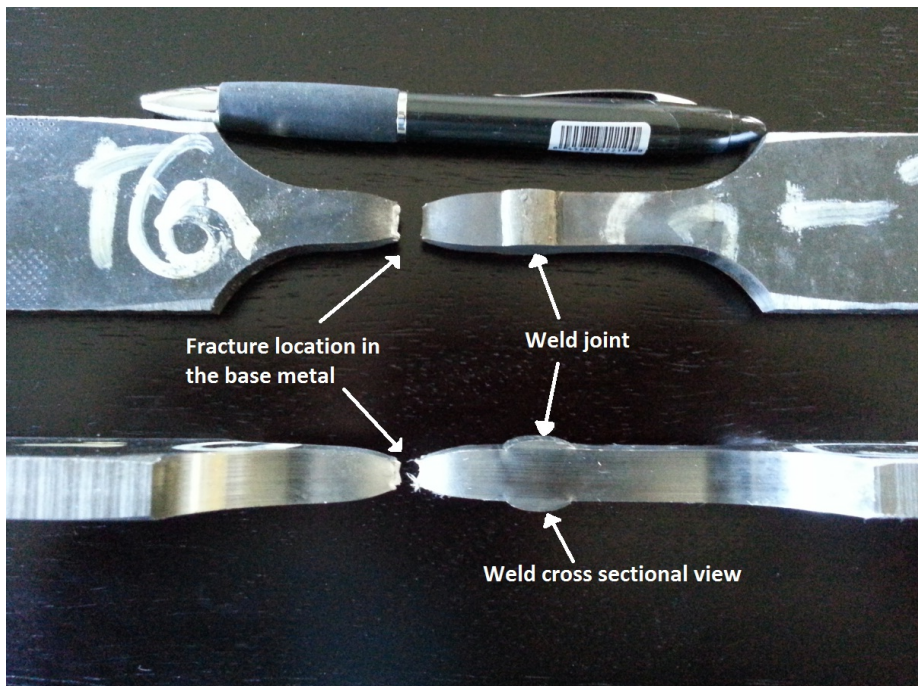


Figure 5-8: Fractured tensile specimen showing the fracture location and position of the welded joint.

It was reported by Evraz Inc. NA that the tensile strength and yield strength of Steel X were 753 MPa and 585 MPa, respectively, and for Steel Y they were 706 MPa and 564 MPa, respectively. Figure 5-9 and Figure 5-10 show the stress-strain curves for Steel X weldments welded using single and tandem electrodes respectively. Figure 5-11 and Figure 5-12 show the stress-strain curves for Steel Y weldments.

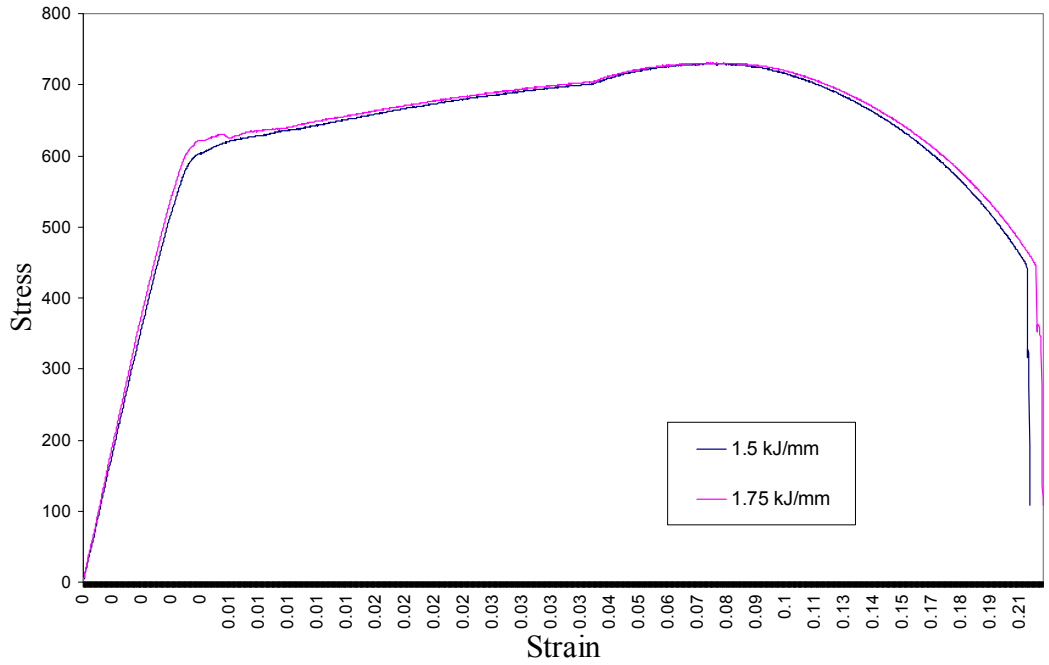


Figure 5-9: Typical stress-strain curves for Steel X welded using single electrodes for two heat inputs.

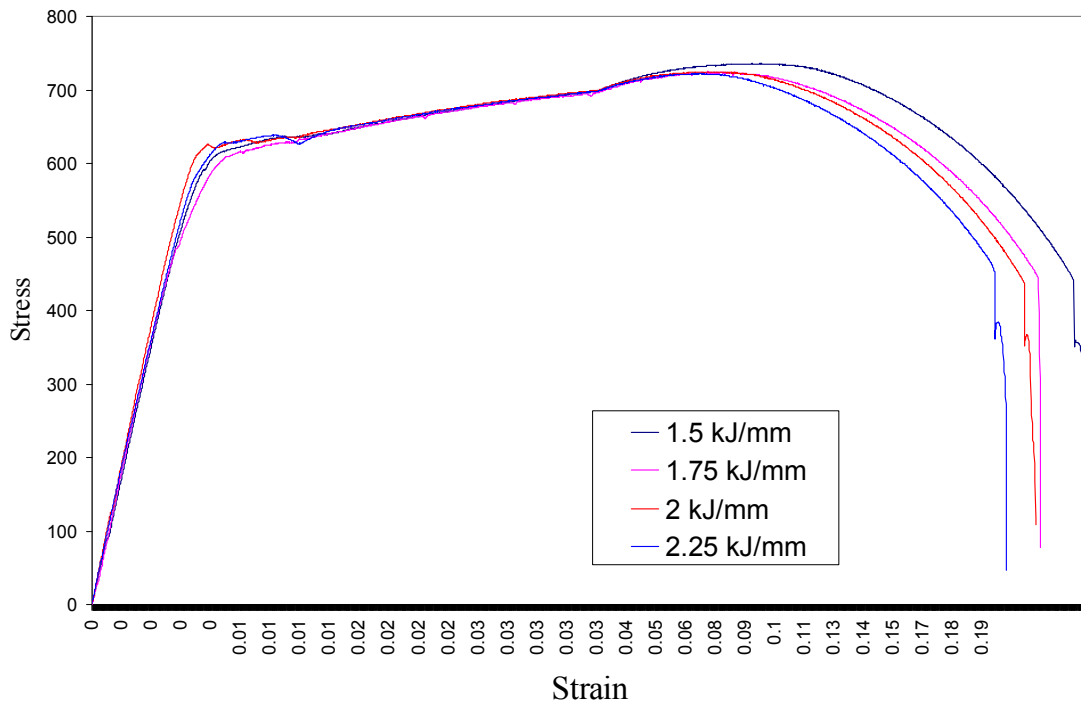


Figure 5-10: Typical stress-strain curves for Steel X welded using tandem electrodes for four heat inputs.

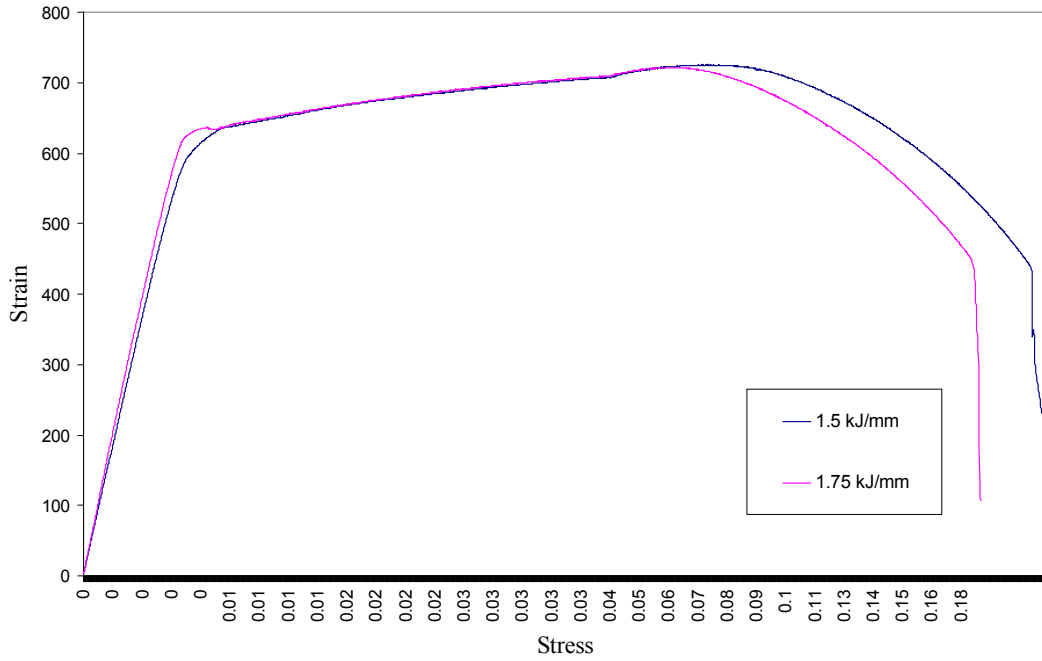


Figure 5-11: Typical stress-strain curves for Steel Y welded using single electrodes for two heat inputs.

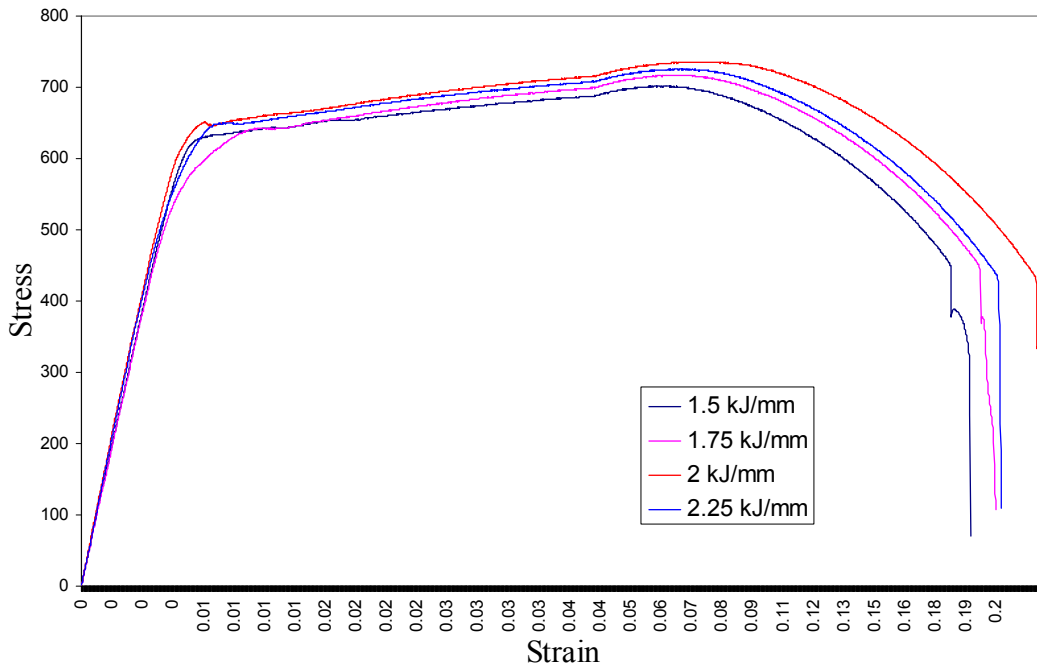


Figure 5-12: Typical stress-strain curves for Steel Y welded using tandem electrodes for four heat inputs.

It can be seen from these figures that the UTS and YS for both the steel weldments are very similar. Since all the specimens broke in the base metal region, the UTS and YS values obtained from the weldments are very close to those of their parent metals. It was reported in the literature [Yang, 2008] that the total elongation of the weldments increases as the heat input decreases. The researchers reasoned that, since heat input affects the total weld metal volume and HAZ volume, higher heat input means high weld metal volume and HAZ volume. This will effectively decrease the amount of the parent metal portion in the gauge length. On the other hand, lower heat inputs will increase the parent metal portion in the gauge length. The measured elongations for the weldments for both Steel X and Steel Y are shown in Table 5-1 and Table 5-2.

Table 5-1: Measured elongation (%) for Steel X weldments

Specimen Identification	Measured Elongation (%)
1.5 kJ/mm (Tandem Electrode)	25
1.75 kJ/mm (Tandem Electrode)	23
2.00 kJ/mm (Tandem Electrode)	23
2.25 kJ/mm (Tandem Electrode)	21
1.5 kJ/mm (Single Electrode)	22
1.75 kJ/mm (Single Electrode)	24

Table 5-2: Measured elongation (%) for Steel Y weldments

Specimen Identification	Measured Elongation (%)
1.5 kJ/mm (Tandem Electrode)	22
1.75 kJ/mm (Tandem Electrode)	22
2.00 kJ/mm (Tandem Electrode)	23.5
2.25 kJ/mm (Tandem Electrode)	23
1.5 kJ/mm (Single Electrode)	22
1.75 kJ/mm (Single Electrode)	20.5

The above dependence, i.e., increasing heat input decreases the percentage elongation, appears to hold for specimens of Steel X welded using tandem electrodes, but for the rest of the weldments no such trend is observed. It is believed that since both the OD and ID welds were done as bevel joints, the weld metal volume produced by both OD and ID welds affected the percentage elongation. So, only OD heat input parameters then should not be related with the elongation. The results agree with the literature [Yang, 2008] when both OD and ID welds are taken into account. When the total weld metal volume (weld metal produced using OD and ID welds - Figure 5-13) is plotted against percent elongation, the trend becomes clearer. It should be noted that total weld metal volume or total molten metal is another way to determine the heat input [ASME, 2007]. Total molten metal volume produced by OD and ID welds is actually an alternative approximation of the heat inputs produced by OD and ID together. Figure 5-14 and Figure 5-15 show the dependency of percentage elongation with total weld metal volume for Steel X weldments welded using single and tandem electrodes. Similar plots are shown in Figure 5-16 and Figure 5-17 for Steel Y.

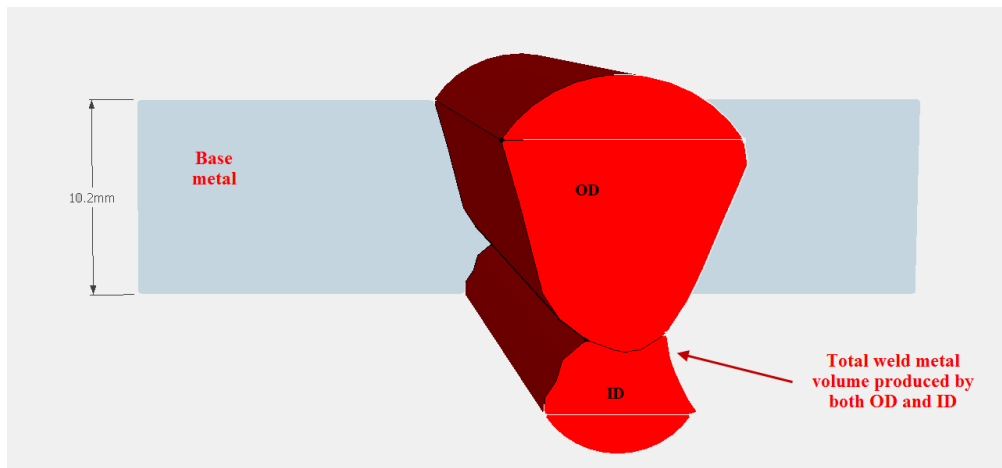


Figure 5-13: 3D view of total weld metal volume produced by OD and ID.

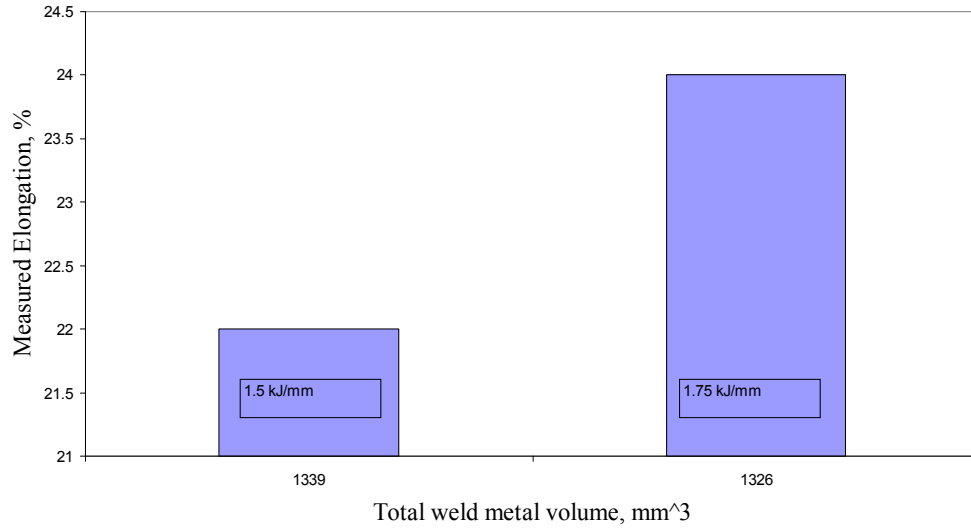


Figure 5-14: Effect of total weld metal volume on percent elongation – Steel X welded using single electrodes.

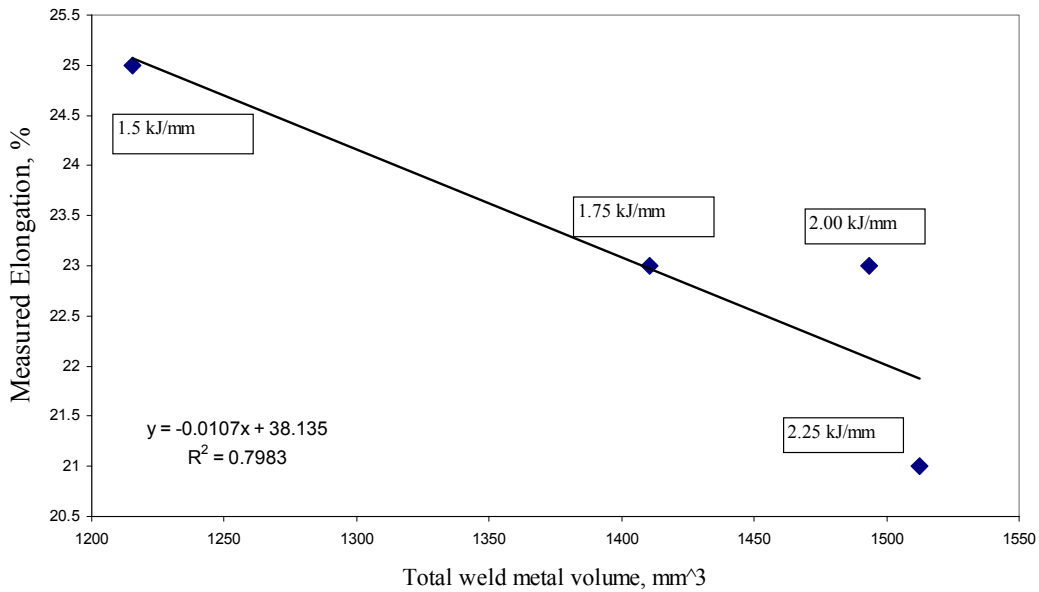


Figure 5-15: Effect of total weld metal volume on percent elongation – Steel X welded using tandem electrodes.

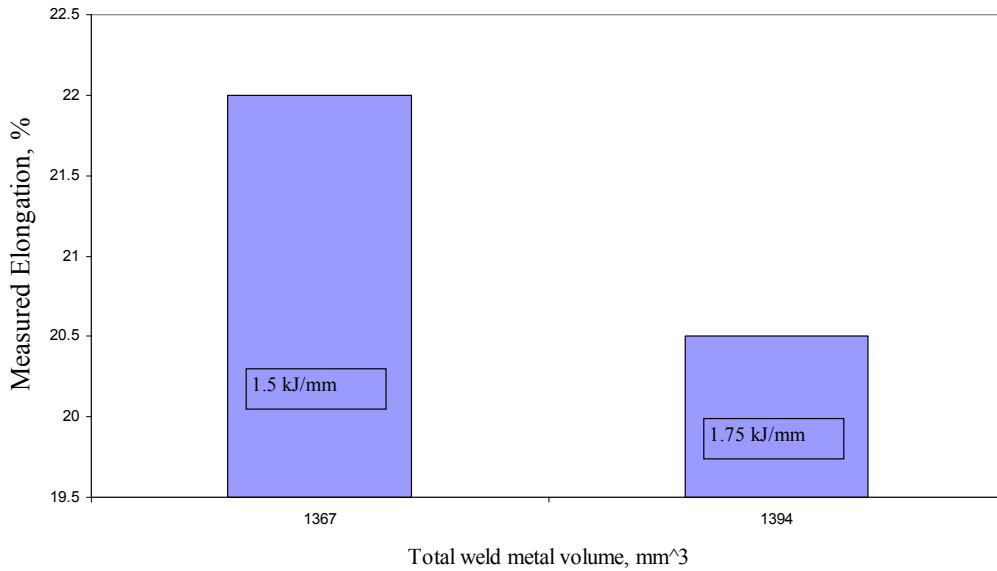


Figure 5-16: Effect of total weld metal volume on percent elongation – Steel Y welded using single electrodes.

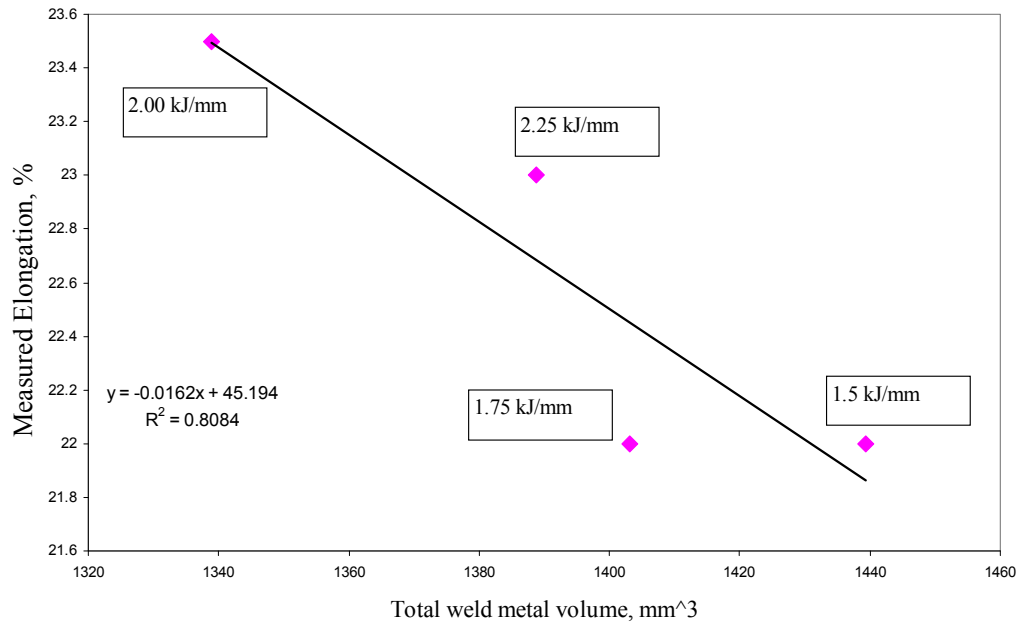


Figure 5-17: Effect of total weld metal volume on percent elongation – Steel Y welded using tandem electrodes.

As mentioned earlier, all the tensile specimens broke in the parent metal region. This result suggests that the weld metal tensile properties are superior to those for the base metal, providing some reinforcement for the HAZ and causing failures to occur in the base metal region. In addition, the hardness of the weld metal was higher compared with the base metal and HAZ regions. The dependency of percentage elongation on the total weld metal volume further confirms this idea. It should be noted that the weld reinforcement was not removed and this weld reinforcement will affect the tensile tests, since the cross-sectional area in the mid region of the tensile specimen gauge length is increased. The larger cross-sectional area, associated with the weld region, is capable of withstanding a higher load relative to the rest of the gage length and may reinforce the HAZ region. As such, it is not surprising that the samples failed in the base metal.

The transverse tensile test results are expressed in terms of the overall tensile strength; weld metal, HAZ and base metal are in series and, therefore, the degree of overmatching could not be resolved [Denys, 1990]. In order to assess the tensile strength of the weld metal, an all weld metal tensile test should be done. Although in an all weld metal tensile test it is possible to measure the tensile properties of the weld metal and then compare with the base metal properties, the HAZ tensile strength cannot be measured in this way. Since the HAZ is very narrow, it is virtually impossible to extract a tensile specimen from the HAZ. It has been reported in the literature [Denys, 1990] that weld metal overmatching results in the plastic strain being concentrated in the HAZ or in the unaffected parent metal, so that failure occurs in the parent metal or in the weld HAZ. If the sample breaks in the parent metal region, then the yield stress value is that of the base metal, as is the case for these specimens. According to the Mackenzie Gas Project, if a transverse tensile test specimen fails in the weld HAZ or in the parent metal region then the weld is acceptable. The weld HAZ of the broken tensile specimens was examined for any mechanical degradation; however, no signs of degradation were found in the transverse weld specimens, as total weld metal volume is reinforcing the HAZ.

5.3 Charpy Impact Testing

The test parameters used to measure the toughness were described previously in Section 3.3.5. Three samples were tested at each temperature; the results shown here are the averages of the three impact values and the error bars are plus or minus one standard deviation. Both sub-size and full size Charpy tests were carried out to evaluate the toughness values of Steel X and Steel Y. For full size Charpy testing, the specimens were prepared following the ASTM A370-03a Standard [ASTM A370, 2003] and were machined to a 600 grit surface finish. During full size Charpy testing, four temperatures were used, i.e., room temperature (23.8°C), -0°C, -20°C and -60°C. In Figure 5-18 the toughness values (full size and sub-size Charpys) of both the steels are shown for different temperatures. Impact values for both tandem and single electrode welds are shown in Figure 5-19 to Figure 5-22.

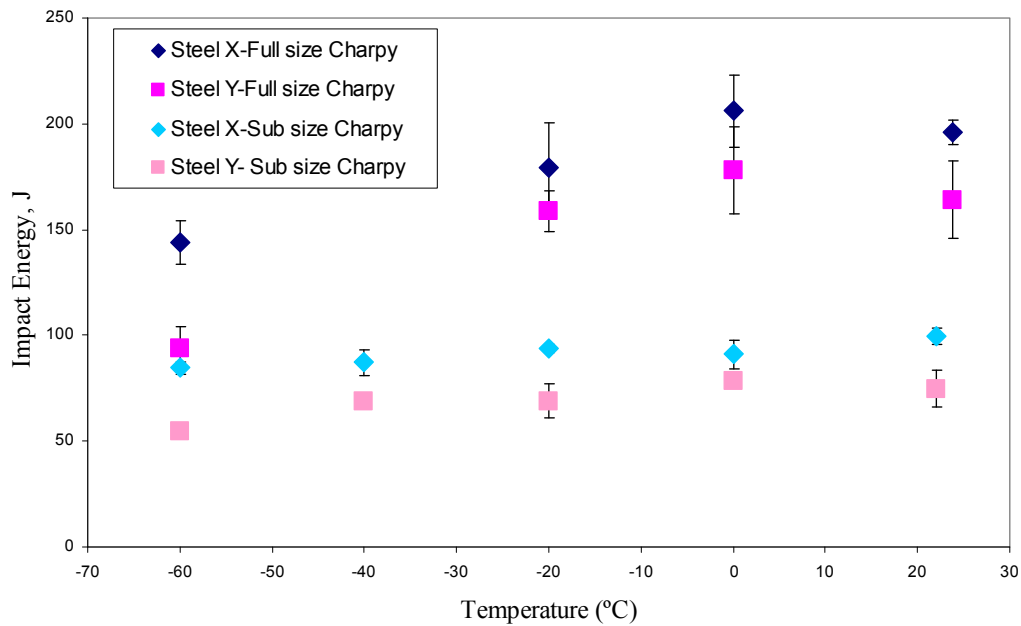


Figure 5-18: Full size and sub-size toughness values for the two steels (base metal) at different temperatures.

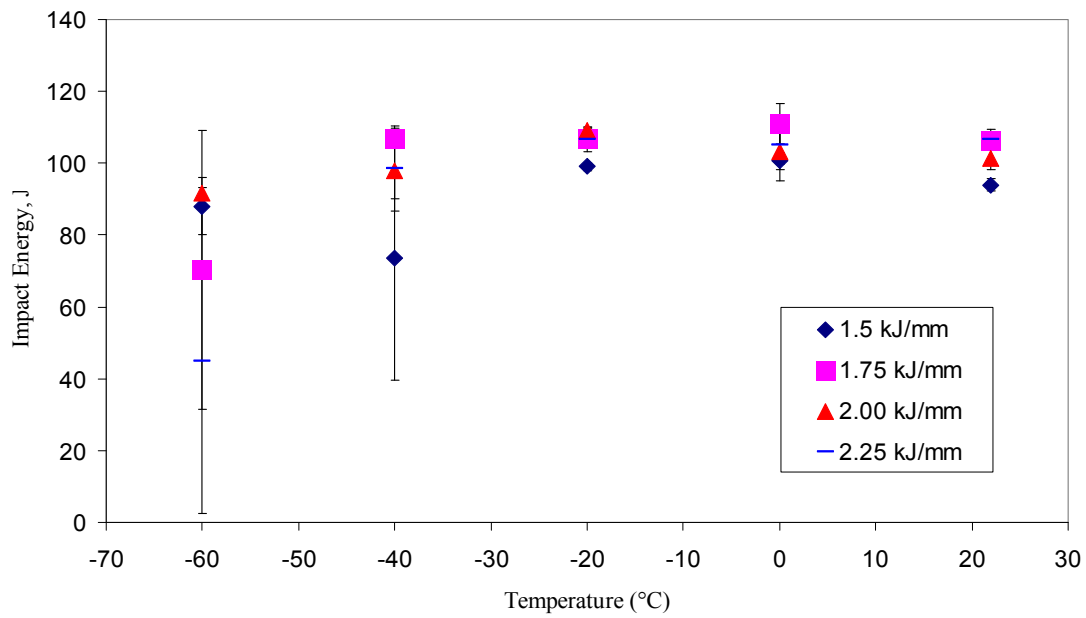


Figure 5-19: HAZ toughness (sub-size) values for different heat inputs - Steel X with tandem welds.

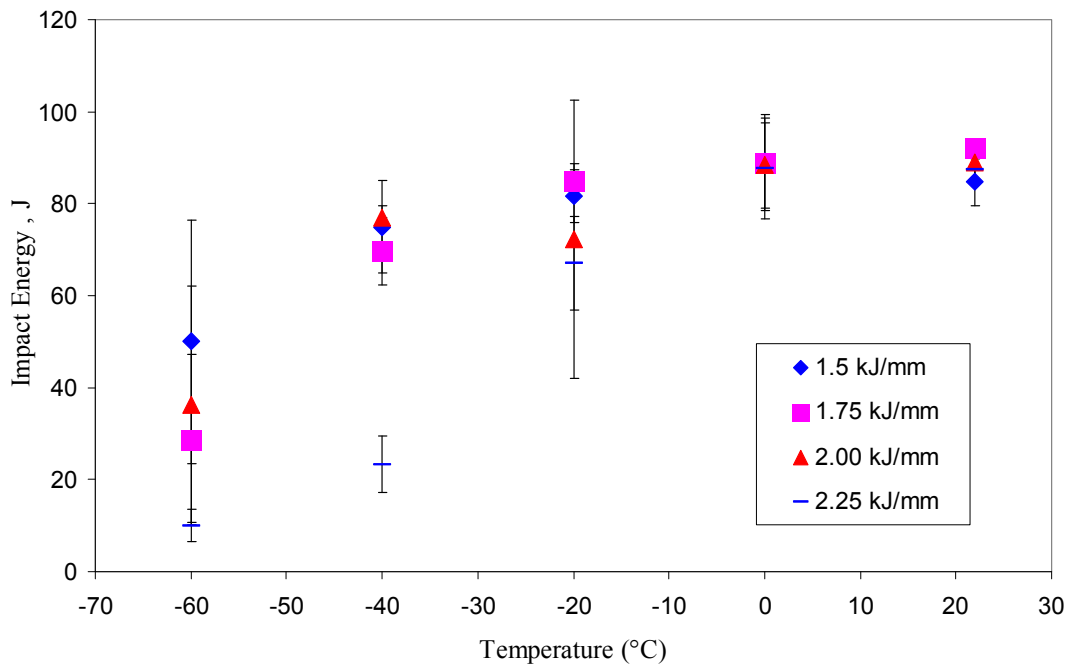


Figure 5-20: Sub-size toughness values for different heat inputs - Steel Y with tandem welds.

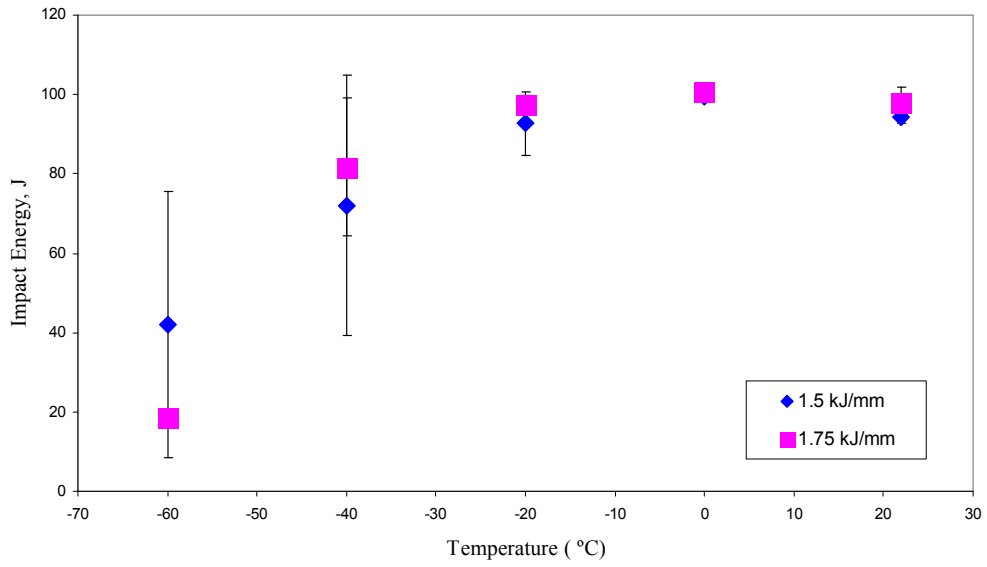


Figure 5-21: Sub-size toughness values for different heat inputs - Steel X with single pass.

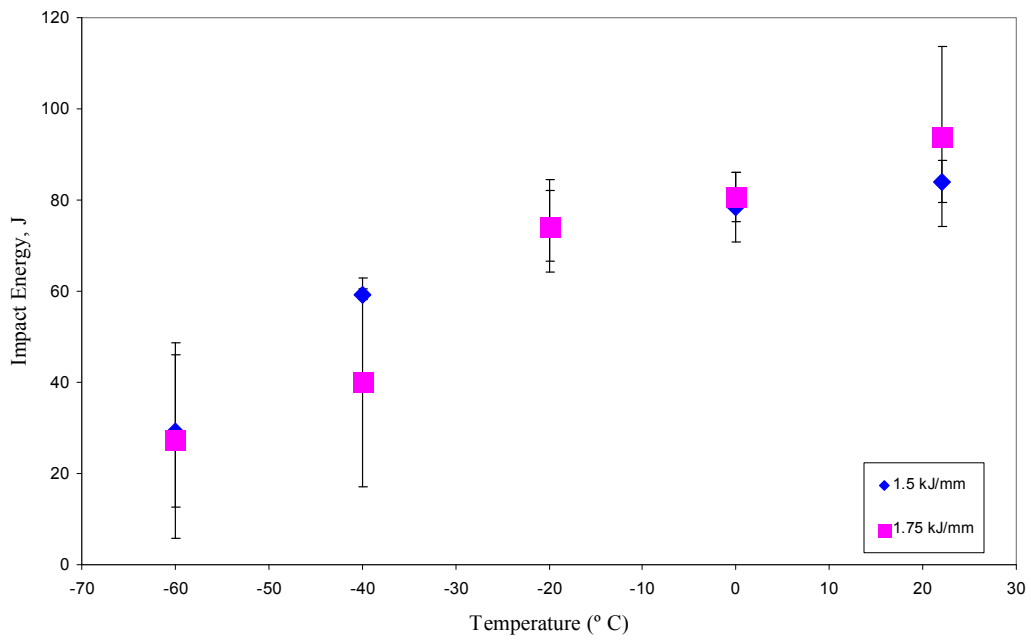


Figure 5-22: Sub-size toughness values for different heat inputs - Steel Y with single pass.

In Figure 5-18, it is clear that the overall toughness values for Steel X are higher than those for Steel Y (not the welds) found from the sub-size Charpy testing. A similar trend was also found for the full size specimens. The impact values are higher, however, compared with the values found for sub-size specimens tested under similar conditions. Full size specimens have larger cross section area compare to sub size specimens; hence a crack propagating through the material needs more energy for full size specimens than sub size specimens. This result was somewhat unexpected as Steel X has double the carbon content of Steel Y, while the compositions of the other alloying elements are about the same(steel Y having slightly higher amount of Nb, Ti, Mo and Mn). In addition, steel processing was the same for the two steels, except for the coiling temperature. Steel Y has a 30°C higher coiling temperature than steel X. These factors will affect the amount of fine precipitates present in the steel and hence affect the toughness properties. [Hiroshi, 2006]. Having lower carbon content and more fine precipitates would result in Steel Y having better toughness. However, our toughness results were not evident of this fact. The precipitate size and distribution could be partially responsible for the toughness difference. A detailed precipitate analysis was carried out using TEM and is discussed in Section 6.1.1.

From Figures 5-19 to Figures 5-22, it can be seen that Steel X welds were found to have better toughness than steel Y welds; ranging from 15 to 65 joules (for both single and tandem electrode welds) for the welding conditions at all test temperatures (22°C, 0°C, -20°C, -40°C and -60°C). The toughness values for single electrode welds (welded using 1.5 kJ/mm and 1.75 kJ/mm heat inputs) for both the steels are quite similar. A general expectation that higher heat input will yield lower toughness is not evident here (Figure 5-21 and Figure 5-22). One possible explanation is that the two heat inputs (1.5 kJ/mm and 1.75 kJ/mm heat input) are fairly close, so there is very little difference in the Charpy values. However, at lower temperatures (-60° C and -40°C) there are some differences, which will be discussed later. Also for tandem electrode welds, at higher temperatures the toughness values are quite close (Figure 5-19 and Figure 5-20).

At lower temperatures, the error bars are larger for specimens welded using both single and tandem electrodes. It was observed that at very low temperatures there were both ductile fracture regions and brittle fracture regions within the same sample (Figure 5-23). For samples with both ductile and brittle regions, the toughness values were more likely governed by the amount of ductile and brittle regions. Samples with larger brittle regions yielded lower toughness values. On the other hand, samples (tested under similar conditions), which had smaller brittle regions, yielded higher toughness values. For example, one sample of specimen A (Steel X welded using a 1.5 kJ/mm heat input) tested at -40°C gave a toughness value of 86 J, while another sample of the same specimen tested at -40°C gave a toughness value of 35 J. Upon visual examination of the fracture surface, it was evident that the tougher sample had more ductile regions (dull gray region). The lower toughness sample had a larger brittle region (shiny appearance). In Table 5-3 Charpy energy values with their respective % shear area is shown for sample A (Steel X welded using a 1.5 kJ/mm heat input) tested at -40°C. A1, A2 and A3 are the three samples that were used to determine toughness values for sample A tested at -40°C. Percent shear area was measured by using ASTM A370 standard [ASTM, 2003].

Table 5-3: Measured % shear area with their respective impact energy for sample A (Steel X welded using a 1.5 kJ/mm heat input) tested at -40°C

Sample Identification	Impact energy, J	Shear area (%)
A1	86	100
A2	100	100
A3	35	20

SEM fractographs further confirmed the presence of ductile and brittle regions on the fracture surface of samples welded and tested under similar conditions. In Figure 5-23, the fracture surface of sample K - Steel Y welded using a 2.0 kJ/mm heat input - tested at

-40°C is shown. Most of the fracture surface is ductile in nature, but part is brittle (less than 20% of the area). The brittle region was found at the opposite end of the machined notch. A similar fractograph was found for Sample C – (Steel X welded using a 2.0 kJ/mm heat input) tested at -40°C. Both ductile and brittle regions were found in the broken Charpy specimen (Figure 5-24 and Figure 5-25). Again, most of the fracture surface was ductile; only a small portion (around 5% area), which lies on the opposite side of the machined notch position, was brittle in nature.

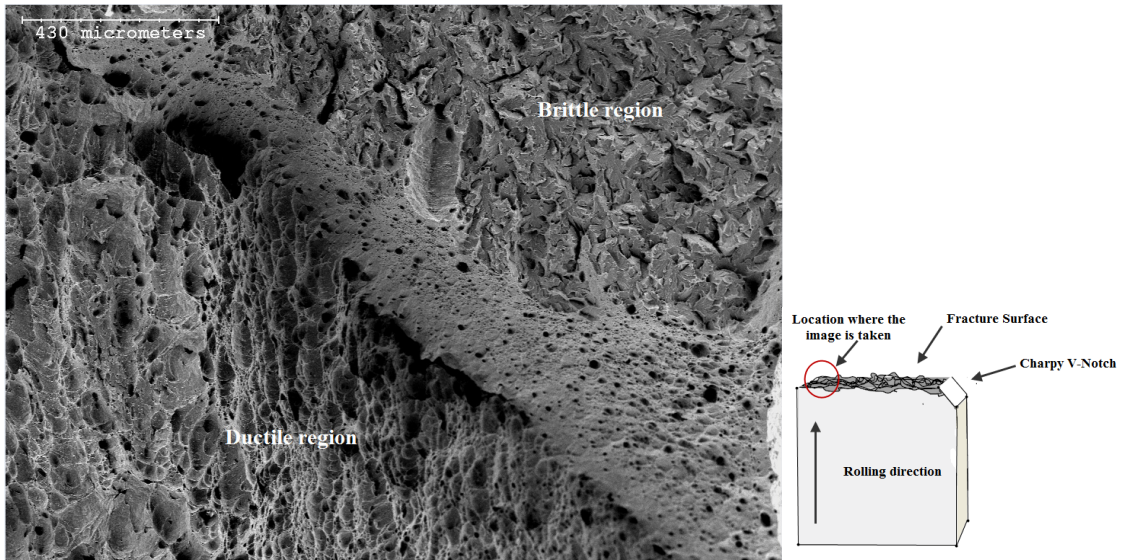


Figure 5-23: SEM SE image of the fracture surface for Sample K (steel Y welded using 2.00 kJ/mm heat input), showing both ductile and brittle regions. The sample was tested at -40°C. The image was taken from the end portion of crack growth.

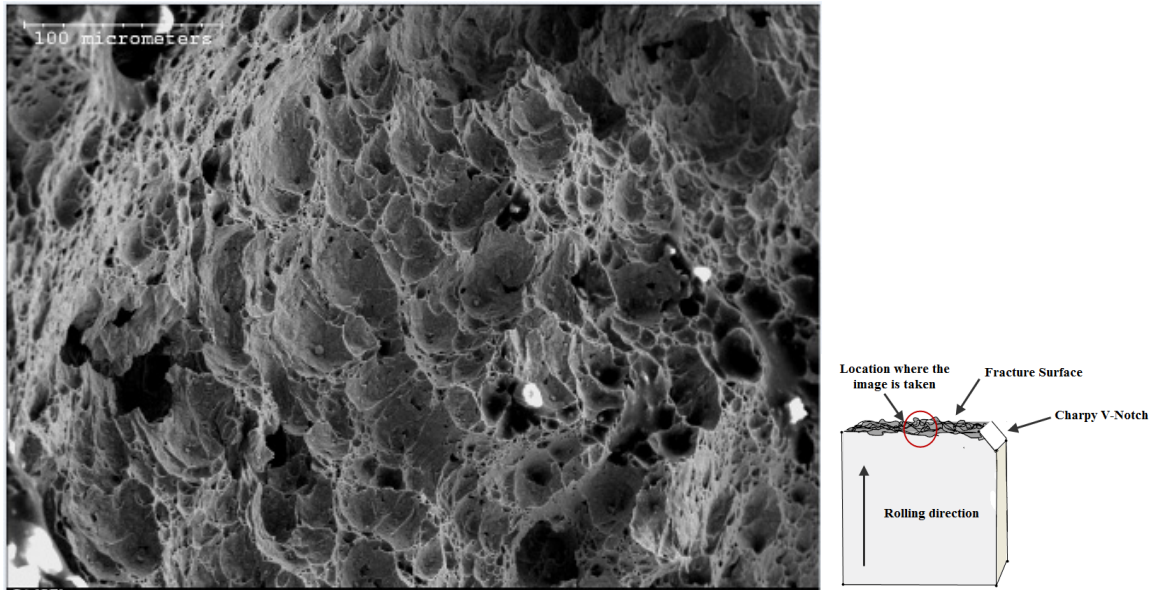


Figure 5-24: SEM SE image of the fracture surface for sample C (steel X welded using 2.00 kJ/mm heat input) tested at -40°C – ductile fracture. The image was taken from the mid portion of crack growth.

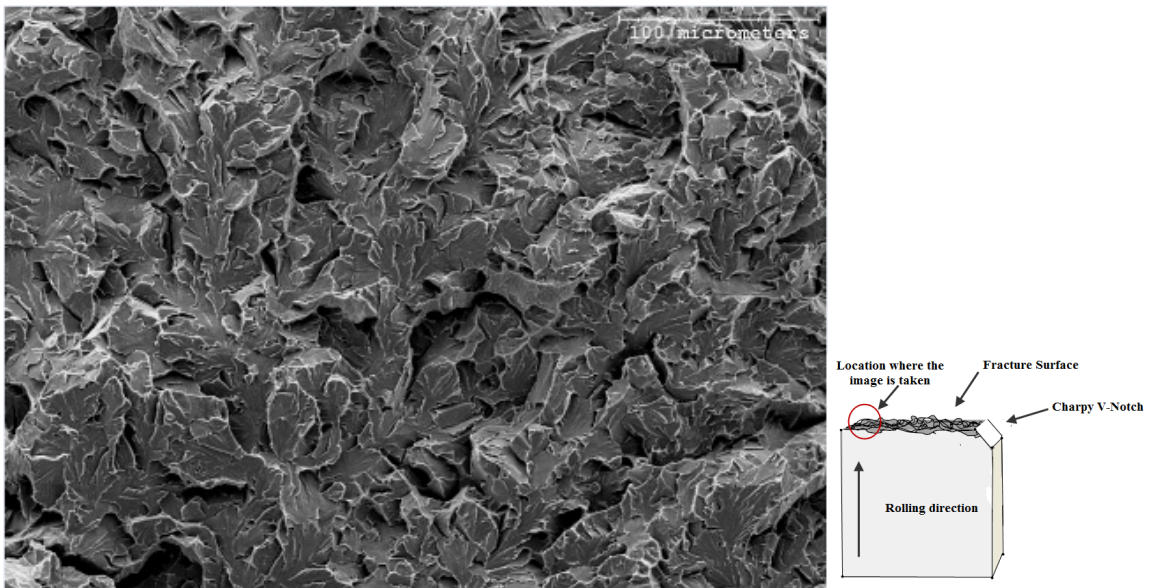


Figure 5-25: SEM SE image of the fracture surface for sample C (steel X welded using 2.00 kJ/mm heat input) tested at -40°C – brittle fracture. The image was taken from the end portion of crack growth.

The above two samples (sample K and sample C) produced impact values of 76 J (sample K) and 92 J (sample C), respectively. It was also found that there were localized ductile zones inside the brittle region, which were not discernable to the naked eye, making it impossible to measure the actual amount of brittle and ductile regions from the fracture surface (Figure 5-26).

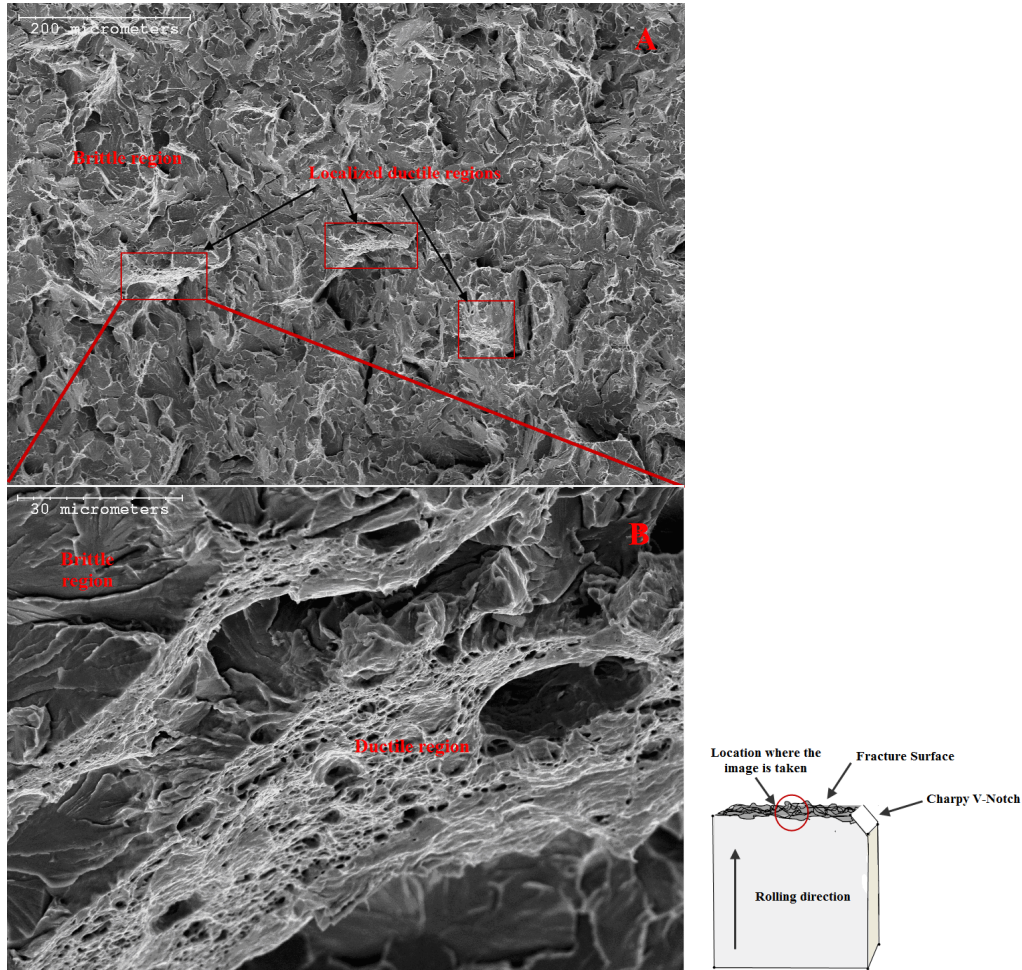


Figure 5-26: A) SEM fractograph showing localized ductile zones (red boxes) inside the primarily brittle region, found in sample C (Steel X welded using 2.00 kJ/mm heat input) and tested at -40°C . B) higher magnification fractograph of one such zone clearly showing ductile region.

It was evident by visual inspection, as a rough estimate, that sample K (Steel Y welded using 2.00 kJ/mm heat input) had a larger brittle region than sample C (Steel X welded using 2.00 kJ/mm heat input) tested at -40°C . For this reason, at lower temperatures there

are larger error bars, as it is possible to have varying amounts of brittle regions in specimens tested under similar conditions. A similar argument can be given to explain the differences found in single electrode welds at lower temperatures. The reason for the varying amounts of ductile and brittle regions in samples tested under similar conditions will be explained in the next section (Fractography - Section 5.3.1).

Careful observation of Figure 5-18, Figure 5-19 and Figure 5-20 indicates that, in some cases, the base metal impact values are lower than the impact values of the welded CGHAZ region. This is surprising at first glance, because the base metal toughness is generally expected to be higher than the CGHAZ toughness. For example, the toughness of Steel X tested at 22°C was found to be 99 J (one sample), while the CGHAZ toughness of sample B (Steel X welded using a 1.5 kJ/mm heat input and tested at 22°C) was 106 J. This apparent surprising result can be explained in terms of the notch placement and propagation during testing. In all cases the notch was placed in the CGHAZ region; however, the crack did not always go through that region. Instead, for welded samples with higher impact toughness values (relative to the base metal), the crack did not go through the CGHAZ region; instead it propagated through the weld metal region. This is shown schematically in Figure 5-27. This deviation in the crack propagation was confirmed by measuring the bead width of the samples broken at -60° (in a brittle nature). It was not possible to confirm this for samples tested at higher temperature, but similar crack deflection behavior was also expected in those samples.

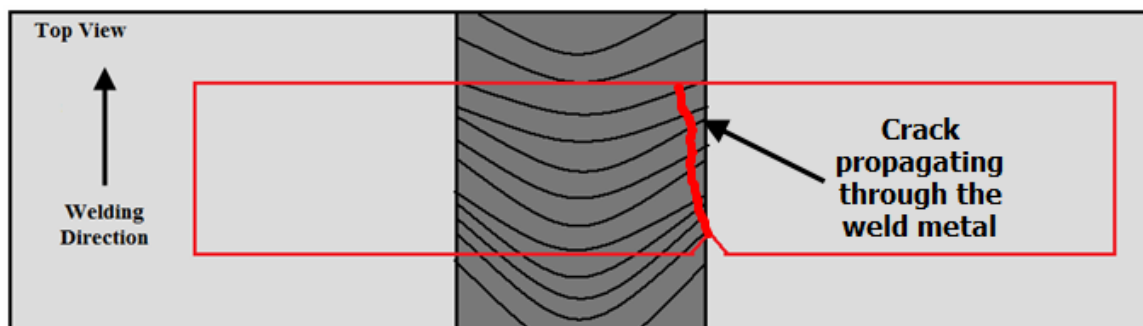


Figure 5-27: Schematic showing crack propagating through the weld metal instead of the CGHAZ region.

A similar argument can be made for impact values found for different heat inputs. As expected, higher heat inputs should yield lower toughness, but in most of the cases, it was found that the toughness values were similar, particularly for tandem electrode welds tested at higher temperatures. Optical images of the notch location for the full size Charpy specimens of base metal samples showed the presence of cracks (Figure 5-28).



Figure 5-28: Full size Charpy notch location showing a pre-existing crack (indicated by the red box). The specimen is Steel X. Steel Y also had these types of cracks.

The cracks were generated during the notch placement using a broaching machine. The presence of pre-existing cracks in the notch location is likely to affect the Charpy test and, hence, the toughness values. The pre-existing cracks affected the propagation of the final crack. Although the cracks were found in the notch location of the full size Charpy samples (used to measure base metal toughness), it is believed that the sub-size Charpy samples (both welded specimens and base metals) also had these types of pre-existing cracks. Sub-size Charpy notch locations were not observed with an optical microscope. Both sub-size and full size Charpy samples notches were produced in a similar manner (using a broaching machine). This uncontrolled phenomenon, occurring during notch placement, affected the toughness results. Because of the location of the notch position

(Figure 3-14) and the presence of pre-existing cracks, it is likely that the Charpy fracture energy values represent the toughness of several microstructural regions (WM to BM), rather than the CGHAZ region, which was the intended region for this study.

5.3.1 Fractographs

By observing the fracture surface, it was evident that Charpy specimens tested at higher temperatures failed by ductile fracture (Figure 5-29). Crack growth was essentially by a process of void coalescence. In this process, as the structure is loaded, local strains and stresses at the crack tip become sufficient to nucleate voids [Anderson, 1994]. These voids are created at second phase particles (Ca-rich and/or Ti-rich particles), either by interface decohesion or particle cracking. In the fractographs, many of these particles are found to be trapped in the voids. The voids grow around the particle as the crack blunts and later links with the main crack. The process continues and the crack grows. Figure 5-30 schematically illustrates microvoid initiation, growth and coalescence, while Figure 5-31 shows trapped particles inside dimples.

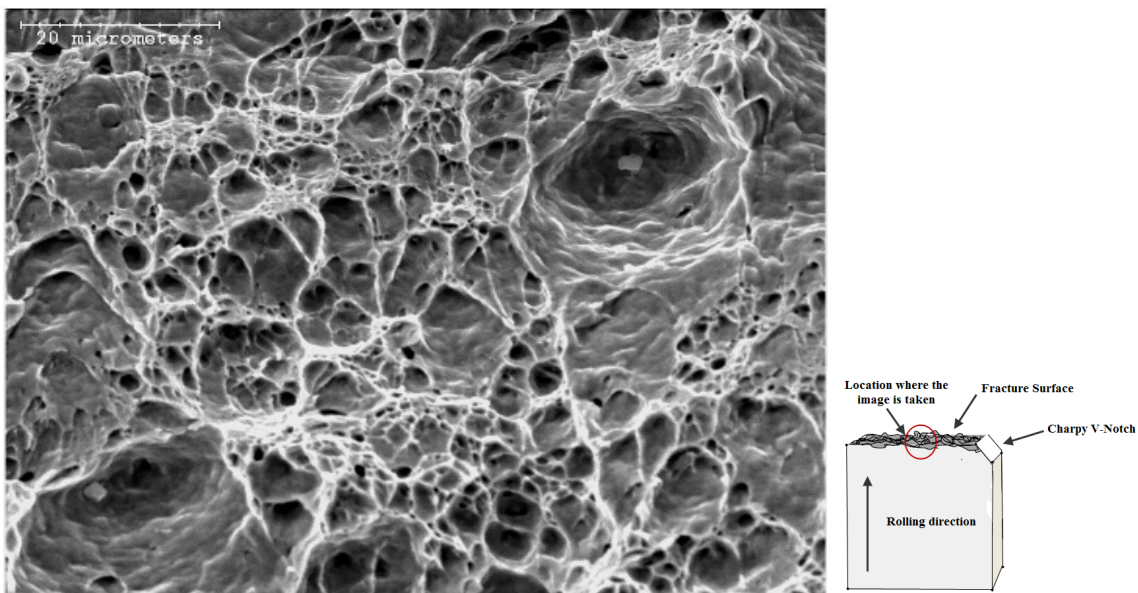


Figure 5-29: SEM SE image of Sample C (Steel X welded using a 2.00 kJ/mm heat input) tested at 22°C showing ductile fracture.

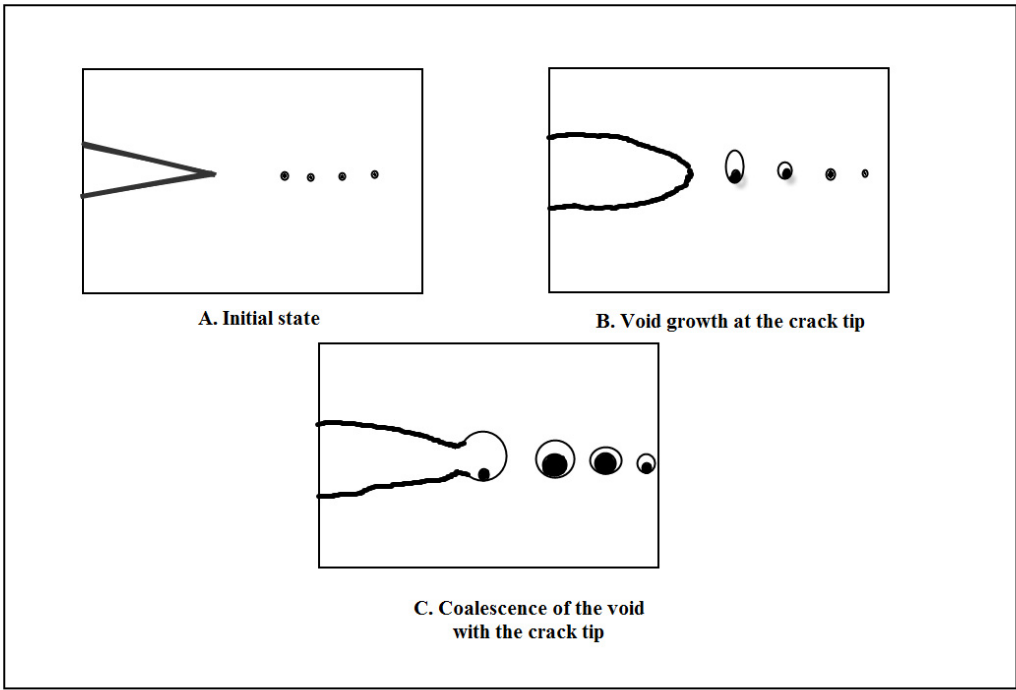


Figure 5-30: Mechanism for ductile crack growth. Based upon original images from [Anderson, 1994].

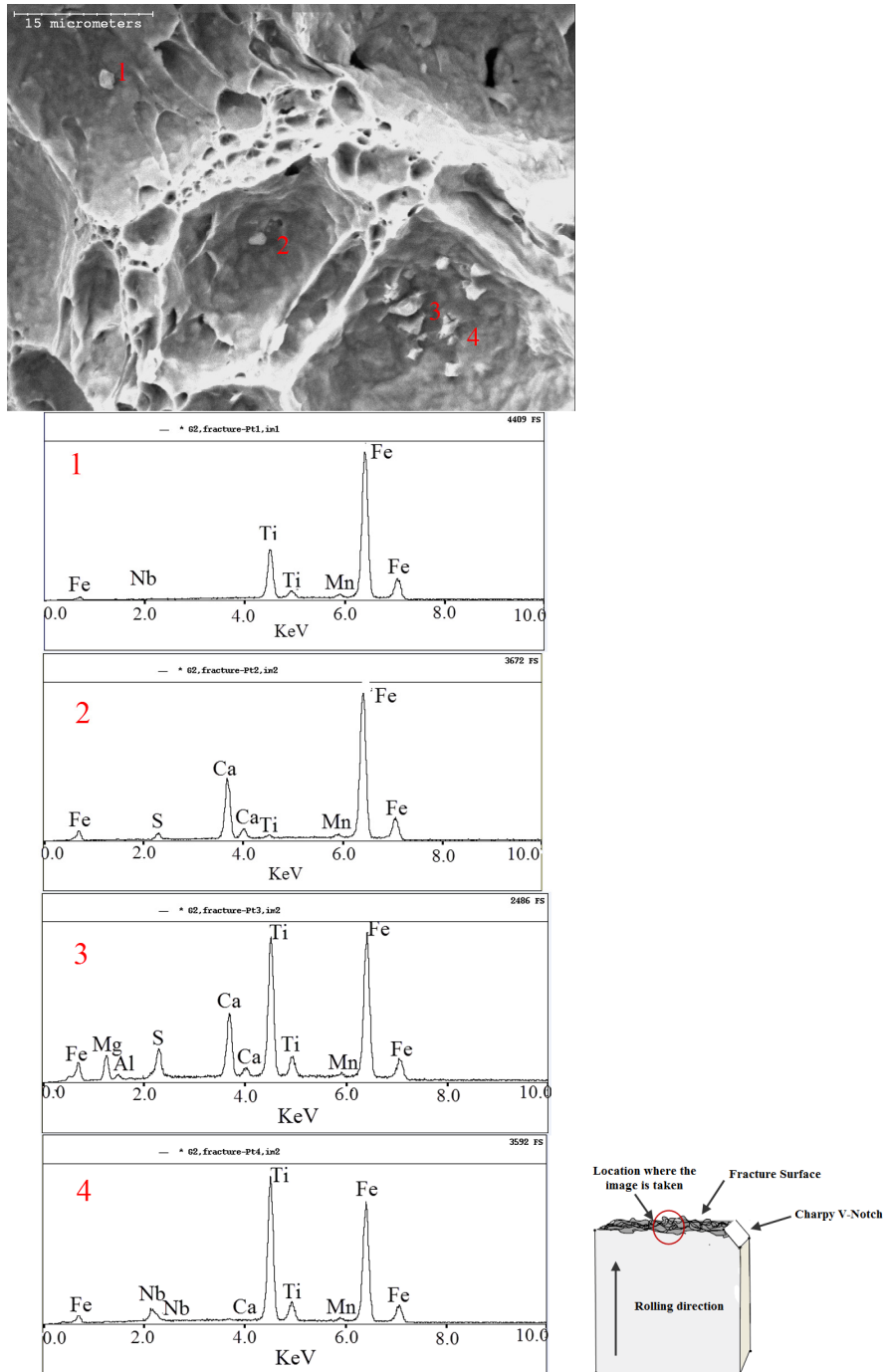


Figure 5-31: SEM SE image of Ti- rich and Ca-rich particles trapped inside dimples. Corresponding EDX analysis is shown as well. The image is from sample G (Steel X - 1.75 kJ/mm) tested at -20°C.

In all the broken Charpy specimens, for both Steel X and Steel Y, large TiN particles were found. Figure 5-32 shows one such example.

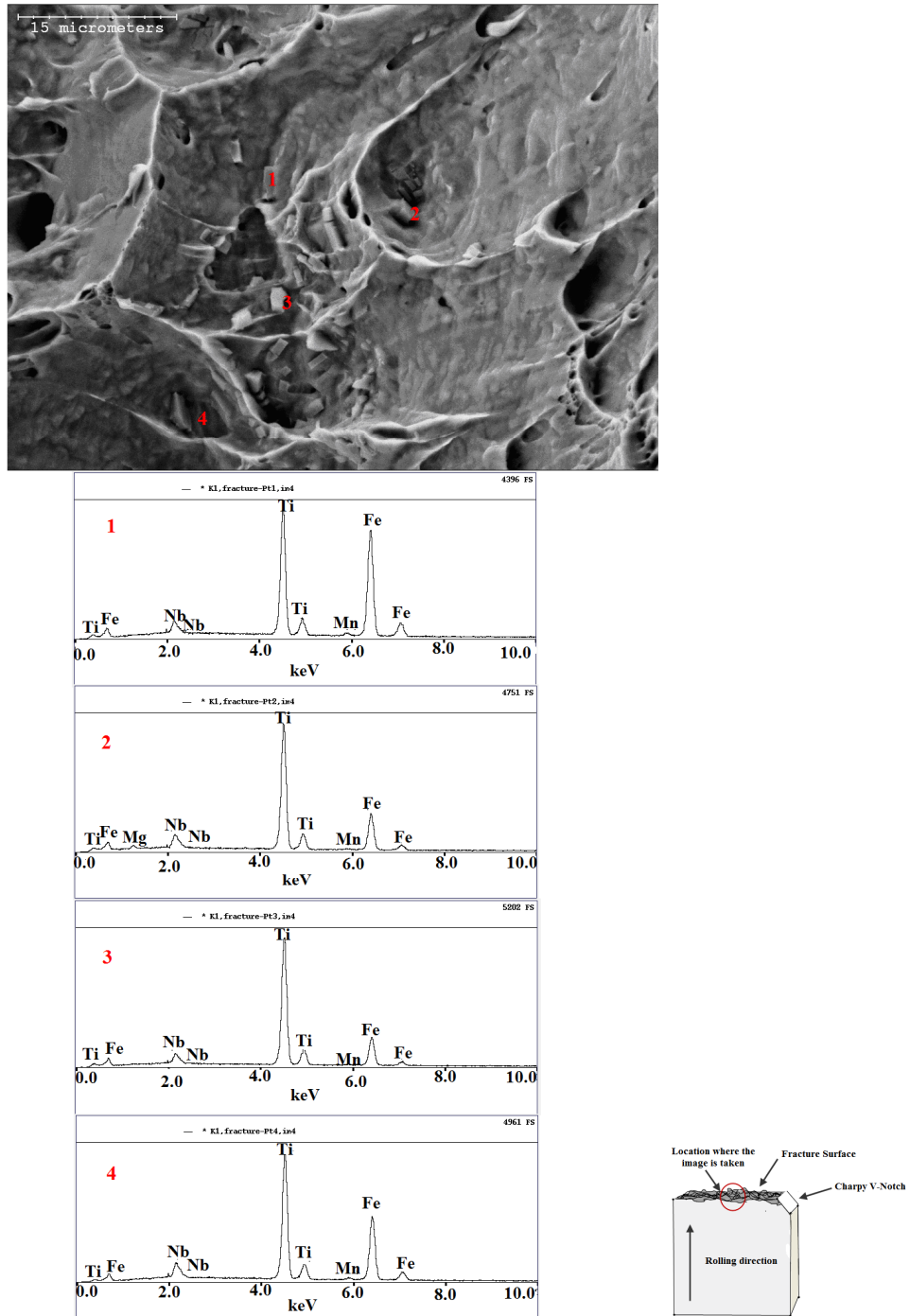


Figure 5-32: SEM SE image showing large broken Ti-rich particles found in sample K (steel Y - 2.00 kJ/mm heat input) – tested at -40°C. EDX spectra from the particles indicated are also shown.

It is believed that the Ti-rich particles were initially much larger in size, but fractured due to impact. Figure 5-33 shows an example where the broken particles are still in close contact. These particles contributed to void formation. The broken particles also produced microcracks, which play an important role in the toughness behavior of materials as discussed later.

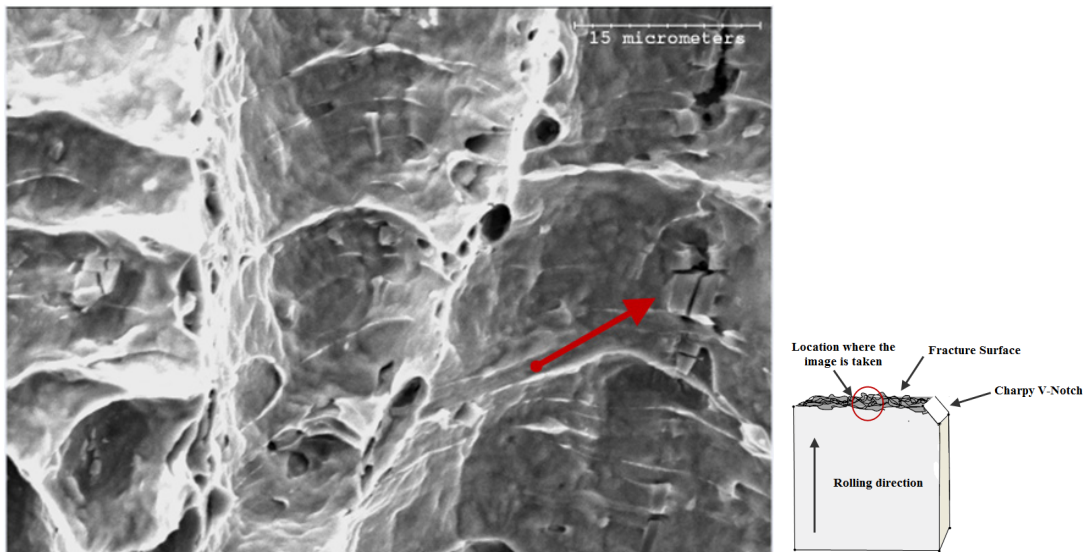


Figure 5-33: SEM SE image of a fracture surface showing a broken Ti-rich particle indicated by the red arrow - sample C (Steel X welded using 2.00 kJ/mm heat input) tested at -40°C .

Smaller Ti-rich particles can effectively act to pin grain boundaries and are beneficial for the steel [Chen, 1987]. However, larger particles cannot resist grain boundary motion. During welding, small Ti-rich particles are dissolved in the steel in HAZ regions, due to the very high temperature around 1300°C . However larger particles (particles larger than $27\ \mu\text{m}$) are not dissolved and remain in the steel. These larger particles have no contribution to grain boundary pinning and they tend to decrease the toughness of the steel [Lau, 1987]. Again, not only the size of the Ti-rich particles matters for resisting grain boundary motion, their distribution also plays an important role. Hence, large particles contribute negatively (decrease the toughness) to the impact energy, due to their size.

5.3.1.1 Effect of Variables on the Fracture Mode

At very low temperatures ($\sim -60^{\circ}\text{C}$), the fracture surface was predominantly brittle in nature. As mentioned earlier, there are both ductile and brittle regions in samples tested at -40°C . Figure 5-34 shows one such example, where the fracture surface is mostly brittle.

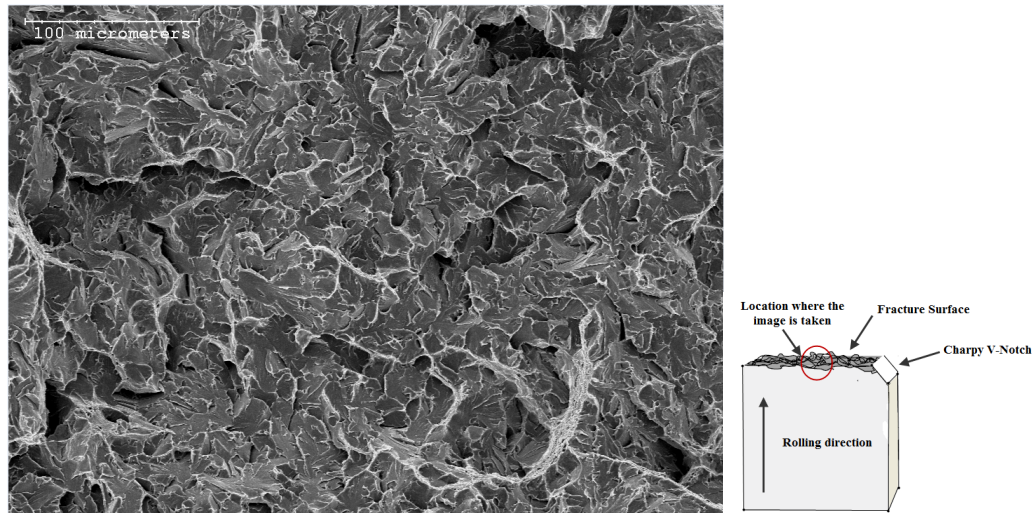


Figure 5-34: SEM SE image of Sample J (Steel Y welded using 1.75 kJ/mm heat input) tested at -60°C , showing brittle fracture.

It is worth noting that the key factors that contribute to brittle fracture are:

- a.) Temperature;
- b.) Dislocation density;
- c.) Grain size.

Temperature is the most important factor. At lower temperatures, the vibrations of atoms in a metal decrease. If a stress is applied, these atoms are not able to slip to a new location and form new bonds, which decreases the amount of slippage and allows for little (or no) plastic deformation [Anderson, 1994] [Dieter, 1988]. This can lead to brittle fracture. Most BCC metals fail by cleavage because there are few active slip systems at low temperatures. However, FCC metals have enough slip systems for ductile behavior, which is why they are not susceptible to cleavage type fracture.

Another important factor which contributes to brittle fracture is dislocation density.

When stresses are applied, the number of dislocations increases. These dislocations tend to pile up and it becomes increasingly difficult for them to move. Hence, the material fractures in a brittle manner [Anderson, 1994].

The last factor that contributes to brittle fracture is grain size. As the grain gets smaller, the dislocations have less space to move before they get stuck at the grain boundary. Since the dislocations cannot move very far, the slip distance is greatly reduced, which reduces the number of dislocations that can pile up [Anderson, 1994]. It should be noted that metals are tougher if the grain size gets smaller.

The process of cleavage fracture is considered to be made up of three steps. These are:

- a) Plastic deformation to produce dislocation pile ups;
- b) Crack initiation;
- c) Crack propagation.

It should be noted that the cracks, which are responsible for brittle type fracture, are not present initially in the material; rather they are produced during the deformation process.

The initiation of microcracks is influenced by the presence and nature of second phase particles. During deformation these particles, which are brittle in nature themselves, crack. Resistance to cracking improves if the particles are well bonded to the matrix. Some smaller particles (with radii $<1 \mu\text{m}$) and also some round shaped particles are more resistant to cracking. The small impenetrable second phase particles greatly reduce the slip distance and hence decrease the number of dislocation pile ups. On the other hand, larger and irregular shaped particles (such as Ti-rich particles) will eventually be cut by the cracks and more microcracks will be generated, which will create large dislocation pile-ups. This will lead to high stresses, easy initiation of microcracks and brittle behavior. Figure 5-35 shows this schematically. It is a well established fact that metals which completely fail in a brittle manner also have undergone some plastic deformation initially [Anderson, 1994]. This initial plastic deformation produces sufficient dislocations, which will eventually cut through the larger, loosely bound second phase particles. When these

large second phase particles crack, they will produce microcracks, which will cut through more second phase particles in front of them. This results in microcrack initiation and will produce large dislocation pile-ups. For this reason some of the broken Charpy samples initially broke in a ductile manner, but during the last stage of crack propagation they broke in a brittle manner. Sample K (Steel Y welded using a 2.0 kJ/mm heat input) (Figure 5-23) is one such example, where the ductile regions were found initially near the notch location, but at the opposite side of the notch brittle fracture occurred.

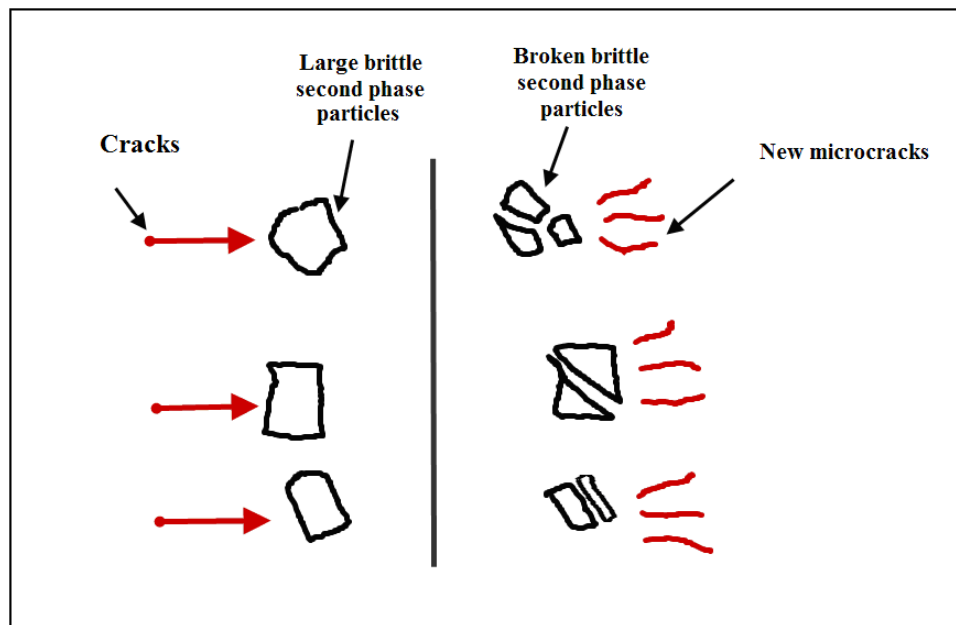


Figure 5-35: Schematic diagram showing initiation of microcracks from broken second phase particles.

The amount and distribution of the second phase particles also play an important role. The more second phase particles present in the material, the more likely it is that microcracks will be produced, which will lead to dislocation pile-ups, promote brittle fracture and decrease the toughness of the material [Anderson, 1994]. In both steels (Steel X and Steel Y), large brittle particles (Ti-rich particles) were present and these particles contributed to producing microcracks and, hence, by producing brittle fracture affected the toughness values.

5.4 Summary

In this chapter results obtained from the mechanical properties of the base metals and the welded specimens were reported. The following can be summarized from this chapter:

Hardness traverses indicated that hardening occurs in the CGHAZ region and softening occurs in the FGHAZ region. The highest hardness was found in the weld metal region. Both the weld metal and CGHAZ region of the welded specimens were found to be harder than the base metals. The CGHAZ hardness increased as the heat input decreased. The hardness traverses of the FGHAZ region show very little dependency on the heat input values.

All transverse weld tensile test specimens broke in the base metal region, indicating that the welds have overmatched strength compared with the base metals. Since both the weld metal and the CGHAZ were harder than the base metals, the welds also showed higher strength than the base metals. Elongation was mostly dependent on the total weld metal volume produced by the OD and ID welds. The degree of overmatching (how much strengthening was provided by the weld metal and the HAZ individually) could not be resolved.

Charpy impact testing of the base metals showed that Steel X has better toughness than Steel Y, although the latter has lower carbon content. Steel X CGHAZ toughness values were found to be higher than Steel Y CGHAZ toughness. The CGHAZ toughness values of the welds (both steels) showed large error bars, particularly at lower temperatures. Varying amounts of brittle and ductile fracture were found to be responsible for the large error bars. SEM fractographs were further analyzed and different modes of fracture were studied. In the next chapter (Chapter 6) microstructural analysis will be discussed to establish relations with the mechanical properties.

Microstructural Analysis

In this chapter the effect of welding on the microstructure of both steels (Steel X and Steel Y) is examined. Both steels were initially examined in the as-rolled condition. After welding with different heat inputs, the weld HAZ, especially the CGHAZ and FGHAZ, was examined thoroughly. Microstructural changes due to the thermal effects of welding were studied using a combination of optical, SEM and TEM metallography. Correlation of mechanical properties with the microstructural analysis is also discussed.

6.1 As-Rolled Base Metal Microstructure

The microstructures of Steel X and Steel Y in the as rolled condition are shown in Figure 6-1 to Figure 6-4. These images were taken from the mid-section of the strip thickness. Parallel sides to the rolling direction were observed in the microscope. The grain sizes for these steels are reported in Table 6-1.

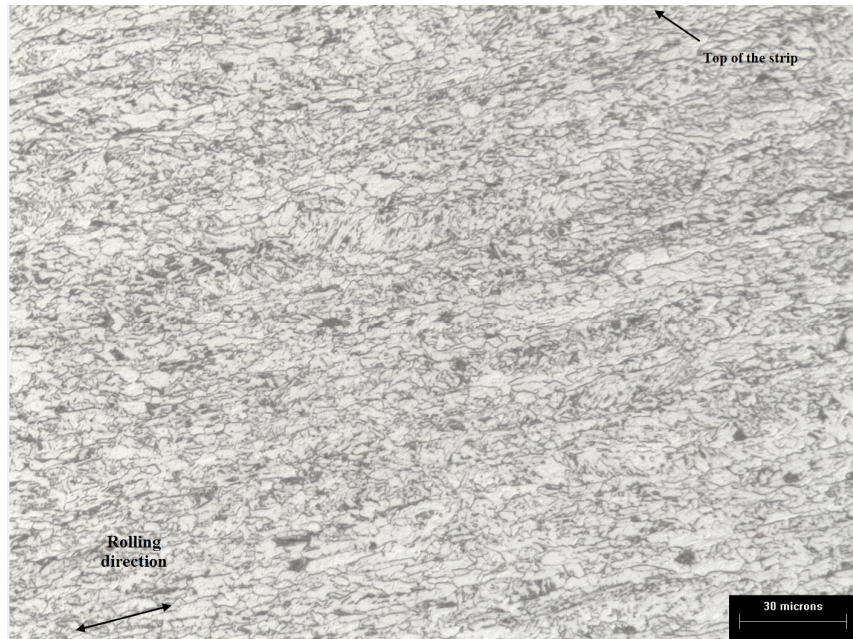


Figure 6-1: As rolled optical microstructure of Steel X.

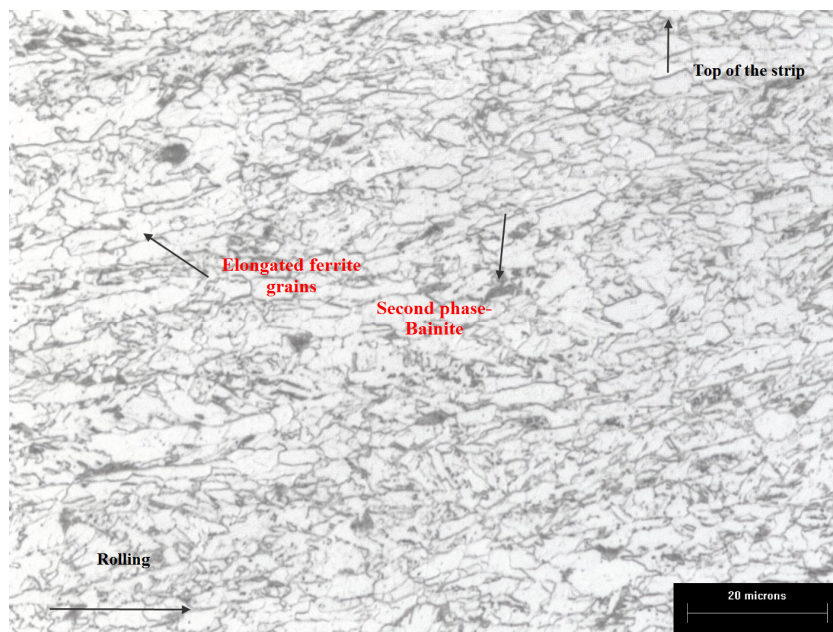


Figure 6-2: As rolled optical microstructure of Steel X (higher magnification).

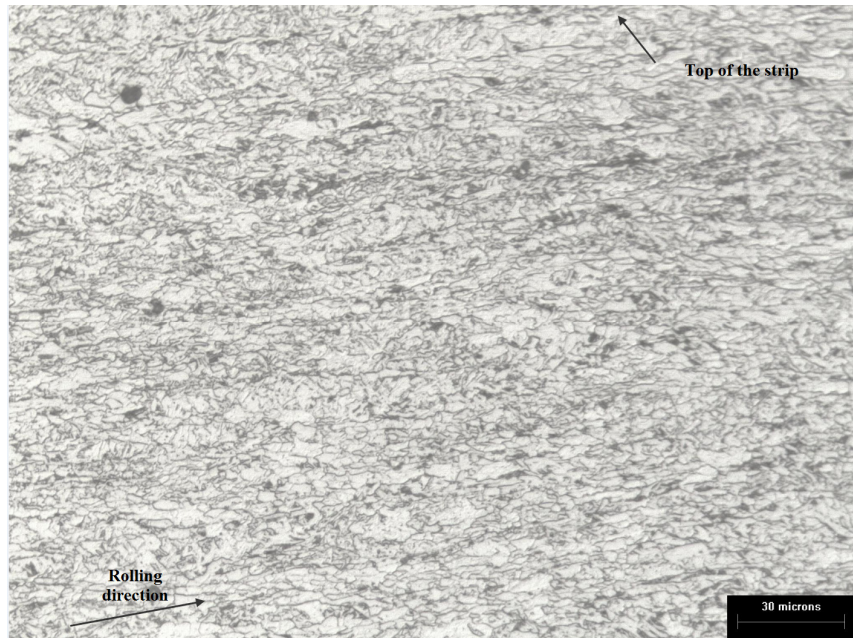


Figure 6-3: As rolled optical microstructure of Steel Y.

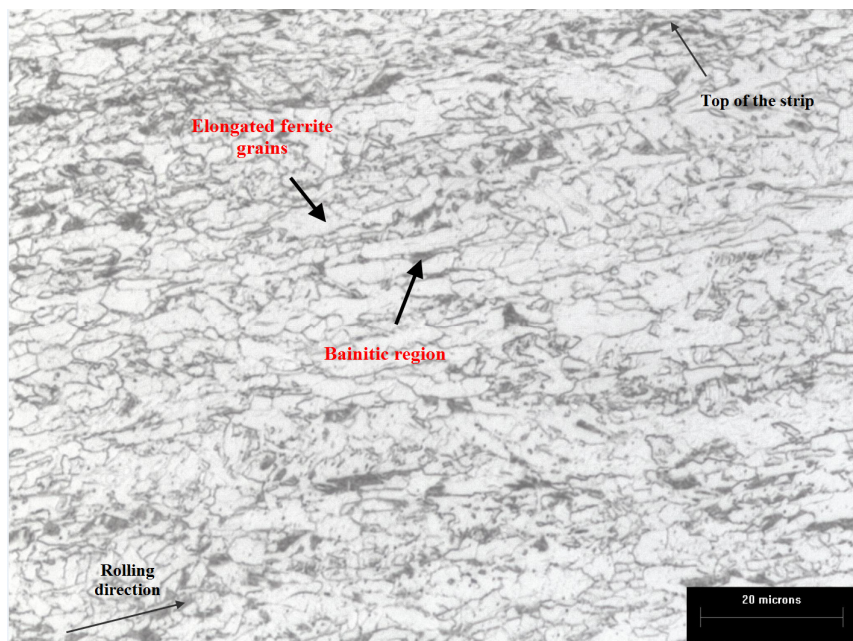


Figure 6-4: As rolled optical microstructure of Steel Y (higher magnification).

Table 6-1: Grain size of as-rolled base metals

Identification	ASTM Grain Size Number	Average Grain Diameter (μm)
Steel X	13	4.6 ± 1
Steel Y	13	4.7 ± 1

From Figure 6-1 to Figure 6-4, it can be seen that both steels have very similar microstructures, consisting of fine elongated ferrite grains (along the rolling direction). Note that the ASTM grain size number for both steels is similar. However, the average grain size area measured using Image J software (see Section 3.3.2) revealed slightly larger grains on average for steel Y. Calculated average grain size areas had large standard deviations. As such, the difference between the two steels is minimal.

It is assumed that the microstructure is mainly ferrite with an aligned second phase. Some researchers have identified similar microstructures as bainitic ferrite or upper bainite based on the optical micrographs [Ranasen, 1972] [Thaulow, 1985]. It is noted that due to the complexities of different terminologies that are used for bainitic structures (e.g., acicular ferrite/bainite, upper bainite, lower bainite and bainitic ferrite), some researchers prefer to generalize the term by using “ferrite with aligned second phase” [Mitchell, 1985]. The dark regions in the optical microstructures were observed with an SEM and were confirmed to be bainite. SEM images of the bainitic structure are shown for Steel X and Steel Y, respectively, in Figure 6-5 and Figure 6-6. The carbides can be seen in these images, as pointed out by the arrow. The amount of the bainitic regions was measured using image analysis software and was found to be $8.3 \pm .6\%$ in Steel X and $7.5 \pm 0.9\%$ in Steel Y. Also, modified Le Pera’s etch revealed that there is approximately $4.5 \pm 0.4\%$ M-A in Steel X and approximately $4.1 \pm 0.4\%$ M-A) in Steel Y (Figure 6-7 and Figure 6-8).

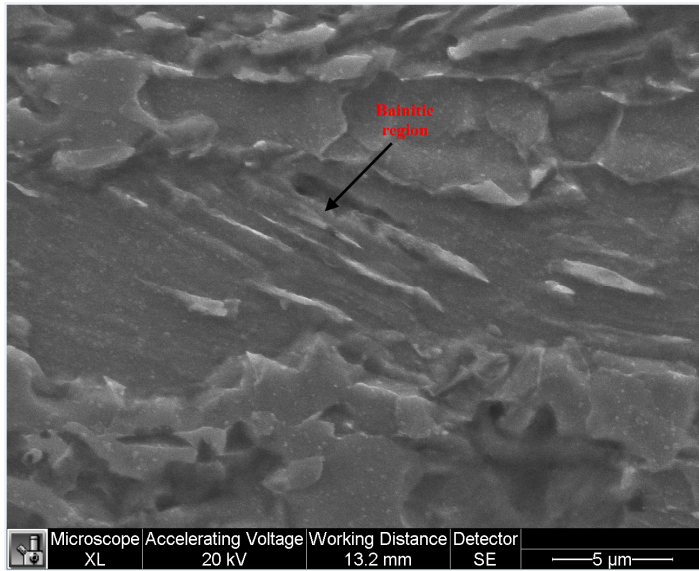


Figure 6-5: SEM secondary electron (SE) image of Steel X showing bainitic region.

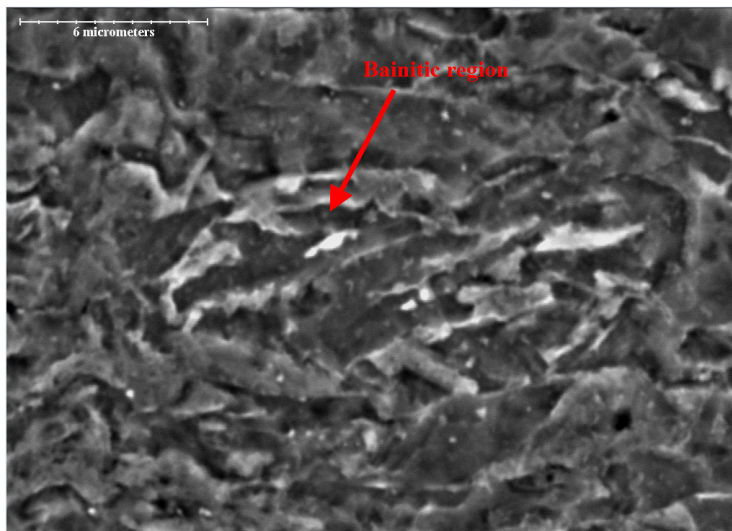


Figure 6-6: SEM SE image of Steel Y showing bainitic region.

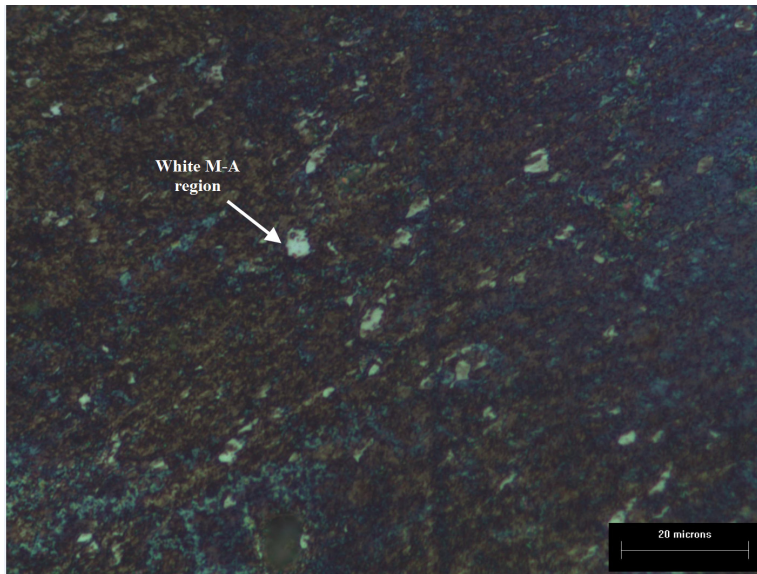


Figure 6-7: Optical micrograph of Steel X showing white M-A region; etched with Le Pera's solution.

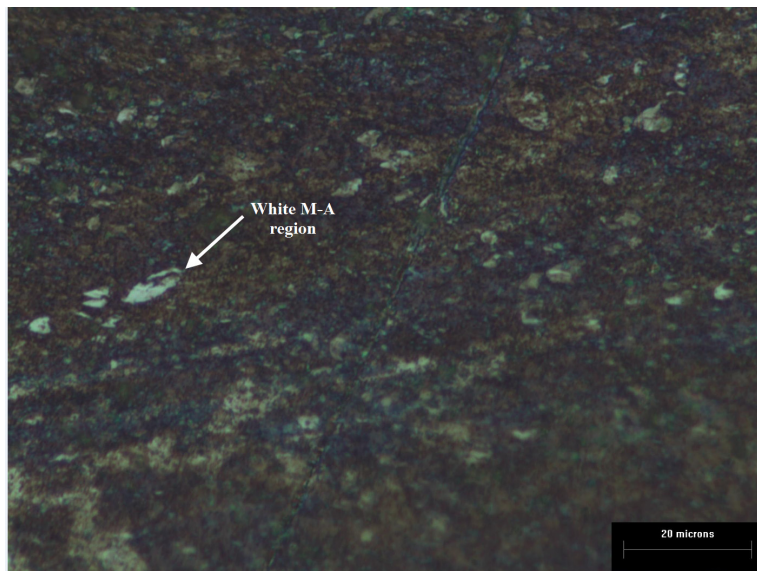


Figure 6-8: Optical micrograph of Steel Y showing white M-A region; etched with Le Pera's solution.

6.1.1 TEM Precipitate Analysis of Steel X and Steel Y

Precipitate analysis was carried out using TEM for both Steel X and Steel Y. The specimen preparation details for TEM were explained in Section 3.3.8.

Particles were counted and their sizes were measured using image analysis software (Image J). A total of 15 images, from each steel (at the same magnification), were analyzed to obtain a representative distribution of particles. Steel X had 473 intermediate size particles (particle sizes ranging from 10 to 250 nm), whereas Steel Y had 407 intermediate size particles (particle sizes ranging from 5 to 170 nm). TEM images from Steel X and Steel Y are shown in Figure 6-9. It is clear that the intermediate size particles are mostly round in shape. The round shaped particles are Nb-rich. Apart from having round shaped particles there were also some cuboidal shaped particles, which are Ti-rich. Figure 6-10 shows one such example where there are both round shaped Nb-rich particles and cuboidal shaped Ti-rich particles in Steel Y. Subsequent energy dispersive x-ray (EDX) analysis of points “a” (Ti-rich) and “b” (Nb-rich) from Figure 6-10 are shown in Figure 6-11. There are also some peaks found for other elements in the EDX analysis; i.e., Cu and Fe. Cu peak is coming from the Cu grid that was used. Also Fe peak is coming from the matrix.

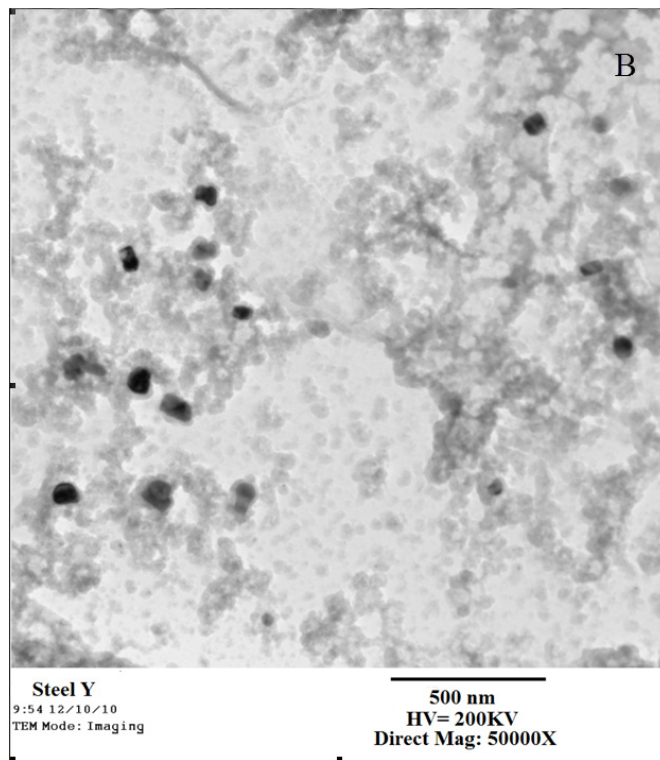
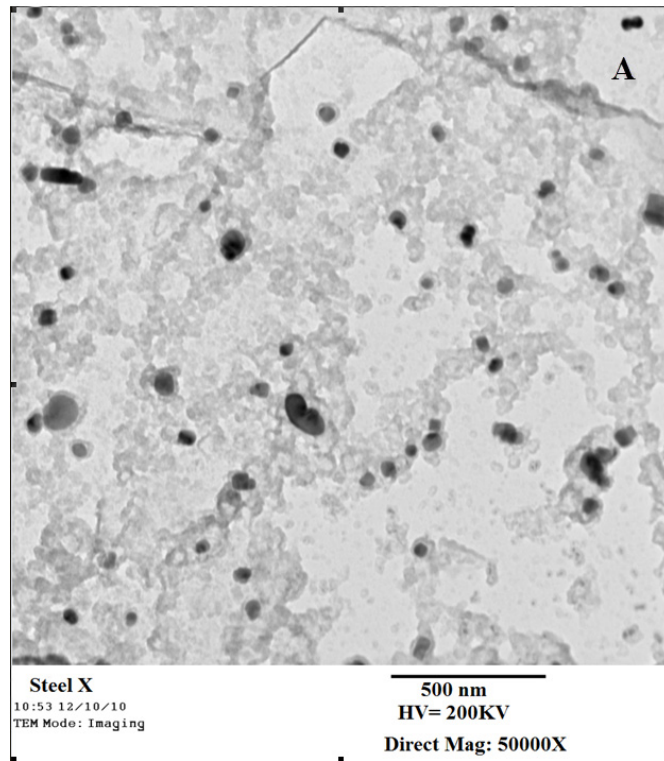


Figure 6-9: A) Representative TEM bright field (BF) images showing intermediate size particles in Steel X and B) Steel Y.

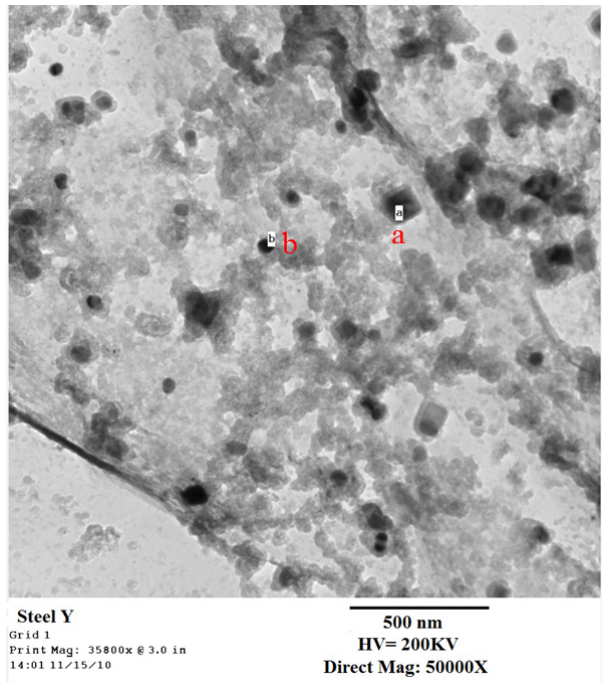


Figure 6-10: TEM BF image of Steel Y showing a cuboidal shaped particle (a) and a round shaped particle (b).

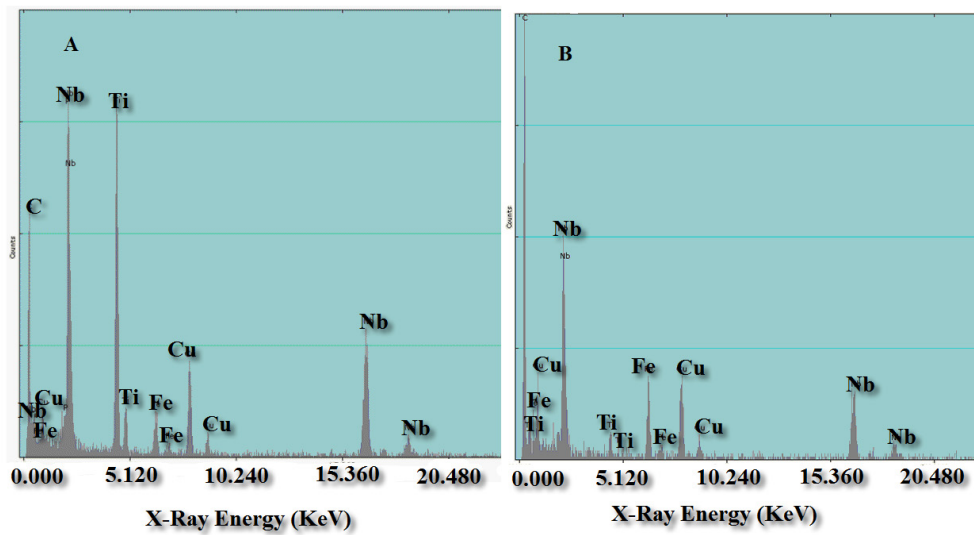


Figure 6-11: EDX spectra from point “a” (A) and point “b” (B) from Figure 6-10.

The Ti-rich particles are formed when the steel is still molten or during solidification. During solidification the Ti-rich particles heterogeneously nucleate on already existing sulphide inclusions [Medina, 1999] [Akhlaghi, 2002] (Figure 6-12). In Figure 6-12 (B), the EDX result showed that there is a Mo peak (L peak). Since the S-K peak overlaps with the Mo-L peak, it is believed that the Mo peak is actually an artifact, rather than the element is S. The EDX result has been corrected accordingly. There are also peaks coming from Mg and Mn (K peaks) indicating that these precipitates are actually mixed type in nature containing MgS and MnS along with CaS. The Ti-rich particles can also form in the solid state at very high temperature. Upon counting the cuboidal shaped particles for both steels (using 15 images for each), Steel X was found to have a total of 36 Ti-rich particles and Steel Y had 51 Ti-rich particles. Some Ti particles are also associated with Nb-rich particles (Figure 6-10). It is believed that these Nb-rich particles nucleated on existing Ti-rich particles. This observation is in good agreement with the solubility data, which shows that Ti-rich particles have a higher solubility temperature than Nb-rich particles [Narita, 1975]. Figure 6-13 shows an example where a Nb-rich (round shaped) particle nucleated on a Ti-rich (cuboidal shaped) particle.

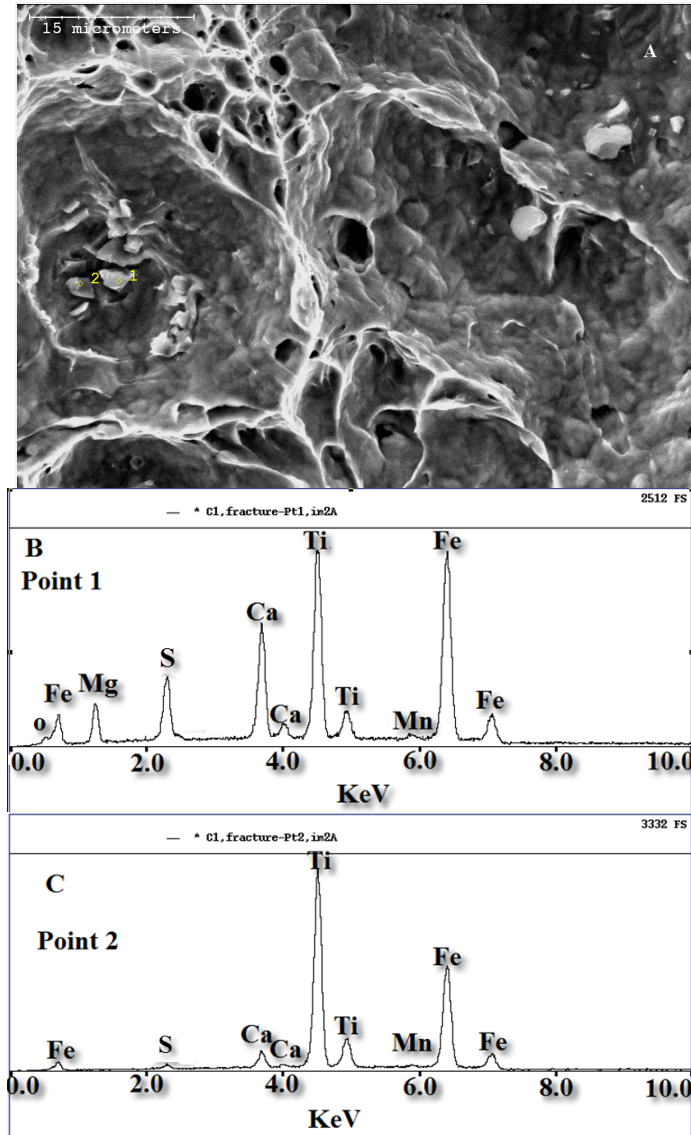


Figure 6-12: A) SEM SE image of fracture surface of Steel X showing points 1 and 2 where EDX analysis was carried out. B) EDX spectrum from point 1 in (a) showing a Ti peak along with a Ca peak. This Ca peak is most likely coming from a CaS inclusion. It is believed that the Ti particle heterogeneously nucleated on this Ca-rich inclusion during solidification. C) EDX spectrum of point 2 showing a Ti peak along with a S peak and Ca peak. The Fe peak is an artifact coming from the surrounding matrix.

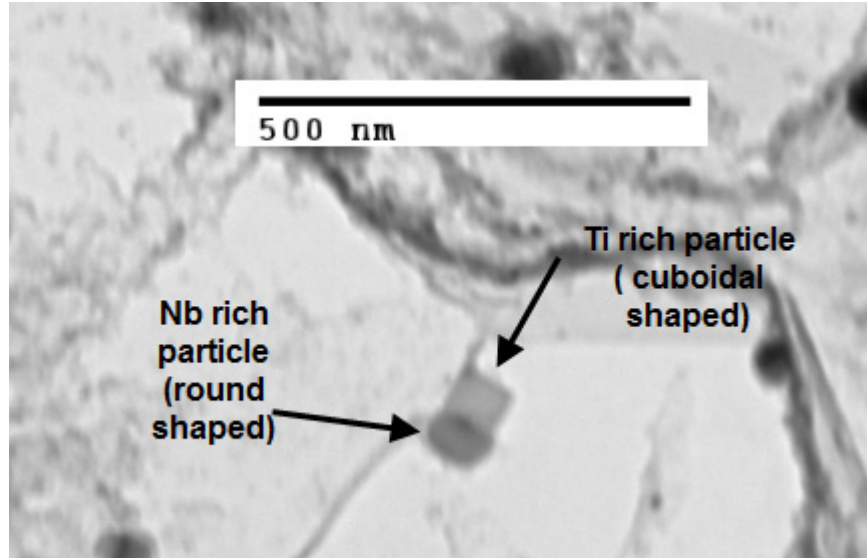


Figure 6-13: Intermediate size Nb-rich precipitate attached to a Ti- rich precipitate.

Some images (15 images from each steel) were taken at a much higher magnification. These images revealed very fine ($\sim 3\text{-}6$ nm) precipitates in the steels. Due to the extreme fineness, it was not possible to count them using image analysis software; rather a manual count was carried out based on area fraction. Steel Y had 45% more finer particles than Steel X. There were some regions in Steel X where there were very few particles, while other regions had many particles, depicting the uneven distribution of finer particles in Steel X compared with Steel Y. Steel Y had finer particles evenly distributed throughout the specimen. Some researchers [Akhlaghi, 2002] [Liu, 1993] have reported that fine Nb-rich particles in low carbon steel precipitate out in the temperature range of 500° to 700°C , which is the coiling temperature range of the current steels. It is believed that these precipitates grow in the ferrite matrix by an aging process [Akhlaghi, 2002]. TEM images at a higher magnification for Steel X and Steel Y, respectively, are shown Figure 6-14.

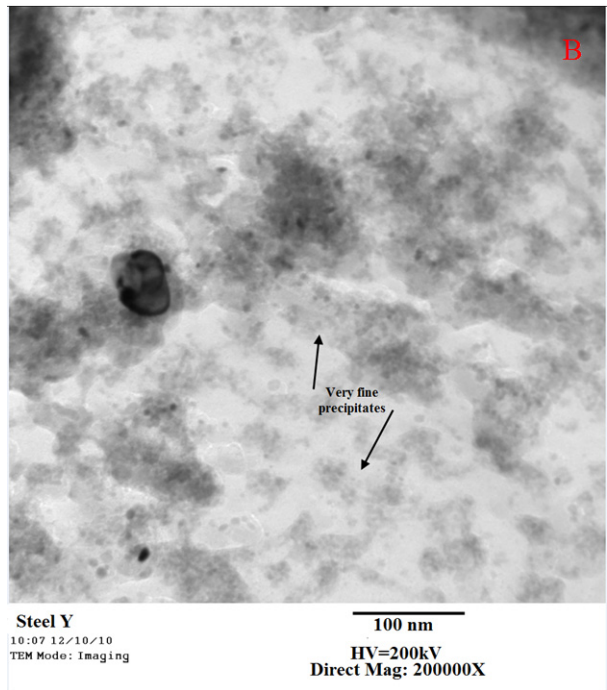
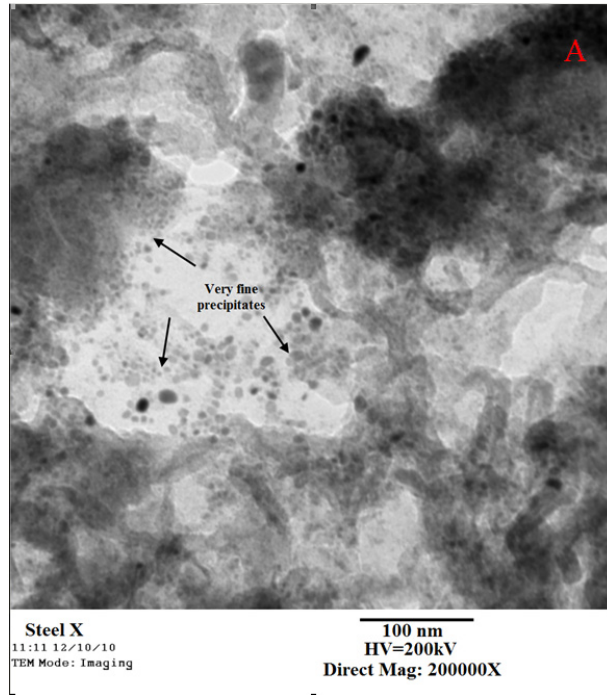


Figure 6-14: A) TEM BF images for Steel X and B) Steel (Y) showing very fine precipitates.

Selected area diffraction (SAD) patterns were obtained from the fine precipitate regions. Diffraction patterns from individual particles were not attainable, which is why a ring pattern was obtained from a cluster of particles. Representative SAD patterns are shown for Steel X and Steel Y, respectively, along with their corresponding regions in Figure 6-15 and Figure 6-16.

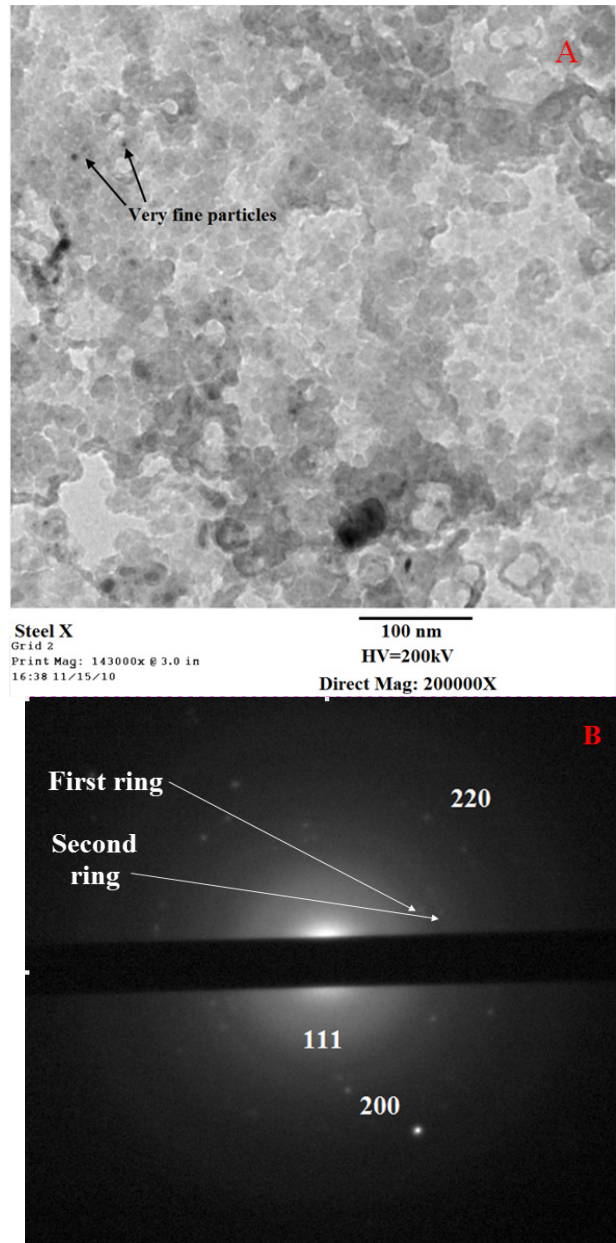


Figure 6-15: A) TEM BF image of Steel X showing fine particles and B) corresponding ring pattern obtained from the clustered region.

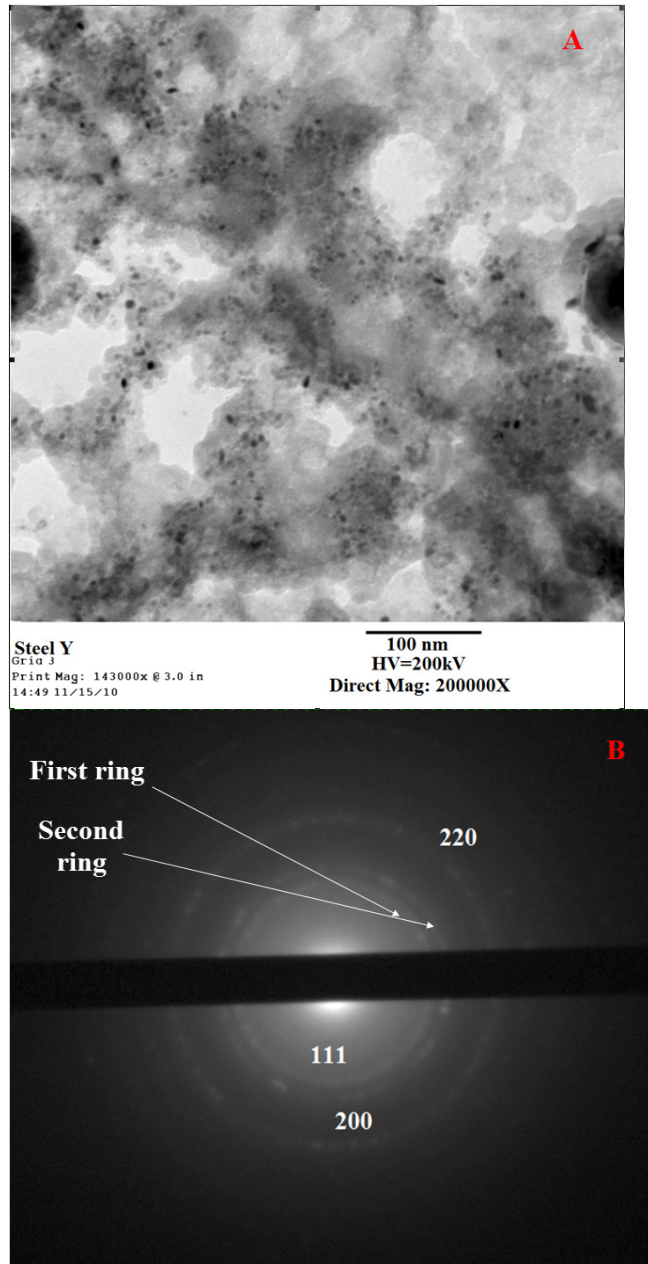


Figure 6-16: A) Region in Steel Y showing fine particles and B) corresponding SAD ring pattern obtained from the clustered region.

The lattice parameter for the ring pattern shown in Figure 6-15 was calculated to be 0.440 nm, whereas the lattice parameter for the ring pattern shown in Figure 6-16 was 0.479 nm. The lattice parameter was calculated by measuring the d spacings using Image J software to count the length in pixels and then using a camera constant of 273 nm×pixel. It should be noted that the camera constant was not calculated individually in this study, the value used (273 nm×pixel) was provided by the operator, which may have deviated from the actual value of the camera constant. Nevertheless, the values obtained for the two steels are close to lattice constants for cubic NbN and NbC (both with a NaCl-type structure), which range from 0.438 nm to 0.46 nm [Akhlaghi, 2002]. It reveals that for both Steel X and steel Y, the fine particles are mostly Nb-rich (close to 0.438 nm). It is possible that C-rich precipitates such as MoC, which may have formed along with Nb carbides [Lee, 2002]. The Mo/Nb ratio was higher in the finer carbides. Although MoC has a different crystal structure (hexagonal) than Nb carbide, Mo can partially substitute for Nb. It is noted that Nb(CN) and Ti(CN) have the same crystal structure (NaCl-type), which makes them mutually soluble [Akhlaghi, 2002] [Narita, 1975]. Also of note that the pattern obtained from Steel X is not well defined compared with the Steel Y SAD pattern. This implies that the region used to obtain the pattern for Steel X had fewer particles than Steel Y. This is later evident when a particle size distribution was done using Image analysis software, where Steel Y is shown to have more fine particles than Steel X.

A particle size distribution was generated using the data provided by Image J and plotted using Microsoft Excel (Figure 6-17). It is evident that Steel X has a higher number of intermediate size particles than Steel Y. Also, the average intermediate particle size in Steel X is larger than in Steel Y. For Steel X, the average intermediate particle size is 65 nm and for steel Y it is 60 nm. It can also be seen that there are 45% more fine particles (3 nm - 6 nm in size) in Steel Y than in Steel X. There are also more fine particles than intermediate size particles in both the steels.

Based on the above data, it is clear that there is a difference in precipitate size and distribution between the two steels. However, the differences are not sufficient to explain the toughness difference between the two steels. Since the regions examined using TEM replica analysis are extremely small, there is always concern as to whether the results are representative of the whole sample. Considering that Steel Y has more fine particles than Steel X, it is expected that Steel Y should have better toughness, since fine particles tend to impede crack propagation. But the toughness values found for Steel Y is the opposite of what is expected. To measure the distribution and size of precipitates in both the steels, a particle dissolution method can be used to verify the results found in TEM replica analysis [Lu, 2009]. It is important that the results should represent the bulk sample rather than a small region as examined in this study. It should be noted that carbon replica precipitate analysis does not include very large particles. Due to their size, they do not get captured in the replica after etching. So it is safe to say that the above precipitate size distribution does not include very large particles (large Ti-rich particles), which are found in the steels (Section 5.3.1). These large particles and their distribution may have played an important role in the toughness values. Measuring the amount and distribution of these particles was beyond the scope of this study. In most cases these particles were found to be broken, making it quite impossible to measure the actual size of the original particles. Nevertheless, the large particles remain an important factor contributing to the toughness values we found in the Charpy specimens.

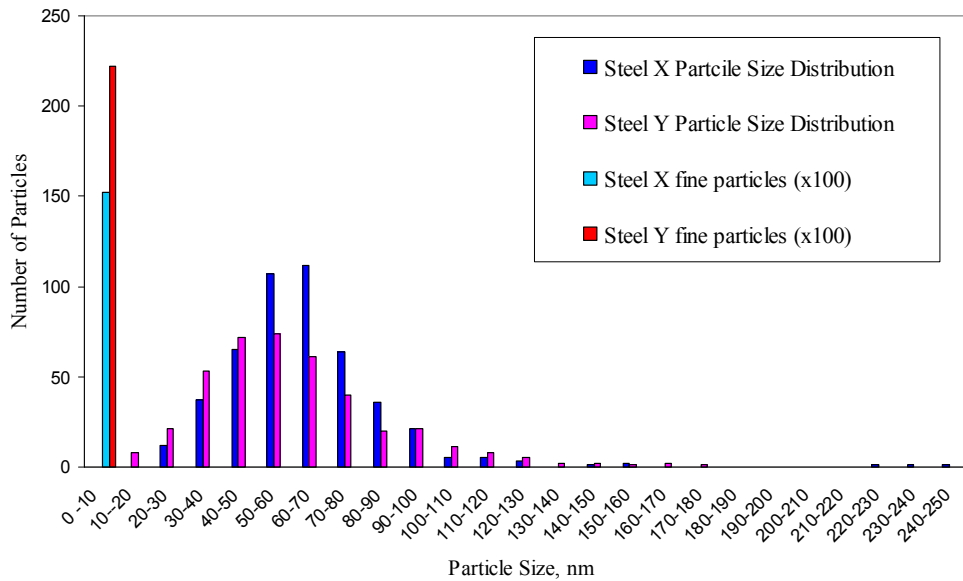


Figure 6-17: Particle size distribution for Steel X and Steel Y.

6.2 As-Welded Microstructure

The as welded microstructures of Steel X and Steel Y were examined for various heat inputs (i.e., 1.5 kJ/mm to 2.25 kJ/mm for tandem electrode welds and 1.5 kJ/mm and 1.75 kJ/mm for single electrode welds). Characterization of these microstructures was done by examining and comparing the CGHAZ and FGHAZ structures present for each heat input level.

6.2.1 CGHAZ Microstructure

The CGHAZ microstructures for both Steel X and Steel Y for different heat inputs are shown in Table 6-2 and Table 6-3. The grain sizes for the CGHAZ region of these steels for various heat inputs are reported in Table 6-4 and Table 6-5. It should be noted that the grain sizes reported here are prior austenite grain sizes (PAGS). The actual grain size is much smaller as discussed in the following section.

Table 6-2: As-welded optical microstructures of CGHAZ region for both Steel X and Steel Y for various heat inputs - tandem electrode welds

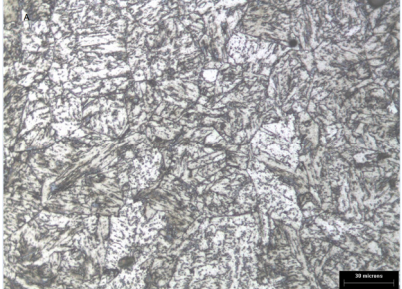
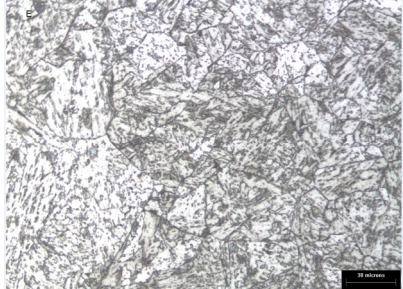
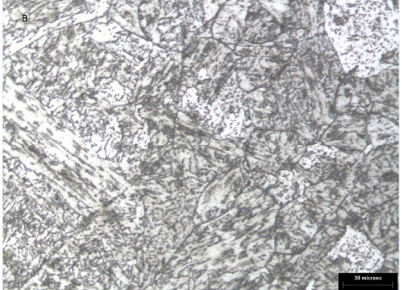
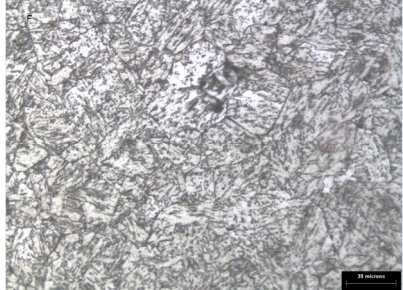
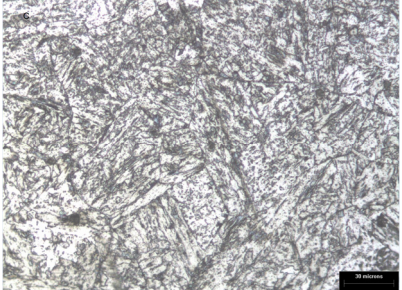
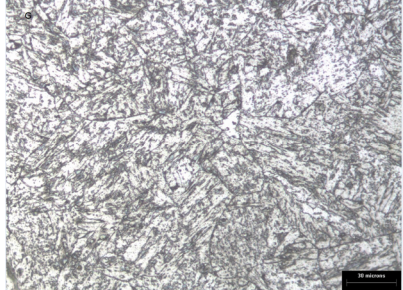
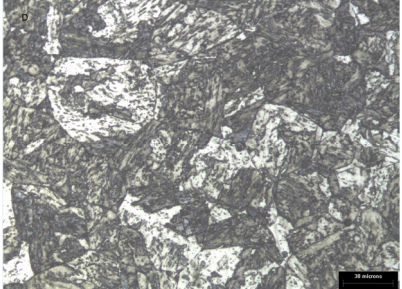
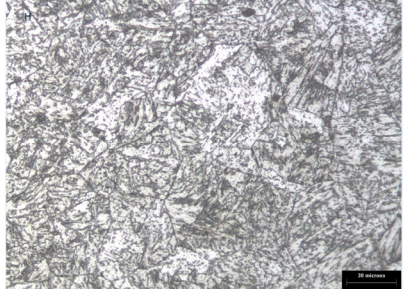
Identification	Steel X	Steel Y
<p>Heat Input- 1.50 kJ/mm Tandem Electrode Weld</p>		
<p>Heat Input- 1.75 kJ/mm Tandem Electrode Weld</p>		
<p>Heat Input- 2.00 kJ/mm Tandem Electrode Weld</p>		
<p>Heat Input- 2.25 kJ/mm Tandem Electrode Weld</p>		

Table 6-3: As welded optical microstructures of CGHAZ region for both Steel X and Steel Y for various heat inputs - single electrode welds

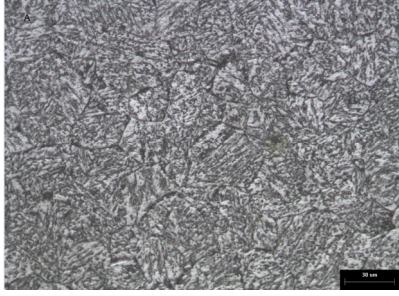
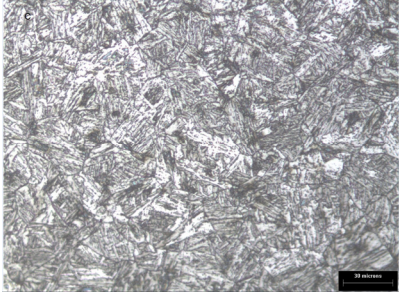
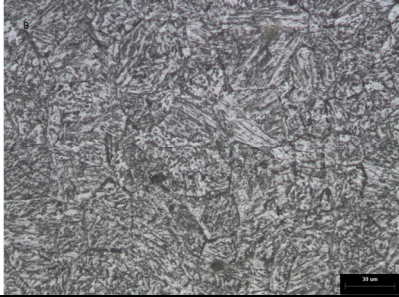
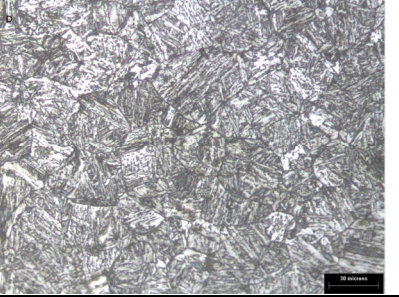
Identification	Steel X	Steel Y
Heat Input- 1.50 kJ/mm Single Electrode Weld		
Heat Input- 1.75 kJ/mm Single Electrode Weld		

Table 6-4: CGHAZ grain size of Steel X for various heat inputs – tandem and single electrode welds

Identification	Heat Input (kJ/mm)	ASTM Grain Size Number	Average Grain Diameter (PAGS) (μm)
Steel X-Tandem Electrode-CGHAZ Region	1.5	7.5	31 ± 7
	1.75	7.5	33 ± 6
	2.00	7.0	35 ± 4
	2.25	7.0	37 ± 4
Steel X-Single Electrode- CGHAZ Region	1.5	7.0	34 ± 9
	1.75	7.0	37 ± 2

Table 6-5: CGHAZ grain size of steel Y for various heat inputs – tandem and single electrode welds

Identification	Heat Input (kJ/mm)	ASTM Grain Size Number	Average Grain Diameter (PAGS) (μm)
Steel Y-Tandem Electrode-CGHAZ Region	1.5	7.5	31 ± 7
	1.75	7.5	33 ± 5
	2.00	7.0	34 ± 12
	2.25	7.0	35 ± 9
Steel Y-Single Electrode-CGHAZ Region	1.5	7.0	36 ± 4
	1.75	7.0	37 ± 3

By examining the microstructures it can be seen that all the CGHAZ microstructures for both the steels show large prior austenite grain size PAGS. More importantly, the CGHAZ PAGS increases as the heat input increases for the same distance from the weld fusion line. A plot of the values shown in Table 6-4 and Table 6-5 is given in Figure 6-18.

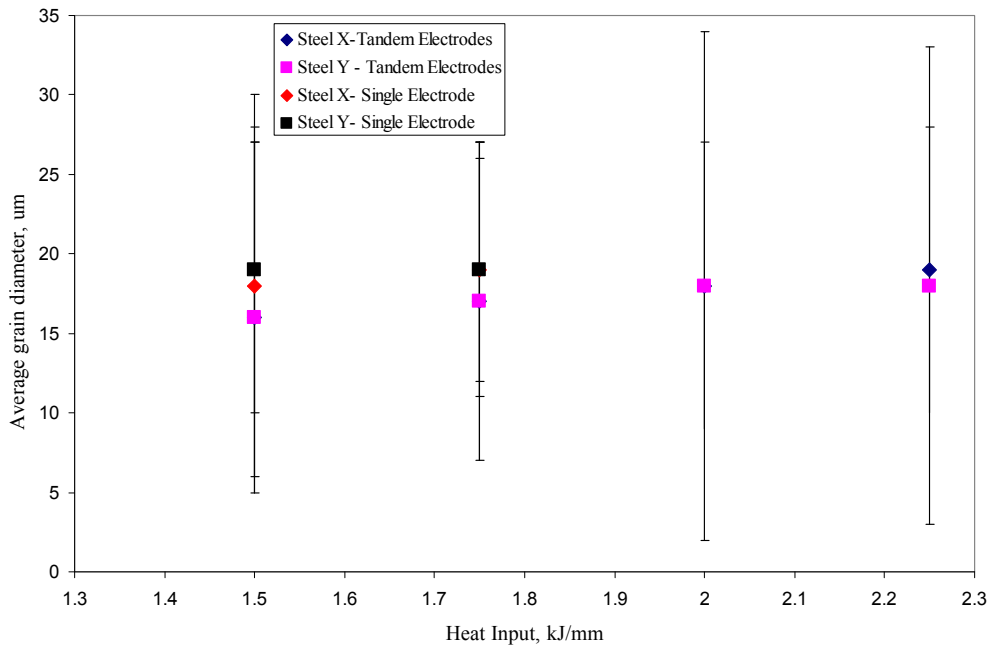


Figure 6-18: Variation of average CGHAZ PAGS with heat input.

It was also found that the single electrode welds had higher PAGS when compared with similar heat inputs for tandem electrode welds. The reason is discussed later. There are large error bars in the plot. This is due to the fact that some of the grains that were measured are close to the fusion line and are very large, whereas other PAGs, which are at some distance from the fusion line, but still in the CGHAZ region are not that large, which resulted in these huge error bars in the plot. At higher temperatures (i.e., higher heat inputs) the prior austenite grains get coarser and grow, since grain growth is thermally activated, and larger grains grow at the expense of smaller ones [Porter, 1981]. It should be noted that during welding the grains transform to austenite in the CGHAZ region and grow to an extent that depends on the peak temperature. The amount of growth is partly controlled by the distance from the weld fusion line, for a given heat input. The grains that are close to the weld fusion line grow much larger than the grains that are at a significant distance from the fusion line. The CGHAZ microstructure consists of large prior austenite grains containing packets of ferrite laths. These plates/laths are known as Widmanstätten side plates. An SEM image of the CGHAZ region of specimen A (Steel X welded using 1.5 kJ/mm heat input - tandem electrode) is shown in Figure 6-19. A prior austenite grain as indicated by a red box in Figure 6-19 (A) is chosen and further magnified (outlined with red marker) in Figure 6-19 (B). It is assumed that the ferrite plates have grown from the prior austenite grain boundaries in different directions. The region between the ferrite laths is believed to be untransformed austenite [Bhadeshia, class lecture notes].

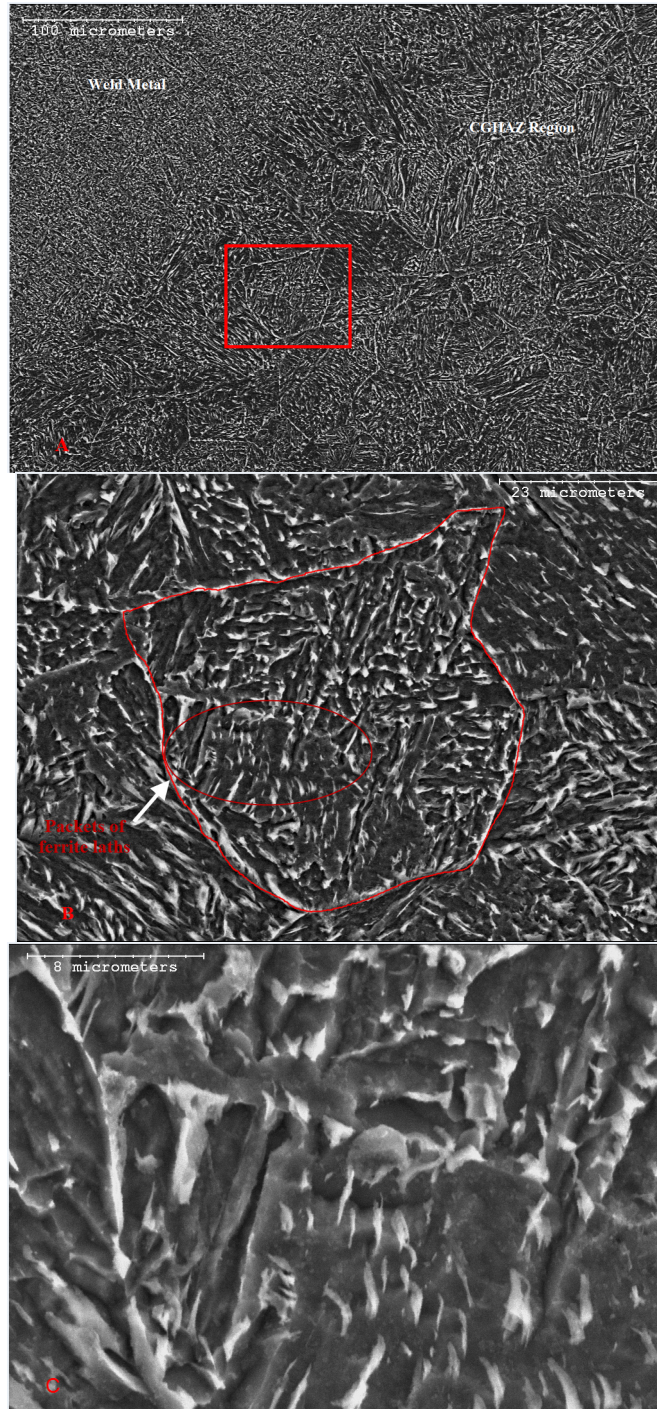


Figure 6-19: A) SEM SE image of CGHAZ region of specimen A (Steel X welded using a 1.5 kJ/mm heat input - tandem electrode) showing large prior austenite grains; B) magnified prior austenite grain from Figure 6-19 (A) and C) magnified image of a prior austenite grain from Figure 6-19 (B).

Another minor morphology that was observed from the magnified image in Figure 6-19 (B) is grain boundary ferrite that grows in the boundary of the prior austenite grain. It should be noted that this grain boundary ferrite is further confirmation that the regions are Widmanstätten ferrite. Both Widmanstätten ferrite and bainitic ferrite have similar formation mechanisms, morphology and crystallography. However the main difference between Widmanstätten ferrite and bainitic ferrite is the transformation temperature and the nucleation sites. The transformation temperature for bainitic ferrite is higher than for Widmanstätten ferrite and the laths for bainitic ferrite grow directly from the austenite grain boundary. The laths for Widmanstätten ferrite usually start to grow at grain boundary ferrite allotriomorph [Ohmori, 1992]. A more highly magnified SEM image of the same grain is shown in Figure 6-19 (C).

Because of the resolution limitations of SEM, some features of that grain (shown in Figure 6-19 (C)) are not fully resolved. However, using image analysis software (Image J), it was possible to measure the size and length of a lath from this image. The lath width is approximately 3 μm and the lath length is approximately 13 μm . CGHAZ regions close to the weld fusion line generally had larger prior austenite grain sizes and larger lath sizes. Values for other lath size measurements are reported in Figure 6-20 and Figure 6-21 for different heat inputs.

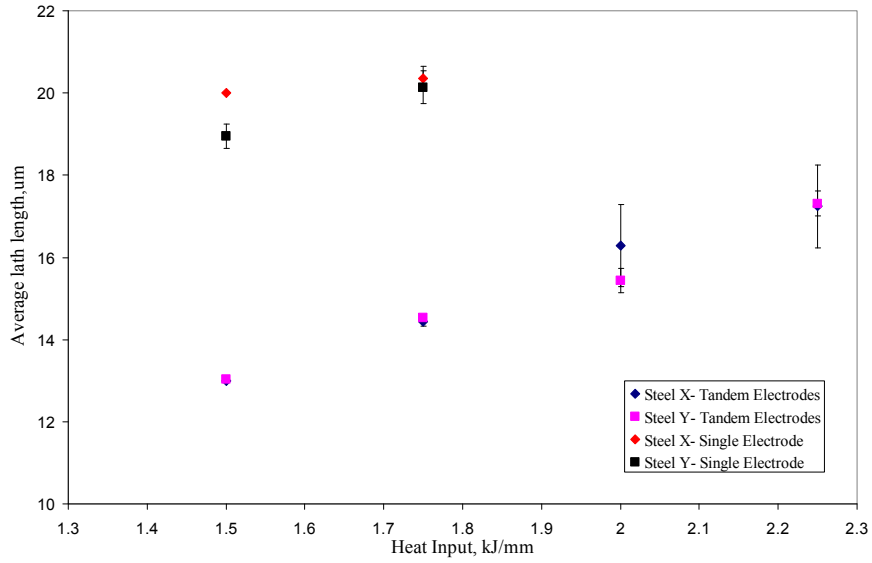


Figure 6-20: Average lath length for different heat inputs. Lath length increases as the heat input increases. Also, single electrode welds have higher lath lengths compared with the same heat input welded using tandem electrodes.

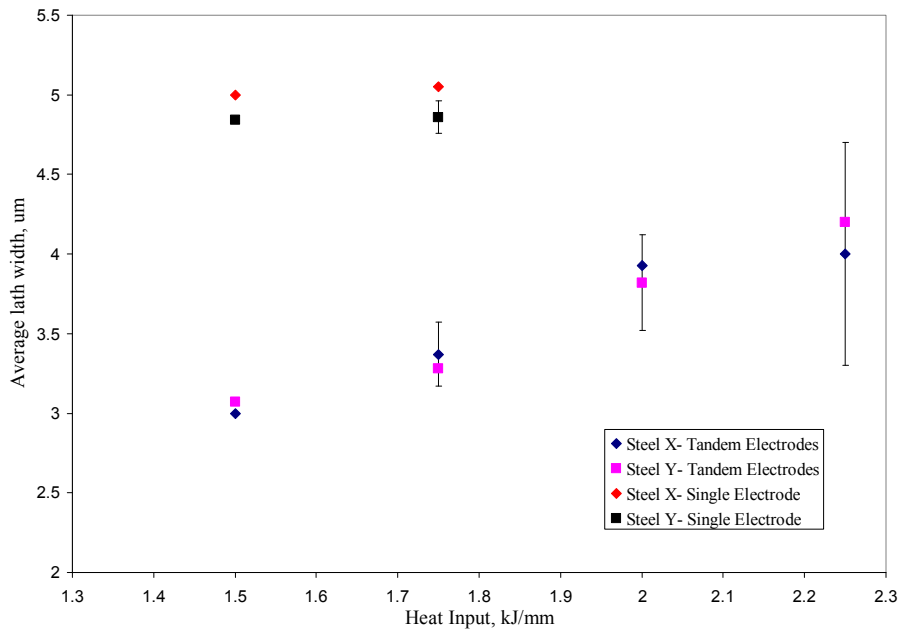


Figure 6-21: Average lath width for different heat inputs.

Another example of the CGHAZ region of another specimen (specimen F, which is Steel X welded using a 1.5 kJ/mm heat input - single electrode) was carried out. Similar results were observed for this specimen. SEM images of the CGHAZ region and subsequent magnified images of a single grain from the CGHAZ region are shown in Figure 6-22. Again the lath sizes were measured and were approximately 5 μm wide and 20 μm long.

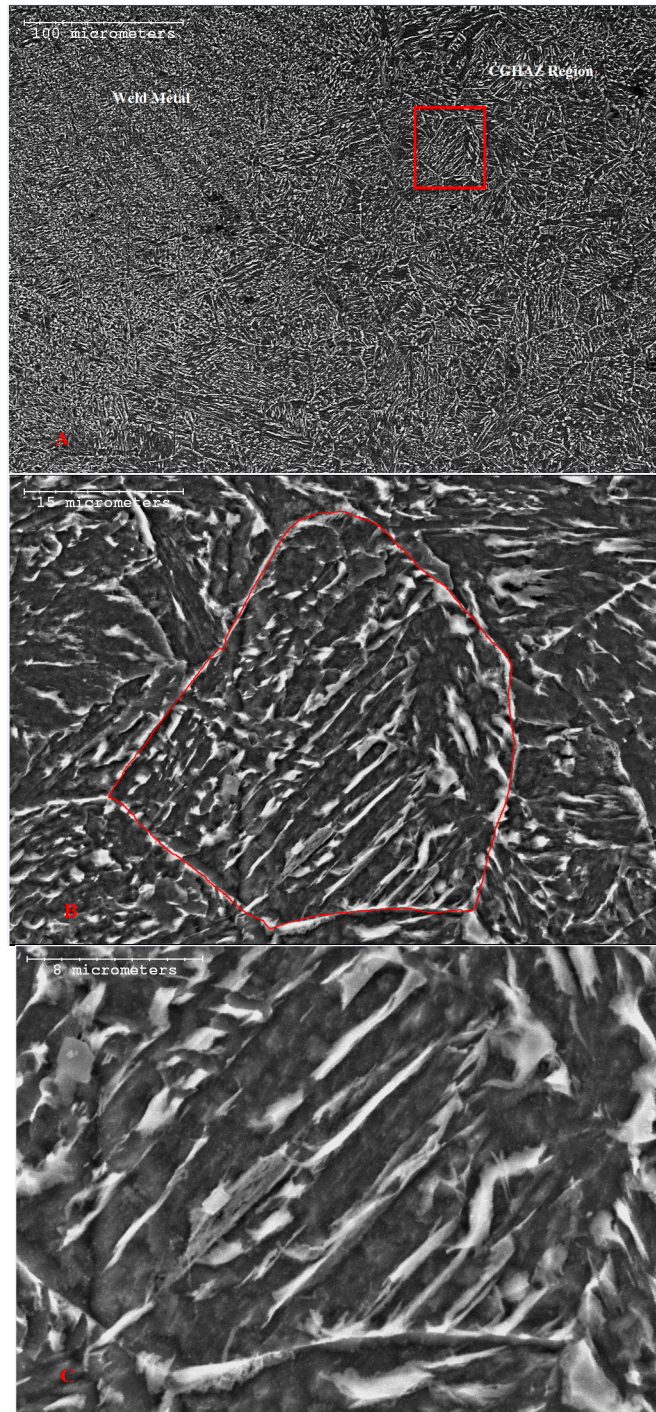


Figure 6-22: A) SEM SE image of CGHAZ region of specimen F (Steel X welded using a 1.5 kJ/mm heat input - single electrode); B) magnified prior austenite grain from Figure 6-22(A) and C) magnified image of a prior austenite grain from Figure 6-22 (B).

One feature worth noting is the difference in the lath sizes. As stated above the lath size for specimen A (Steel X welded using a 1.5 kJ/mm heat input - tandem electrode) is smaller than the lath size for specimen F (Steel X welded using 1.5 kJ/mm heat input - single electrode). From Figure 6-19(A) and Figure 6-22(A), it can be seen that the grains chosen for subsequent lath size measurement are close to the weld fusion line. The grain in Figure 6-19(A) is “closer” to the fusion line than the grain in Figure 6-22(A). As discussed above, grains closer to the fusion line have larger lath sizes and larger PAGS. In this case, the prior austenite grain diameter is larger in specimen A - $\sim 27 \mu\text{m}$ than specimen F - $\sim 18 \mu\text{m}$; but the lath size is smaller in specimen A compare to specimen F. Although the two specimens have similar heat inputs (1.5 kJ/mm), one specimen is welded using tandem electrodes (specimen A) and the other one is welded using a single electrode (specimen F). As discussed in Section 4.3, for tandem electrodes it is assumed that a 0.75 kJ/mm heat input is provided by the lead arc and the remaining 0.75 kJ/mm heat input is provided by the trail arc. Essentially, the steel is experiencing 0.75 kJ/mm heat input at a given time. For the single electrode weld, the heat input calculation is straightforward and specimen F (steel X welded using 1.5 kJ/mm heat input – single electrode) experiences the whole 1.5 kJ/mm heat input at a given time. Since the lower heat input (~ 0.75 kJ/mm) has a faster cooling rate, the lath size will be smaller as there is less diffusion in the matrix. The stages of ferrite lath formation and growth in the prior austenite grains involve a diffusional mechanism [Poorhaydari, 2005] [Ohmori, 1992]. The thickening of the laths takes place by “the coalescence of the sub-laths and the diffusional migration of ferrite/austenite interfaces” [Ohmori, 1992]. Specimen F (steel X welded using 1.5 kJ/mm heat input – single electrode) experiences a higher heat input (1.5 kJ/mm) from a single electrode. The cooling rate would be somewhat lower, because of the high heat input, so there is enough time for diffusion and to grow the laths forming the larger laths in the specimen. A similar argument can be made to explain the fact that single electrode welds have larger PAGS just as they have larger lath sizes. This result is also reported in the

literature [Otterberg, 1980], where the researchers found that a higher heat input resulted in an increase in the width of the grain boundary ferrite within the prior austenite grain boundary and the lamellar ferrite width (Widmanstätten ferrite or bainitic ferrite).

6.2.2 FGHAZ Microstructure

The FGHAZ microstructures for both Steel X and Steel Y for different heat inputs are shown in Table 6-6 and Table 6-7. The grain sizes for the FGHAZ region of these steels for various heat inputs are reported in Table 6-8 and Table 6-9.

Table 6-6: As-welded optical microstructures of FGHAZ region for both Steel X and Steel Y for various heat inputs - tandem electrode welds

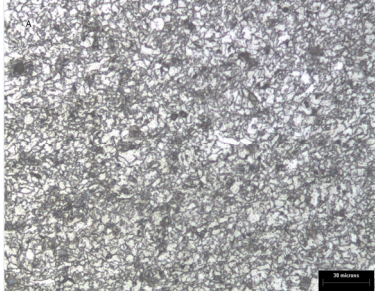
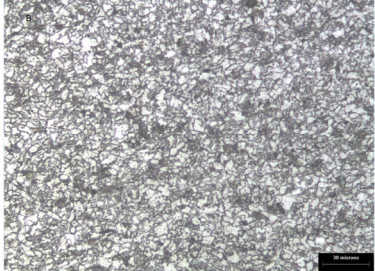
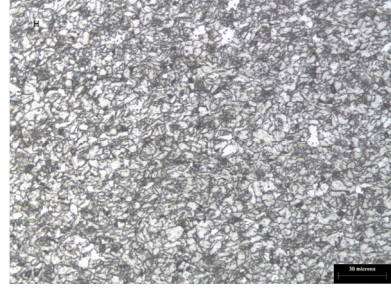
Identification	Steel X	Steel Y
<p>Heat Input- 1.50 kJ/mm Tandem Electrode Weld</p>		
<p>Heat Input- 1.75 kJ/mm Tandem Electrode Weld</p>		
<p>Heat Input- 2.00 kJ/mm Tandem Electrode Weld</p>		
<p>Heat Input- 2.25 kJ/mm Tandem Electrode Weld</p>		

Table 6-7: As welded optical microstructures of FGHAZ region for both Steel X and Steel Y for various heat inputs - single electrode welds

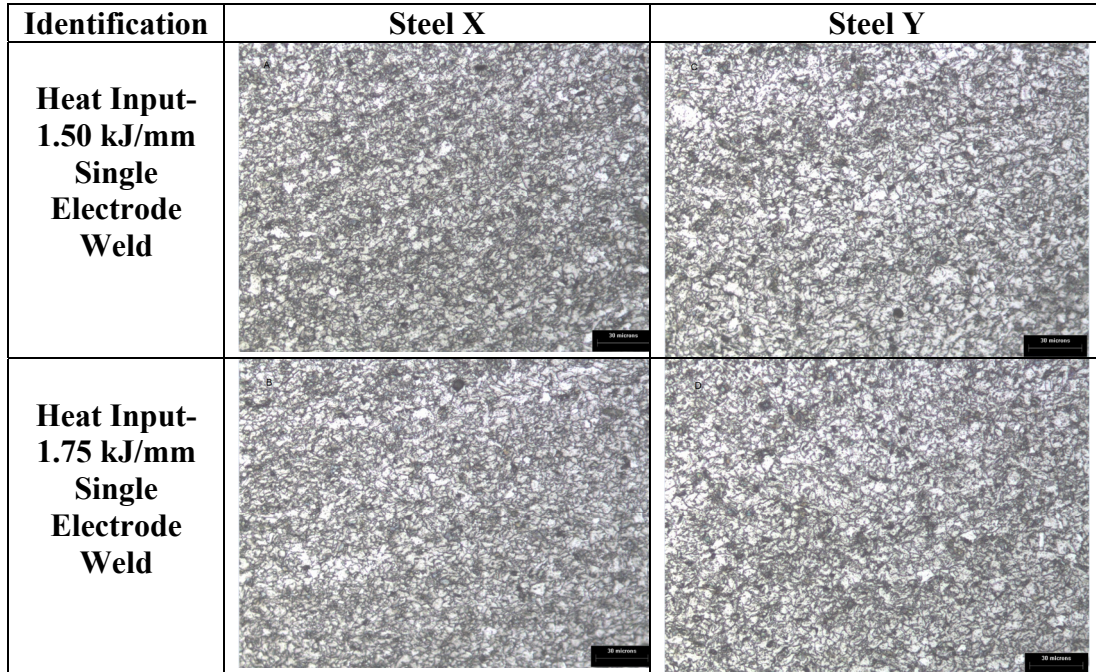


Table 6-8: FGHAZ grain size of Steel X for various heat inputs – tandem and single electrode welds

Identification	Heat Input (kJ/mm)	ASTM Grain Size Number	Average grain diameter (μm)
Steel X-Tandem Electrode-FGHAZ Region	1.5	13.0	4 ± 1
	1.75	12.5	5 ± 1
	2.00	12.5	5 ± 2
	2.25	12.5	5 ± 2
Steel X-Single Electrode-FGHAZ Region	1.5	13.0	4 ± 1
	1.75	13.0	4 ± 2

Table 6-9: FGHAZ grain size of steel Y for various heat inputs – tandem and single electrode welds

Identification	Heat Input (kJ/mm)	ASTM Grain Size Number	Average grain diameter (μm)
Steel Y-Tandem Electrode-FGHAZ Region	1.5	13.5	4 ± 1
	1.75	13.0	4 ± 1
	2.00	12.5	5 ± 1
	2.25	12.5	5 ± 1
Steel Y-Single Electrode-FGHAZ Region	1.5	13.0	5 ± 1
	1.75	13.0	5 ± 1

By examining the microstructures, it can be seen that the overall FGHAZ microstructure is quite similar regardless of the heat inputs or type of steel used. The FGHAZ microstructure consists of polygonal ferrite. The grain size is slightly larger than for the base metal. Note that the base metal microstructure is elongated in the rolling direction, while the FGHAZ microstructure is not. During the weld thermal cycle the temperature gets high enough to transform this region to austenite. However, due to the distance from the fusion line, the temperature rise is not sufficient to coarsen the austenite grains [Poorhaydari, 2005]. Moreover, because of limited dissolution; there are precipitates which tend to pin the grain boundaries during this stage, resulting in small austenite grains. The cooling rate is moderate enough so that the austenite grains transform into ferrite grains [Poorhaydari, 2005].

6.3 Correlation of Mechanical Properties with Microstructure

This section tries to correlate microstructural analysis with separate studies discussed in previous chapters, i.e., mechanical properties (microhardness, tensile testing and Charpy testing). Performing microstructural analysis helps in understanding the mechanical properties of the material.

6.3.1 Correlation between Hardness and Microstructure in HAZ

Generally, the hardness of a metal depends on the hardness of different phases that are present in it. So, it is important that the hardness trends that are found in the different zones of Steel X and Steel Y correlate with the microstructures present in those zones (weld metal, CGHAZ, FGHAZ and parent metal).

As mentioned earlier in Section 6.1, the microstructure of both Steel X and Y consists of elongated ferrite grains along with bainite. Hence, the hardness values are quite similar for both steels (the base metal hardnesses for Steel X and Steel Y were $256 \text{ HV} \pm 7$ and $248 \text{ HV} \pm 7$ respectively). The weld metal hardness for both the steels is higher than the base metal hardnesses (average weld metal hardness in Steel X was $\sim 293 \pm 9 \text{ HV}$ and in Steel Y it was $\sim 288 \pm 10 \text{ HV}$). The chemistry of the weld metal is attributed by filler metal chemistry, base metal dilution along with contribution from the active flux. Having very leaner chemistry, the base metal itself tends to decrease the alloying elements in the weld metal region. That is why very highly alloyed filler metal is generally used to compensate this base metal dilution effect. Appropriate chemistry in the weld metal will yield good toughness values along with higher hardness values. The high hardness in the weld metal region in the sample is due to the presence of acicular ferrite. The presence of acicular ferrite was confirmed when optical and SEM microscopy was carried out. Acicular ferrite has a less organized microstructure (having fewer parallel laths in any one direction) compared with Widmanstätten ferrite and bainite, which has parallel laths and which are identically oriented [Bhadeshia,

1993]. As mentioned in the Literature Review (Section 2.6.2), acicular ferrite has an interlocked nature of its ferrite laths, which provides the best combination of strength and toughness [Bhadeshia, 1993] [Kim, 2005]. Thus, the hardness levels of the weld metal region for both steels are very high.

As mentioned in Section 5.1, hardening occurs predominantly in the CGHAZ regions for both Steel X and Steel Y welded using different heat inputs. It should also be noted that, in the CGHAZ region, the microstructure was found to be Widmanstätten ferrite (Section 6.2.1), with different ferrite lath sizes (Figure 6-19 and Figure 6-22) oriented in different directions. The sizes of these ferrite laths have a profound affect on the overall hardness and toughness values, which in turn depend on the heat input [Poorhaydari, 2005]. Specimen A (Steel X welded using a 1.5 kJ/mm heat input tandem electrode) has a higher hardness value (~304 HV - the highest hardness recorded) than Specimen F (Steel X welded using a 1.5 kJ/mm heat input - single electrode). This specimen has a maximum hardness of 285 HV. As shown in Figure 6-19 and Figure 6-22, Specimen A has smaller lath sizes than specimen F for the reasons described in Section 6.2.1. Schematically, this dependency of hardness values on ferrite lath sizes is shown in Figure 6-23.

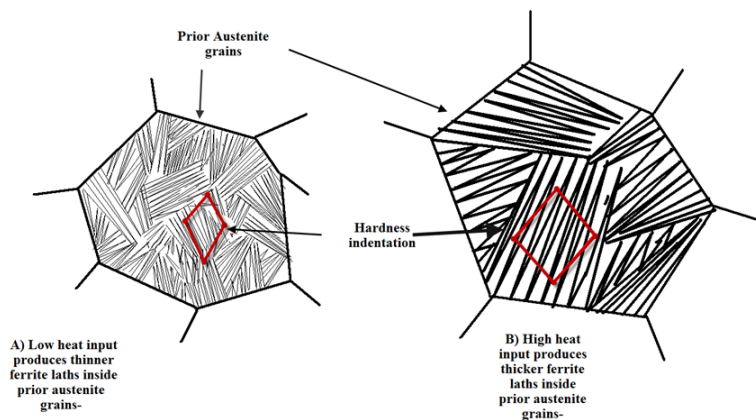


Figure 6-23: Schematic showing dependency of hardness values due to ferrite lath sizes.

The CGHAZ region, which is close to the fusion line, has a large PAGS and large ferrite laths within them. The laths are thicker, as in this region the cooling time is

longer. As the distance from the fusion line increases, the PAGS tends to decrease and the lath widths increase because of a comparatively slower cooling rate. The hardness in this region is somewhat lower than the region closer to the fusion line. So, it is evident that lath size differences, which arise because of heat input differences, also affect the hardness values. A smaller lath size gives overall high hardness values, whereas larger lath size generates comparatively low hardness values.

The FGHAZ regions for both Steel X and Steel Y welded using different heat inputs consist of polygonal ferrite (Section 6.2.2). Because of this polygonal ferrite microstructure, softening occurs in this region for the hardness traverses from the base metal towards the weld metal. The hardness of the base metal is somewhat higher than that in the FGHAZ, because of the pancaked microstructure of the ferrite grains and the high solute level in the base metal. The overall transformation temperature is lower, which in turn gives high hardness values [Poorhaydari, 2005]. The hardness is somewhat higher at the CGHAZ-FGHAZ boundary, because this region has a slightly higher cooling rate (compared to the other regions in FGHAZ). So when a hardness traverse is carried out, the hardness falls in the FGHAZ region (softening occurs). On moving towards the CGHAZ-FGHAZ boundary, the hardness tends to increase; hardness continues to increase towards the fusion line and the peak hardness is in the weld metal region. In the CGHAZ there is a change in ferrite lath sizes as the heat input changes. In the FGHAZ the microstructure is polygonal ferrite, so the hardness values for this region did not show much variation. Note that the grain size also varied very little in this region (Section 6.2.2).

One important point to note here is that the extend of Hall-Petch relation applicable for hardness values with respect to its microstructure cannot be established here as the hardness values found in CGHAZ/FGHAZ/ base metal region are strongly depended on different features of the respective microstructures rather than the grain size.

6.3.2 Correlation between Tensile Strength and Microstructure

The relationship between the yield strength and grain size is given by the Hall-Petch relationship, provided by Hall and Petch from their experimental findings [Petch, 1953]:

$$\sigma_y = \sigma_o + k_y d^{1/2} \dots\dots\dots 6.1$$

Here, σ_y is the yield strength, σ_o is the friction stress, k_y is the strengthening coefficient and d is the grain size. According to this relationship, yield strength and grain size are inversely proportional. A similar relationship holds for both Steel X and Steel Y. Steel X has a slightly smaller grain size than Steel Y as reported in Table 6-1. The yield strength of Steel X is higher (753 MPa) than Steel Y (706 MPa).

Transverse weld tensile specimens welded using different heat inputs for both steels broke in the base metal region. The yield strength values found in all the weld tensile specimens are therefore very close to each other. It is believed that the presence of the harder weld metal region and harder CGHAZ region (compared with the base metals) in the gauge length influenced the percent elongation as discussed in Section 5.2. The harder weld metal region is due to the presence of acicular ferrite and the harder CGHAZ region is due to the presence of large PAGS containing ferrite laths. Both these microstructures are quite different from the microstructure of the base metals (as described in the previous sections). Hence, the transverse weld tensile properties are affected by the microstructure of the weld metal and CGHAZ. Both the weld metal and CGHAZ region have very good strength compared with the base metals and, hence, all the specimens broke in the base metal.

6.3.3 Correlation between CGHAZ Toughness and CGHAZ Microstructure

The CGHAZ microstructure consists of large PAGS containing ferrite laths. It is expected that smaller and thinner laths inside the PAGS will yield high toughness values. In other words, CGHAZ toughness will depend on the heat input values. Lower heat inputs produce smaller and thinner laths, which will have higher toughness values compare to thicker and larger laths. High input produces thicker laths inside the PAGS and will yield low toughness values.

The CGHAZ toughness values obtained and reported in Section 5.3 do not conclusively show the above mentioned trend. There are discrepancies found in the CGHAZ toughness values from the general trend, i.e., a high heat input will yield low toughness and low heat input will yield high toughness. The reasons behind these discrepancies are mainly notch location and deviation of the crack (see Section 5.3). Since the crack does not go through the CGHAZ region for several cases, it is unlikely that the toughness values will be affected by the CGHAZ microstructure. There were cases where the crack propagated through the weld metal region, giving very high toughness values (higher than the base metal toughness). This complicates the correlation of the CGHAZ toughness values with the CGHAZ microstructure. It should be noted that Charpy V-notch testing is not very sensitive due to the large blunt tip which goes into several microstructural regions [Lau, 1987]. It is therefore very difficult to correlate the toughness values with the microstructure as the crack could propagate through several microstructural regions (WM, CGHAZ, FGHAZ and BM).

6.4 Summary

In this chapter, microstructural characterization of Steel X and Steel Y was discussed both qualitatively and quantitatively. Correlation of the mechanical properties and thermal analysis with the microstructure was discussed. The following points can be summarized from this chapter:

1.) Both Steel X and Steel Y have very similar microstructural features, as seen from optical and SEM imaging. The microstructure of Steel X and Steel Y is mainly elongated (along the rolling direction) ferrite grains. There are also some regions, which are believed to be bainitic. Le Pera's etch revealed M-A regions in both the steels.

2.) The CGHAZ microstructure is Widmanstatten ferrite which consists of large prior austenite grains containing ferrite laths for all specimens welded using different heat inputs. As the heat input is increased, both PAGS and lath size increase. Single electrode welds have larger PAGS and lath sizes, when compared with tandem electrode welds welded using similar heat inputs.

3.) FGHAZ microstructures, for all specimens welded using different heat inputs, were polygonal ferrite. The grain sizes varied very little in this region of the welded structure.

4.) Hardness variation for different heat inputs for both steels was found to be dependent on the microstructure of the individual region (WM, CGHAZ, FGHAZ and base metal). Base metal hardness for both steels was quite similar, as both steels had very similar grain size and microstructure. The weld metal had the highest hardness due to the presence of acicular ferrite. The CGHAZ hardness mostly depended on the ferrite laths found in the large PAGS. Thinner laths yielded high hardness, whereas thicker laths give lower hardness values. In the

FGHAZ region, the hardness did not vary much. For all the welded specimens the FGHAZ had similar microstructure consisting of polygonal ferrite.

5.) The yield and tensile strengths of all welded specimens tested gave values close to their respective base metals yield and tensile strength. All the specimens broke in the base metal region, revealing that the weld metal and CGHAZ region had higher strengths than the base metals. The hardness values also confirmed this finding. The weld metal and CGHAZ hardness was higher than in the base metals.

Concluding Remarks

In this chapter conclusions obtained from the results described previously will be drawn. Also, recommendations for future work are presented.

7.1 Conclusions

In this study, two types of X80 steels were used to evaluate the effect of SAW on mechanical properties and the microstructure of the steels. Modified V-groove bevel welds were performed, which simulated the actual production weld to connect real pipes. Both tandem and single electrode welds with an AC power source were used, with OD and ID welds performed using no preheat.

In terms of weld performance, the weld bead shape, penetration depth, bead width and reinforcement height increased with heat input. Also, simple calculations of heat input for tandem electrode welds could not be applied directly, since the total molten metal calculated for single and tandem electrode welds do not correlate for identical heat input values. Weld bead shape parameters did not influence impact toughness, Charpy impact energies were found to be affected by the SP ratios. Increasing the SP ratio values tended to decrease the CVN values.

Microhardness measurements were carried out from the weld metal through the HAZ and into the base metal. Steel X (0.06 wt% C) had higher hardness values than Steel Y (0.03 wt% C). The hardness traverses showed that there was initial softening in the FGHAZ region and then hardening occurred in the CGHAZ region. The peak hardness was found in the weld metal region. The microstructure of the CGHAZ and FGHAZ region influenced the hardness values. Increased hardness values in the CGHAZ were attributed

to refinement of the ferrite lath size compared with the FGHAZ which consisted mainly of polygonal ferrite. Hardness values were also dependent on the heat input. Increasing heat input decreased the hardness values.

Transverse tensile tests of the welded joints suggest that the weld metal region has a higher strength than the parent metal and the HAZ region. All the samples broke in the parent metal region. However, the level of overmatching properties could not be resolved using such tests.

The microstructures of both steels were similar, with elongated ferrite grains and a small fraction of bainite. The CGHAZ microstructure was comprised of mainly large prior austenite grains with ferrite laths of different shapes and sizes in them. The FGHAZ microstructure was mainly polygonal ferrite. The mechanical properties of the two steels suggest that Steel X (with more carbon) was tougher than Steel Y (with less carbon). As this result is quite surprising, precipitate analysis was carried out to determine any differences in the precipitate size and distribution in the two steels. TEM analysis of carbon replicas indicated that there were 45% more fine particles in steel Y, than in steel X, although this was not conclusive evidence for the toughness difference between the steels. Fractography of Charpy impact specimens revealed that there were large Ti-rich particles in both the steels. It was suggested that these large particles may be responsible for the toughness difference between the steels. The Charpy impact toughness of the CGHAZ is controlled by the size and orientation of the ferrite laths inside the prior austenite grains.

7.2 Future Recommendations

1.) It is surprising that the higher carbon steel (Steel X) exhibited higher toughness than Steel Y (with less carbon). Although precipitation analysis was carried out to see the distribution of precipitate sizes, it was noted that such an analysis (using carbon replicas) does not include very large particles, which may be responsible for the toughness difference. A detailed precipitate analysis should be carried out to resolve this issue.

2.) In this study, various heat inputs were used to join modified V-groove steels. To accommodate higher heat inputs, the land geometry was changed. It is believed that this change in land geometry affected the final microstructure of the weld HAZ, by providing material as a heat sink and counteracting the higher heat input in this way. In future investigations, it is recommended that the land geometry should be kept constant and then the heat input should be varied. A thicker material should be used.

3.) In this study, the OD welds were performed first and then ID welds were performed. The steel was not heated prior to welding. The ID welds were performed long after the OD welds; hence, the temperature was close to room temperature. In actual DJ welds, the ID weld is performed right after the OD weld. Hence, it is logical to think that after the OD is done, the temperature is no longer at room temperature, but some higher temperature. For future investigations, it is recommended that the ID weld should be performed right after the OD weld, as to better simulate the actual condition. In this study, since some of the specimens did not have overlapping OD and ID welds, any further investigation involving ID welds was disregarded. However future investigations should involve both welds and to ensure overlapping of OD and ID welds, higher inputs for ID welds can be used.

4.) Transverse tensile testing was performed to evaluate the overmatching properties of the welded joints. Although this test is sufficient to reveal whether the welded joint is overmatched or not, it cannot quantify the extent of overmatching. This would actually require all weld metals to be tensile tested. However, it may be difficult to extract

specimens from the weld metal region due to the geometry, and nearly impossible for the case of the HAZ region. It is recommended that future investigations should carry out all weld metal tensile tests along with transverse tensile tests.

References

[Akhlaghi, 2002] Akhlaghi, S. and Ivey, D.G.,” Precipitation Behaviour of a grade 100 structural steel.” Canadian Metallurgical Quarterly. Vol 41(1): pp 111-119.2002.

[Ali, 1990] Ali, A., and Bhadeshia, H. K. D. H., “Aspects of the Nucleation of Widmanstatten Ferrite.” Materials Science and Technology. Vol. 6: pp. 781-784. 1990.

[Anderson, 1994] Anderson, T.L.,Fracture Mechanics: Fundamental and Application.2nd Edition, CRC Press.1994.

[Antaki, 2003] Antaki, G.A., Piping and Pipeline Engineering: Design, Construction, Maintenance, Integrity, and Repair. Marcel Dekker Inc., 2003.

[Aran, 1984] Aran, A., Gulec, S., “Fracture Toughness Studies in Different Regions of Weld Heat Affected Zones on a C-Mn Steel.” Journal of Materials Science Letters. Volume 3: pp. 512 – 514. 1984.

[Arc Welding, 2000] The Procedure Handbook of Arc Welding. 14th Ed., Cleveland, OH. Section 5.2 - 5. 2000.

[ASME, 2007] ASME Boiler and Pressure Vessel Code, Section II – Materials (2007) .American Society of Mechanical Engineers. Online version available at:
http://www.knovel.com/web/portal/browse/display?_EXT_KNOVEL_DISPLAY_bookid=1777&VerticalID=0

[ASME, 2008] ASME Code for Pressure Piping, Section B31.3. American Society of Mechanical Engineers. pp.60.2008.

[ASME, 2008] ASME Boiler and Pressure Vessel Code, Section IX: Welding and Brazing Qualifications. American Society of Mechanical Engineers.2008.

[ASTM A370, 2003] ASTM Standard A370-03a, "Standard Test Methods and Definitions for Mechanical Testing of Steel Products," ASTM International, 2003.

[ASTM E112, 2006] ASTM Standard E112-96, "Standard Test Methods for Determining Average Grain Size," ASTM International, 2006.

[ASTM E23, 2003] ASTM Standard E23-02a, "Standard Test Methods for Notched Bar Impact Testing of Metallic Materials," ASTM International, 2003.

[ASTM E92, 2003] ASTM Standard E92-82, "Standard Test Method for Vickers Hardness of Metallic Materials," ASTM International, 2003.

[Avner, 1974] Avner, S. H., Introduction to Physical Metallurgy. 2nd Ed., McGraw-Hill.1974.

[AWS, 2004] AWS Welding Handbook-Volume 2: Welding Processes Part 1 (9th Edition). American Welding Society. Miami, FL. 2004.

[Bae, 2006] Bae, J.H., Yoo, J.Y., Kim, K.S., Kim, C.M., and Kang, K.B., "Development of High Strength Linepipe Steels With Excellent Weldability." Posco Technical Report. Vol. 10 (1). pp. 12-20. 2006.

[Bai, 2002] Bai, D., Cooke, M.A., Asante, J., Dorricott, J., United States Patent No. 6,682,613 B2, Process for Making High Strength Micro-Alloy Steel. 2002.

[Barbaro, 2010] Barbaro, F.J., Bowie, G.F., and Holmes, W., "Welding the First ERW X80 Grade Pipeline." Technical Paper by Blue Scope Steel. pp. 1-12. 2010.

[Bhadeshia, ---]Bhadeshia, H. K. D. H., Class Lecture Notes.

[Bhadeshia, 1982] Bhadeshia, H. K. D. H., “Thermodynamic Analysis of Isothermal Transformation Diagrams.” *Met.Sci.* Vol. 16 : 159-165.1982.

[Bhadeshia, 1985] Bhadeshia, H. K. D. H., “Diffusional Formation of Ferrite on Iron and its Alloys.” *Progress in Materials Science* . Vol.29: pp. 321-386.1985.

[Bhadeshia, 1993] Bhadeshia, H. K. D. H., and Svensson, L. E. , “Modelling the Evolution of Microstructure in Steel Weld Metal.” *Institute of Materials. London.* pp.109-182. 1993.

[Bhadeshia, 2001] Bhadeshia,H.K. D. H., *Bainite in Steels. 2nd Ed.*, Institute of Materials. 2001.

[Bhadeshia, July 1985] Bhadeshia, H. K. D. H., “Diffusion-Controlled Growth of Ferrite Plates in Plain Carbon Steels.” *Materials Science and Technology.* Vol. 1(7): pp.497-504.July, 1985.

[Calphad, 2006] <http://www.calphad.com/iron-carbon.html-Online> - source accessed on 25th September, 2011.

[Chandel, 1986] Chandel, R. S. and Bala, S. R., “Effect of Welding Parameters and Groove Angle on the Soundness of Beads Deposited by SAW Process.” *ASM International. New York, USA.* pp. 379-385. 1986.

[Chen, 1987] Chen, Z., Loretto, M.H., and Cochrane, R.C., *Mater. Sci. Tech.*, Vol. 3, pp. 836 -844. 1987.

[Collins, 1983] Collins, L.E., Godden, M.J., and Boyd, J.D., “Microstructures of Linepipe Steels.” *Can.Metall.Q.* Vol.22 (2): pp.169-179. 1983.
(www.ingentaconnect.com/content/maney/cmq)

[Croft, 1984] Croft,N.H., Gray, J. M., and DeArdo, A. J., “Submerged Arc Weld Metal

Toughness in Microalloyed Linepipe Steels – the Effects of Post Weld Heat Treatment.”, ASM. pp. 897-913.1984.

[De Meester, 1997] De Meester, B., “The Weldability of Modern Structural TMCP Steels.” ISIJ International. Vol. 37 (6): pp.537-551. 1997.

[Denys, 1990] Denys, R.M., “Implications of Overmatching/Undermatching of Weld Metal Yield Strength, The Metallurgy, Welding and Qualification of Microalloyed (HSLA) steel Weldments” AWS. Texas. pp. 572-573. 1990.

[Dieter, 1988] Dieter, G.E., *Mechanical Metallurgy*. SI Metric Edition, McGraw –Hill, ISBN 0-07-100406-8. pp. 252. 1988.

[Dolby, 1983] Dolby, R.E., “Advances in Welding Metallurgy of Steel.” Metals Technology. Vol. 10(9): pp.349-362. 1983.

[Easterling, 1992] Easterling, K., Introduction to Physical Metallurgy of Welding. 2nd ed., Butterworth-Heinemann Ltd. 1992.

[El-Khazen, 2009] John El-Khazen., “Low temperature Cleavage Fracture of Microalloyed Bainitic Plate Steels”, Masters Thesis, Queen’s University. 2009

[Gladman, 1997] Gladman, T., The Physical Metallurgy of Microalloyed Steels. The Institute of Materials. London. pp.16 1997.

[Godden, 1981] Godden, M.J., and Boyd, J.D., “Characterization of Microstructures in Weld Heat-Affected Zones by Electron Microscopy.” Proc.Microstructural Science. 13th Annual Technical Meeting of the International Metallographic Society. Elsevier North-Holland Inc. Vol. 9: pp. 343-354.1981.

[Gourd, 1980] Gourd.L.M., Principles of Welding Technology. Edward Arnold.1980.

[Gunuraj, 1999] Gunaraj, V., and Murugan, N., “Application of Response Surface Methodology of Predicting Weld Bead Quality in Submerged Arc Welding in Pipes.” *Journal of Materials Technology*. Vol. 88(1): pp. 266-275. 1999.

[Gupta, 1987] Gupta, P.C., Ghose, P.K., Sharma, S.K., “Effect of Polarity on Melting Rate in Submerged Arc Welding.” *Indian Welding Journal*. Volume 19 (3): pp. 228 - 233. 1987.

[Hamad, 2008] Hamad, F., Collins, L., and Volkers, R., “Effects of GMAW Procedure on the Heat Affected Zone (HAZ) Toughness of X80 (Grade 550) Linepipe.” *Proceedings of IPC2008, 7th International Pipeline Conference*. September 29-October 3, 2008, Calgary, Alberta, Canada.

[Hillenbrand, 2002] Hillenbrand, H.G., Heckmann, C.J., and Niederhoff, K.A., “X80 Line Pipe for Large Diameter High Strength Pipelines.” *APIA Annual Conference. X80 Pipeline Workshop*. October 27-30. Hobart. Australia. 2002.

[Hiroshi, 2006] Hiroshi, Nakata., Chikara, Kami., Nobuyuki, Mathuo., “Development of API X80 Grade Electric Resistance Welding Line Pipe With Excellent Low temperature Toughness.” *JFE technical Report*. Vol.12.2006.

[Hoskins, 2002] Hoskins, S.J., “The Weldability of TMCP Microalloyed Structural Steels”, *Masters Thesis, University of Alberta*. 2002.

[Houldcroft, 1989] Houldcroft, P.T., *SUBMERGED-Arc Welding*. 2nd Edition Abington Publishing..Cambridge, England.1989.

[Hrivnak, 1995] Hrivnak, I., “Granular Bainite in High Strength Steel Welds.” *Metallic Materials*. Vol. 33(1):pp. 24-30. 1995.

[Imai, 2002] Imai, S., “General Properties of TMCP Steels.” Proceedings of the Twelfth (2002) International Offshore and Polar Engineering Conference, Kitakyushu, Japan. May 26–31. 2002.

[Jackson, 1950] Jackson, C. E . and Shrubbsall, A.E., “Weld J”, Vol. 29(5). pp. 231-242. 1950.

[Joarder, 1991] Joarder, A., and Sarma, D.S., “Bainite Structures in 0.2C-3.6Ni Steel.” Materials Transactions. JIM. Japan. Vol. 32(8): pp. 705-714.1991.

[Jonsson, 2011] Unpublished work of Katherine Jonsson. MSc. Candidate. University of Alberta. Edmonton, Alberta. Canada.

[Kasuya, 1993] Kasuya, T., and Yurioka, N., “Prediction of Welding Thermal History by Comprehensive Solution.” Welding Journal. Vol. 72 (3): pp. 107-s-115-s.1993.

[Kielhorn, 2001] Kielhorn, W.H., Adonyi, Y., Holdren, R.L., Horrocks, R.C., Nissley, N.E., “Survey of Joining, Cutting, and Allied Processes.” AWS Welding Handbook – Volume 1: Welding Science and Technology. American Welding Society. Miami. 2001.

[Kim, 2005] Kim, B., Uhm, S., Lee, C., Lee, J., and An, Y., “Effects of Inclusions and Microstructures on Impact Energy of High Heat-Input Submerged-Arc-Weld Metals.” Journal of Engineering Materials and Technology. Vol. 127(2): pp. 204-213. 2005.

[Koo, 2004] Koo, J.Y., Luton, M.J., Bangaru, N.V., Petkovic, R.A., Fairchild, D.P., Petersen, C.W., Asahi, H., Hara, T., Terada, Y., Sugiyama, M., Tamehiro, H., Komizo, Y., Okaguchi, S., Hamada, M., Yamamoto, A., Takeuchi, I., “Metallurgical Design of Ultra-High Strength Steels for Gas Pipelines.” Electronic Design. Volume 52 (2): 2 - 10. 2004.

[Kou, 2002] Kou, S., Welding Metallurgy. 2nd Ed., John Wiley and Sons, Inc. 2002.

[Krauss, 2005] Krauss, George., Steels: Processing, Structure, And Performance. 2005 Ed., ASM International.2005

[Kubli, 1956] Kubli, R.A., Shrubbsall, H.I., “Multipower Submerged-Arc Welding of Pressure Vessels and Pipe.” Welding Journal. pp. 1128 – 1135. November 1956.

[Kurny, 2002] Kurny, A.S.W., Introduction to Metal Joining Technology. 1st Ed., The Publications-cum-Information Office. Directorate of Advisory, Extension and Research Services. Dhaka.2002.

[Laitinen, 2006] Laitinen, R., “Improvement of Weld HAZ Toughness at Low Heat Input by Controlling the Distribution of M-A constituents.” Academic Dissertation to be Presented with the Assent of the Faculty of Technology. University of Oulu. Linnanmaa. pp. 22-24. 2006.

[Lau, 1987] Lau, T.W., North, T.H., and Glover, A.G., Proc. 6th Int. Conf. on Offshore Mechanics and Arctic Engineering, OMAE, Houston, TX. Vol.3: pp.57-69. 1987.

[Lee, 2002] Lee, W.B., Hong, S.G., Park, C.G., and Park, S.H., “Carbide precipitation and high –temperature strength of hot –rolled high-strength, low-alloy steels containing Nb and Mo.” Metallurgical and Materials Transactions A. Vol. 33(6): pp. 1689-1698. June .2002.

[Liessem, 2004] Liessem, A., Erdelen-Peppler, M., “A Critical View on the Significance of HAZ Toughness Testing” (Paper IPC04-0315). International Pipeline Conference. Calgary. 2004.

[Liessem, 2007] Liessem, Andreas., Knauf, Gerhard., Zimmermann, Steffen., “Strain Based Design- What the Contribution of a Pipe Manufacturer Can Be. ” International Society of Offshore and Polar Engineers. Paper No. ISOPE-2007-SBD14. pp.1-8.2007

[Lincoln, 1994] Lincoln Electric, "How to Make Single Electrode Submerged Arc Welds." Technical Bulletin C5.600. 1994.

[Liu, 1993] Liu, W.J., "Computer Simulation of VC Precipitation at Moving Gamma/Alpha Interfaces." Metallurgical Transactions A, vol. 24A(10): pp. 2195. October. 1993.

[Losz, 1990] Losz, J.M.B., and Challenger, K.D., "HAZ Microstructures in HSLA Steel Weldments." Proc. First United States- Japan Symposium on Advances in Welding Metallurgy. American Welding Society. Miami, FL. Pp. 323-357. 1990.

[Lu, 2009] Jungfang, L., "Quantitative Microstructural Characterization of Microalloyed Steel," PhD Dissertation, University of Alberta. 2009.

[Mackenzie, 2004] Mackenzie Gathering System. Project Specification for Arctic Engineering. Engineering Design. Vol. 2. 2004.

[Madariaga, 2001] Madariaga, . I., Gutierrez, I., and Bhadeshia, H. K. D. H., "Acicular Ferrite Morphologies in a Medium-Carbon Microalloyed Steel." Metallurgical and Materials Transactions A. Vol. 32: pp. 2187. 2001.

[Mangonon, 1976] Mangonon, P.L., "Effect of Alloying Elements on the Microstructure and Properties of a Hot-Rolled Low-Carbon Low-Alloy Bainitic Steel." Metall. Trans. A. Vol. 7(A):pp. 1389-1400.1976.

[Matsuda, 1991] Matsuda, F., Li, Z., Bernasovsky, P., Ishihara, K., and Okada, H., "An Investigation on the Behaviour of the M-A Constituent in Simulated HAZ of HSLA Steels." Welding in the World (UK). Vol. 29(9-10): pp. 307-313.1991.

[Medina, 1999] Medina, S.F., Chapa, M., Valles, P., Quispe, A. and Vega, M.I., "The

Influence of Ti and N Contents on Austenite Grain Control and Precipitate Size in Structural Steels.” ISIJ International. vol. 39(9): pp. 930. 1999.

[Mitchell, 1985] Mitchell, P.S., Hart, P.H.M., and Morrison, W.B., “The Effect of Microalloying on HAZ Toughness.” Proc. Microalloying’95, Iron and Steel Society Inc, Warrendale. Pp.149-162.1985.

[NACE, 2009] ANSI/NACE MR 0175/ISO 15156-1, “Petroleum and natural gas industries — Materials for use in H₂S-containing environments in oil and gas production — Part 2: Cracking-resistant carbon and low-alloy steels, and the use of cast irons.” NACE International. 2009.

[Narita, 1975] Narita, K., “Physical Chemistry of the Groups IVa (Ti, Zr), Va (V, Nb, Ta) and the Rare Earth Elements in Steel.” Transactions ISIJ. vol. 15: pp. 145. 1975.

[Niles, 1975] Niles, R. W. and Jackson C. E., “Weld Thermal Efficiency of the GTAW Process.” Welding Journal (Miami, FL). Vol. 54(1). pp. 25-32. 1975.

[Ohmori, 1992] Ohmori, Y., Ohtsubo, H., Jung, Y.C., Okaguchi, S., and Ohtani, H., “Morphology on Bainite and Widmanstätten Ferrite.” Proc. Pacific Rim Symposium on the Roles of Shear and Diffusion in the Formation of Plate – Shaped Transformation Products. Minerals, Metals and Materials Society . Warrendale, PA. pp. 1981-1989. 1992.

[Otterberg, 1980] Otterberg, R., Sandstrom, R., and Sandberg, A., “Influence of Widmanstätten Ferrite on Mechanical Properties of Microalloyed Steels.” Met. Tech. Vol. 7(10): pp.397-408.1980.

[Patchet, 1998] Patchet, B.M., Welding Metallurgy, The Metals Blue Book – Welding Filler Metals. 2nd ed. CASTI Pub. and American Welding Society (AWS), 1998.

[Pepin, 2009] Pepin, J. T., “Effects of Submerged Arc Weld (SAW) Parameters on Bead

Geometry and Notch-Toughness for X70 and X80 Linepipe Steels”, Masters Thesis, University of Alberta. 2009.

[Petch, 1953] Petch,N.J., “The Cleavage Strength of Polycrystals,” Journal of the Iron and Steel Institute. Vol.174.pp. 25-28. 1953.

[Pollack, 1988] Pollack, H., Materials Science and Metallurgy. 4th Ed., Prentice Hall.1988.

[Poorhaydari, 2005] Kioumar, P.A.,Pachett,B.M., and Ivey, D.G., “Estimation of Cooling Rate in the Welding of Plates with Intermediate Thickness.”Welding Journal. pp.149-s-155-s. October, 2005.

[Porter, 1981] Porter, D.A., and Easterling, K.E., Phase Transformation in Metals and Alloys, Van Nostrand Reinhold, Wokingham, Berkshire. 1981.

[Radu, 2009] Radu, Iulian., PCL Industrial Contractors Inc. Private Communication. 2009.

[Ranasen, 1972]Rasanen, B., Tenkula, J., “Phase Changes in the Welded Joints of Constructional Steels.” Scandinavian Journal of Metallurgy. Volume 1 (2): pp. 75 – 80.1972.

[Samuel, 1984] Samuel, F.H., “Some Aspects of Bainites in an HSLA Steel.” Z. Metallkd. Vol. 75(12): pp.967-972.1984.

[SAW guide, ---] Submerged Arc Welding Guide. Guide for Processes and Equipment. Section 1(C5.600). Lincoln Electric.Cleveland, Ohio,USA. pp.3

[SAW, 1982] Submerged Arc Welding. Miller Electric MFG. CO., Appleton, WI, USA. pp. 8-20. 1982.

[Sharma, 2009] Sharma, U., “Microstructural Characterization of Microalloyed Linepipe Steels”, Masters Thesis, University of Alberta. 2001.

[Shi, 2008] Shi, Y., Han, Z., “Effect of Weld Thermal Cycle on Microstructure and Fracture Toughness of Simulated Heat-Affected Zone For A 800 Mpa Grade High Strength Low Alloy Steel.” Journal Of Materials Processing Technology. Vol. 207(1-3): pp. 30-39. October, 2008.

[Shiga, 1990] Shiga, C.,”Effects of Steelmaking , Alloying and Rolling Variables on the HAZ Structure and Properties in Microalloyed Plate and Linepipe.” Proc. The Metallurgy, Welding and Qualification of Microalloyed (HSLA) Steel Weldments. American Welding Society. pp.327-350. 1990.

[Smartweld version 2.1, 2011] The SmartWeld App files are the result of a Sandia National Laboratories collaborative project (1993-2011) with principal investigators Phillip Fuerschbach (philmar@q.com) and Richard Eisler (roenrick@msn.com). Downloaded from the website <http://smartweld.sourceforge.net/>- accessed on June 20th, 2011.

[Smith, 1993] Smith, W., Structure and Properties of Engineering Alloys. 2nd Ed., McGraw Hill. 1993.

[Spanos, 1995] Spanos, G., Fonda, R. W., Vandermeer, R. A., and Matuszeski, A., “Microstructural Changes in HSLA-100 Steel Thermally Cycled to Simulate the Heat-Affected Zone During Welding.” Metall. Mater. Trans. A. USA. Vol. 26A(12): pp. 3277-3293. 1995.

[Thaulow, 1985] Thaulow, C., Gunleiksrud, A., Paauw, A. J., and Naess, O. J., “Heat Affected Zone Toughness of a Low Carbon Microalloyed Steel.” Met. Constr. Vol. 17(2): pp. 94-99. 1985.

[The Fabricator, 2010] <http://www.thefabricator.com/article/arcwelding/improving-productivity-with-submerged-arc-welding>.-Online source accessed on 29th August, 2012.

[Thomas, 1977] Thomas Jr., R. D., “Submerged Arc Welding of HSLA Steel for Low-Temperature Services.” Metal Progress, Vol. 111(4): pp. 30-36. 1977.

[Tuliani, 1969] Tuliani, S.S., Boniszewski, T., and Eaton, N. F., “Notch Toughness of Commercial Submerged-Arc Weld Metal.” Welding and Metal Fabrication. Vol. 37(8): pp. 327-339. 1969.

[Voort, 2004] Voort, V., and George F., ASM Handbook, Volume 09 - Metallography and Microstructures. ASM International. 2004.

[Wang, 1992] Wang, S-C., Yang, J-R., “Effects of Chemical Composition, Rolling and Cooling Conditions on The Amount of Martensite/Austenite (M/A) Constituent Formation in Low Carbon Bainitic Steels.” Materials Science and Engineering A. Vol. 154(1): pp.43-49.June, 1992.

[Wells, 1952]Wells,A.A., “Weld J.”Vol. 31(5). Pp. 63-267.1952.

[Wemen, 2003]Weman, K., “Chapter 7: Submerged Arc Welding.” Welding Process. Handbook. Woodhead Publishing Limited, England. 2003.

[Widgery, 2006] Widgery, David., “Consumables for X100 girth Welding.” International Institute of Welding. IIW Doc No. XI-E-1004-06.2006.

[Yang, 1986] Yang, J. R., Bhadeshia. H.K.D.H., “Advances in Welding Science and Technology” ed. S. A. David. ASM. Metals Park. Ohio, USA. pp.187-191.1986.

[Yang, 1992] Yang, L. J., Chandel, R. S., and Bibby, M. J., “The Effects of Process

Variables on the Bead Width of Submerged Arc Weld Deposits.” *Journal of Materials Processing Technology*. Vol. 29: pp. 133-134. 1992.

[Yang, 2008] Yang Y., “The Effect of Submerged Arc Welding Parameters On The Properties of Pressure Vessel and Wind Turbine Tower Steels”, Masters Thesis, University of Saskatchewan. 2008.

[Yang, 2009] Yang, H.S., Bhadeshia, H. K. D. H., “Austenite Grain Size and the Martensite-Start Temperature.” *Scripta Materialia*, Vol. 60: pp.493-495. 2009.

[Zhou, 2010] Zhou, M., DU, L., and Liu, X., “Microstructure and Mechanical Properties of X80 Pipeline Steels in Different Cooling Schedules.” *Acta Metall. Sin. (Engl. Lett.)* Vol.23(3): pp.171-175. June, 2010.

Appendix A

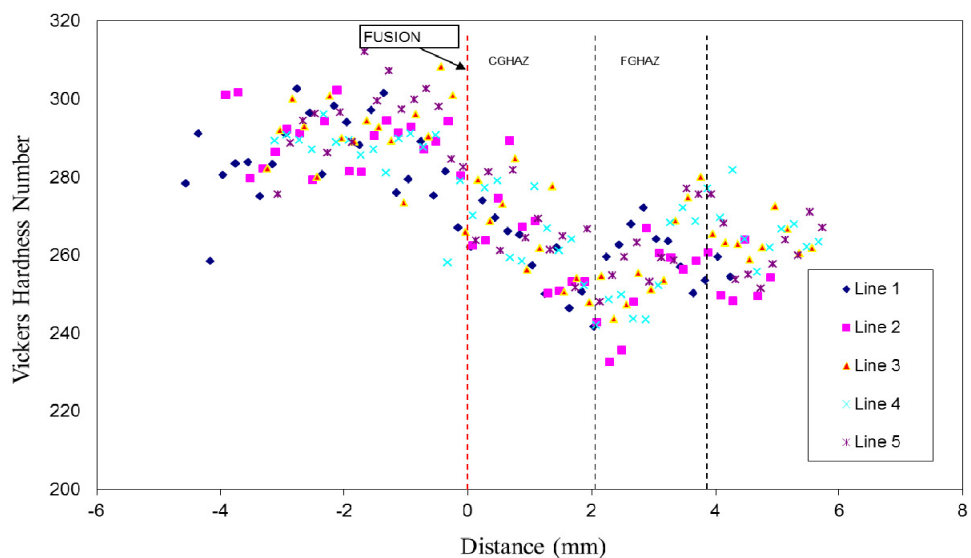


Figure B-1: Microhardness variation of Steel X welded using 1.75 kJ/mm heat input.

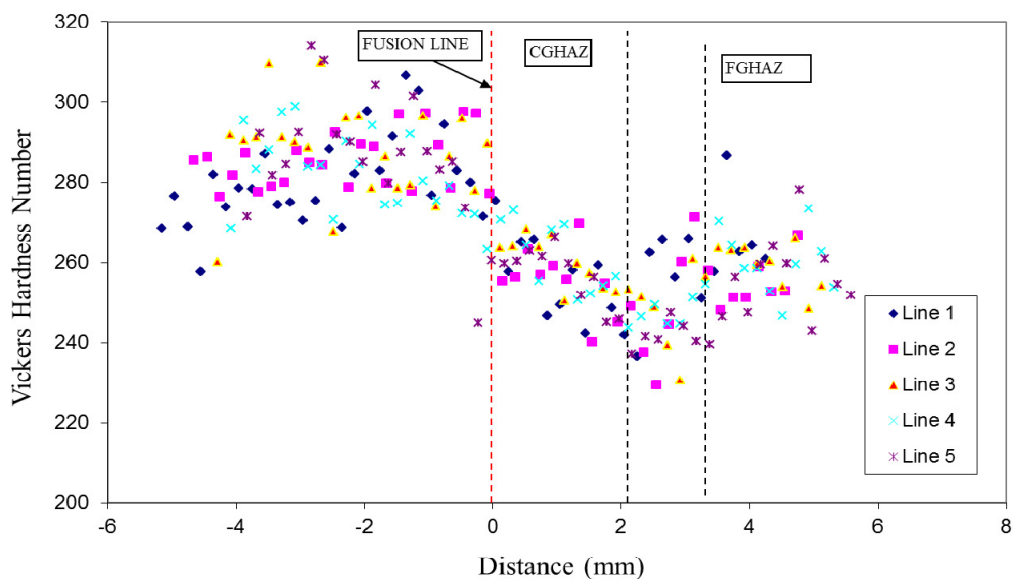


Figure B-2: Microhardness variation of Steel X welded using 2.00 kJ/mm heat input - tandem electrode.

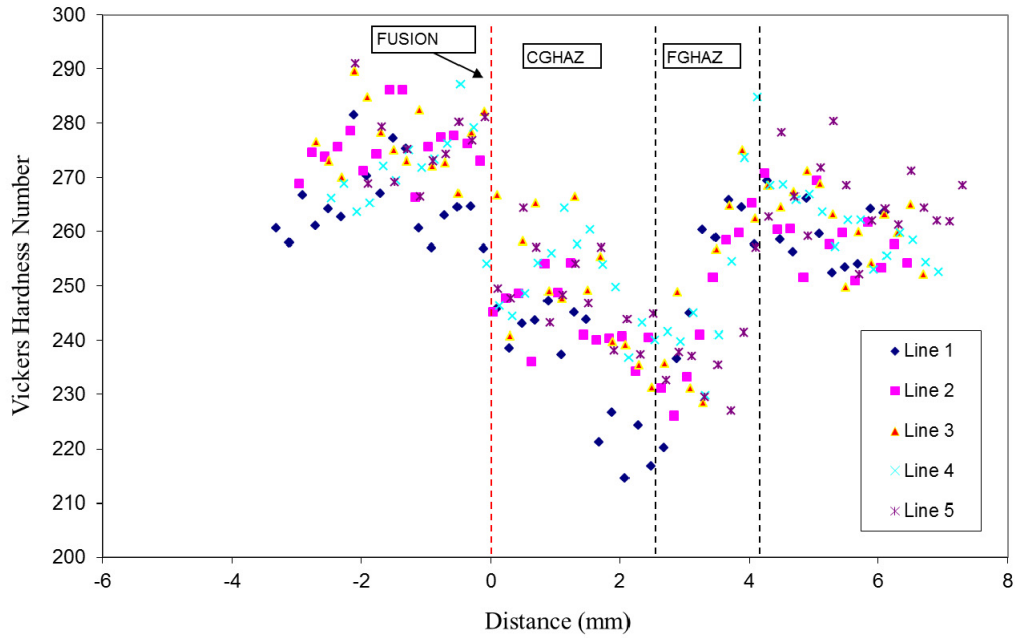


Figure B-3: Microhardness variation of Steel X welded using 2.25 kJ/mm heat input - tandem electrode.

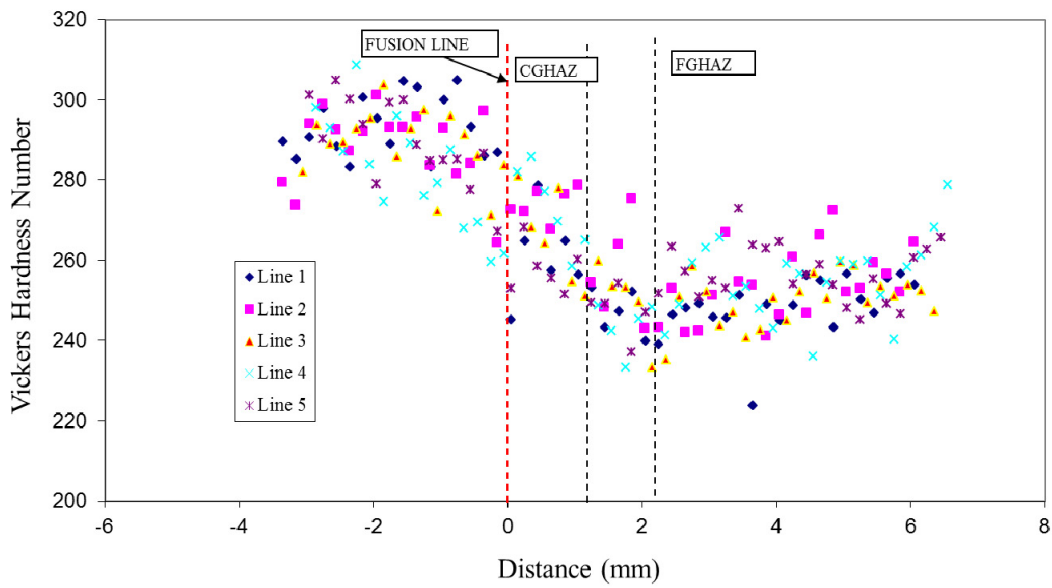


Figure B-4: Microhardness variation of Steel X welded using 1.5 kJ/mm heat input - single electrode.

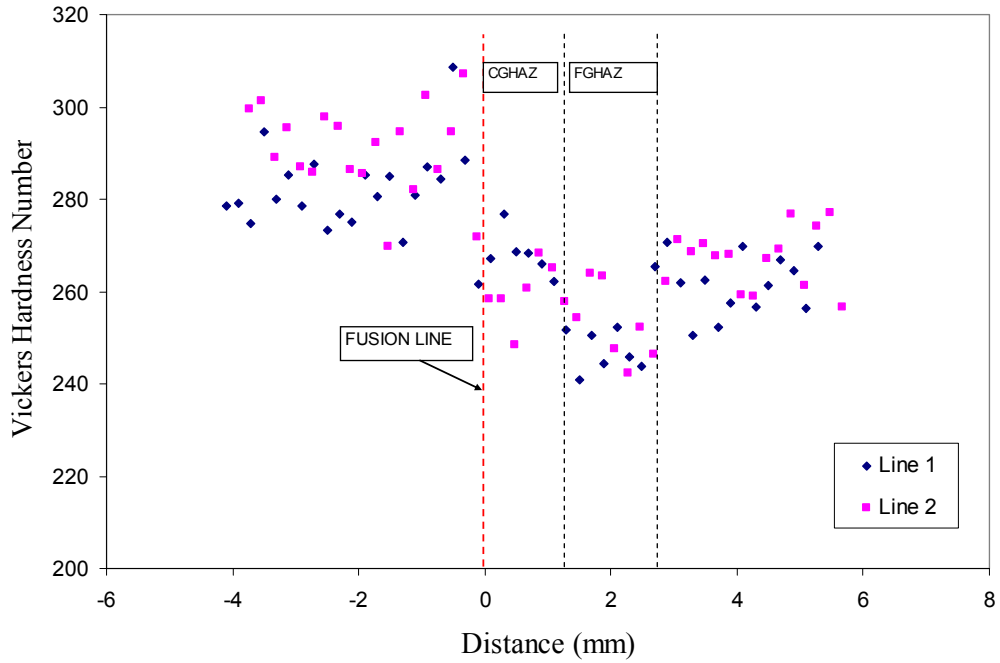


Figure B-5: Microhardness variation of Steel X welded using 1.75 kJ/mm heat input - single electrode.

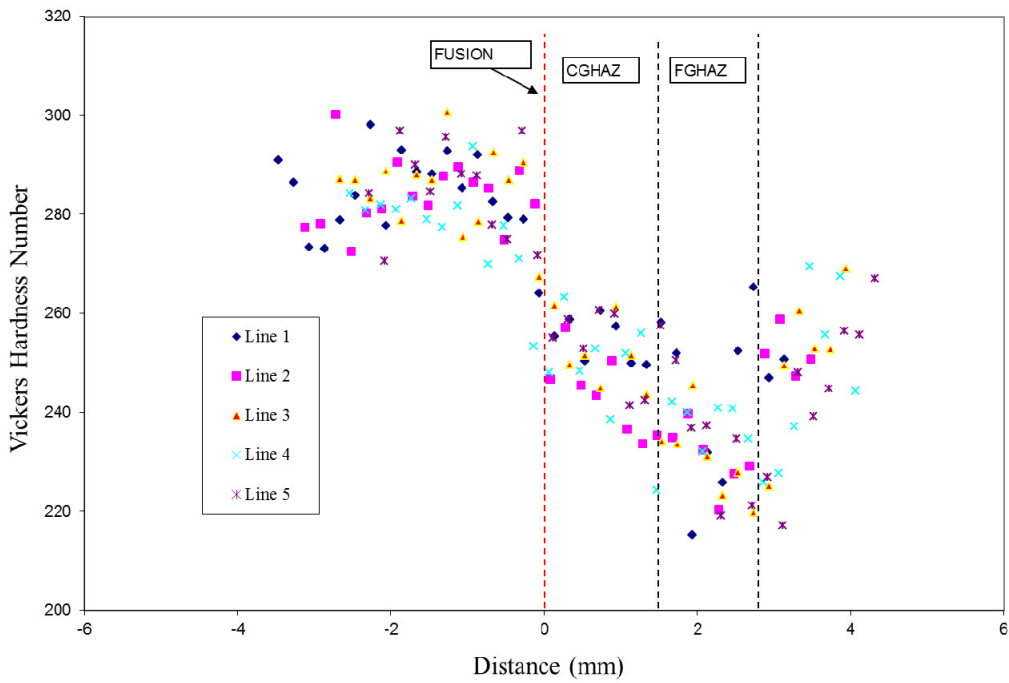


Figure B-6: Microhardness variation of Steel Y welded using 1.75 kJ/mm heat input - tandem electrode.

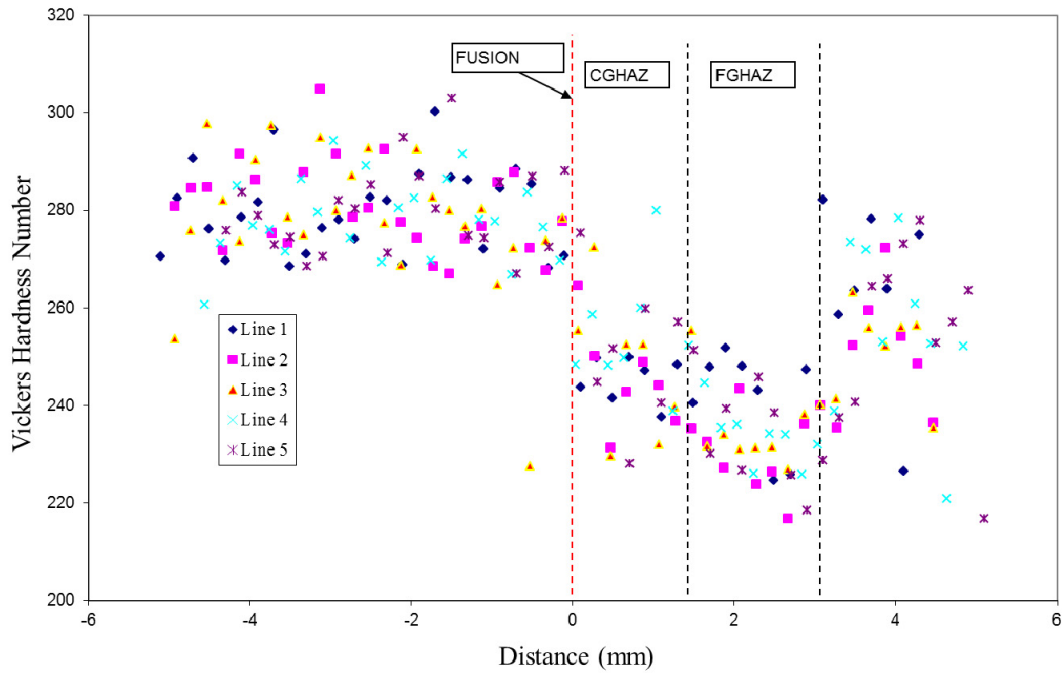


Figure B-7: Microhardness variation of Steel Y welded using 2.00 kJ/mm heat input - tandem electrode.

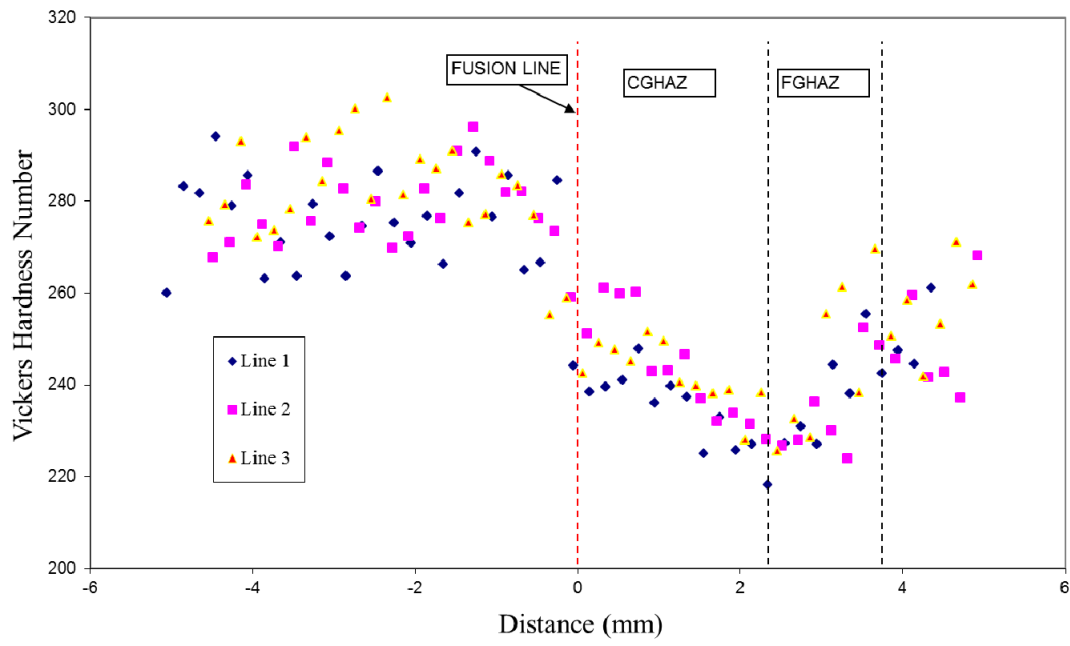


Figure B-8: Microhardness variation of Steel Y welded using 2.25 kJ/mm heat input - tandem electrode.

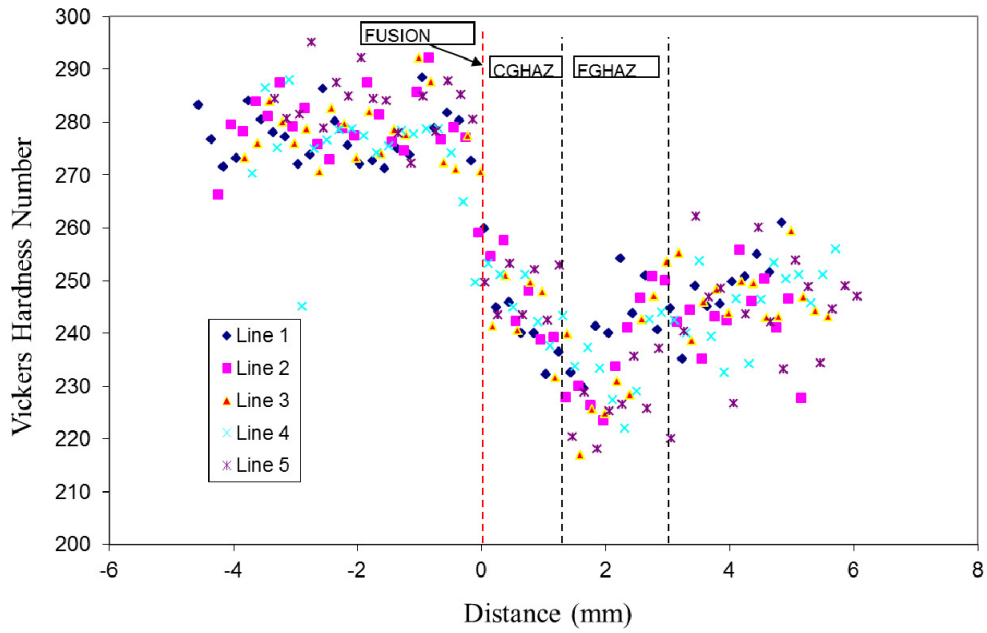


Figure B-9: Microhardness variation of Steel Y welded using 1.5 kJ/mm heat input - single electrode.

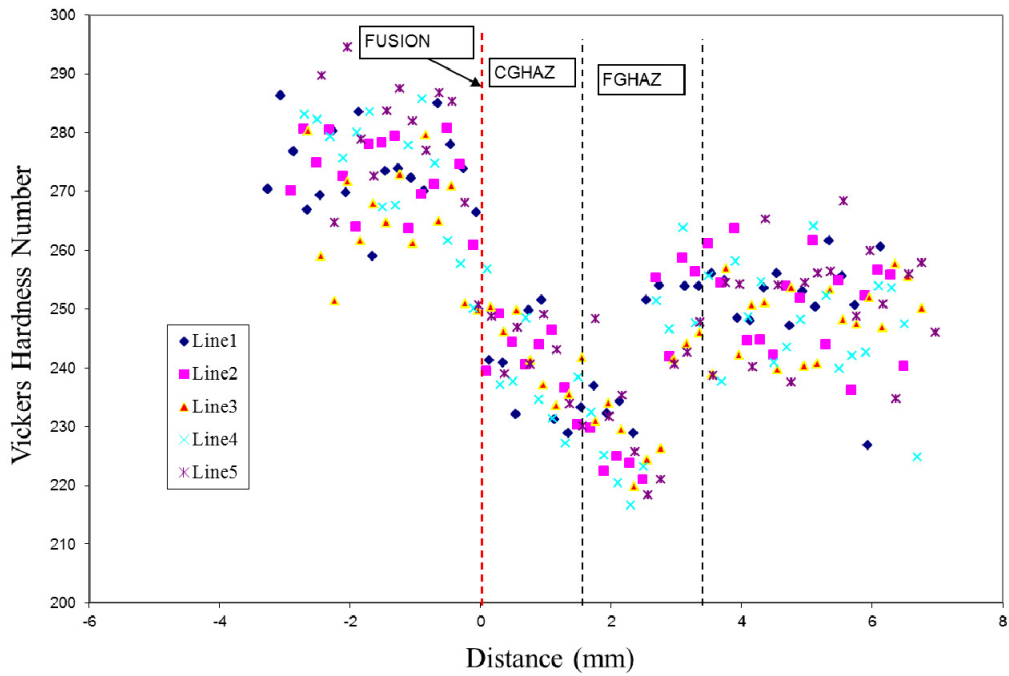


Figure B-10: Microhardness variation of Steel Y welded using 1.75 kJ/mm heat input - single electrode.